Optical Studies of Thermoluminescent Materials

By
Phillip James Fox, B.Sc.(Hons)

A Thesis
presented for the degree of
DOCTOR OF PHILOSOPHY
in the
Department of Physics and Mathematical Physics
UNIVERSITY OF ADELAIDE

June 1990

Contents

Summary

The research carried out concerned the physics of phenomena which have arisen in the application of thermoluminescence (TL) to geological and archaeological dating.

In order to better understand the physics of the processes involved it is useful to examine the emission spectra of the TL materials being studied, instead of simply the conventional two-dimensional "glow-curve". This thesis begins by describing the theory and development of an extremely sensitive TL spectrometer which has been built in this laboratory, particularly the modifications made by the author. These have extended the spectral range into the red (up to 740 nm) and ultra-violet (down to 250 nm). The analysis procedures have been developed considerably.

The following chapter describes the application of this spectroscopic technique to a range of different minerals of relevance to TL, with brief comments on the physics involved. These materials were TL phosphors, four calcite samples, several sulphur activated minerals and some unusual feldspar samples.

The next chapter describes the topic which has been studied in greatest detail, namely the effect on the emission spectra of several Australian quartz samples, after they had been bleached by three different wavelengths of light for various times. The interpretation of the results obtained is discussed, with emphasis on the observation that for some of the quartz samples, emission centers above 3.0 eV appear to be preferentially bleached.

The following short chapter details the modifications to the glow oven so that it could measure the photoluminescence (PL) of some of the quartz samples described earlier. The PL is stimulated by the intense exposure to optical light at 550 nm. The

results indicted the importance of a shallow trap (corresponding to the 110°C trap in quartz) in the decay process and provide data to compare with the results of the following chapter.

The penultimate chapter shows some results of attempts to try to kinetically model the PL decay process. A computer was used to solve the simultaneous differential kinetic equations which describe the movement of charge carriers within the crystal lattice. Several different models were studied and the results seemed to show a close link between the sensitive 325°C trap and a thermally shallow trap. There was also the possibility that the conduction band was relatively unimportant for decay curves measured at low temperatures.

The final chapter provides a brief summary with suggestions for further modifications to the equipment and for future research.

Statement

This thesis contains no material which has been accepted for the award of any other degree or diploma in any university, and to the best of the author's knowledge and belief, contains no material previously published or written by another person, except where due reference is made in the text.

The author consents to the thesis being available for photocopying and loan.

Phillip J. Fox

Adelaide

June, 1990

Acknowledgements

Firstly I would like to thank my supervisor Professor J.R. Prescott, without whose help and guidance this Ph.D. project would not have been possible. I would also like to thank the other members of the Archaeometry group, J. Hutton, G. Robertson, N. Spooner and particularly R. Akber for their help and for useful discussions during my time with them.

Much of the computer work could only have been done with the help of B. Fuller of the electronics workshop and K. Briggs wrote many of the plotting routines.

I would also like to thank the workshop, particularly G. Eames for the fabrication of parts of the equipment.

Thanks must also go to N. Wild for his help in fixing the equipment whenever it went wrong.

The atmosphere in any department is important in providing a happy working environment and that in this Physics department is an example to all. My thanks go to all the other post–graduate students, academic members of staff and other members of staff for making my stay so enjoyable.

On a more personal note I would like to thank my family for their support, especially my Mother and Father. Finally I would like to thank Chiew–Lee.

This thesis was written using the "LaTeX" document preparation system. All the figures were plotted using either "M11DRAW" or "IDL".

Chapter 1

Introduction

1.1 Introduction and History

According to the Chamber's Dictionary of Science and Technology, thermoluminescence (usually abbreviated to "TL") is the "release of light by previously irradiated phosphors upon subsequent heating". TL is actually a surprisingly common phenomenon, which is exhibited by over two-thirds of all known minerals, in addition to some less likely materials such as fish scales, bones, dental enamel, organic solids, metalo-organic compounds (Horowitz 1984).

Historically TL has been known about for many centuries, at least from medieval times, but was probably first reported scientifically by Robert Boyle in 1663. He observed a "glimmering light" from a diamond heated against his "Naked Body" (Becker 1973). In 1897 J.J.Thompson, writing in Smithsonian Reports, credits Prof. E. Wiedemann with the naming of the process as "thermoluminescence" and he is also considered to have been the first to perform detailed scientific experiments on TL (Becker 1974). Of interest to this thesis is the first detailed study of the spectra of a TL material reported by Morse (1905). In this study two fluorite samples were photographed whilst being heated and thus their spectrum recorded. Many narrow

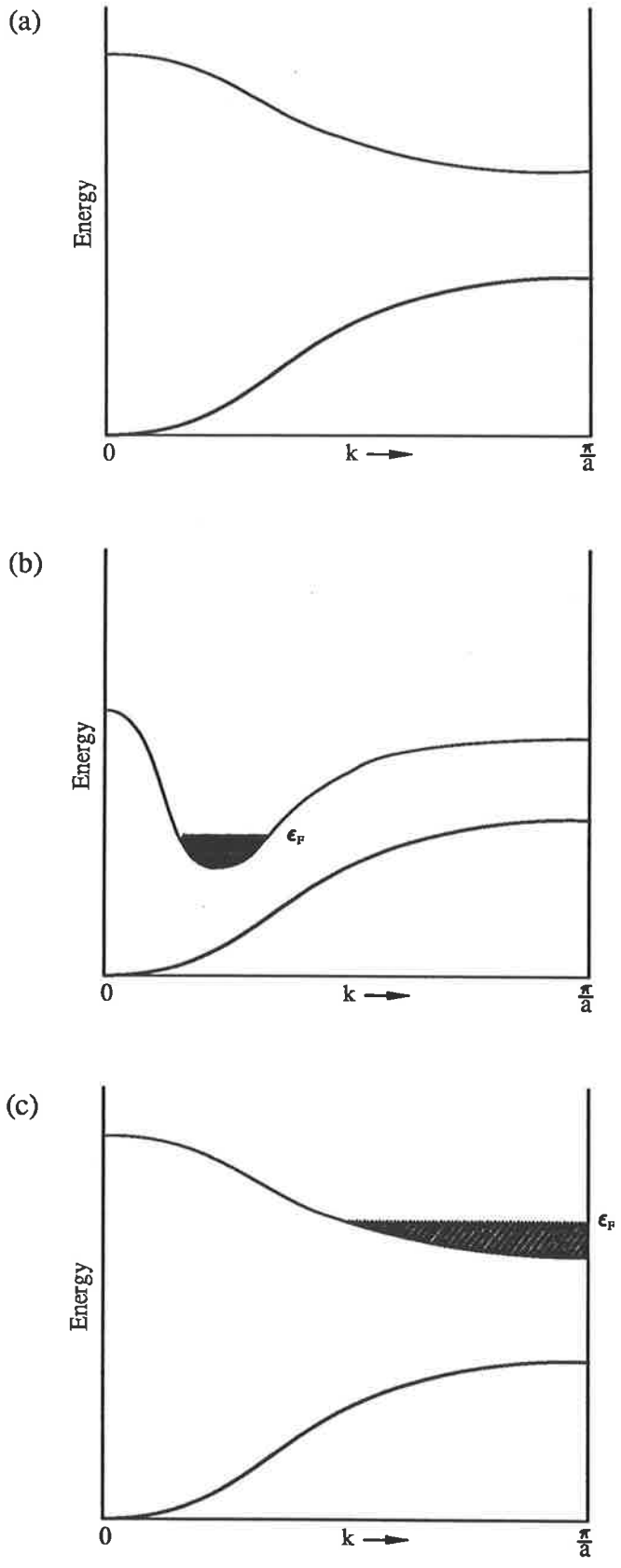

Figure 1.1: Occupied states and band structures of a) an insulator, b) a metal or semimetal because of band overlap and c) a metal because of electron concentration. k is the lattice wavevector, π/a is the boundary of the first Brillouin zone and ϵ_F is the Fermi level. The shaded regions represent electron occupancy (after Kittel 1976).

band wavelengths were measured but no conclusions about the impurities responsible for the emission could be drawn.

1.2 Thermoluminescence

Central to the mechanism for the production of TL is the band theory of solids. The free electron model can explain quite adequately the heat capacity, thermal conductivity, electrical conductivity, magnetic susceptibility of metals but cannot explain, for example, the 10^{32} ohm-cm resistivity range between a good insulator and a good conductor (Kittel 1976). The reason for this is that the free electron model ignores the interaction between the conduction electrons and the ion cores of the crystal. When a periodic potential is introduced into the simple model, it turns out that the electrons form energy band with band gaps in between, where wavelike electron orbitals are forbidden.

If one or more of the bands is only 10–90 percent filled then the solid behaves as a metal; if the bands are entirely full except for one or two bands slightly filled or empty, the crystal is a semi-conductor or semi-metal; and if the energy bands are filled or empty then no electrons can move in an applied electric field and the crystal is an insulator (see figure 1.1).

Most important for the production of TL is the role extrinsic and intrinsic crystal defects play in an insulator. They cause localised breakdowns in the regular lattice band structure, causing localised energy levels to appear within the energy gap. These "traps" may capture electrons and holes liberated when an electron is raised from the valence band to the conduction band (transition (a) in figure 1.2).

In the case of TL, light is given off when these trapped electron or holes are released when the crystal is heated. Figure 1.2 shows that there are three types of luminescent transition which results from the recombination of a released charge carrier with a carrier, of opposite charge, that is still trapped (termed a centre). These are the band-to-band, band-to-centre and trap-to-centre transitions. If the transition involves the absorption or emission of a lattice phonon, i.e. the transfer of crystal momentum, then the process is termed indirect (transition (a) and (b) in figure 1.2), whilst for direct transitions, no momentum transfer is needed (transition (c) and (d) in figure 1.2). Vital to the production of TL, is whether or not each transition will be radiative. For direct transitions there is a relatively large probability that a photon will be emitted since it would require several phonons to be created at once to dissipate the electron's energy (a typical phonon energy would lie between 0.02–0.05eV, Kittel 1976). However the energy released in an indirect transition is considerably less than the band-gap energy and so it can be released either by phonons (non-radiatively) or by photons (radiatively) (McKeever 1984). The probability of a radiative to a non-radiative transition is dependent on the crystal temperature by a factor $\exp(-W/kT)$, where k is Boltzmann's constant, T is the temperature and W is the thermal energy required to release a trapped charge carrier from a luminescence center. The increase in temperature may cause this charge carrier to be subsequently retrapped at a non-radiative or "killer" center (Schön 1951 and Klasens 1946).

The length of time an electron or hole remains trapped depends on the thermal depth, E, of the trap relative to its respective band edge, the crystal lattice temperature T, and a factor s which depends on the number of times per second a trapped

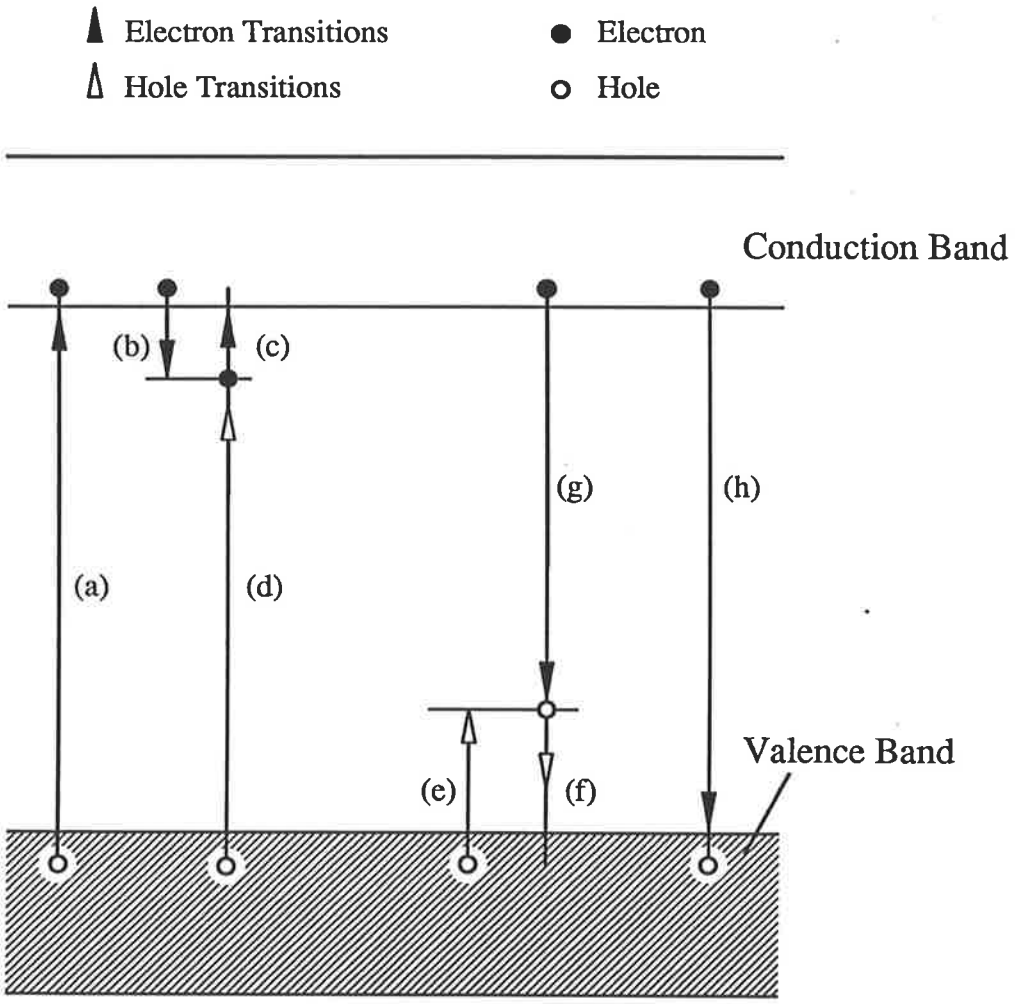

Figure 1.2: Schematic band diagram showing the electronic transitions in an insulator: a) ionization; b) and e) electron and hole trapping respectively; c) and f) electron and hole release; d) and g) indirect recombination; h) direct recombination.

electron interacts with the crystal phonons multiplied by a transition probability (McKeever 1984). Assuming there is no retrapping of the released charge carrier, then to first order, the equation which relates the rate of release of trapped charge carriers to the crystal temperature is

$$dn/dt = -sn\exp(-E/kT) \tag{1.1}$$

where n is the concentration of trapped electrons or holes and t is the time. With a linear heating rate β, equal to dt/dt, the luminescence intensity, $I(t)$, which is proportional to $-dn/dt$, is

$$I(t) = n_0 s\exp(-E/kT)\exp\left[-s/\beta\int_{T_0}^{T}\exp(-E/kT)\,dt\right], \tag{1.2}$$

where T_0 is the starting temperature. If retrapping is not negligible and there are N available retrapping sites, then to second order

$$I(t) = n_0^2 s\exp(-E/kT)/N\left[1+\frac{n_0 s}{k\beta}\int_{T_0}^{T}\exp(-E/kT)\,dt\right]^2. \tag{1.3}$$

1.3 Thermoluminescence Applications

Some of the more important applications of TL are discussed below.

1.3.1 Dating

For some materials electron or hole trapping lifetimes can be greater than 10^6years, and so it was realised that one practical use of TL could be as a technique for dating (Aitken 1985). Radioactivity in the environment, due to uranium, thorium and potassium, causes the gradual build up of trapped charge carriers. This dose, which is gradually absorbed by the crystal, is directly related to the amount of TL which

is subsequently measured. If the dose rate of the environment as well as the sensitivity of the sample are known, then the age since the sample was last heated can be calculated simply from the so–called "age equation":

$$Age = \frac{Natural\ TL}{(TL/unit\ radiation\ dose) \times (radiation\ dose\ rate)}. \qquad (1.4)$$

The crystal sensitivity is determined by use of artificial laboratory sources and the environmental dose rate by *in situ* phosphors or γ-ray spectroscopy and laboratory α-counting of a portion of the "environment". In reality, equation 1.4 needs some modification to account for the different efficiencies of the various types of radiation and for the non-linearity of the TL growth curve – a plot of the TL against dose (Aitken 1985).

Probably the main application of this has been to measure the TL of quartz crystals and other materials extracted from pottery samples. The age corresponds to the time since the pot was last fired. See for example Robertson and Prescott (1988).

A relatively recent application of TL dating (Debenham and Aitken 1984, Smith *et al* 1985) has been to stalagmitic (speleothem) calcite. Its importance lies in its use to provide age limits to the hominid occupation of limestone caves (Debenham and Aitken 1984). In their dating method the 280°C TL emission from calcite grains is viewed by a photomultiplier through heat absorbing and blue filters. This results in the removal of all the TL emission above 500 nm, which can include a signal which is insensitive to radiation exposure (Smith *et al* 1989). In chapter four the results of some studies of a selection of calcite samples is given. The study was a collaboration involving the use of both TL and electron spin resonance and demonstrates the effectiveness of such studies.

1.3.2 Dating Sediments

The use of TL in sediment dating has great potential to be developed into a technique for determining the chronology of the last million years in a wide range of situations (Wintle and Huntley 1982). The results of experiments presented in this thesis are of direct interest to recent developments in the field of sediment dating.

Increases in the amount of TL with depth observed in undersea sediment cores mean that relative ages of parts of these cores can be found (Bothner and Johnson 1969, Huntley and Johnson 1976). The mechanism by which the TL of the sediments is zeroed was shown to be due to its exposure to sunlight before being laid down (Wintle and Huntley 1980).

Based on this finding, several methods have been developed for determining the age of a sediment layer since it was last exposed to sunlight. There are predominantly two methods: the partial bleach method of Wintle and Huntley (1980) and the total bleach method of Singhvi *et al* (1982). Here "bleach" refers to the change in the TL of a material caused by its exposure to sunlight or artificial light sources.

In the partial bleach it is assumed that the bleach has not been complete. The method involves two sets of natural samples which are used to construct two growth curves (graphs of TL against laboratory dose), the only difference between the two sets being that one would be given a short sunlamp bleach in addition to the added laboratory dose. The extrapolated intersection of the curves gives the equivalent dose, that is the dose received by the sample after its bleach.

The total bleach method assumes that the amount of bleaching has been sufficiently long so as to reduce the natural TL to a level beyond which no further

reduction is observed. The equivalent dose is found by plotting the growth curve of the sample and finding its extrapolated intercept with the value of the residual TL.

A new method for dating sediments was introduced by Huntley *et al* (1985). This method is based on the observation that a component of the trapped charge is very sensitive to the bleaching light and is removed very rapidly, within several seconds. This release of trapped charge results in an emission (photoluminescence) which can be measured directly. The bleaching light is provided by an argon–ion laser. This technique is particularly suited to quartz and Spooner (1987) has shown that it is the 325°C TL peak of quartz which is removed very quickly. This method has been successfully used to find the equivalent dose of stranded South Australian beach dunes (Huntley *et al* 1985).

1.3.3 TL Dosimetry

TL dosimetry is basically the use of TL materials to measure radiation dose. The importance of this can scarcely be over estimated especially in the field of radiotherapy where the treatment of cancer requires the total dose given to a patient to be known very accurately (Herring and Compton 1971). Other important areas which use TL dosimeters are in the fields of personal radiation monitoring for scientists and workers in the nuclear industry, food sterilisation, archaeology, scientific research and the testing of materials (Horowitz 1984). TL dosimetry is important because it is capable of measuring doses from $10^{-2}\mu$Gy up to 10^{7}Gy, dosimeters are small, some dosimeters approximate closely to human tissue for radiotherapeutic uses, they can be very hardy, they can store their TL for long periods, they are accurate, they are insensitive to the environment in which they are placed, TL is easy to measure and

this can be automated, TL dosimeters are convenient to wear and they can be reused many times (Horowitz 1984).

In this thesis (in chapter four) several common TL phosphor dosimeters are studied. A wider understanding of these materials could lead to the development of better experimental techniques and methods for measuring radiation dose.

1.3.4 Earth and Space Sciences

The dating technique described above is also applicable to geology, as a way of determining the age of a mineral. A vivid example of this is given by Smith and Prescott (1987) who were able to date the eruption of a volcano in Southern Australia to about 5000 years BP because the lava from the volcano had flowed over a sand dune, thus wiping out the existing TL.

Other applications include the use in space science to measure how close to the sun a meteor had ventured before it collided with the Earth and how long ago the meteorites fell to earth (McKeever and Sears 1979). Sediments can now be dated by using the principle that the TL is originally reduced, not by heat, but by the exposure to sunlight during the weathering and transport of the sediment material prior to deposition (see later).

1.3.5 Solid State Physics

TL has proved to be extremely useful in the study of the defects in minerals. Indeed TL is perhaps the most sensitive technique available for detecting the presence of the relevant defects in crystals (Townsend and Kelly 1973, McKeever 1985). However as McKeever (1985) points out, the understanding of the defect state of a mineral

can be best understood when TL is used in conjunction with other techniques, like optical absorption and electron spin resonance. In chapter 4 some investigations of a comparison between TL emission spectra and electron spin resonance data are presented for a selection of calcite samples.

1.4 TL Spectroscopy

In most cases the TL that is recorded is simply the number of photons for a particular temperature interval integrated over the spectral window of the light collecting optics and the detector. By simultaneously measuring the wavelength or photon energy of the emitted light, the amount of information available is very much increased. Such measurements provide information about the number and type of emission centers which contribute to each TL glow peak. This may be vital when dealing with polymineral mixtures where the "3-D" apparatus can allow the various minerals to be differentiated and identified (McKeever *et al* 1983). An example of this is given in chapter 5 where the use of a TL Fourier transform spectrometer allowed the measurement of the emission spectra of bleached quartz samples. By comparing these spectra with those of unbleached, reference samples, it could be determined which emission centres were participating in the decay process.

Binder *et al* (1968) have pointed out that a correctly calibrated emission spectrum can ensure that the maximum detector sensitivity is matched to the emission centers, ensuring the greatest signal-to-noise ratio.

Another, less obvious advantage of 3-D emission spectroscopy, has been pointed out by Levy *et al* (1971). The 2-D glow curves may not be suitable for determining

TL kinetic parameters such as E, s and the order of the glow peak, unless it can be shown that the detector signal is proportional to the number of processes occurring per unit time. In the case where the wavelength sensitivity of a detector in a 2-D system is changing quickly, the glow curves cannot be used for kinetic determinations since the shape of the glow curve may be modified by the measuring device. However the glow curves obtained from a 3-D spectrometer can be used, because they can be calibrated for the response of the apparatus.

On the negative side, 3-D systems are inherently less sensitive than 2-D ones since there is a spectrometer in between the sample chamber and the detector. Spectrometers have slits and other optical components which will reduce the amount of light reaching the detector. For materials which are not particularly sensitive the natural TL may be too weak to record. In this case the samples need artificial laboratory irradiation, which is satisfactory provided the emission processes do not depend significantly on the dose or the dose rate. If these assumptions do not necessarily apply, then it is advantageous to construct a 3-D apparatus which has the greatest sensitivity possible so that the natural TL spectra of as large a range of materials as possible can be measured. It was with this in mind that the TL Fourier Transform Spectrometer, described in chapter 3, was built.

1.5 This Thesis

This thesis can be divided up into two main parts.

The first section (consisting of chapters 2, 3 and 4) deals with the theory of Fourier transform spectroscopy and the redesign of a TL spectrometer based on these

principles. Over the last ten years this spectrometer has evolved through several phases to the stage where it can now be used in a routine and convenient manner to study the emission spectra of TL materials (Jensen 1982, Akber 1986). The aim of redesigning the instrument was to continue this evolution by extending its spectral response into the red (up to 740 nm) and into the ultra–violet (down to 250 nm). Examination of the TL emission spectrum reveals details of the hole centres which is unavailable to conventional "2–D" glow curves. This information is essential if a fuller understanding of the behaviour of the TL material is to be obtained.

The equipment described by Akber (1986) had a rather limited spectral response between 350 nm and 600 nm and thus a limited number of hole centre emissions could be examined. The aim of redesigning the spectrometer was to more than double its effective spectral range (in photon energy space) and so be able to examine correspondingly more emission centres. In chapter 4 emission spectra of several materials are presented. One of the aims of this chapter was to validate the modifications described in chapter 3 by comparing the TL emissions with those described elsewhere. A wide range of materials was studied since different materials emit in different regions of the spectrum accessible to our spectrometer. To a lesser extent this chapter also represents some extensions to research previously carried out in this department, particularly on the phosphor dosimeters and feldspars.

The second main section of this thesis is presented in chapters 5, 6 and 7. These chapters describe research which follows on, in part, from the work done in this department by Spooner (1987), and research which has not been performed in this department before, but which is related to previous work. The bleaching behaviour of

quartz is of vital importance to sediment dating and a more complete understanding of the interaction of photons with trapped charge carriers and their subsequent recombination with emission centres may enable newer, more reliable dating techniques to be developed in addition to the furthering of our understanding of a phenomenon which is of interest in itself.

These chapters deal specifically with the bleaching behaviour of quartz and how the bleaching mechanism may operate. In chapter 5 the changes in the emission spectra of four different quartz samples are examined both before and after illumination with selected bleaching wavelengths. The aim of this chapter was to obtain experimental evidence which could be used in chapter 7 to develop realistic models describing the bleaching decay mechanism of quartz. In chapter 6 further experimental results of this phenomenon are described, also for later use in chapter 7. Here the actual photoluminescence decay curves of two quartz samples were measured as the samples were illuminated ("bleached") with intense light. Further, these curves were recorded as the samples were held at different temperatures. The modifications to the existing spectrometer which allowed these data to be recorded are also described. Finally, the results from chapters 5 and 6 are used in chapter 7 to model the photoluminescent decay behaviour of a sample of quartz. Simpler models are eliminated in favour of more complex models involving the possible existence of direct transitions between the bleaching charge traps and the hole centres.

The sorts of questions which present themselves to be considered concerning the bleaching mechanism are:

Was the effect of the bleaching the same for all the quartz samples?

Was the emission spectrum affected over the entire spectral range? or was the bleaching selective?

Was there any difference between the bleaching of natural and irradiated quartz?

Was there any difference in the bleaching of quartz due to the different wavelengths used?

What was the nature of the photoluminescence decay curves – that is, were they simple exponentials?

Does the shape of the decay curves depend on temperature?

Were there any other charge traps participating in the decay mechanism?

Could simple theoretical models adequately account for the shape of the decay curves observed?

What degree of complexity needed to be introduced into the theoretical models in order to produce adequate agreement between theory and experiment?

Chapter 8 is the last chapter and in it this thesis is summarized with suggestions for possible future research, which have arisen or may do so as a result of the research presented here.

Chapter 2

Fourier Transform Spectroscopy

2.1 Introduction

The TL spectra presented in this thesis were obtained using a Fourier transform spectroscope. It is therefore appropriate to describe briefly the history, development and theoretical background of Fourier transform spectroscopy (FTS) and the practical realisation of FTS by use of a computer.

The history of FTS really begins as far back as 1845, when Fizeau and Foucault, for the first time, published some research "on the interference phenomena between two light rays for the case of large path differences" (Connes 1984) and a few years later Fizeau, this time alone, extended this work into the infra-red (IR) range. Their source was the Sun and with an alcohol thermometer as the detector, they were able to obtain the first quantitative IR spectra using the interference method. Later Fizeau showed that yellow sodium light was a doublet.

It has often been said that the real inventor of FTS was A.A. Michelson (Gebbie 1984). The two areas for which he is best known in interferometry are the ether drag experiments and "on a method of making the wavelength of sodium light the actual and practical standard of length", Michelson (1887). He introduced the visibility

technique to find spectral distributions in the cases where the spectra were symmetric about some wavenumber (Loewenstein 1966). Using his method, Michelson discovered that some spectral lines which seemed to be singlets were in fact unresolved doublets or multiplets. However the limitations in the visibility technique, that is, its inability to reconstruct the whole spectrum, meant that its use fell into disuse (Chamberlain 1979).

The first true interferogram was recorded by Rubens and Wood in 1911, as part of their studies of a Welsback mantle but even then they used a trial and error method by comparing their interferograms with those of known spectra (Rubens and Wood 1911). It was not until 1951 that the first numerically Fourier transformed interferogram was published by Fellgett (1951). In addition he pointed out the advantage to the signal–to–noise ratio (see later). The other major advantage of FTS, over other types of spectronomy, is its inherently greater ability to transmit more of the radiant energy through the interferometer (Jacquinot and Dufour 1948). It is this "throughput" advantage which is of greatest importance to TL.

Only a brief review of the theory of FTS will be presented here. For a more detailed account see, for example Bell (1972) and Chamberlain (1979).

2.2 Basic Principles

The perfect interferometer would consist of a point source in combination with an input lens to produce a beam of parallel light rays which would then be divided into two by a beamsplitter, one beam travelling to a fixed mirror and the other to a mirror capable of orthogonal translation relative to the fixed mirror. After reflection

the beams travel back to the beamsplitter to be recombined and divided again. The beam travelling to the detector is focused onto the detector and the power of the beam detected (Chamberlain 1979). A graph of the detected power against the variable path difference experienced by the two beams is called an interferogram, and the Fourier theory allows the reconstruction of the source spectrum from it.

2.2.1 Throughput

In reality point sources cannot deliver finite radiant energy (Chamberlain 1979), but the essential details outlined above will be the same for an extended source provided it is kept small. Figure 2.1 shows such an interferometer (the mirrors and beamsplitter have been left out) where A_S and A_D are the source and detector aperture areas, Ω_C, Ω_S, Ω_D and Ω_T are the solid angles of the collimator, source, detector and focusing lens respectively.f_C and f_T are the focal lengths of the lenses L_C and L_T which both have areas A. So then

$$A = \Omega_C f_C^2 = \Omega_T f_T^2 \tag{2.1}$$

and because $\Omega_S = \Omega_D$

$$f_C^2 = \frac{A_S}{A_D} f_T^2 \tag{2.2}$$

and the étendue or throughput, E, is defined as

$$E = \Omega_C A_S = \Omega_T A_D \tag{2.3}$$

(Jacquinot 1954). Physically, E is a measure of how much energy an interferometer is able to transmit through the spectrometer.

For a grating spectrometer the area of the source is limited by the entrance slit and so, for a given resolving power, the throughput or Jacquinot advantage of an

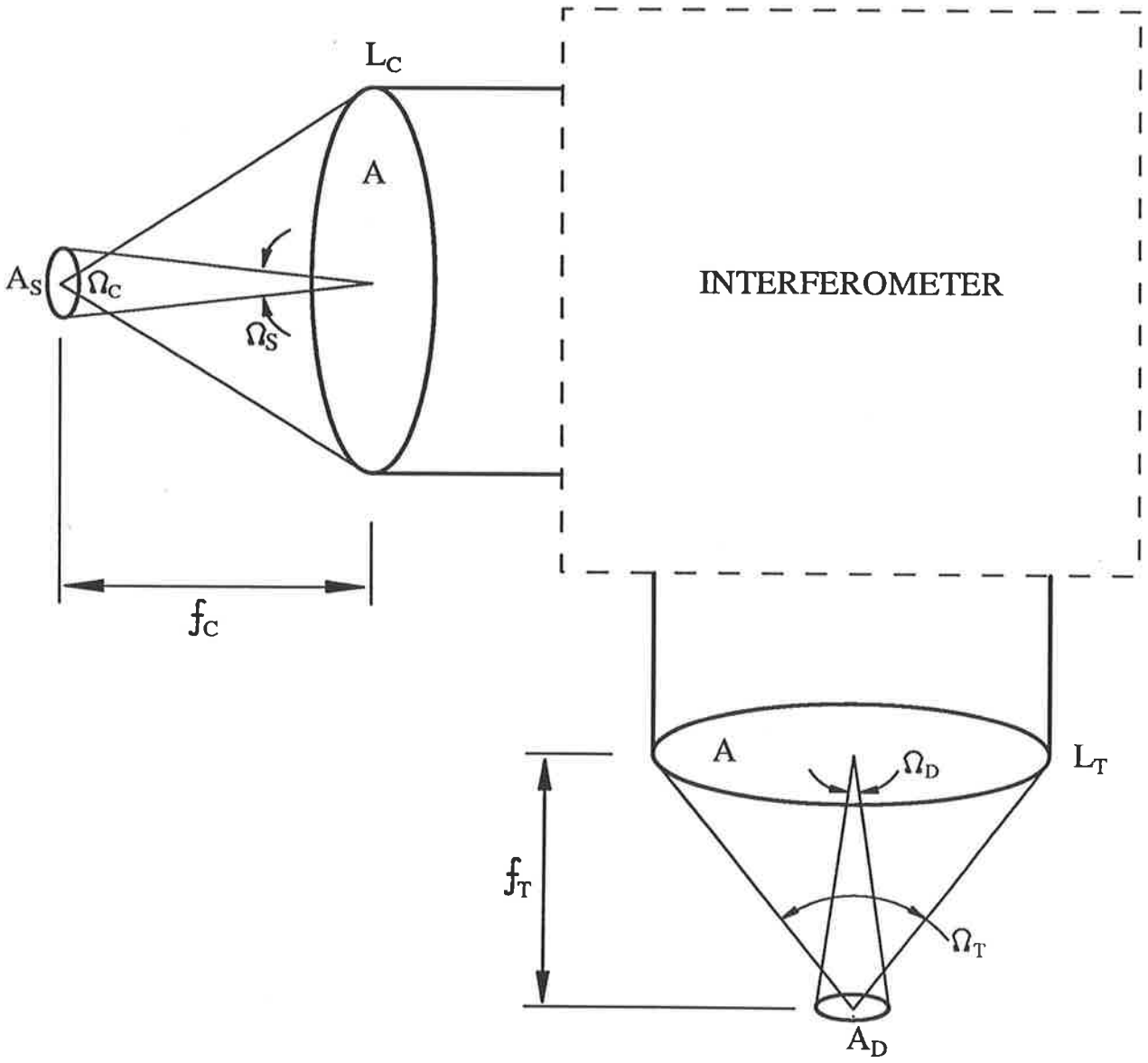

Figure 2.1: Schematic diagram of the optical system of an interferometer highlighting the throughput (after Chamberlain 1979).

interferometer can be a hundred times greater (Jacquinot 1984).

2.2.2 Multiplex Advantage

The multiplex or Fellgett advantage (Fellgett 1951) arises because the whole spectrum is observed continuously as the data is being recorded. For a grating instrument the data is taken by recording each small spectral band separately, one after the other. If the spectral range of interest ranged from wavenumbers of σ_{min} to σ_{max} then, if the resolution is R, the number of spectral elements measured M would be

$$M = \frac{\sigma_{max} - \sigma_{min}}{R}, \tag{2.4}$$

measured in a total time T (see figure 2.2). For a grating instrument each small band is observed for a time T/M. Thus the signal–to–noise ratio of the grating instrument will be proportional to $(T/M)^{1/2}$ whilst for the interferometer proportional to $T^{1/2}$. Hence the gain in sensitivity is $M^{1/2}$. Actually the term "advantage" is a misnomer since whether or not it is an advantage depends on the type of noise present in the signal. For detector noise which is independent of the signal, the multiplex advantage certainly applies. This is the case in the IR region of the spectrum where photon energies are less than kT at room temperature. Even cooling to very low temperatures cannot prevent thermal noise from dominating (Chamberlain 1979). In the optical region, however, the case is altered because the detectors are able to measure individual photon events and the dominant noise contribution is due to the statistical fluctuations in the numbers of photons arriving at the detector. In this case the separate noise contribution from M small bands exactly cancels the multiplex advantage. It can still apply to detector noise though, but this is usually

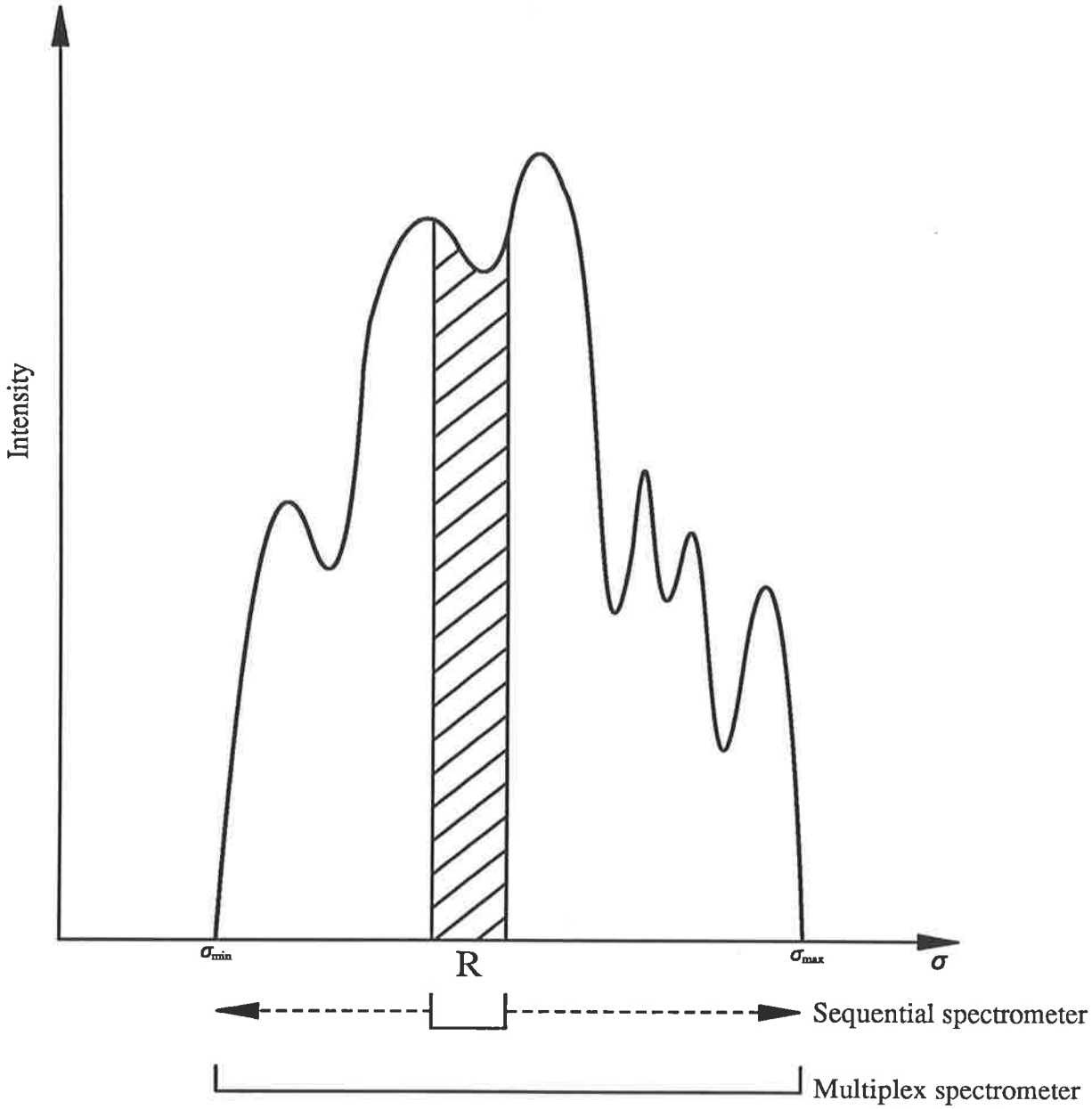

Figure 2.2: Graph demonstrating the principle of the multiplex advantage. The whole of the spectrum is observed for the whole time as opposed to the sequential spectrometer where only a narrow window is viewed (after Chamberlain 1979).

small compared to the photon noise. Indeed multiplexing can be a disadvantage. For instance when measuring astronomical signals, where the major noise component is due to random source fluctuations caused by atmospheric scintillations. In this case the disadvantage to the signal–to–noise ratio is $M^{-1/2}$ (Mertz 1965).

2.2.3 Fourier Analysis

The basic equation which relates the interferogram to the spectrum is

$$B(\sigma) = \int_{-\infty}^{\infty} [I_R(x) - 1/2\, I_R(0)] \exp^{-2\pi i \sigma x}\, dx, \tag{2.5}$$

where $B(\sigma)$ is the spectral flux density at a given wavenumber σ, and $I_R(x)$ is the measured photon flux at a particular optical path difference x. $\frac{1}{2}I_R(0)$ is the flux in the limit as $x \rightarrow \infty$ (that is at $I_R(\infty)$). Equation 2.5 is the basis of all FTS and to derive it one need only assume the law of superposition and the fact that the electric field at any point is a real quantity (Bell 1972).

Equation 2.5 is for the general case for asymmetric interferometers where no assumptions have been made concerning the relative reflectivities of the two mirrors. If the mirror reflectivities are the same and the interferogram is symmetrical about zero path diference, then only the *cosine* Fourier transform need be calculated, thus

$$B(\sigma) = \int_{-\infty}^{\infty} \left[I_R(x) - \frac{1}{2} I_R(0)\right] \cos(-2\pi i \sigma x)\, dx. \tag{2.6}$$

2.2.4 Apodisation

The integral in equation 2.5 has infinite limits which in any practical situation cannot be realised. This means that the calculated spectrum differs from the true spectrum– the usual result is the introduction of sidelobes. The mathematical procedure for

correcting for the truncation at limits of the interferogram is called apodisation. Essentially the procedure involves multiplying the measured interferogram by a function whose value falls from a maximum at zero path difference to some small value at the scan limit (Chamberlain 1979). The effect is to reduce the sidelobes by a factor which depends on the type of apodisation function chosen but at the cost of a reduced resolution. The majority of the TL spectra studied were rather broad band and since the scan limits are taken well beyond the the region of coherence (see later) truncation effects were not a significant problem.

Another, less obvious, advantage to apodisation is that the regions of the interferogram with high signal–to–noise can be more heavily weighted against the regions with a low signal–to–noise ratio (Bell 1972). This is especially important to the present thesis because the interferograms are recorded well beyond the extinction path difference where the signal–to–noise ratio of the data falls below unity. The interferograms measured for this thesis are of TL processes which are dynamical, that is the signal is changing with time. In order to Fourier transform them, the interferograms have to have this dynamical trend removed otherwise misleading artifacts would be introduced into the calculated spectra (Akber 1986). By recording the interferograms as described above the straightening process is more precise but at the expense of increased noise in the spectra.

The spectra presented here have all been apodised using a Gaussian function, f given by

$$f(x) = \exp\left[-1/2\left(\frac{x - zpd}{\sigma}\right)^2\right], \tag{2.7}$$

where zpd is the zero path difference and σ is the standard deviation of the function.

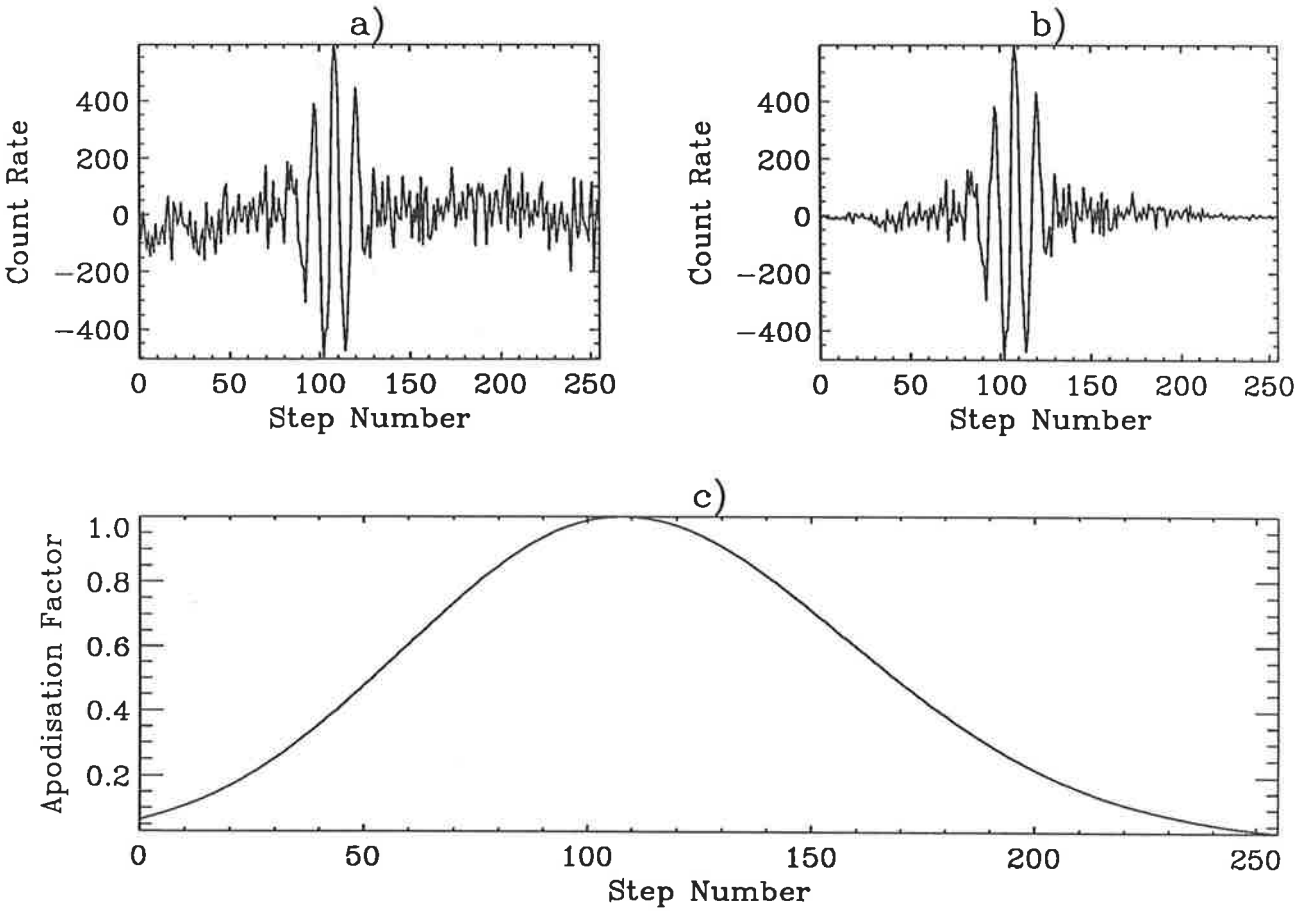

Figure 2.3a: Figure showing a) a raw interferogram, b) the same interferogram after apodisation by a Gaussian function given in c).

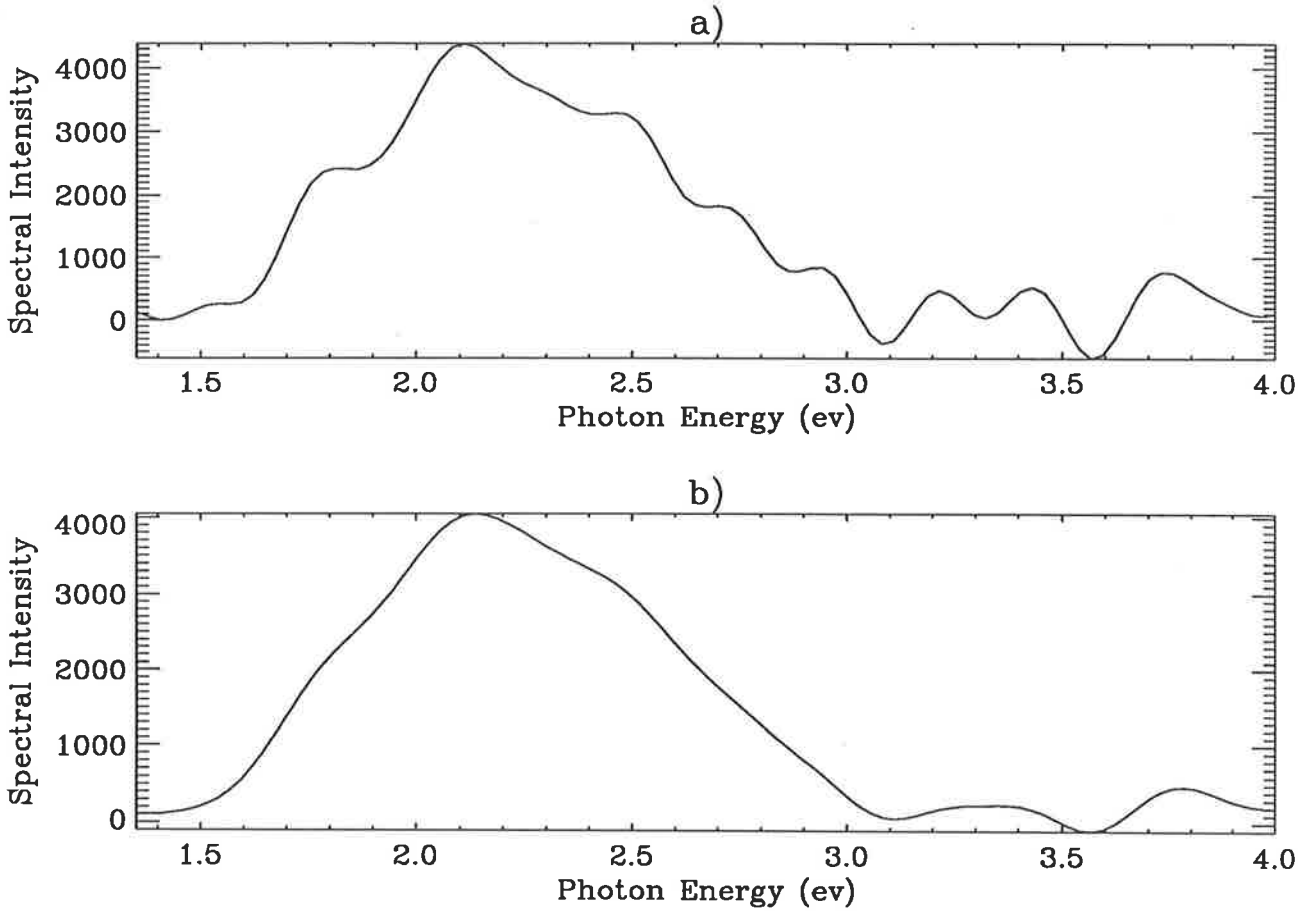

Figure 2.3b: Spectra calculated from a) unapodised and b) apodised interferograms given in figure 2.3a respectively.

The value of σ chosen was 20 steps to provide a broad region near *zpd* where the data would be relatively unaffected and to reduce the low signal–to–noise region to near zero. The Gaussian function, its effect on a typical interferogram and the resulting apodised and unapodised spectra are shown in figure 2.3.

2.2.5 Resolution

The resolution of an interferometer can be defined to be the broadening of a very narrow spectral line caused by the instrument or measuring technique (Bell 1972). For an unapodised monochromatic source the spectral profile which is actually obtained is given $sinc\, z = \sin(z)/z$, where $z = 2\pi(\sigma - \sigma_0)L$. σ_0 is the wavenumber of the source and L is the maximum optical path difference. This $sinc\, z$ function is called the instrument line shape function because it is what is obtained from the apparatus with a monochromatic source.

The Rayleigh criterion for the successful separation of two spectral lines of equal intensity is that the peak wavenumber of one line should correspond to the first minimum of the second line. For triangular apodisation, where the spectrum is proportional to $sinc^2\,(z/2)$, the resolution between two lines of peak wavenumbers σ_1 and σ_2 is

$$(\sigma_1 - \sigma_2) = 1/L \tag{2.8}$$

For an unapodised spectrum, where the calculated spectrum is proportional to $sinc\, z$, the resolution is

$$(\sigma_1 - \sigma_2) = \frac{1}{2L}. \tag{2.9}$$

Thus L can be considered to be the limiting factor which determines the minimum

resolution possible. Other factors are important though. Beyond the extinction optical path difference, sampling the interferogram further only increases the noise in the computed spectrum without increasing the resolution.

The above discussion is strictly applicable to very small sources, which results in light rays parallel to the optical axis, passing through the interferometer. If the source is extended then there will be rays of light which make angles, θ, relative to the optical axis. If the optical path difference (OPD) between the two mirrors in the interferometer is $2d$ then the OPD, Δ, for an oblique ray is

$$\Delta = 2d \cos \theta \tag{2.10}$$

This means that the oblique rays have a smaller OPD than the parallel rays. The result of this is to expand the interferogram which produces a spectrum, different from the true spectrum, which depends on the wavenumber and the solid angle subtended by the source (Bell 1972). The first effect is that the computed wavenumbers in the spectrum will be shifted to lower values by a small amount given by

$$\overline{\sigma} = \sigma_0(1 - \frac{\Omega}{4\pi}), \tag{2.11}$$

where Ω is the solid angle subtended, σ_0 is the wavenumber of the source and $\overline{\sigma}$ is the mean wavenumber after the spectrum has been spread out towards lower values (Loewenstein 1966). The existing equipment has a field of view subtending a solid angle of about 0.24 steradians with the centre of the mirrors (Akber 1986), which results in a wavenumber shift of under two percent. This effect is ignored since it is small in comparison to the resolution of the interferometer.

The second effect of the extended source is that there is a wavenumber spread,

$\delta\sigma$, given by

$$\delta\sigma = \sigma_0\Omega/2\pi, \tag{2.12}$$

and is entirely on the low wavenumber side of the source wavenumber (Bell 1972). For our instrument, the resolving power is

$$R \equiv \sigma/\delta\sigma = 2\pi/\Omega, \tag{2.13}$$

and works out to be 26. Equation 2.13 represents the ultimate resolving power of the interferometer.

2.2.6 Aliasing

In any practical situation, if a digital computer is to Fourier transform an interferogram, it must be recorded at discrete intervals. The Fourier transform of this digitised interferogram: the sampled spectrum $B_S(\sigma)$, is related to the complete spectrum $B_C(\sigma)$ by

$$B_S(\sigma) = \sum_{n=-\infty}^{\infty} B_C\left[\sigma - n(\Delta\sigma)\right] \tag{2.14}$$

where

$$\Delta\sigma = 1/\Delta\delta, \tag{2.15}$$

and $\Delta\delta$ is the interval between successive steps of the interferogram (Bell 1972). This means that every time $\sigma = n(\Delta\sigma)$ we get the full spectrum for all integers n. Provided $\Delta\delta$ is small enough the spectra will be separate, however if $\Delta\delta$ is large there will be considerable overlap or aliasing of the spectra and the true spectrum will contain false detail. An example of this is shown in figure 2.4.

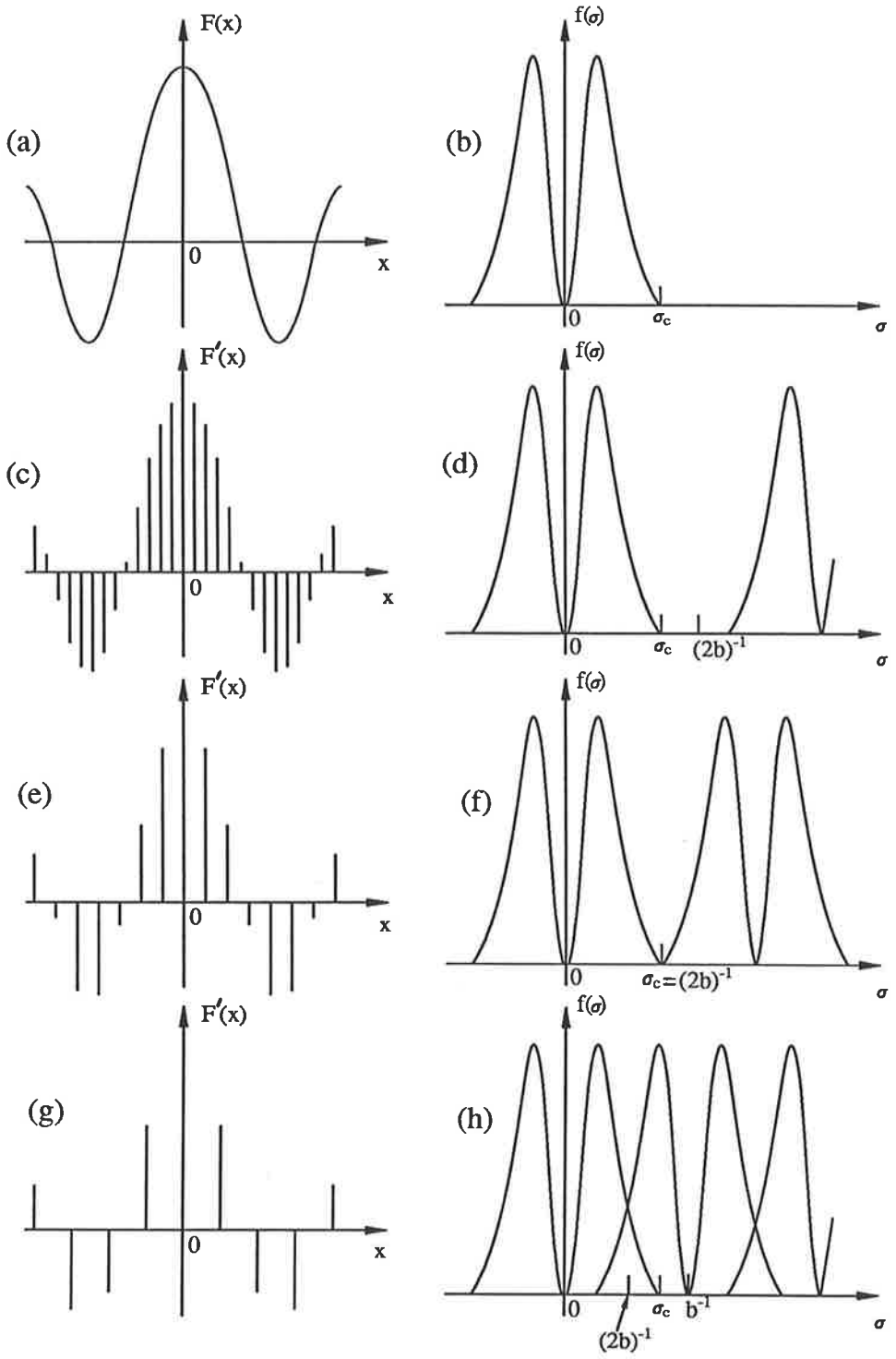

Figure 2.4: Figure to demonstrate the aliasing effect. At the left are a continuous function F(x) and three sampled versions. To the right are the corresponding Fourier transforms. The pairs (e) and (f) are for the critical sampling frequency and (g) and (h) is an aliased or none unique transform.

For there to be no aliasing, the step interval must not exceed

$$\Delta\delta \leq \frac{1}{2(\sigma_{max} - \sigma_{min})} , \tag{2.16}$$

where σ_{max} and σ_{min} delimit the region in the spectra which is of interest (Chamberlain 1979).

2.2.7 Noise

The effect of noise in FTS has been discussed earlier in section 2.2.2 where the dominant noise contribution in the optical region is due to statistical fluctuations in the numbers of photons measured. In this case, multiplexing does not affect the signal–to–noise ratio.

The noise inherent in an instrument can also be artificially magnified by the way the interferogram is recorded and analysed. If a single–sided interferogram is recorded then only the *cosine* Fourier transform need be calculated, whereas for a two–sided interferogram the spectrum is obtained from the modulus of the *sine* and *cosine* transforms. In the latter case the noise components are always positive as a result of taking the modulus. For the single *cosine* transform, though, the noise components average out to zero (Connes 1960, Loewenstein 1966). In addition the computation time is doubled. Provided the signal–to–noise ratio of the interferogram is greater that about 10 the two–sided transform is virtually identical to the transform of the single–sided (Chamberlain 1979). The reason that two–sided interferograms are recorded is that there is usually a small phase error between the true ZPD and the maximum on the recorded interferogram. Unless this error is corrected for, artifacts may be introduced into the calculated spectrum of a one–sided interferogram. The transform

of a double–sided interferogram automatically corrects for this phase error.

2.3 Computation

Unless otherwise stated all the programming modifications described in section 2.3 were performed by the author.

2.3.1 The Fast Fourier Transform

There are very few valid reasons for using the discrete Fourier transform (DFT) in preference to the fast Fourier transform (FFT) (Chamberlain 1979). One good reason is if the spectral range is very narrow and the number of points is small. This is because the FFT provides all the spectral ordinates between 0 and σ_{max} (Chamberlain 1979). For our instrument though this is not an important consideration because in the operational range of interest (between wavenumbers 13,000cm^{-1} and 40,000cm^{-1}) there are relatively few spectral points below 13,000cm^{-1} compared to the number in the total spectral range.

The unique construction of the TL interferometer described here provides another reason why the DFT can be used in preference to the FFT. The interferograms are produced by stepping a movable mirror backwards and forwards to vary the OPD between the two beams of light. The device used to step this mirror is a piezoelectric transducer (PZT). Unfortunately the operation of this PZT is not linear, that is the applied voltage is not proportional to the displacement. One of the fundamental requirements of the FFT is that the interferograms must be recorded at equal intervals of the OPD. This means that if the FFT is to be used, a new set of points needs to be calculated from the recorded interferogram suitably corrected for this non–

linearity. The problem is to weigh the time saving by using the FFT against the time wasted by having to interpolate a new interferogram. In tests performed on sample interferograms it was found that the DFT offered a marginal time saving in computer time over the combination of the FFT and interpolation.

2.3.2 Computer Hardware

The initial operation of the instrument is described by Jensen (1982). At this time the control of the apparatus and the analysis of the data was performed by a CBM Pet computer, The data from one sample required a few days to be Fourier transformed in this way. Akber (1986) describes the use of a faster computer, namely an Olivetti M24 MS–DOS computer, to do the analysis. Instead of days, it now took only 30 minutes for the same sized file to be transformed. Since then the analysis programs, written in Turbo–Pascal and Microsoft–Pascal have been further modified to produce greater time savings.

The major time saving has been achieved due to the realisation that the time required by the central processing unit of the computer to access a value in a stored array is much less than the time to actually calculate the same value. The program now produces arrays of 2000 *sines* and *cosines* and the Fourier transform program simply looks up the closest value in the relevent array. Provided the arrays contain enough values of the *sines* and *cosines* there is negligible difference between the spectra calculated both ways (see figure 2.5). The file of a typical sample now takes about 4 minutes to analyse.

Akber (1986) has pointed out that one way to reduce the computational time would be to transfer the data to a mainframe computer for analysis. The time required

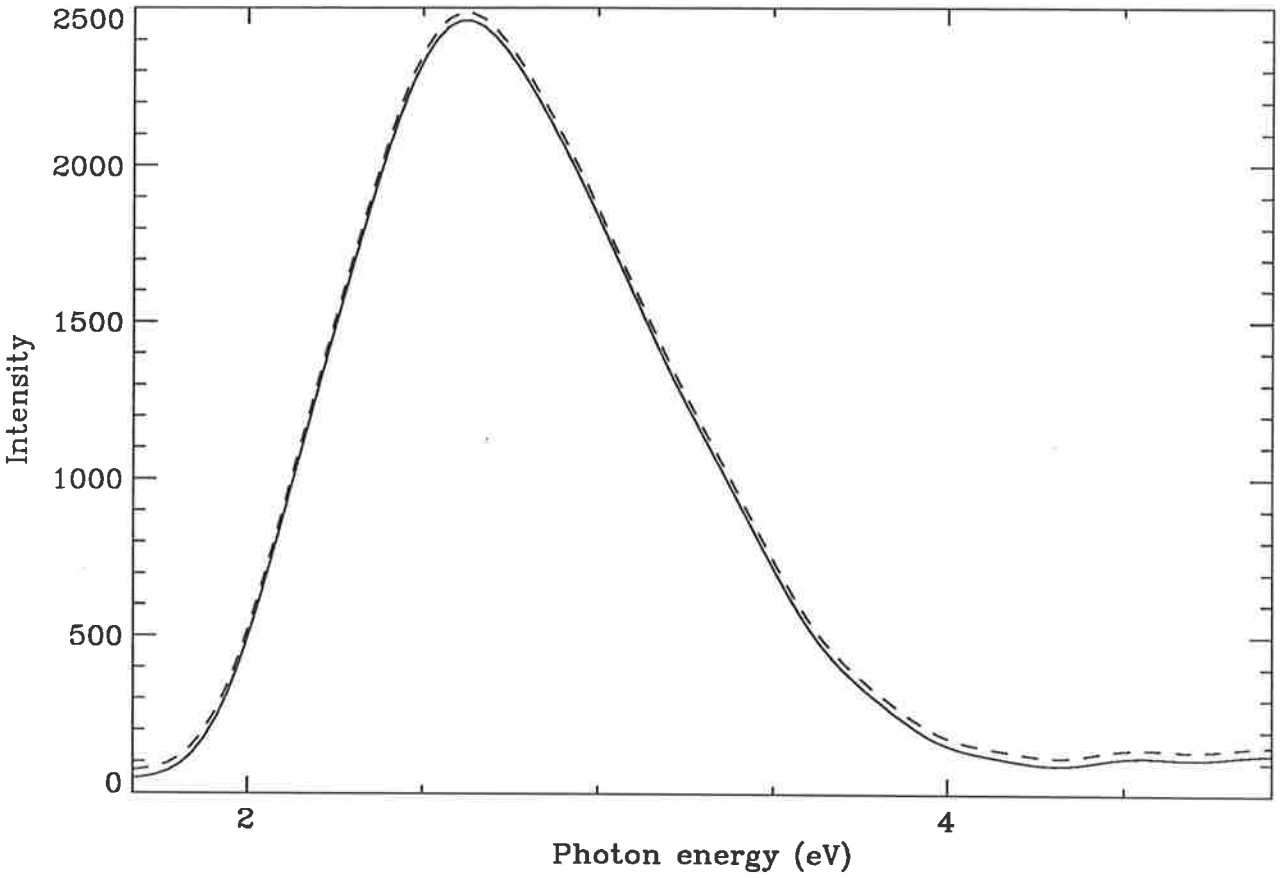

Figure 2.5: Graph showing a spectrum of natural LW quartz that had been transformed by calculating the individual sines and cosines (full line) and by looking these values up in a table (broken line). The broken line has been offset by a small amount.

to transfer a file of 40 interferograms from the MS–DOS computer to the departmental mainframe computer is about 3 minutes which negates any possible advantage even neglecting possible mainframe queue times.

2.3.3 The Discrete Fourier Transform

In his thesis Akber (1986) describes how the spectra had been calculated at equal intervals in wavelength. This was done by converting the spectral intensity, $B(\sigma)$, at a particular wavenumber into the corresponding wavelength intensity, $B(\lambda)$, using

$$B(\lambda) = B(\sigma)/\lambda^2. \tag{2.17}$$

Presumably the reason wavelength spectra were calculated instead of wavenumber (or equivalent energy) spectra was that the wavelength spectra were easier to interpret, that is, one thinks more readily in terms of wavelengths than wavenumbers. However, this method has serious problems because by calculating at equal wavelength intervals the noise–to–signal component in the spectrum is artificially magnified. At longer wavelengths (above 500 nm say) this effect is hardly noticeable but towards the lower wavelength region (say below about 400 nm) it can dominate the spectra. The reason for this is as follows. Assuming Poisson counting statistics the percentage of noise in a small slice, $\delta\sigma$, of the wavenumber spectrum is given by

$$\frac{\sqrt{B(\sigma)\delta\sigma/\sigma}}{B(\sigma)}, \tag{2.18}$$

and in a slice, $\delta\lambda$, of wavelength space the corresponding percent is

$$\frac{\sqrt{B(\lambda)\lambda\delta\lambda}}{B(\lambda)}. \tag{2.19}$$

Converting equation 2.18 to wavelength space gives

$$\frac{\sqrt{B(\lambda)\lambda\delta\lambda}}{B(\lambda)\lambda^2}, \tag{2.20}$$

and so the percentage of noise in wavenumber space is less by a factor λ^2 than the noise in wavelength space.

2.3.4 Computation of the Spectrum

The computational steps involved in preparing a raw interferogram before it is transformed are described in detail by Akber (1986) and are only described here briefly.

The raw interferograms recorded have several features about them which, if not corrected for, would produce spurious artifacts in the computed spectra. The first of these has been mentioned earlier, that is the light from the TL process is not constant during the time each interferogram is being recorded. This trend is removed by fitting a second order polynomial to the raw data and then reducing the function to an horizontal line which allows the interferogram to be straightened. Akber (1986) has shown that this method is successful for a wide range of possible interferogram shapes.

The next step involves subtracting $I_R(\infty)$ or $\frac{1}{2}I_R(0)$ (see equation 2.6) from each point of the interferogram. In effect this value is just the average of the intensity of the straightened interferogram. Lastly the non–linearity trend in the interferogram due to the PZT stepper must be removed. This is done by recording several interferograms produced by He–Ne laser whose wavelength is well known (632.8 nm). Since the peak–to–peak distance of these interferograms should all be the same the sample interferograms can be stretch or compressed accordingly to give intensities at equally

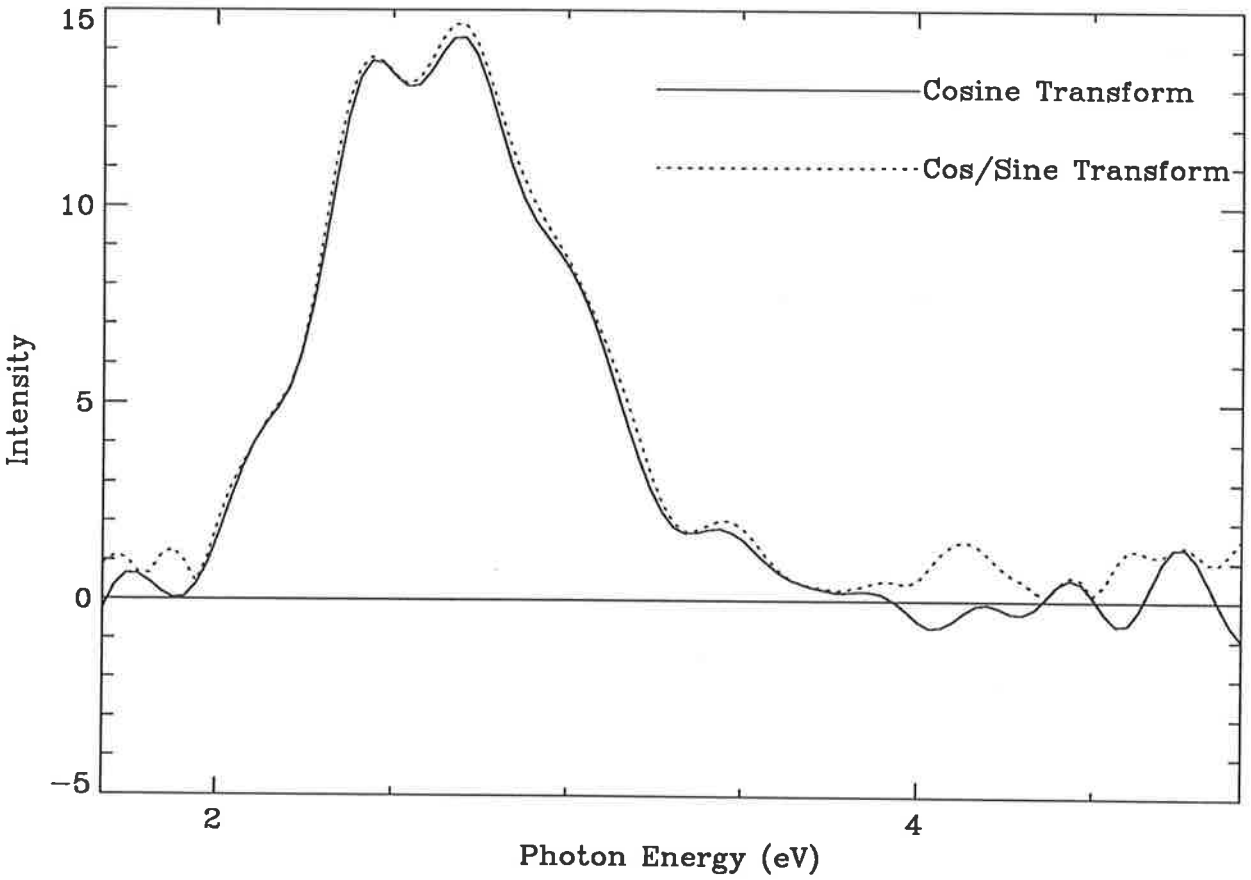

Figure 2.6: Spectra calculated firstly by using the cosine Fourier transform only (unbroken line), and by the sine and cosine transform (dashed line). The horizontal line is simply the zero intensity level (for reference).

spaced steps.

So then, if j is an integer and

$$S(j) = [I_R(j\Delta\delta) - I_R(\infty)]\,, \tag{2.21}$$

then, for a two sided interferogram, the digitised form of equation 2.5 is

$$B(\sigma) = \left\{ \left[\sum_{j=-N/2}^{(N/2)-1} S(j)\, cos(2\pi\sigma\Delta\delta) \right]^2 + \left[\sum_{j=-N/2}^{(N/2)-1} S(j)\, sin(2\pi\sigma\Delta\delta) \right]^2 \right\}^{1/2} \tag{2.22}$$

where N is the number of points in the interferogram (Bell 1972). As shown in section 2.2.7 however it can be advantageous to calculate only the cosine transform, given by

$$B(\sigma) = \sum_{j=-N/2}^{(N/2)-1} S(j)\, cos(2\pi\sigma\Delta\delta) \tag{2.23}$$

By fitting a parabola through the maximum point on the interferogram (at $S(0)$) and through one point on each side ($S(-1)$ and $S(1)$) the linear phase error, ϵ (see section 2.2.7) can be found by

$$\epsilon = [S(1) - S(-1)]/2[S(-1) + S(1) - 2S(0)] \tag{2.24}$$

(Bell 1972).

Equation 2.23 now becomes

$$B(\sigma) = \sum_{j=-N/2}^{(N/2)-1} S(j, \Delta\delta - \epsilon)\, cos[2\pi\sigma(j\Delta\delta + \epsilon)] \ . \tag{2.25}$$

The program has been modified to calculate the two one–sided Fourier transforms on either side of zero path difference and then to average them to produce the final spectrum. Figure 2.6 shows a comparison of spectra obtained using equation 2.22 and equation 2.25 and clearly demonstrates the effectiveness of this method in reducing the noise in the spectra ratio.

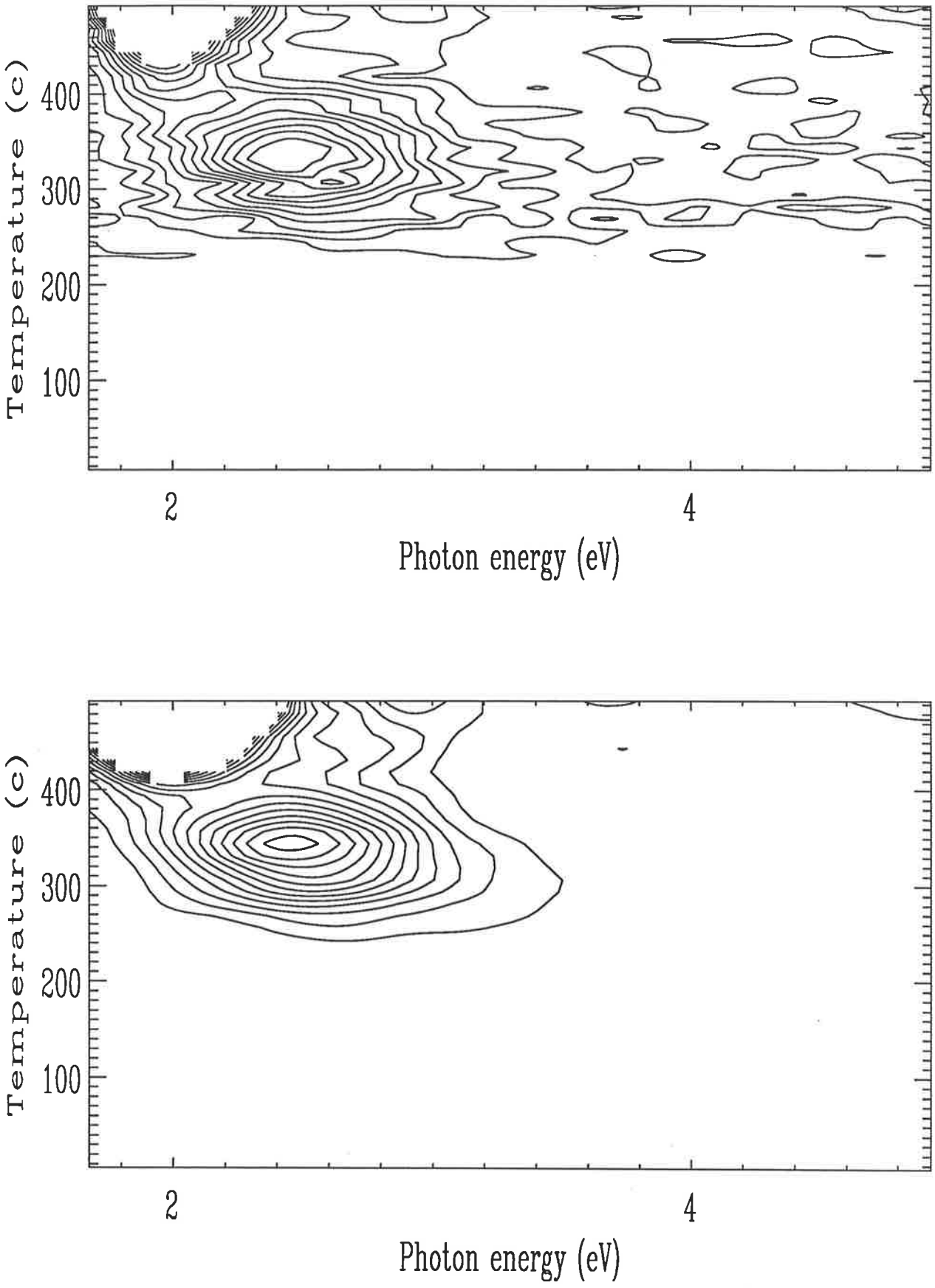

Figure 2.7: The top figure is a contour plot of a quartz sample that was an average of two weight normalised spectral files. Below is the same file but with smoothing along both axes.

2.3.5 Smoothing the Spectra

The question of whether to smooth data can be quite difficult to answer, indeed there is a lot to be said for presenting the data exactly how they are (Press *et al* 1986). However the advantages of smoothing can be significant. The data presented here have been smoothed: both along the wavenumber and the temperature axes. The reasons for smoothing are twofold. Firstly for some TL materials, whose spectra can be rather broadband and of relatively low intensity, the spectra can have noise fluctuations whose frequency is smaller than the resolution the interferometer allows for. This could be misleading and suitably smoothing the spectra makes the genuine features become much clearer. Secondly random noise fluctuations at the limits of the calculated spectral range, where the spectral response of the instrument is relatively low, can be artificially amplified when the spectra are corrected. Smoothing these fluctuations prevents misleading artifacts from being introduced. The method chosen for smoothing the data has been described by Press *et al* (1986). Any linear trend in the data is removed first and then the program uses a fast Fourier transform to low–pass filter the data.

Figure 2.7 shows the effect of smoothing along the spectral and temperature axes on a complete file of a sample of quartz. This file was an average of two identical samples. The smoothing has eliminated the sharp edges on the contour diagram introduced when the files were averaged. This means that any small temperature drifts between samples that are to be averaged, can be neglected.

2.4 Conclusion

In this chapter the largely theoretical aspect of FTS have been considered. In the next chapter the practical aspects of modifying a real Fourier transform spectrometer are described.

Chapter 3

The Equipment

In the last chapter the theoretical and computational aspects of FTS were discussed. In this chapter the modifications involved in extending the spectral range of a practical Fourier transform spectrometer are described.

3.1 Introduction

As mentioned in chapter 1 the reason for the construction of the TL interference spectrometer, initially described by Jensen (1982), was that the sensitivity of this type of instrument is inherently greater than other types which are usually based on dispersive optical principles, that is, they have prisms or gratings and slits.

TL spectrometers have probably been in operation since around 1956 (Dutta and Ghosh 1956, Halperin and Kristianpoller 1958, Brunner 1964 and Ellis and Rossiter 1969). These early instruments were generally slow scanning prism types with little or no computer control (in some cases the spectra were displayed on an oscilloscope and then photographed to make a permanent record). The disadvantage of slow scanning is that the sample temperature must be either static or changing very slowly (Harris and Jackson 1970). The advantage of fast scanning rates (that is, the frequency with

which the whole spectrum is recorded) is that no corrections need to be made for the change in relative intensity during the scan time (Harris and Jackson 1969, Binder and Cameron 1969). By interfacing a computer to convert, store, and display data during the experiment, Mattern *et al* (1971) were able to increase the amount of information obtained and later could prepare stereographic "3-D" plots of intensity against photon energy and temperature. This technique has been widely copied (for example, Nambi *et al* 1974, Cooke *et al* 1977, Mehta and Sengupta 1979, Matthews and Stoebe 1982 and Townsend *et al* 1983) and all suffer a loss in sensitivity due to the necessity for entrance and exit slits which reduces the solid angle "throughput" of the instrument.

Recently instruments with no exit slits have been constructed using CCD (charged coupled device) array detectors (Bakas 1984, Imaeda *et al* 1985 and Hornyak and Franklin 1988). Instead of an exit slit to define the dispersed wavelength band, the whole spectrum is first amplified by an image intensifier before being focussed onto the CCD array. This method increases the optical integration time for each spectral band since the detector is measuring the photon signal for the whole time of the experiment. Since the noise in the signal is determined by Poisson statistics, the greater the signal, the greater the signal–to–noise ratio.

A novel TL spectrometer for use with extended sources has been described by Bailiff *et al* (1977). In this design the monochromator has been done away with completely and replaced by a rotating disc with 16 narrow band pass filters mounted on the periphery. As the sample is heated, the disc is rotated rapidly at 8 rev s^{-1}, each revolution corresponding to one spectral measurement. Although this instrument

needs no slits, it still suffers from the requirement to rotate the disc rapidly in order to keep the scanning time short. This means that each spectral element is viewed for a relatively short time, thus reducing the sensitivity. Of course, a modification of this apparatus could be envisioned, whereby the sample heater plate assembly is replaced by a rotating multi-sample disc holder (similar to that used by the Risø automatic TL reader system). Each of the identical samples is now glowed separately for a different filter with the whole process completely automatic. Presumably, this type of instrument would offer the greatest sensitivity of all, albeit with limited resolution.

Fourier transform techniques have usually been applied to the infra-red region of the electro-magnetic spectrum (Gebbie 1984), and relatively little has been done in the visible and ultra-violet (UV) region (Aryamanya-Mugisha and Williams 1985). Essentially this is because the effects of photon noise negate any advantages in the signal–to–noise ratio over dispersive techniques. This reasoning does not apply to TL however, because the number of photons that are emitted is determined by the sample, in contrast to a constant illuminating source of arbitrary intensity (see for example, Stubley and Horlick 1985). The advantage that FTS offers to TL is its throughput from an extended source, which, simply put, increases the number of TL photons which reach the detector. The problem of applying FTS to the visible–UV region now becomes more of a technical challenge involving the precision of the optical components and the precise control of the stepping motor which changes the optical path difference. For descriptions of some recent optical–UV Fourier transform spectrometers see, for example, Tittel *et al* (1984), Aryamanya-Mugisha and Williams (1985), Stubly and Horlich (1985) and Thorne *et al* (1987).

3.2 The Apparatus

3.2.1 Introduction

A detailed description of the spectrometer has been given by Jensen (1982) and Akber (1986). A review of the existing apparatus will be given followed by detailed account of the modifications made by the author.

3.2.2 The Previous Design

The Design Due to Jensen

The initial design and construction of the Fourier transform spectrometer was undertaken by Jensen (1982). The performance goals were a spectral range of 300–650 nm and a resolution of around 20 nm. In addition the interferometer had to be interfaced to a conventional TL oven, so that the light collecting optics had to be matched to the size of the standard sample discs (which were 9.7 mm in diameter). It also had to double as a conventional "2-D" glow system.

Figure 3.1 (after Jensen 1982) shows a simplified block diagram of the whole apparatus, showing the relationship of the various components to each other.

Figure 3.2 shows a detailed schematic diagram of the optical system. The input optics, which gathered the light from the source, S, consisted of 3 lenses L_1, L_2 and L_3 and an aluminium coated front surface mirror M. L_1 was a 50 mm diameter aspheric lens with a focal length (fl) of 33 mm. L_2 was a 50 mm diameter field lens (200 mm fl) which was located in the focal plane of an 81 mm diameter (102 mm fl) Fresnel lens, L_3. The mirror, M, enabled the plane of the optical axis to be reflected from the vertical to the horizontal.

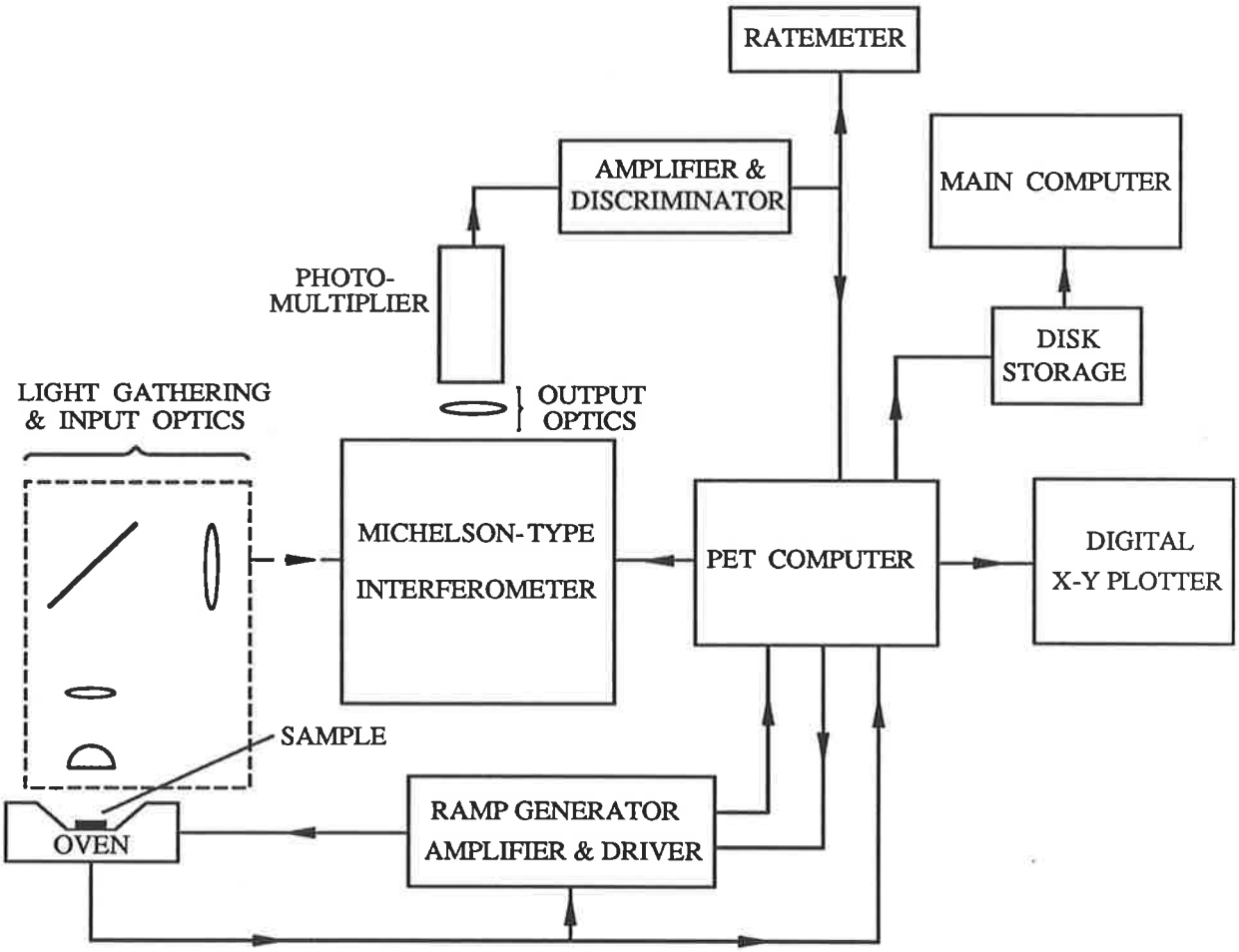

Figure 3.1: Block diagram showing the main components of the 3-D system and their interaction with oneanother (after Jensen 1982).

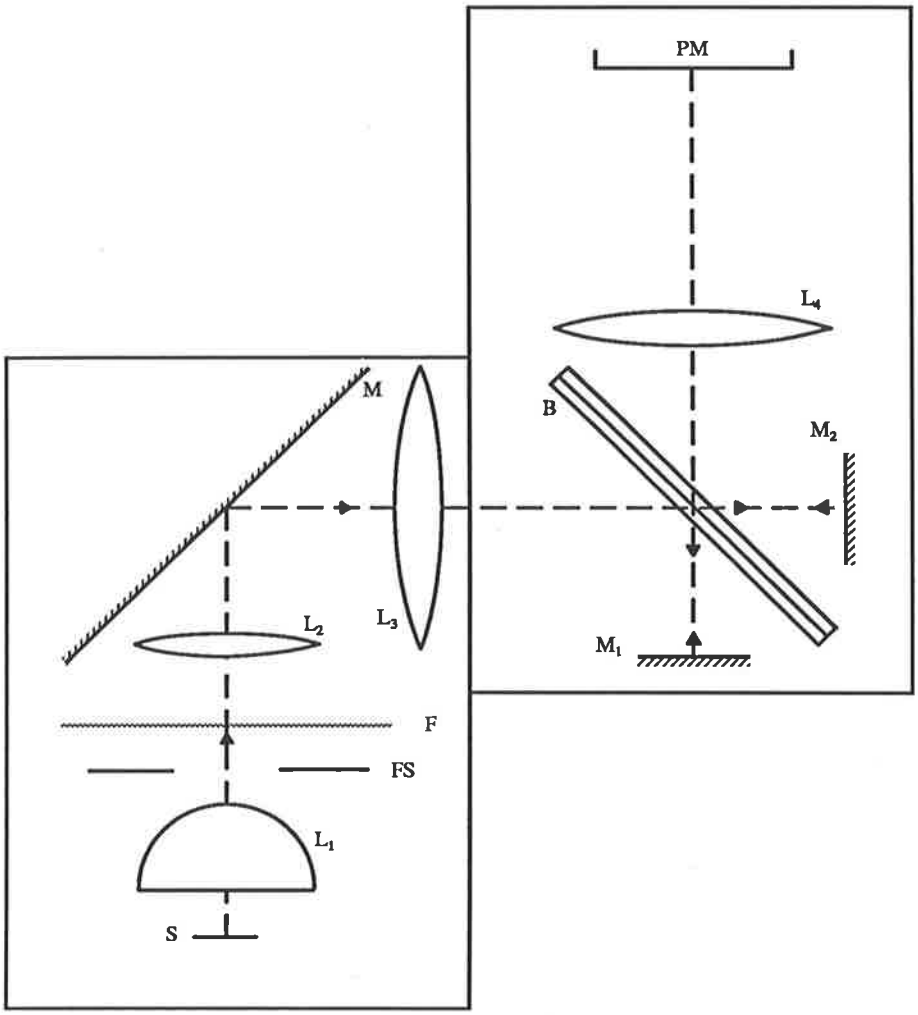

Figure 3.2: Detailed schematic diagram of the optical layout of the 3-D system. The components have been described in the main text (after Prescott *et al* 1989).

The light rays next passed through a beamsplitter, B, which consisted of two identical glass plates one of which had been partially coated with a layer of aluminium, which provided the necessary equal division of the beam. The two beams were then imaged onto two flat aluminium coated front surface mirrors M_1 and M_2, which were aligned orthogonally to one another. M_1 was fixed whilst M_2 was capable of linear translation along the optical axis. After the beams had been recombined at B a lens, L_4 (which was a combination of two 81 mm diameter Fresnel lenses with a fl of 71 mm, to give an effective fl of 36.5 mm), produced an image of S on the photocathode of the EMI 9635QA photomultiplier tube (PMT). Ray diagrams of the input and output optics are given in figure 3.3.

The PMT was operated in photon–counting mode using amplifier and discriminator electronics. The housing of the PMT was a Peltier cooling unit which allowed the PMT to be operated at temperatures down to –25°C (the 9635 PMT was only operated at room temperature).

These optical components and the detector housing were bolted onto a 2 cm thick steel base plate which was mounted onto a solid wooden table. The TL oven was mounted on rails that enabled it to be positioned under the aspheric lens and then it could be raised to make a vacuum seal with the aspheric lens holder, which was bolted onto this base plate.

Optical alignment was by grub screws which made contact with the front surfaces of M_1 and M_2 and by a lever arrangement on M_1 alone.

The TL oven was of a conventional design (similar to that of Littlemore Scientific Engineering Co., Oxford, England) and basically consisted of a water cooled nichrome

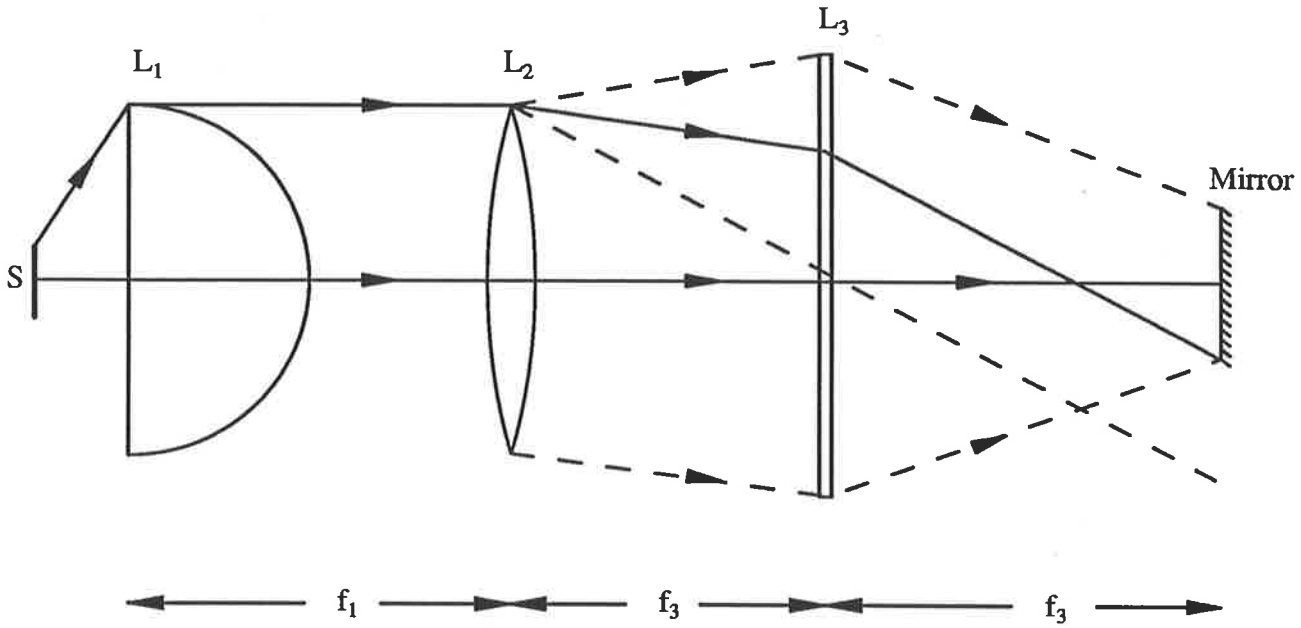

Input Optics

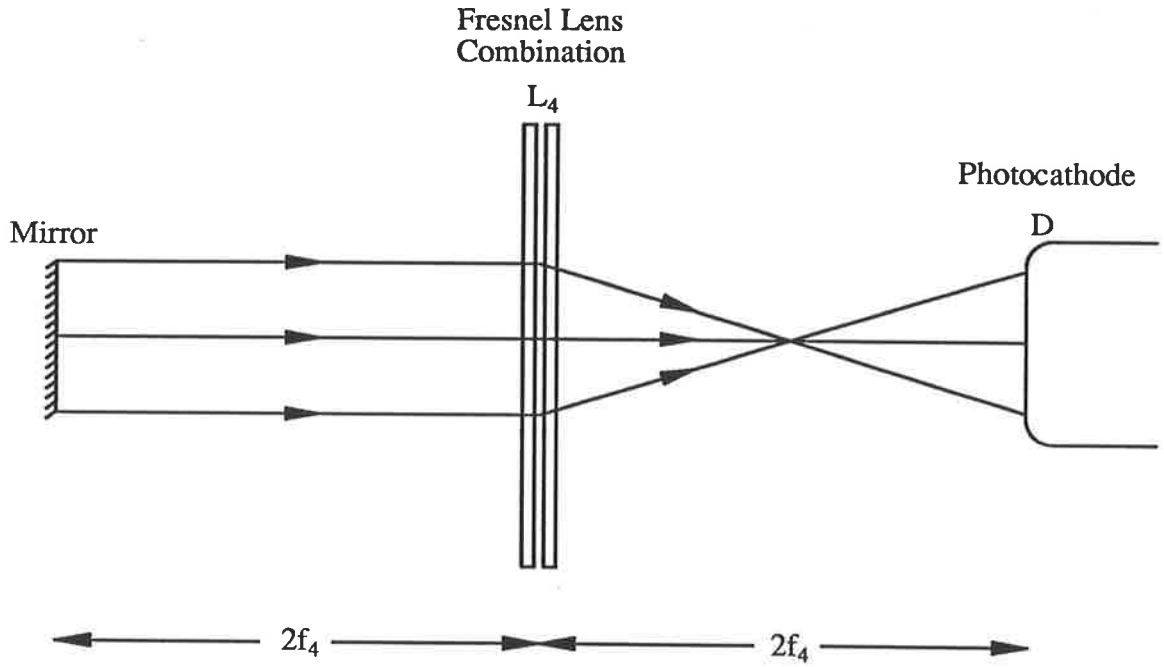

Output Optics

Figure 3.3: Schematic ray diagram of the original optical layout due to Jensen (1982). At the top is the input section of the optics and below the output optics. For simplicity, the beamsplitter-compensator combination has been omitted (after Jensen 1982).

heating strip with a chromel–alumel thermocouple welded onto the base, and the various gas and vacuum inlet and outlet ports.

One of the most critical aspects of the operation of the interferometer was the way the movable mirror was translated. A double leaf–spring assembly was used in order to ensure that the mirror was constantly perpendicular to the optical axis during translation. The mirror was stepped forwards and backwards by a Burleigh PZ–44 piezo–electric translator. This piezo-electric transducer suffered from a hysteresis effect which meant that the step size varied slightly during the cycle and the forward and reverse cycles differed from one another (Prescott *et al* 1988). However once the PZT transducer was in a cyclic state (after being stepped forwards and backwards 40 or 50 times) each cycle was highly reproducible.

The electronics used to control the equipment and record the data was essentially the same as a conventional 2-D TL system. The temperature rise was controlled by comparing the signal from the thermocouple with a linear ramp signal. A Commodore PET computer controlled the operation of both the 3-D and 2-D TL experiments, in addition to collecting the data. The only difference between the 2-D and 3-D operation was that a manually selected heating rate stepped the PZT transducer in synchrony with the linear heating ramp.

The PMT output was fed into a combined amplifier and discriminator which resulted in identical TTL pulses of width $50ns$. These pulses were then prescaled before being counted alternately by separate 16–bit buffers (this allowed the data from one buffer to be stored in the PET computer whilst the other could continue to count).

The data could then be displayed as glow curves or interferograms immediately or stored for later Fourier transformation.

The Modifications Made by Akber

Jensen had proved the design feasibility and was able to obtain spectra of some constant intensity light sources and a selected fine grain pottery sample. However it was not until after the modifications made by Akber (1986) that spectra could be measured reproducibly.

The design changes made by Akber were mainly concerned with the mechanical rigidity of the optical system. In the old design, the stresses experienced by the optical steel base plate, as the oven was evacuated and flushed with Argon, were sufficient to destroy the fine optical alignment.

The solution by Akber was to have essentially no contact at all between the oven and the optical system. This was achieved by making the aspheric lens and its holder into a separate component which could make a vacuum seal with the oven chamber. Evacuation and Argon gas flushing could now be done without any contact with the optical system thus maintaining the fine alignment. Coupling of the oven chamber (and the aspheric lens) with the spectrometer was via steel rails which allowed the oven to be positioned directly under the input light orifice. The oven could then be jacked up until a micro–switch was engaged – indicating that the aspheric lens was correctly positioned. The only contact that the oven had with the optical system was via a thin rubber disc which helped to reduce the amount of stray light entering the interferometer. Akber (1982) was able to achieve fine alignment easily by positioning

a broadband light source and a partially silvered glass plate above it, just behind the oven table. Its positioning meant that when the oven table was completely removed the light was situated directly beneath the field lens. Using the manual voltage controls on the piezoelectric control console the central fringe pattern produced by the interferometer, could be brought into the field of view of the operator, looking in the silvered mirror. A new star gimbal mount for the fixed mirror had two separate piezoelectric transducers attached which allowed the mirror to be minutely tilted until the desired alignment was obtained. This fine alignment appeared as circular, symmetrical fringes – each one filling the field of view. Any mis-alignment resulted in the observation of many parallel fringes. Zero path difference was obtained by observing the central bright white fringe in the field of view. This allowed the voltage supplied to the actual stepping transducer to be biased so that zero path difference was recorded near the middle of the scans (resulting in two–sided interferograms).

Another change was to the optical table itself. The steel base plate was bolted onto a 75 kg flat slate slab which in turn rested on a frame of hollow square tubing. In between were placed a couple of layers of neoprene which helped to absorb vibrations.

Akber also made some minor improvements to the electronics of the system and to the analysis procedures for calculating the spectra (see chapter two).

3.3 Modifications to the Apparatus

The existing spectral response of the interferometer was effectively between 350 nm and 600 nm. The lower wavelength limit was determined by the transmission characteristics of the optical components and the upper limit by the falling quantum

efficiency of the existing PMT (EMI 9635QA). The main modifications envisioned were intended to give a spectral range of 250 nm to 740 nm.

3.3.1 The Photomultiplier

The EMI 9635QA was designed as a high gain (up to 10^8) and low dark current PMT, to be operated in the photon counting mode for use in very low light photometric applications (EMI PMT Catalogue 1982). Unfortunately it is unsuited to applications involving the detection of photons with wavelengths greater than about 600 nm. The EMI 9558QB PMT, in comparison, has a much greater spectral range with its quantum efficiency falling to less than one percent at around 830 nm. Figure 3.4 shows the graphs of the quantum efficiency against wavelength for both the 9635 and the 9558 PMTs. On the negative side though, the 9558 has a significantly lower gain (around 10^6) than the 9635 and its dark emission is also greater, thus requiring cooling. A graph of the cathode dark current density versus temperature of several PMTs with different cathode materials is given in figure 3.5.

Cooling a PMT can significantly change its gain and spectral response. Changes to the gain are usually of the order of 0.3 %/ °C and are so small that they can be disregarded (Schonkeren 1970). The relative spectral sensitivities of two PMTs with cathode materials of response S11 and S20 are shown in figure 3.6. For the 9558 (which has an S20 cathode) the changes are very small for a temperature drop from 20°C to –20°C. For the 9635 though (whose response is similar to S11), there is clearly a major reduction in the spectral response for wavelengths below 400 nm which is why the 9635 PMT was never cooled. The reason for this reduction in spectral response is that the average escape depth of the electrons increases as the temperature falls

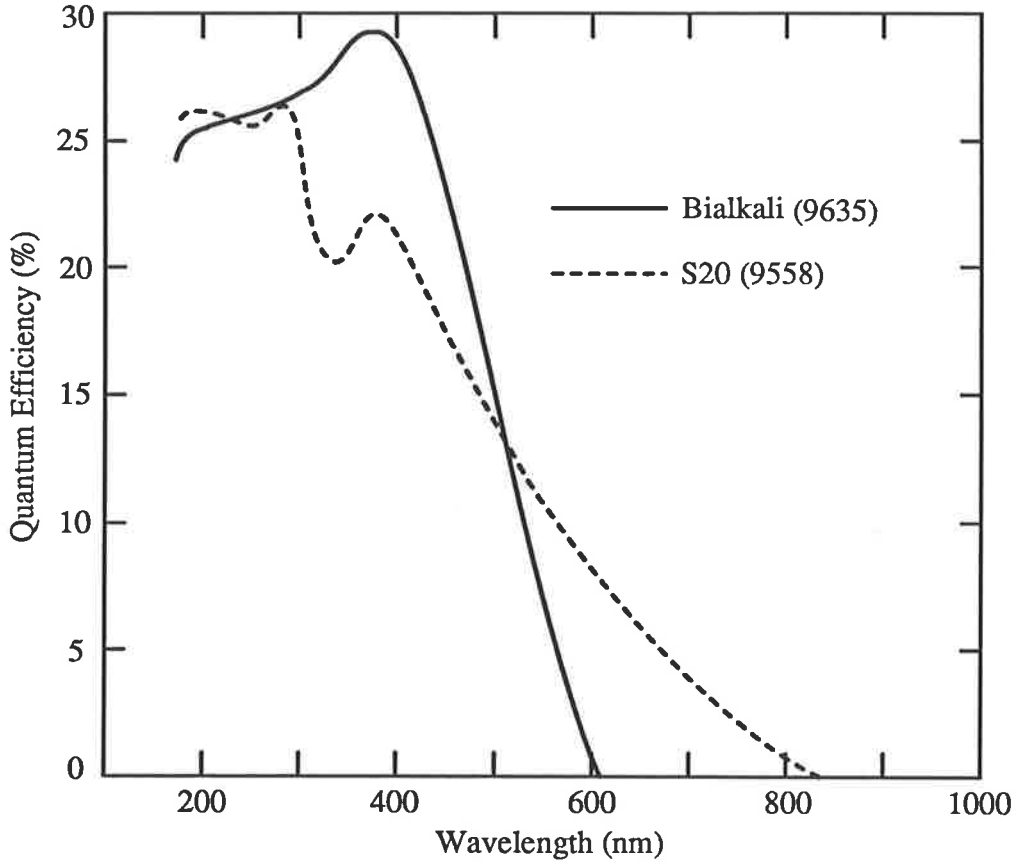

Figure 3.4: Graphs of the spectral response (in terms of the quantum efficiency) against the wavelength for the EMI 9635QA PMT and the EMI 9558QB PMT (taken from the EMI PMT handbook 1982).

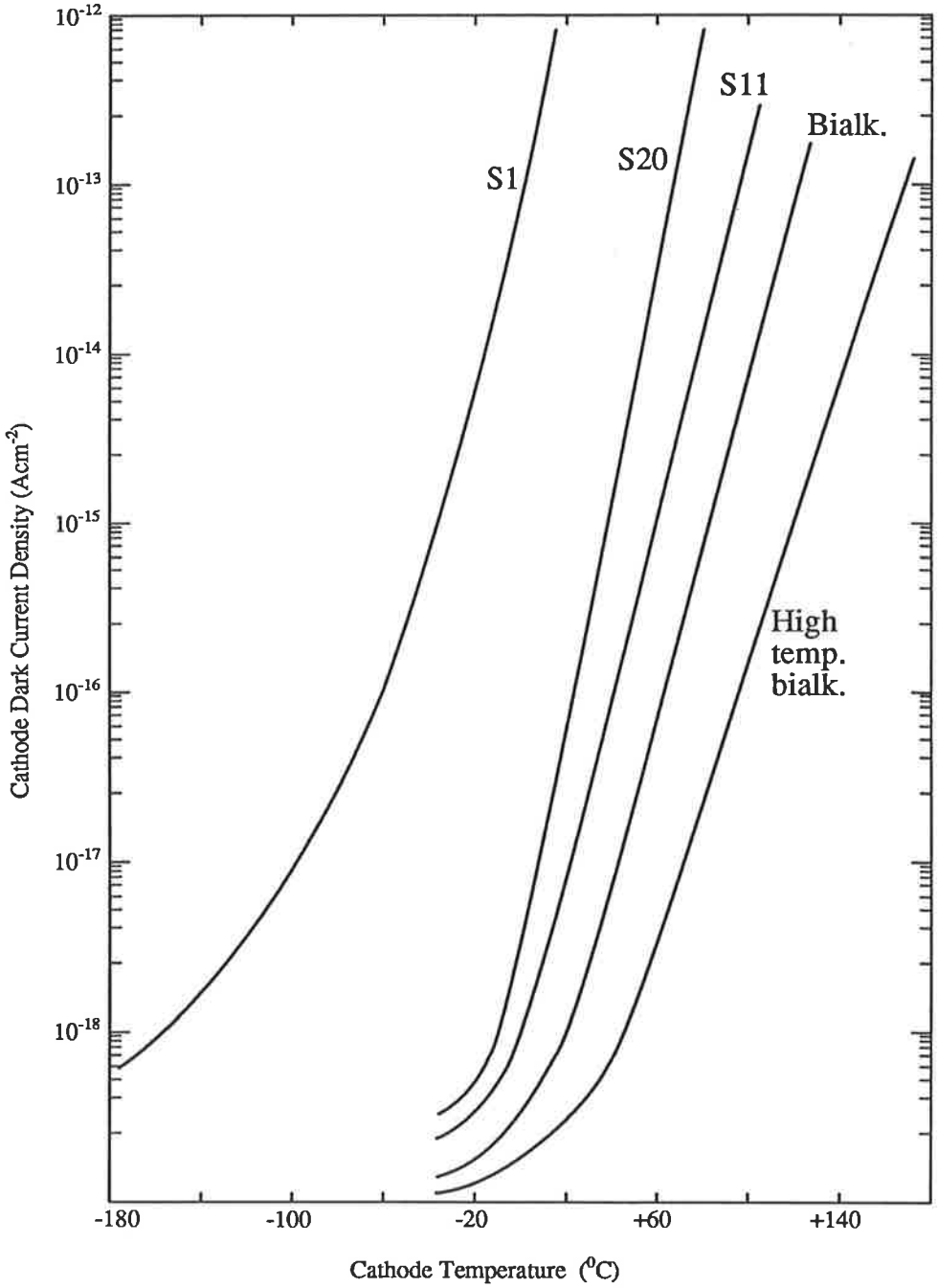

Figure 3.5: Variation of the cathode dark current with temperature, for various photocathode materials. The 9635 PMT has a bialkali photocathode and the 9558 PMT has an S20 photocathode (from the EMI PMT handbook 1982).

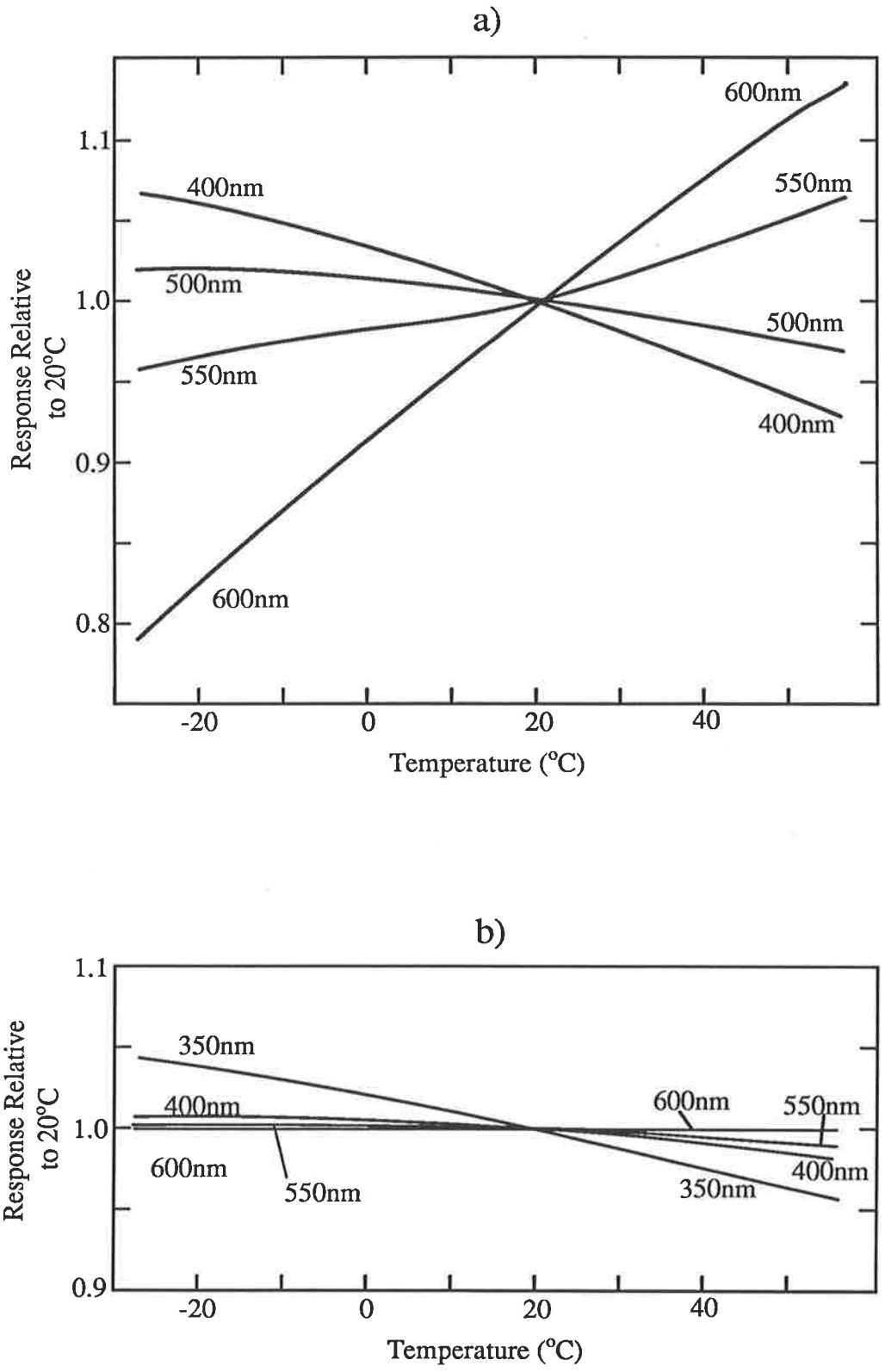

Figure 3.6: Relative spectral sensitivities (as a function of temperature) of a) an S11 cathode (which has a similar response to a bialkali cathode) and b) an S20 cathode (after Schonkeren 1970).

and the resistance of the photocathode also increases sharply (Schonkeren 1970). The 9558 PMT was always operated at -25°C.

The discriminator level was chosen by use of the plateau test (Prescott personal communication). For a particular value of the EHT voltage, the discriminator level was reduced and for each level the number of single electron counts recorded. Such a plot for the 9558 PMT is shown in figure 3.7. The discriminator level required was just at the end of the plateau. This position is indicated by the arrow in figure 3.7. Beyond this value thermionic electron emission from the dynodes dominates the signal. The operating voltage was chosen in a similar way but now for a given discriminator threshold setting and amplifier gain, the EHT was increased and the number of counts again recorded. Figure 3.8 shows the plateaux for four different discriminator voltages. In this case the operating voltage corresponds to the beginning of the plateau region.

One of the problems with the 9558 PMT was that during the alignment stage of the interferometer the bright light used to observe the interference fringes also illuminated the photocathode and caused an increase in the dark count rate. This increased dark count rate decayed away over a period of several minutes. The solution to this problem was to position an iris shutter just before the PMT housing. During alignment the shutter would be closed preventing the illumination of the photocathode.

3.3.2 The Quartz Optics

To extend the spectral response of the interferometer into the UV, the major modification involved replacing the glass and plastic optical components with their quartz analogues. Figure 3.9 shows the transmission curves of several materials commonly

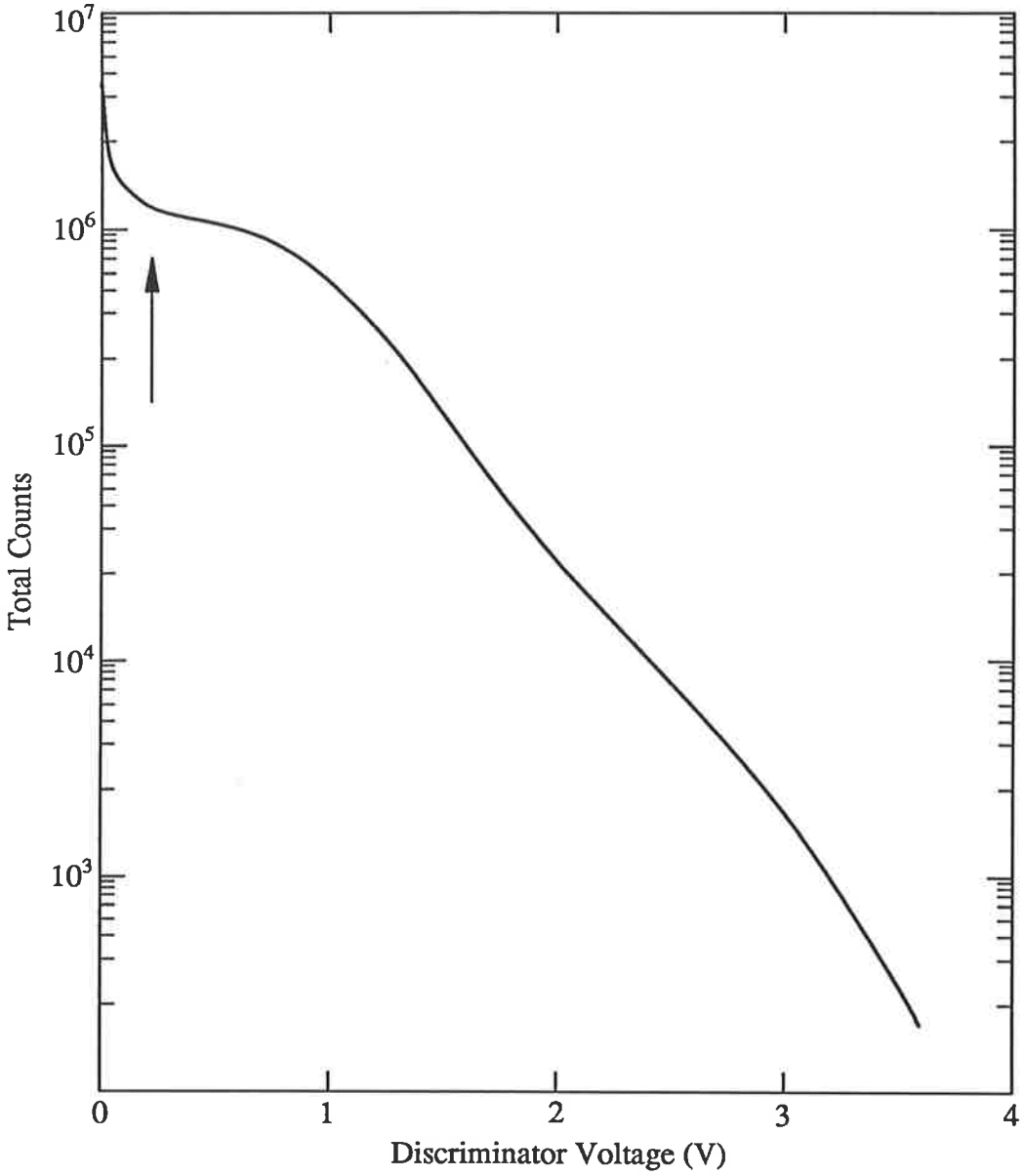

Figure 3.7: Plot of the total number of counts recorded on a multi-channel analyser against the disciminator voltage, to show the plateau region, as the discriminator voltage was reduved. The arrow indicates the desired discriminator level.

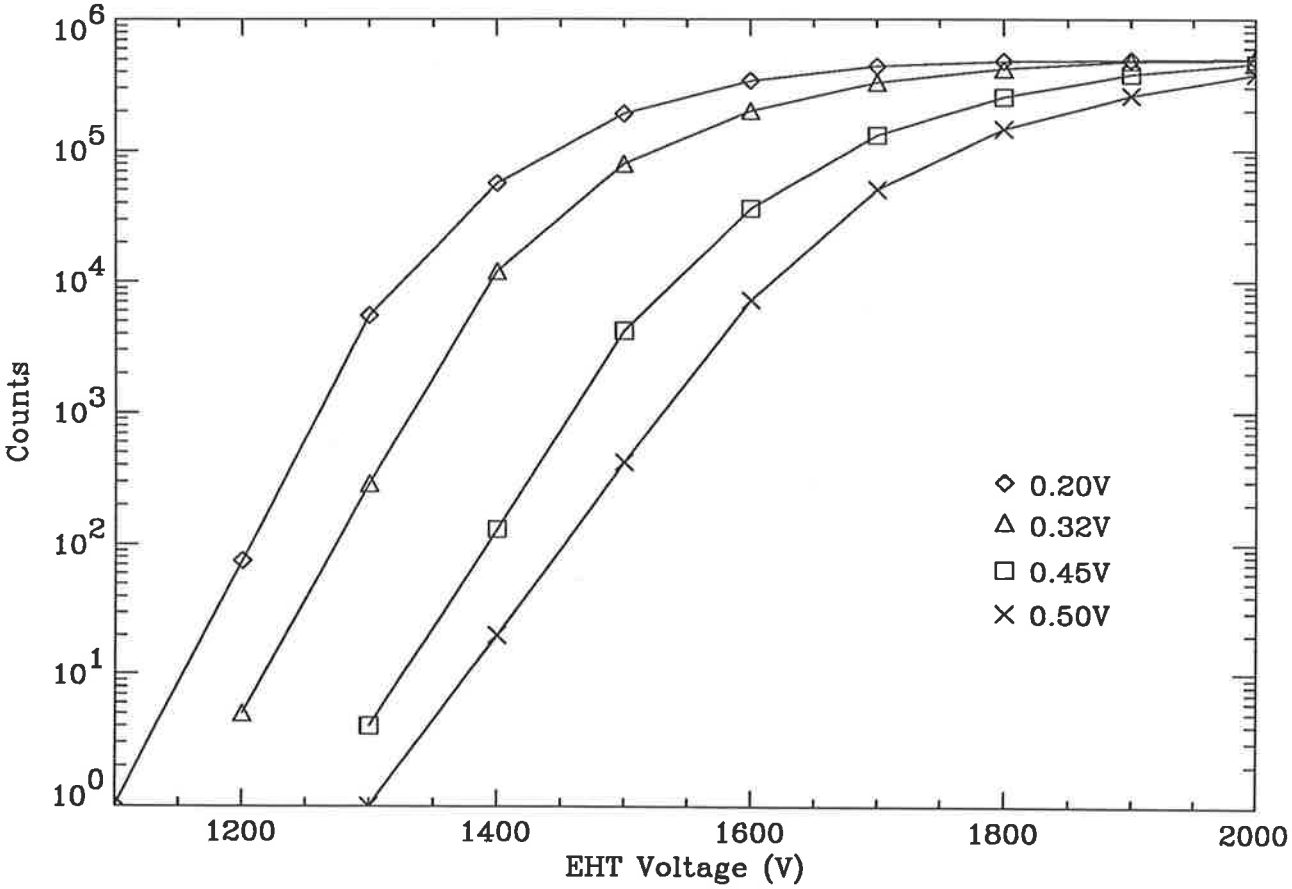

Figure 3.8: Plateau test (for four different discriminator voltages) of the total number of counts against the operating (EHT) voltage.

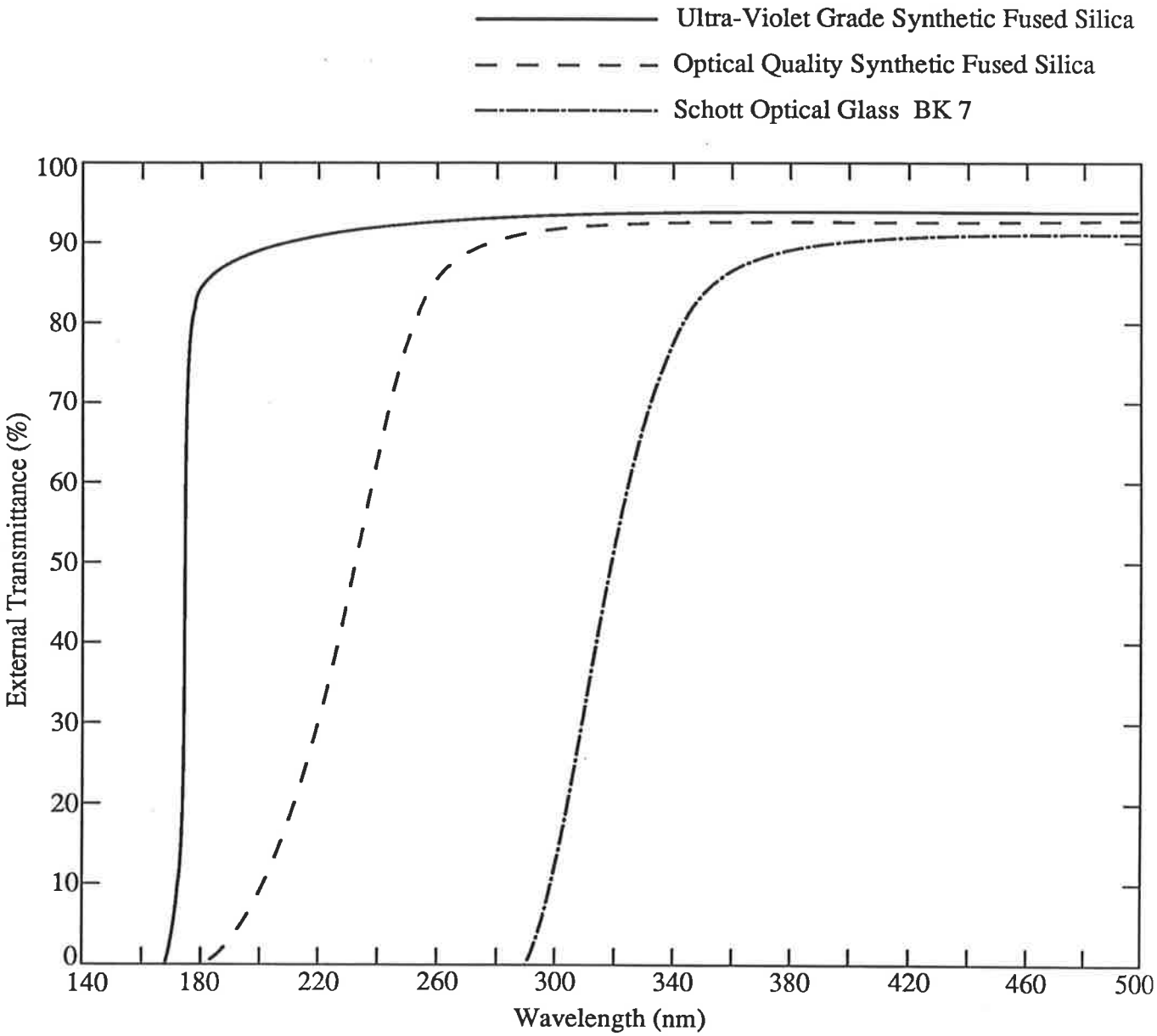

Figure 3.9: Transmission curves of Schott BK7 optical glass, optical quality synthetic fused silica and UV grade synthetic fused silica. The replacement optical components were made from optical quality synthetic fused silica.

used in the manufacture of optical components (the quartz components referred to in this chapter are "synthetic fused silica").

In practice a one–for–one replacement of the existing optical components was not possible. For example, the output lens of the existing system consisted of two thin Fresnel lenses whose combined focal length was 36.5 mm. An equivalent quartz lens would have had to have been especially manufactured involving long delays and great expense. The same was true for the replacement of the glass aspheric lens. Quartz aspheric lenses are simply not routinely manufactured, but on the advice of the quartz lens supplier (Melles Griot) a combination of two plano–convex quartz lenses placed close together would perform almost as well. The choice of a replacement for the two Fresnel lenses was more difficult. The replacement had to be a single lens because of the limited space available between the beamsplitter and the PMT cooling unit. The closest available lens was a 50 mm diameter symmetric bi–convex quartz lens with a focal length of 50 mm. In order to see what effect this would have on the throughput of the spectrometer, experiments were performed to compare the performance of a glass equivalent of the proposed quartz lens with the existing output lenses. Figure 3.10 shows the effect on the interferograms of introducing a 50 mm diameter field stop immediately before the output Fresnel lenses, compared to the normal case. Also shown is the interferogram produced with the glass lens substitute and with the same stop as above. For all the interferograms the illumination was the same. The figure clearly shows that the intended quartz replacement would make no difference to the throughput of the instrument. In fact this replacement may have been doubly advantageous because by blurring the image of the disc on the photocathode, the

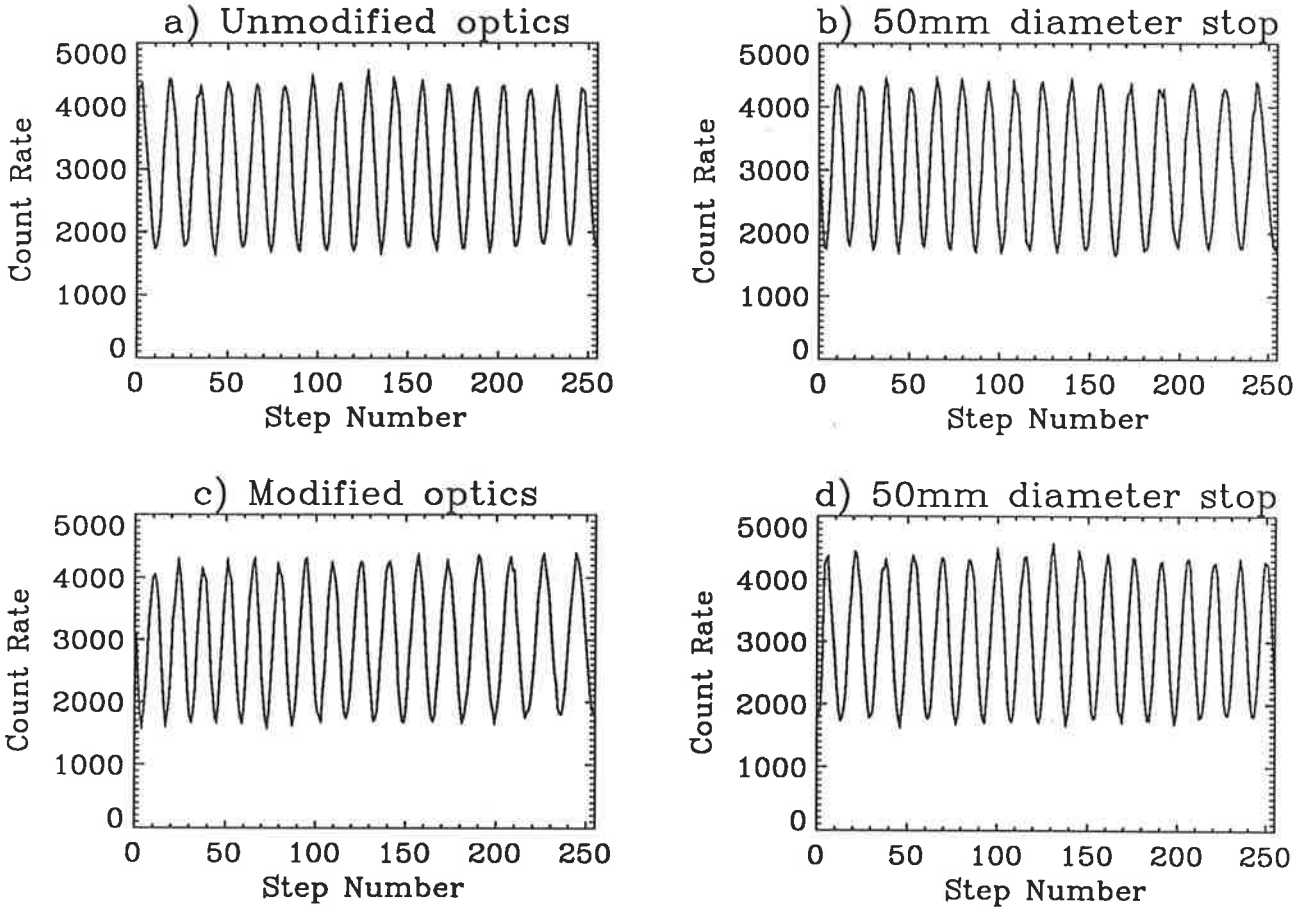

Figure 3.10: This figure shows the comparison between the original optical design and the new quartz optical design. a) is the old unmodified optics, b) is the same as a) but with a 50mm diameter stop just before the output optics. c) is the same as a) but with a 50mm focal length output lens instead of the existing double Fresnel lens combination, and d) is the same as c) but with the 50mm stop in place.

effects of any non-uniformities in the spectral response of the photocathode may have been reduced (Schonkeren 1970).

Figure 3.11 shows the ray diagram of the optical system after the modifications had been made. For simplicity the beamsplitter and the mirrors have been omitted.

The Beamsplitter

The quartz beamsplitter and compensator combination were obtained from a local supplier – "Quentron Optics" (now defunct) as dimensionally identical replacements for the existing glass combination. The coating of the new beamsplitter was supervised by the author at another local firm "A.G. Thompson". Initially it was hoped that a single aluminium coating would suffice to provide the partial reflection/transmission properties. However, it proved impossible to judge precisely the amount of aluminium that should be deposited in order to take into account the oxidation of the aluminium (the effect of which was to make the beamsplitter more transparent). In the event a thin layer of SiO_2 had to be deposited on top of the aluminium to prevent oxidation. The amount of SiO_2 deposited was measured by interference using a monitoring beam of light which was a part of the vacuum deposition equipment. Unfortunately the lowest monitor wavelength of light available was 500 nm. Ideally a monitoring wavelength of around 300 nm would have been preferred so as to minimize the interference effects caused by the thin film of SiO_2 at the shorter wavelengths where the sensitivity of the instrument is lowest. The reflection and transmission curves of the original glass beamsplitter and the quartz beamsplitter are given in figure 3.12.

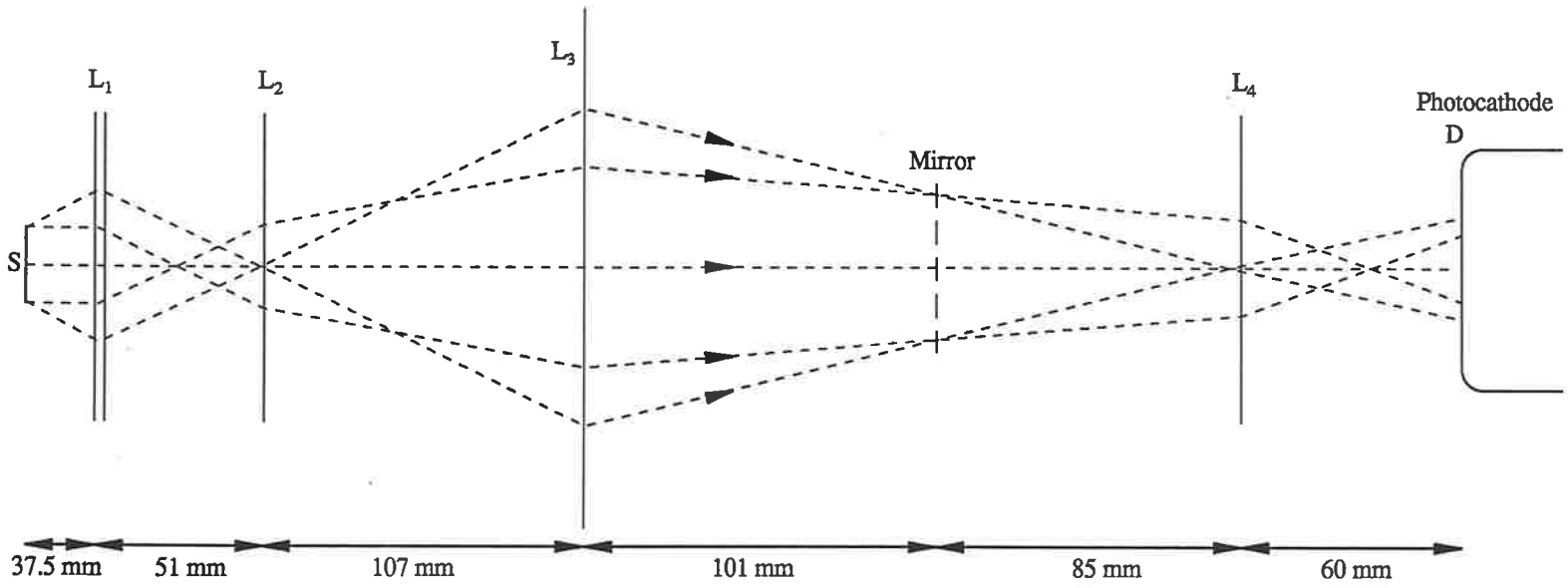

Figure 3.11: Schematic diagram of the optical system showing the relative position of the quartz optical components. The broken lines are example optical rays. The vertical broken line is one of the mirrors, included for reference. The beamsplitter has been omitted.

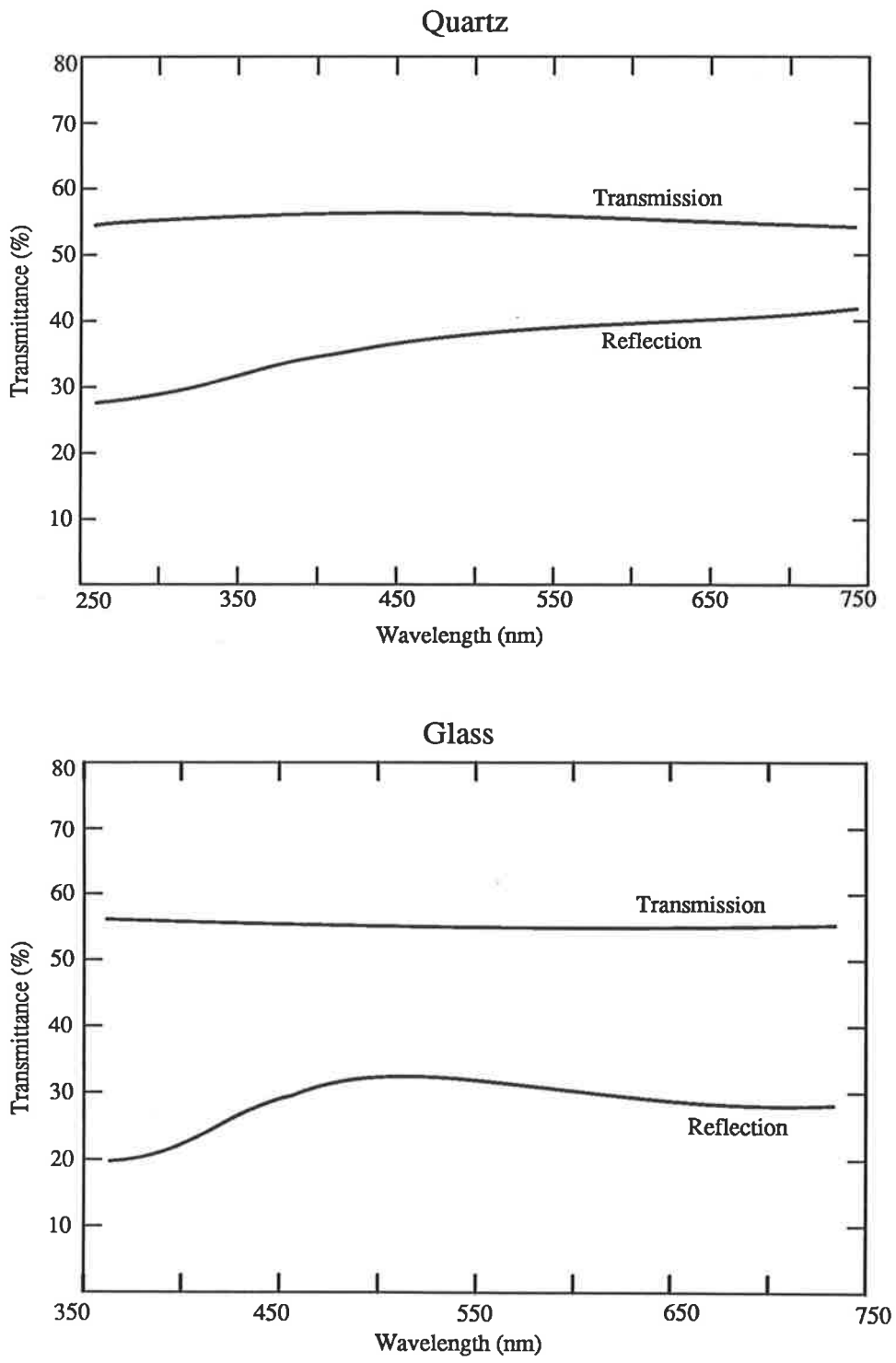

Figure 3.12: Transmission curves of the original glass and the new quartz beamsplitter. The transmission curves were for normal incidence and the reflection curves were for a 45° angle of incidence.

3.3.3 The Mirrors

Connes (1960) and Chamberlain (1979) have discussed the effects on the spectra due to distortions at reflecting surfaces. In general the defects caused by the distortions become greater as the wavelength gets shorter. As an example Connes (1960) calculated that for a spherical surface distortion with a sagitta given by

$$\frac{r^2}{2R_S}, \tag{3.1}$$

where r is the radius out from the centre of the mirror and R_S is the radius of curvature of the distortion, the calculated spectrum is

$$B(\sigma)sinc(2\sigma R^2/R_S), \tag{3.2}$$

where R is the maximum radius of the mirror. The *sinc* function first goes to zero when $\sigma = \sigma_S = R_S/2R^2$ and so the highest wavenumber present in the spectrum must be much less than σ_S (Chamberlain 1979).

In the initial design the mirror mounts had three small grub screws which were used to provide a degree of fine alignment of the mirror tilt. The contact points of these screws on the edge of the mirror surface may have produced significant distortions, which, although not important at 350 nm, would be significant further into the UV. Figure 3.13 shows the revised design of both the moveable and fixed mirror mounts. The mirrors are now held fixed in the mounts with even pressure around the front surface edges. Fine alignment was performed via the rear attachment bolts and rubber O ring washers. Tightening the bolts compressed the O rings and provided the necessary degree of tilting. Figure 3.14 shows interferograms produced by light from a monochromator for wavelengths below 350 nm, using this revised

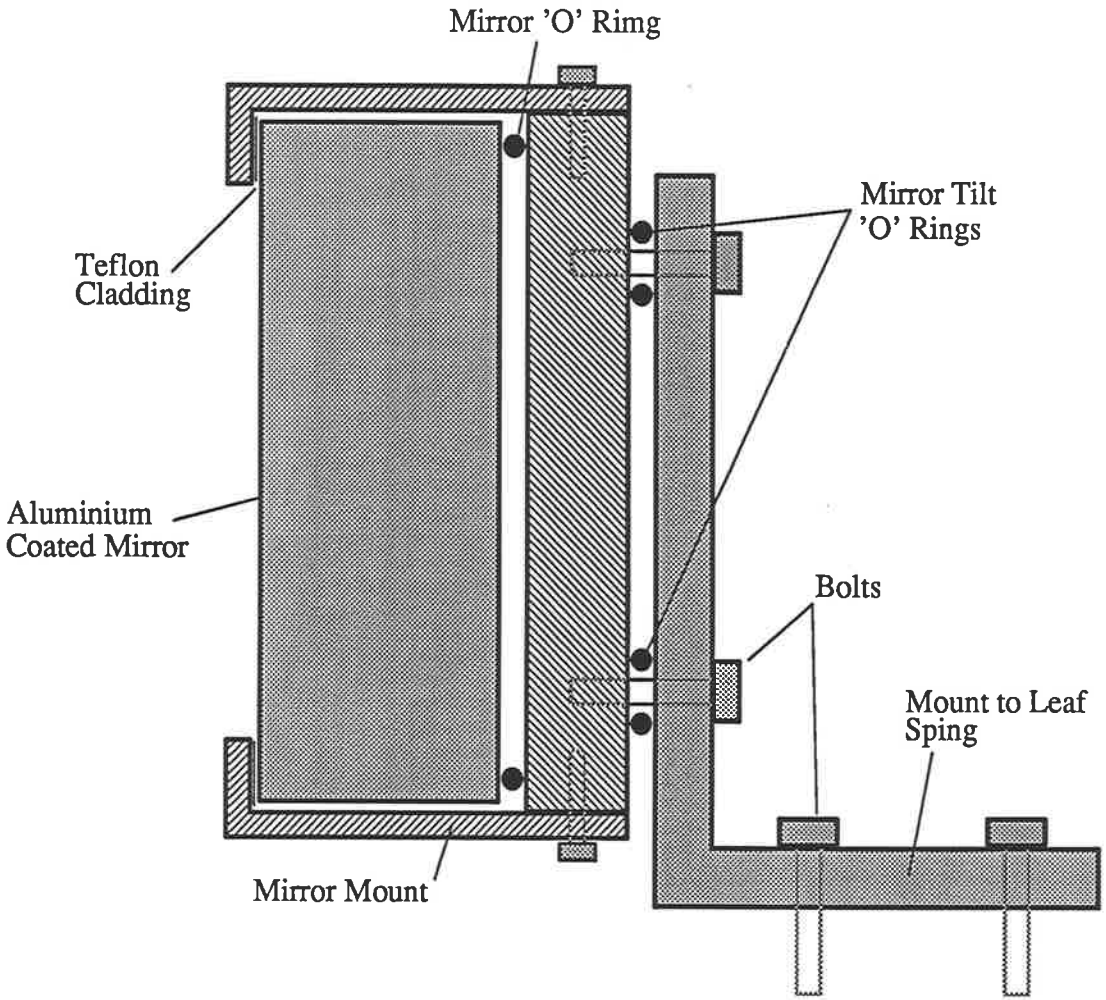

Figure 3.13: Diagram of the revised design of the mirror mount holders, showing the new tilting system based on O ring washers.

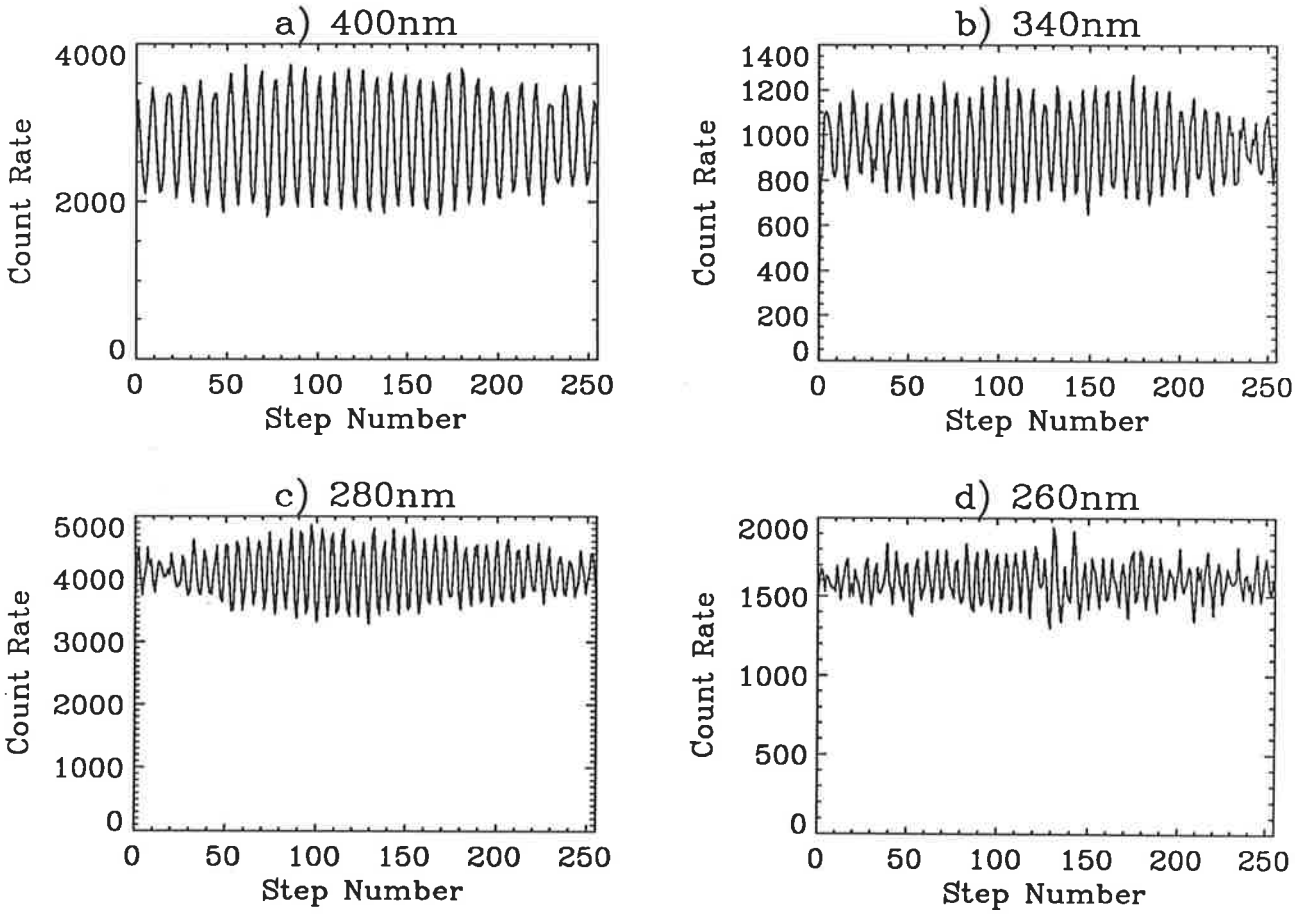

Figure 3.14: This figure shows some interferograms obtained with the new quartz optical design. The light source was a Xenon lamp with a monochromator attached.

design. There was a significant reduction in the amount of mirror distortion. This is shown up by comparing this figure with figure 2.6 of Akber (1986). A convenient way of expressing the amount of incoherence in the interferograms was to calculate the ratio of the average value of the amplitude of the modulation to the average interferogram intensity. At 350 nm the improvement in this ratio was about 40%. In other words, for the same average intensity, the amplitude of the modulation was about 40% greater than with the old optical design.

3.3.4 Sample Discs

One of the disadvantages of using the 9558 PMT was that at glowing temperatures above about 320°C, the incandescent glow from the sample and its disc began to swamp out the TL signal of interest. Therefore it was vital that the sample disc incandescence be kept as low as possible. The obvious way of achieving this was to use sample discs made from materials with a low thermal emissivity. Aluminium discs were found to have an incandescence typically 25% that of stainless steel discs at a given temperature and hence aluminium discs were always used.

For some TL materials, such as quartz, where the TL glow peaks of interest lie above 300°C the 9558 PMT cannot be used since the TL signal is swamped by the incandescence. In these cases the 9635 PMT was used because of its low sensitivity to the red.

3.3.5 Filters

For a spectral range of 500 nm to 740 nm the existing Kodak gelatin neutral density filters were perfectly adequate. However below 500 nm the transmission of, for ex-

ample a neutral density 1 filter, reduced quickly to below three percent at 400 nm. These filters were then, clearly unsuited to wavelengths in the violet–UV region.

A simple and cheap method of producing neutral density filters capable of use over the whole spectral range of interest was to perforate a sheet of supermarket aluminium foil with small, evenly spaced holes. This was done by lying the foil on a bed of tissue paper and then perforating it with a sharp needle, producing holes about 1 mm in diameter. The degree of attenuation was determined by the density of holes made and the positioning of the holes was determined beforehand by ruling a grid onto the foil. Although such filters are quite delicate, figure 3.15 shows that they provide good, flat attenuation over the whole spectral range from 250 nm to 740 nm.

3.3.6 Calibration

With the new optical components and photomultiplier, the apparatus required recalibration to produce a curve which would allow spectra to be corrected for the varying response of the equipment to the different wavelengths. The procedure adopted was similar to that used by Akber (1986). Using the EMI 9635QA PMT in both the 2–D and the 3–D PMT holders in turn, the illumination wavelength from a Bausch and Lomb monochromator was varied between 250 nm and 740 nm (this PMT still gave a response at this wavelength provided the intensity was high enough), giving the percentage of light transmitted at each wavelength.

Next, the spectral response of each PMT was calculated from the data supplied by the manufacturers and from interferograms recorded at various wavelengths (also between 250 nm and 740 nm), any spectral coherence effects were also accounted for.

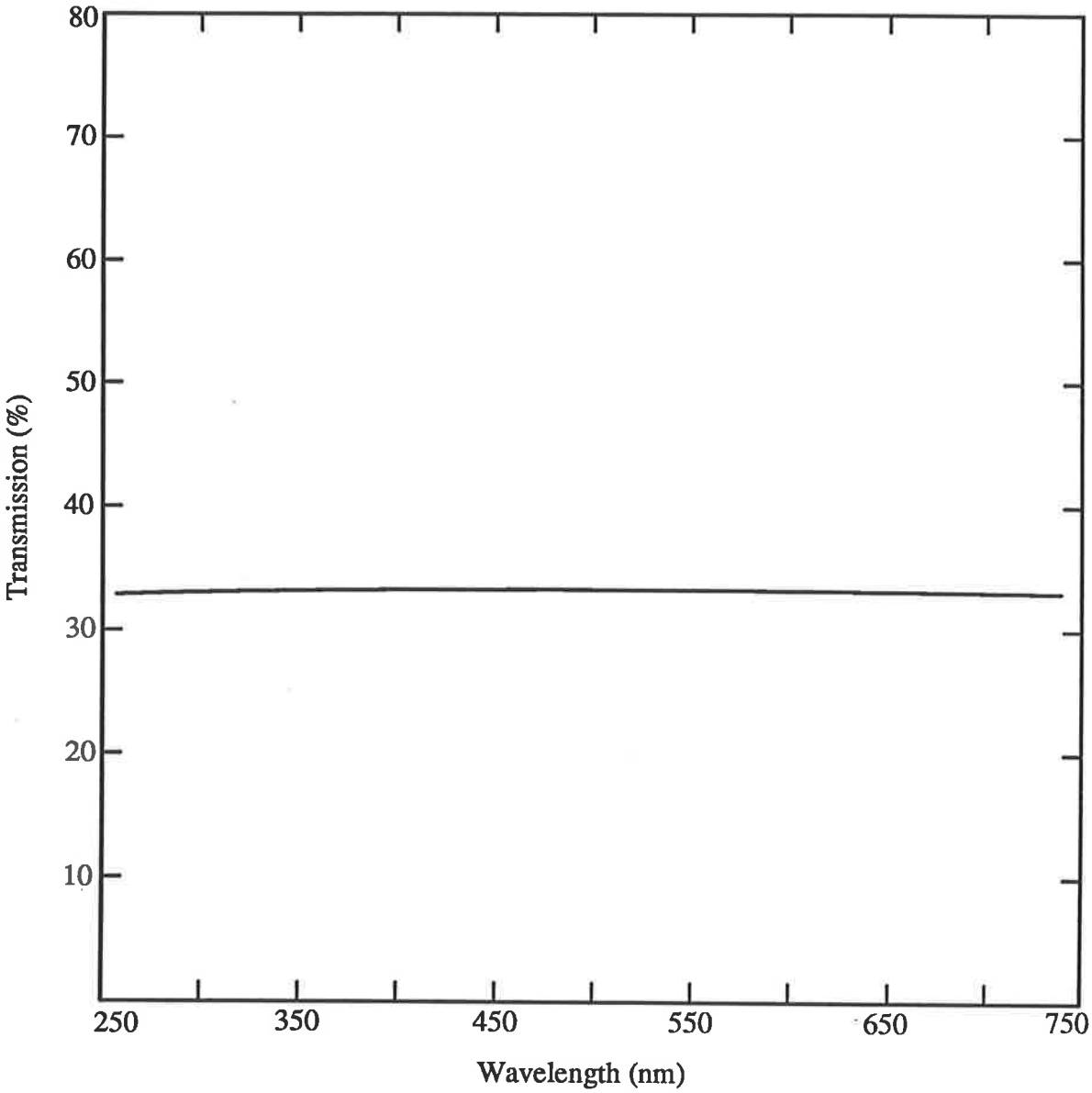

Figure 3.15: Transmission curve for an aluminium perforated filter.

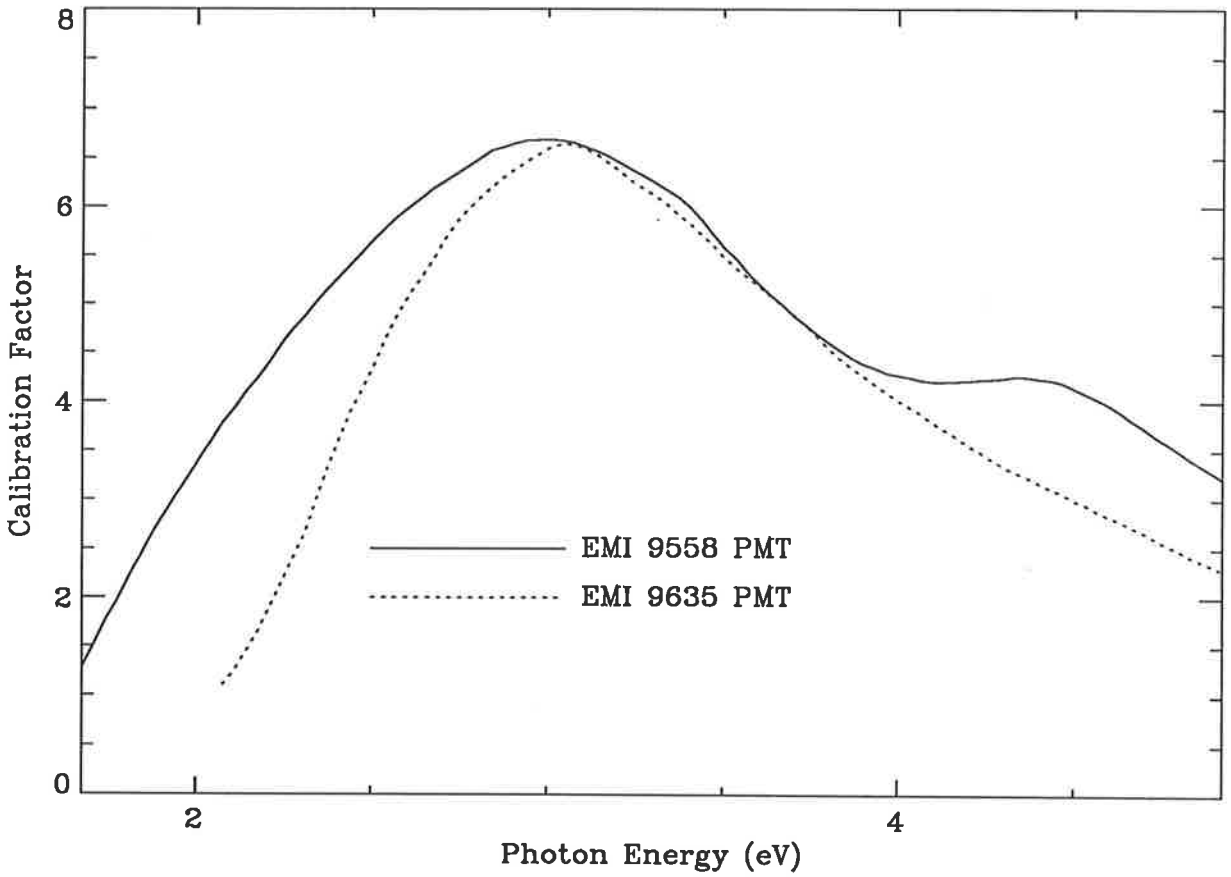

Figure 3.16: These two graphs are the spectral calibration curves for the EMI 9558QB PMT and the EMI 9635QA PMT. The curve for the 9635 does not extend below about 2.1eV (600nm).

This last effect showed up as a decreasing ratio of the modulation in the interferograms relative to the average signal as the wavelength was reduced (see figure 3.14).

Figure 3.16 shows the final calibration curves for both the 9635 and 9558 PMTs.

3.4 Conclusion

In this chapter the modifications necessary to extend the spectral range of the spectrometer into the red and ultra–violet were described. In the next chapter the emission spectra of a broad range of TL materials is presented. Comparisons are made with equivalent spectra measured with the previous design. In this way it will be demonstrated that the modifications have been successful and that the calibration was correct.

The next chapter is also of interest since the studies represent extentions to research already carried out in this department, particularly on the phosphor dosimeters and the feldspars.

Chapter 4

Thermoluminescent Materials

4.1 Introduction

In the previous chapter the design modifications to extend the spectral range of the interferometer were described. This chapter will demonstrate its capabilities and enable comparisons to be made between spectra recorded both before and after these modifications were made. Also in the ultra–violet and red end of the spectral range, comparisons are made between known emission peaks of several samples.

Four groups of samples are described. Six dosimeters, four speleothem calcite samples, four feldspar samples and some minerals whose emission was thought to be due to sulphur. These studies show the usefulness of using emission spectroscopy and, in the case of the calcite samples, how such information can be used with other techniques such as electron spin resonance.

For convenience 2–D glow curves (with a temperature resolution of about 12°C) constructed from the corrected spectra are also shown alongside the corresponding spectral contour plots. These glow curves are intended to aid the determination of the temperature at which each emission occurred. They are certainly not intended to be used as comparisons with glow curves measured with conventional 2–D apparatus,

where selective filters are used and where the choice of PMTs and these filters may vary from one laboratory to another. The glow curves presented here are superior to those where no spectral correction was possible since the peaks are directly representative of the number of recombination processes occuring at any given temperature.

The role that the author played in the collection and interpretation of the experimental data is outlined in each section.

4.2 TL Phosphors

The spectra presented here were recorded using the modified apparatus described in chapter 3 and hence they differ in some respects from the spectra published previously by Fox *et al* (1988). In that paper the spectra were recorded using the previous design of the spectrometer whose response was limited to 600 nm to 350 nm. Here the spectra were recorded for wavelengths between 740 nm and 250 nm. Also, in that paper the glow curves were reconstructed from the raw data, whereas here (and in all the later sections of this chapter) the glow curves were formed from the corrected spectral data. Essentially the comments in Fox *et al* (1988) concerning each phosphor are still valid but, where necessary, the text from that paper has been amended to account for any changes or differences observed, otherwise it is the same.

The data presented here were recorded totally by the author. Nearly all of the interpretation was also performed by the author except for some additional input by J.R. Prescott.

4.2.1 Introduction

Most of the spectral information on TL phosphors in the literature has been obtained using scanning monochromator type instruments. This means that relatively large doses are required to give a sufficiently large signal. By virtue of its greater optical throughput, Fourier transform spectroscopy provides a technique for studying TL spectra at doses several orders of magnitude less than with dispersive instruments (Jensen and Prescott 1982).

The apparatus used to record the spectra has been described in detail in chapter 3. All the contour diagrams have been corrected for the spectral response of the instrument and for all samples the heating rate was 5 Ks^{-1}.

In this section information on six dosimeter phosphors is presented, these were: Harshaw $CaSO_4$:Dy, LiF:Mg,Ti (TLD–100), CaF_2:Dy (TLD–200), $BaSO_4$:Eu, Mg_2SiO_4:Tb and AL_2O_3:Ti, Si. For each of the phosphors, spectra are shown for a dose of 1 Gy and for a dose of about 30 mGy (depending on the TL sensitivity). In most cases these spectra were for doses considerably less than any previously published and indicate details of traps and luminescence centres under conditions where saturation was not significant. In some cases differences in the spectra were seen for the two doses. Comparisons were made with work at higher doses.

In each case a conventional "glow curve" of TL intensity versus temperature was also obtained from the spectrally corrected data. These glow–curves were all calculated from spectral files which had been corrected for the spectral response of the interferometer. Each glow curve is shown with its corresponding 3D spectrum.

In four of the phosphors studied here, the high TL sensitivity observed resulted

mainly from the addition of rare–earth (RE) elements and the spectra corresponded to transitions in the RE ion. Merz and Pershan (1967) and Nambi *et al* (1974) have studied the effects that different RE dopants have in CaF_2 and $CaSO_4$, respectively. Both papers concluded that the RE elements had little effect on the glow–curve peak temperatures, and that the spectra obtained were characteristic of the RE element and matched energy changes of the 4f and 4f5d electron configurations (Dieke and Crosswhite 1963). The crystal field has little effect on these transitions. Marfunin (1979) explains this in terms of the range of the wavefunctions of the 4f electrons which do not overlap those of the 3d electrons. Mechanisms have been put forward by several authors whereby RE ions become excited and then relax to the ground state with emission of radiation. Essentially two models have been given by Nambi *et al* (1974) for TL production in $CaSO_4$. In the first, electrons and holes are trapped in the normal way during irradiation at defect sites independent of the RE ion. Recombination could then lead to an excited state of the RE ion which decays radiatively. In the second and favoured model, during the irradiation the electrons could be trapped at the ion itself $RE^{3+} + e^- \rightarrow RE^{2+}$, and heating would release holes to recombine to form excited states $RE^{2+} + h^+ \rightarrow RE^{3+*}$ (McKeever 1985).

A separate model based both on TL spectra and optical absorption in $CaSO_4$:Dy has been proposed by Matthews and Stoebe (1982). This model differs from that of Nambi *et al*(1974) because the RE ion acts only as the luminescence centre, not as the centre of recombination, which takes place at a radical. The recombination energy is then resonantly transferred to the Dy where the luminescence takes place. This model has the advantage that it does not require the existence of an RE^{2+} ion

for luminescence and so can explain the emission spectra of RE^{2+} such as Eu^{2+} in $BaSO_4$ which the other models do not account for (Stoebe and Morgan 1984). A further new model has been suggested by Stoebe and Morgan. This model is based on the work done by Krystek (1980) on $BaSO_4$, who identifies a U_{Ba}–SO_4 hole trap, that is, a barium vacancy linked to a sulphate radical. Holes released during heating recombine with trapped electrons, with the resultant energy being non-radiatively transferred to a nearby RE ion where once again luminescence would take place.

4.2.2 Results

$CaSO_4$:Dy

Figures 4.1 and 4.2 show the 2–D glow curves and contour plots of TL intensity against photon energy and temperature for doses of 15 mGy and 1.0 Gy respectively. The main emission peaks occur at a temperature of about 220°C and photon energies of 2.59 (480), 2.18 (570) and 1.82 eV (680 nm) in good agreement with many other authors (for example, Yamashita *et al* (1968). These emission energies can be attributed to the $^4F_{9/2} \rightarrow {}^6H_{15/2}$ (2.59 eV), $^4F_{9/2} \rightarrow {}^6H_{13/2}$ (2.18 eV) and $^4F_{9/2} \rightarrow {}^6H_{11/2}$ (1.82 eV) energy transitions in the 4f subshell of Dy^{3+} (Dieke and Crosswhite 1963, Marfunin 1979). There are no notable differences between figures 4.1 and 4.2 except for the relative intensity of the 120°C peak which has decayed much more in figure 4.2 than in figure 4.1 and in this range the spectra and glow–curves are not dose dependent. Nambi *et al* (1974), suggest that the temperatures at which the emission peaks occur are characteristic of the depth of hole traps caused by, for example, SO_4^-, SO_3^-, O_3^- radicals (see also Danby *et al* 1982).

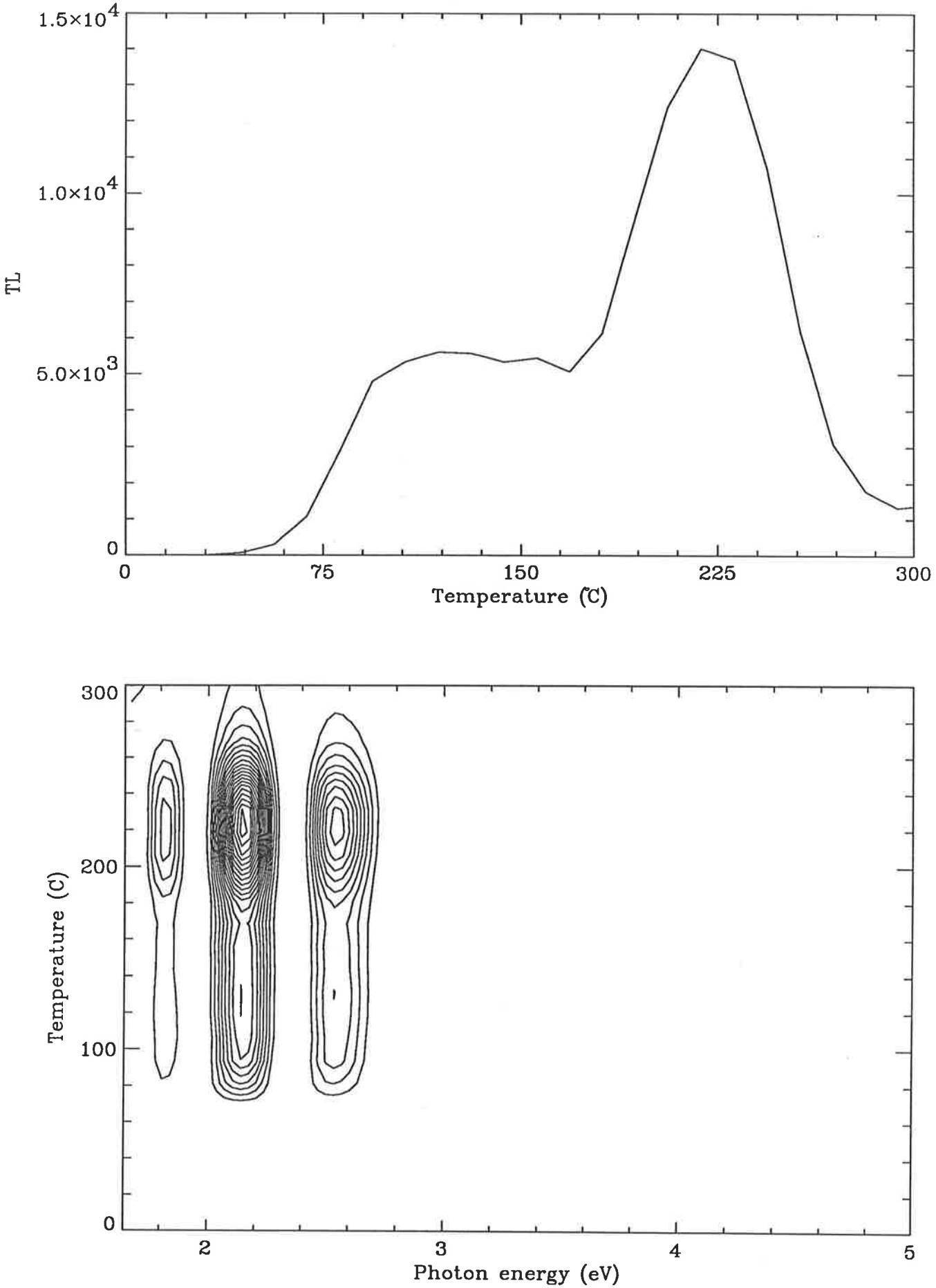

Figure 4.1: $CaSO_4$:Dy for a dose of 15mGy and a wait of about 5 minutes. Above is the 2–D glow curve constructed from the spectral file and below is the contour plot of this spectrum.

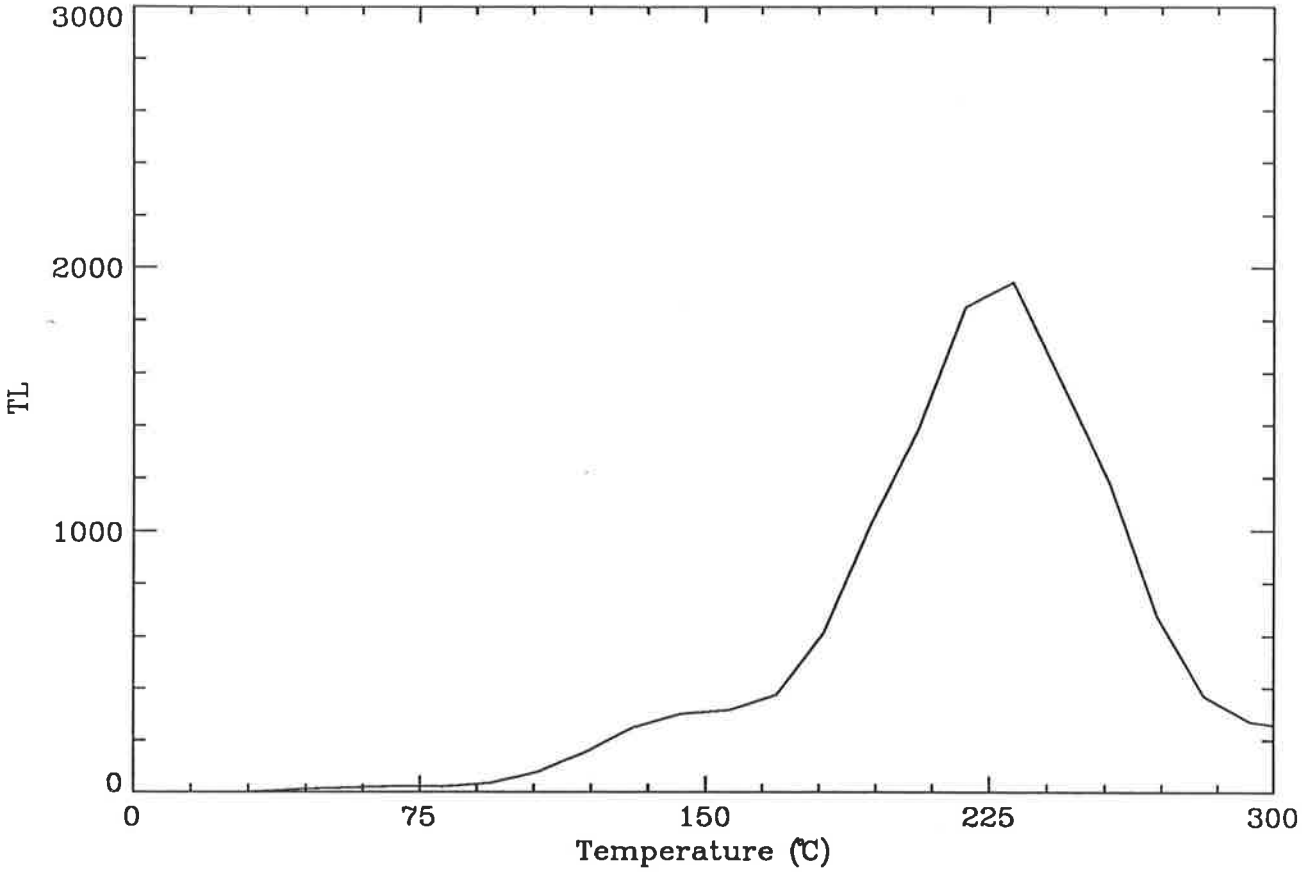

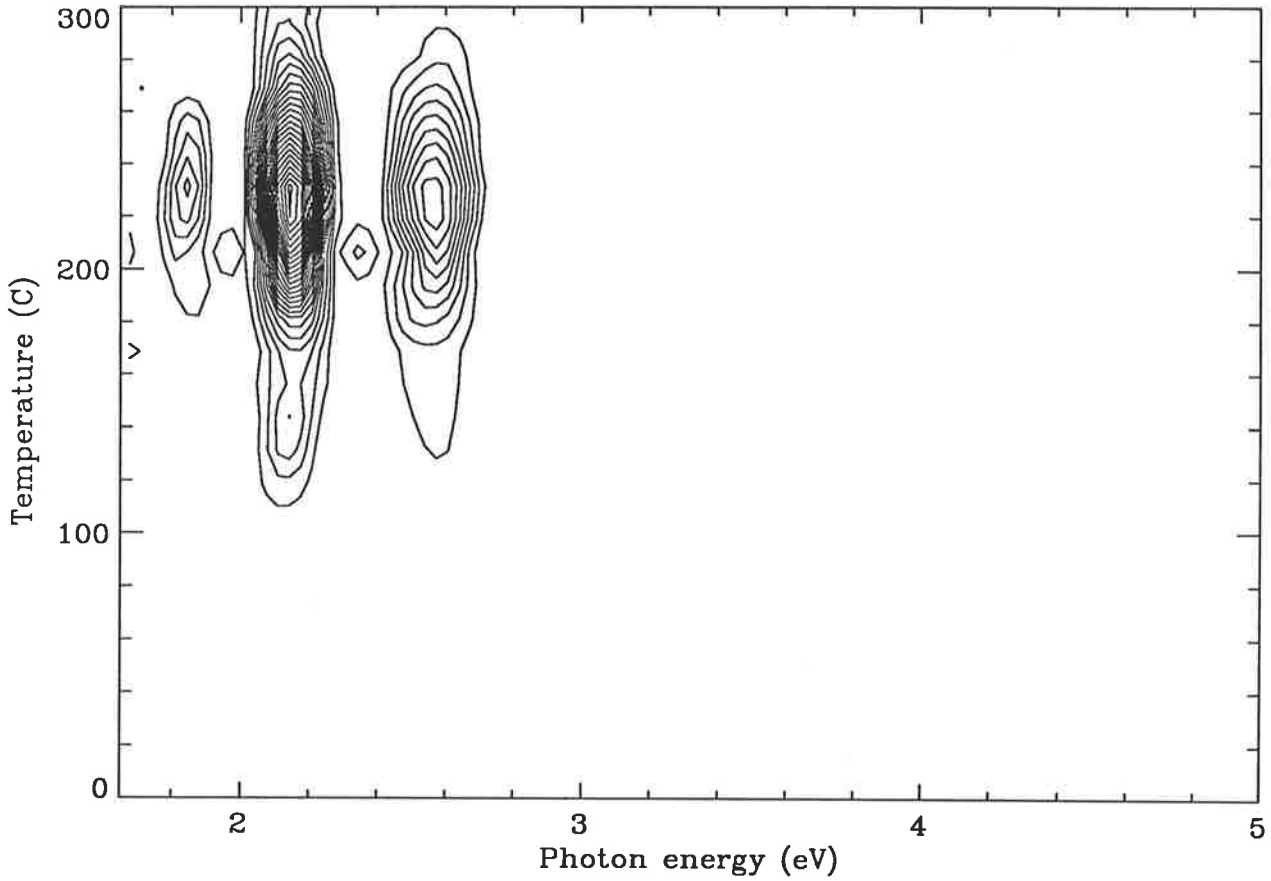

Figure 4.2: $CaSO_4$:Dy for a dose of 1.0Gy and a wait of about 2 days. Above is the 2–D glow curve constructed from the spectral file and below is the contour plot of this spectrum.

CaF_2:Dy (TLD–200)

Figures 4.3 and 4.4 are the plots for doses of 15 mGy and 1.0 Gy respectively. Since it has the same Dy activator as $CaSO_4$, the spectral response of this phosphor was almost identical, even to the fine spectral detail. However, the trap structure was different, as evident by the location of the peaks on the temperature axis. This is shown clearly in the 2D glow–curves accompanying each spectrum.

The main emission peak temperatures agree with previous work. They were close together and overlap considerably and fall at about 120°C (I), 140°C (II), 210°C (III) and 250°C (IV) (Binder and Cameron 1969). The TL dose response was known to be a strong function of dose and this was evident for the two plots, where the relative heights of the obvious peaks II, III and IV changed markedly over the dose range used in this case (15 mGy–1.0 Gy). The changes correspond very closely to those described by, for example, Binder and Cameron (1969). Merz and Pershan (1967) studied CaF_2:RE^{3+} in detail with similar conclusions to Nambi *et al* (1974). Their model for the trapping of holes in the crystal lattice was partly based on V_k centres, that is, a hole trapped at an F_2 molecule. Work on $CaSO_4$ and CaF_2 has been reviewed by Sunta (1984) and by Horowitz (1984).

There was no evidence of the differences in spectra for different glow–peak temperatures described by Sunta (1984) for TLD–200. In particular, while there was weak emission and indications of specific wavelengths in the range 500–550 nm and below 450 nm, which may well correspond to Tb^{3+} impurities, there was no indication that these appear at temperatures above 300°C, preferentially or otherwise. The same was true for the spectra of $CaSO_4$.

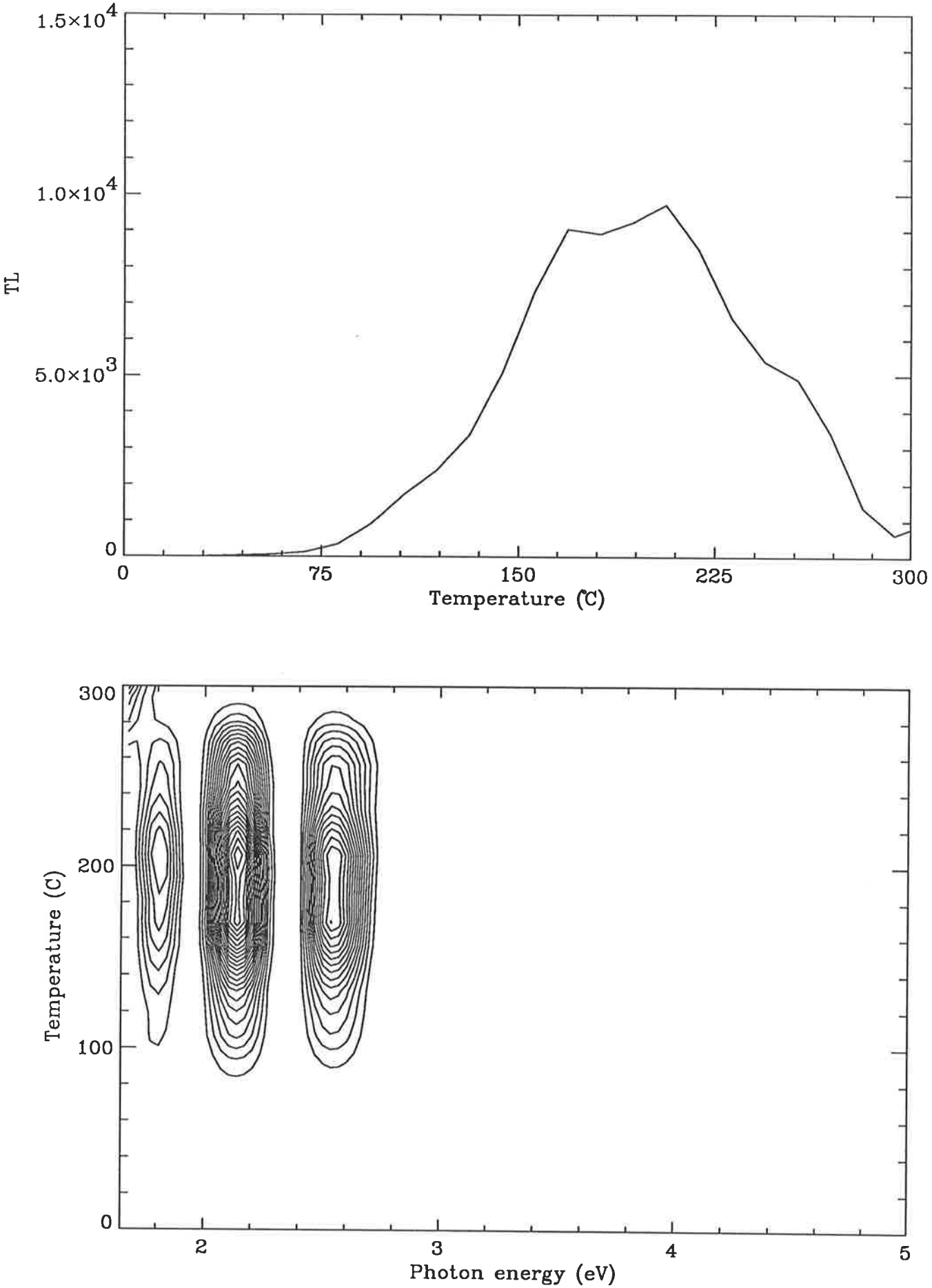

Figure 4.3: CaF_2:Dy for a dose of 15mGy and a wait of about 5 minutes. Above is the 2–D glow curve constructed from the spectral file and below is the contour plot of this spectrum.

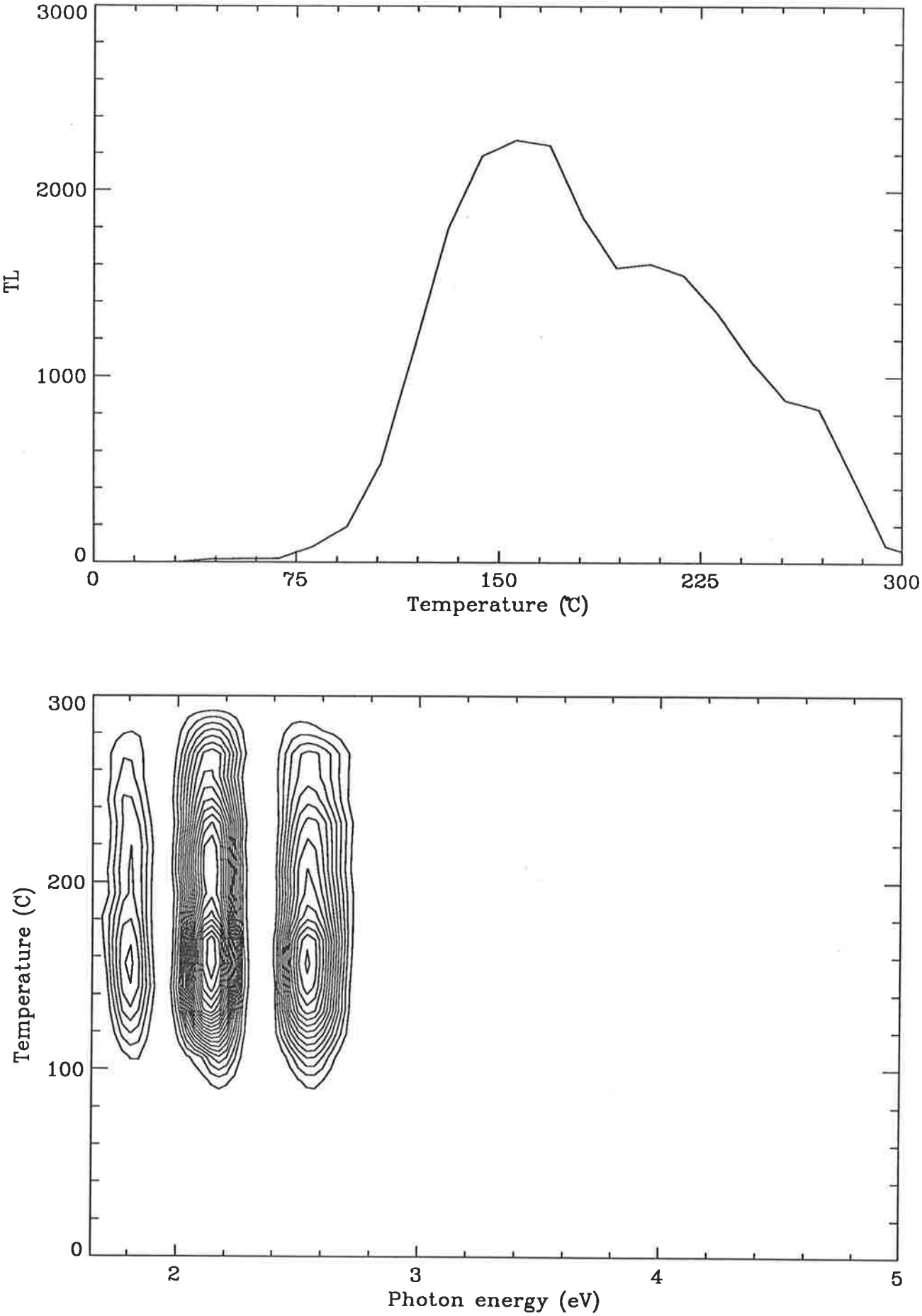

Figure 4.4: CaF_2:Dy for a dose of 1.0Gy and a wait of about 2 days. Above is the 2–D glow curve constructed from the spectral file and below is the contour plot of this spectrum.

$BaSO_4$:Eu

This phosphor has been described by Yamashita *et al* (1985). This reference discusses a variety of alkali–earth sulphates activated with Eu. The sample used in the present work was obtained by courtesy of T. Wada of that group and was in the form of phosphor embedded in a Teflon sheet (Okamoto *et al* 1986).

Figures 4.5 and 4.6 show the plots for doses of 15 mGy and 1.0 Gy respectively. Both plots show glow–curves in agreement with Okamoto *et al* (1986), with a main emission peak at around 220°C and distinct shoulders at around 180 and 260°C although our equipment failed to resolve these peaks in temperature. All three peaks occur at a photon energy of 3.31 eV (375 nm) which agrees with the spectra obtained by Yamashita *et al* (1985). The broad band of emission peaking near 3.31 eV was attributed by Yamashita *et al* (1985) to the $4f^6 5d \rightarrow 4f^7$ transition in Eu^{2+}. There is also a suggestion (especially in figure 4.5) in our work of emission below about 1.9 eV which would correspond to the Eu^{3+} transitions observed in $CaSO_4$ by Calvert and Danby (1984) at these energies. $BaSO_4$:Eu resembles $CaSO_4$:Dy in that the emission peaks correspond to the release of holes (Krystek 1980) who identified these traps to be the SO_4^- and O_2^- defects or barium vacancies associated with a neighbouring SO_4^- radical (U_{Ba}–SO_4^- hole traps).

Mg_2SiO_4:Tb

The plots for 15 mGy and 1.0 Gy are shown in figures 4.7 and 4.8 respectively. The main emission peaks are at 210 and 260°C, which were unresolved in this plot. The emission energies are 3.27 (380), 2.82 (440), 2.53 (490), 2.26 (550), and 1.95 eV (636

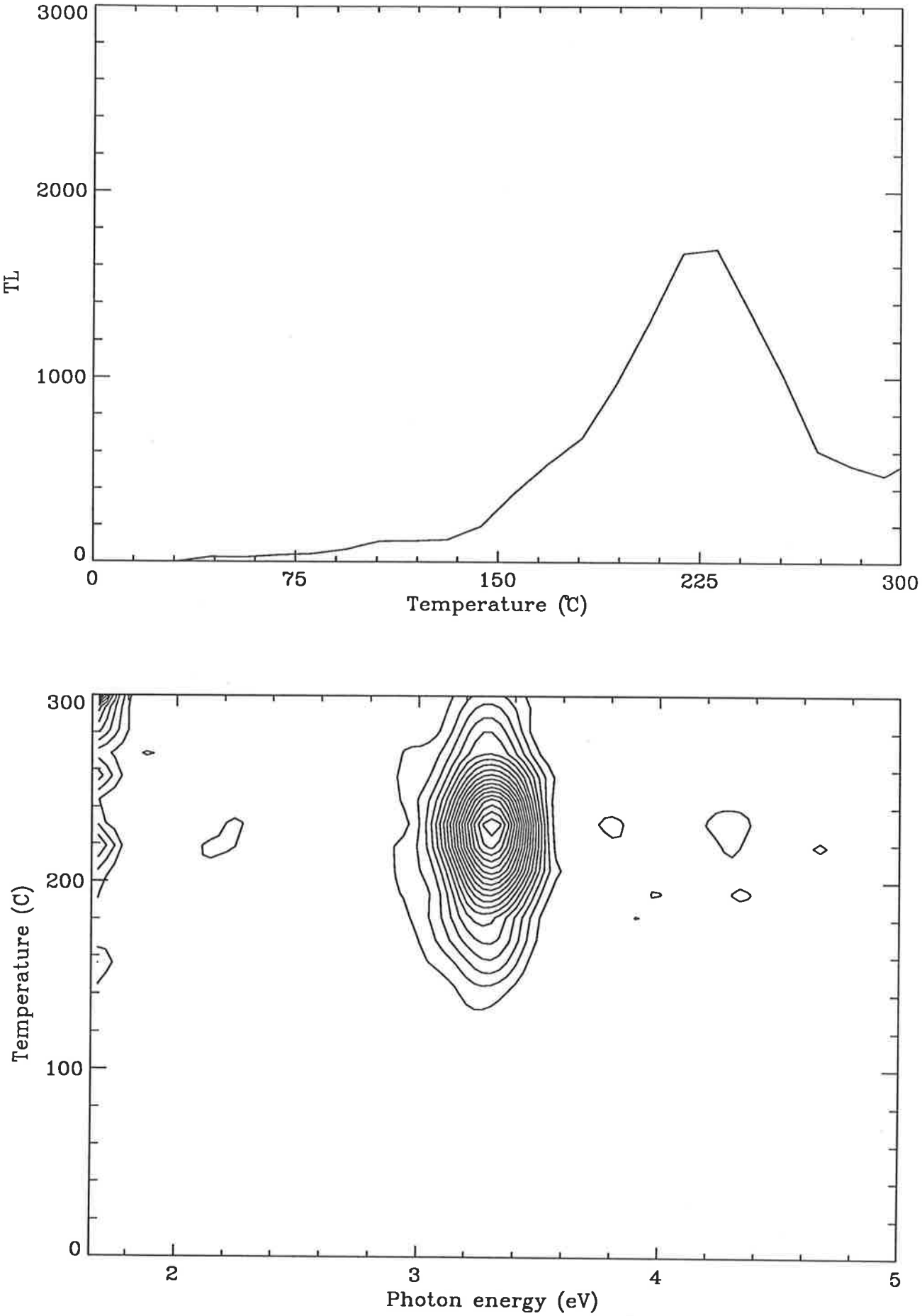

Figure 4.5: $BaSO_4$:Eu for a dose of 15mGy and a wait of about 5 minutes. Above is the 2–D glow curve constructed from the spectral file and below is the contour plot of this spectrum.

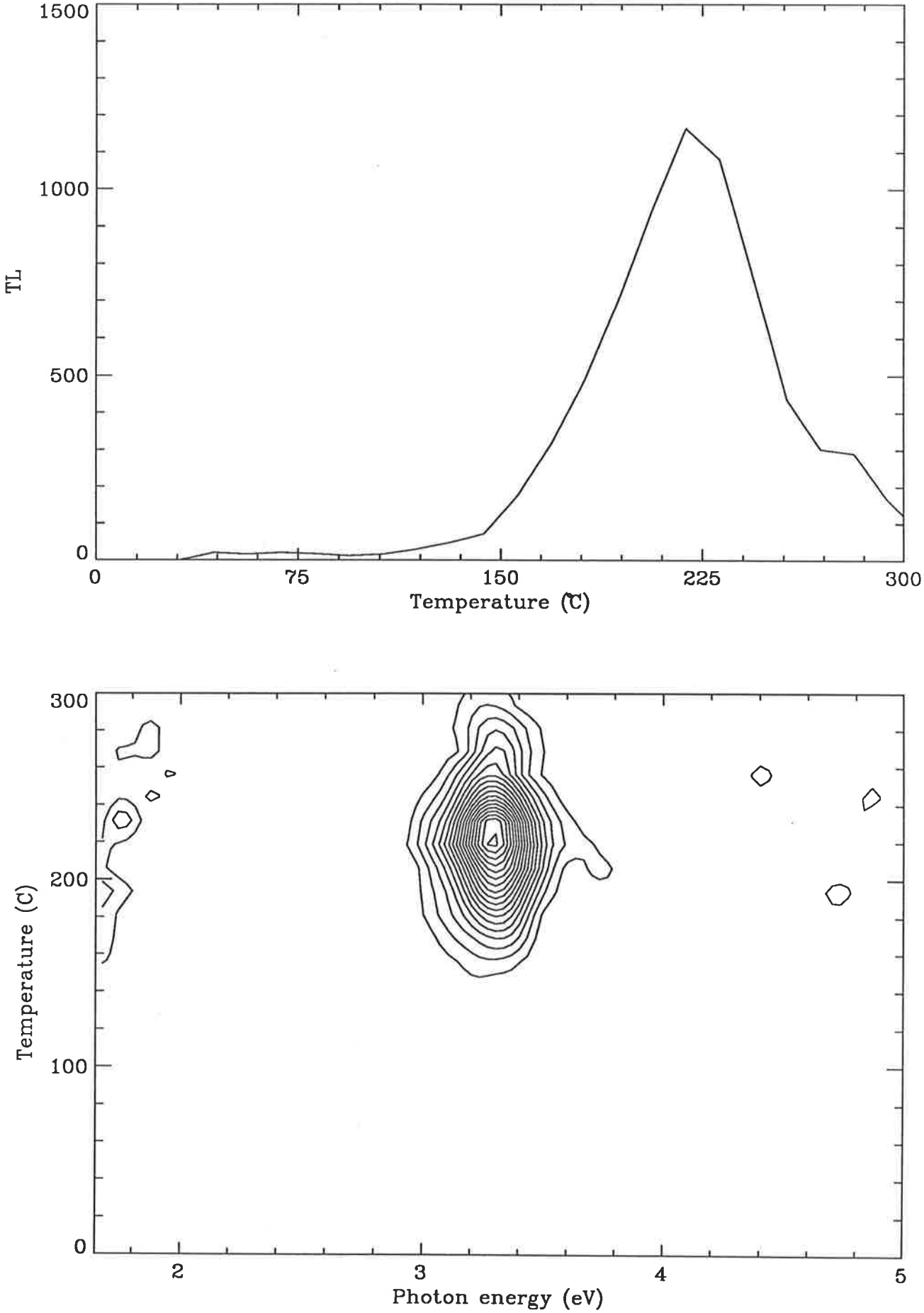

Figure 4.6: $BaSO_4$:Eu for a dose of 1.0Gy and a wait of about 2 days. Above is the 2–D glow curve constructed from the spectral file and below is the contour plot of this spectrum.

nm), which correspond to the $^5D_3 \rightarrow {}^7F_6$, $^5D_3 \rightarrow {}^7F_4$, $^5D_4 \rightarrow {}^7F_6$, $^5D_4 \rightarrow {}^7F_4$ and $^5D_4 \rightarrow {}^7F_3$ energy transitions respectively of terbium (Dieke and Crosswhite 1963, Marfunin 1979). There is little difference between the curves at these two doses except for the hint of some emission near 3.0 eV (414 nm) in figure 4.8 which may be due to the $^5D_3 \rightarrow {}^7F_5$ energy transition.

LiF:Mg, Ti (TLD–100)

LiF has been extensively studied because of its widespread use as a tissue equivalent dosimeter. It had a characteristic peak at 210°C and a number of smaller ones at both higher and lower temperatures. The spectra at doses of 30 mGy and 1.0 Gy are shown in figures 4.9 and 4.10. Although the doses administered differed by more than an order of magnitude, these spectra differed from each other only in detail. Further they were similar to curves obtained by Townsend *et al* (1983). The dose was not stated by these authors but was presumably larger than ours because the apparatus that they used to obtain it was an f:4.5 grating monochromator. The spectra of Fairchild *et al* (1978) were also similar at their lowest doses of 5 Gy and 15 Gy.

Both Townsend *et al* (1983) and Fairchild and co–workers remark that the spectrum must be due to overlapping peaks. There was evidence for this in both figures 4.9 and 4.10 although in the former case statistical fluctuations may well have generated an artifact. While being in general agreement with the work of Townsend and co–workers and Fairchild and co–workers, our spectra differ in detail from theirs. Thus the main peak (conventionally denoted as peak 5) was at ~210°C in all cases, but ours were separated from peak 5 and emitted at markedly different photon en-

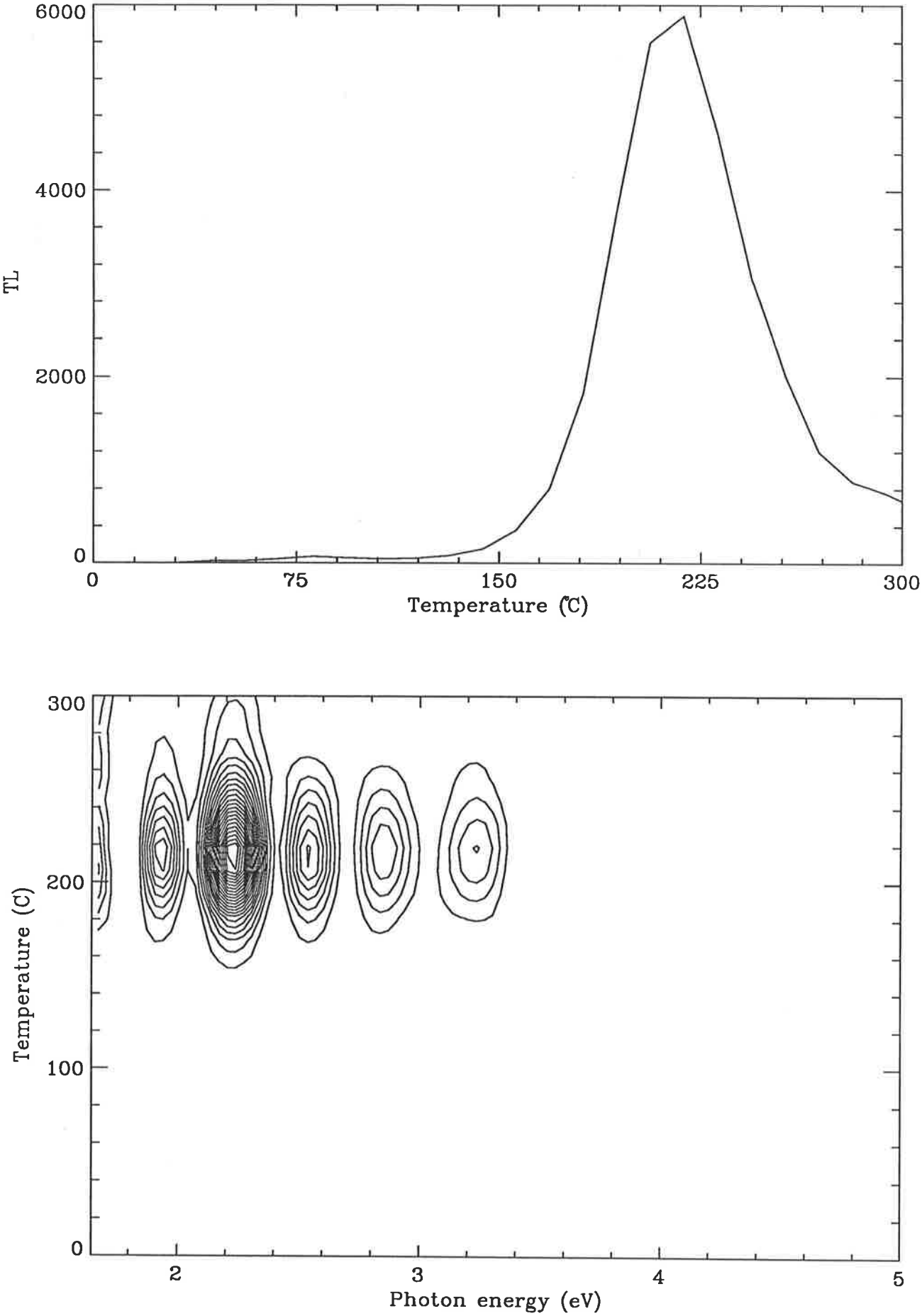

Figure 4.7: Mg_2SiO_4:Tb for a dose of 15mGy and a wait of about 5 minutes. Above is the 2–D glow curve constructed from the spectral file and below is the contour plot of this spectrum.

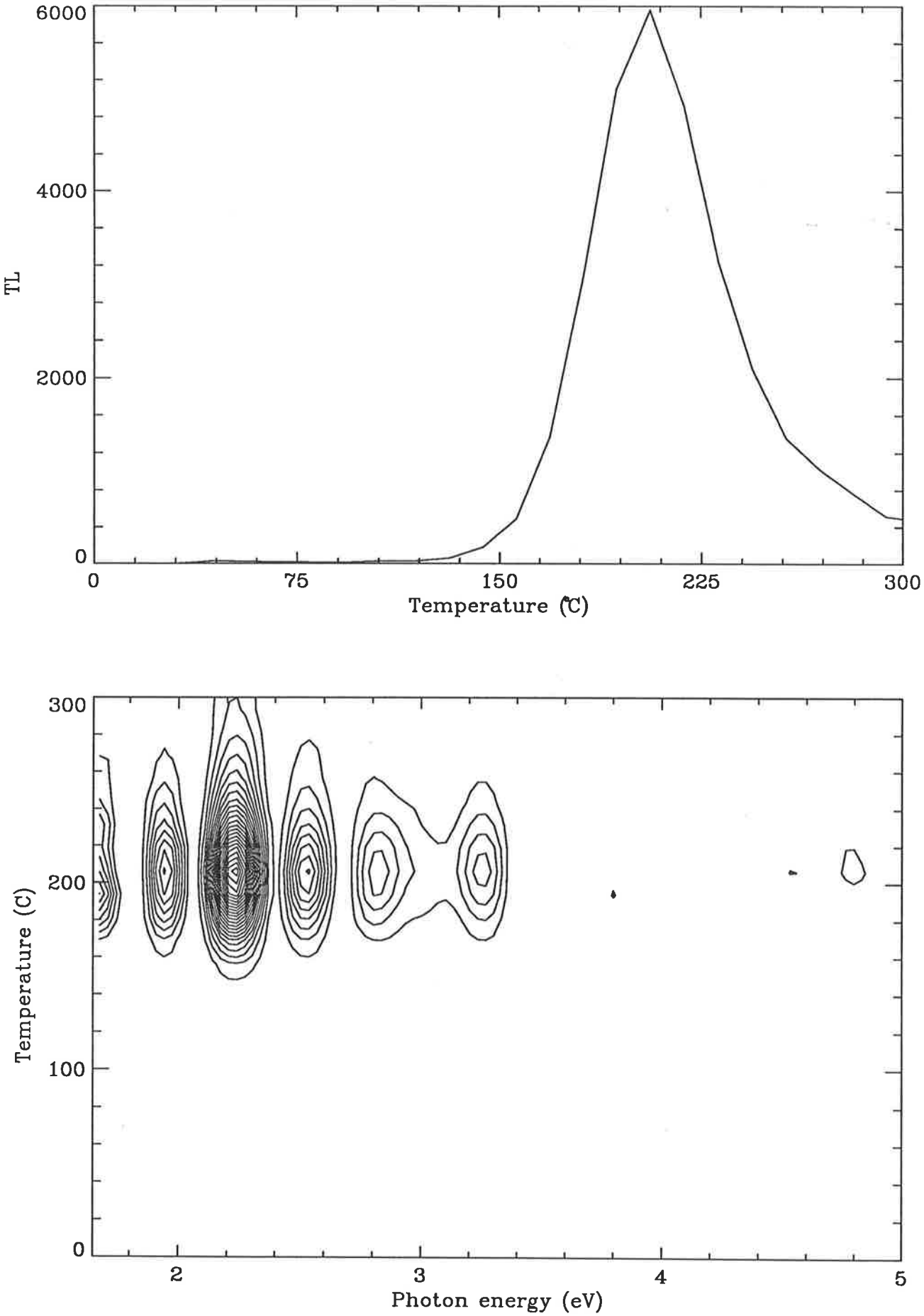

Figure 4.8: Mg_2SiO_4:Tb for a dose of 1.0Gy and a wait of about 2 days. Above is the 2–D glow curve constructed from the spectral file and below is the contour plot of this spectrum.

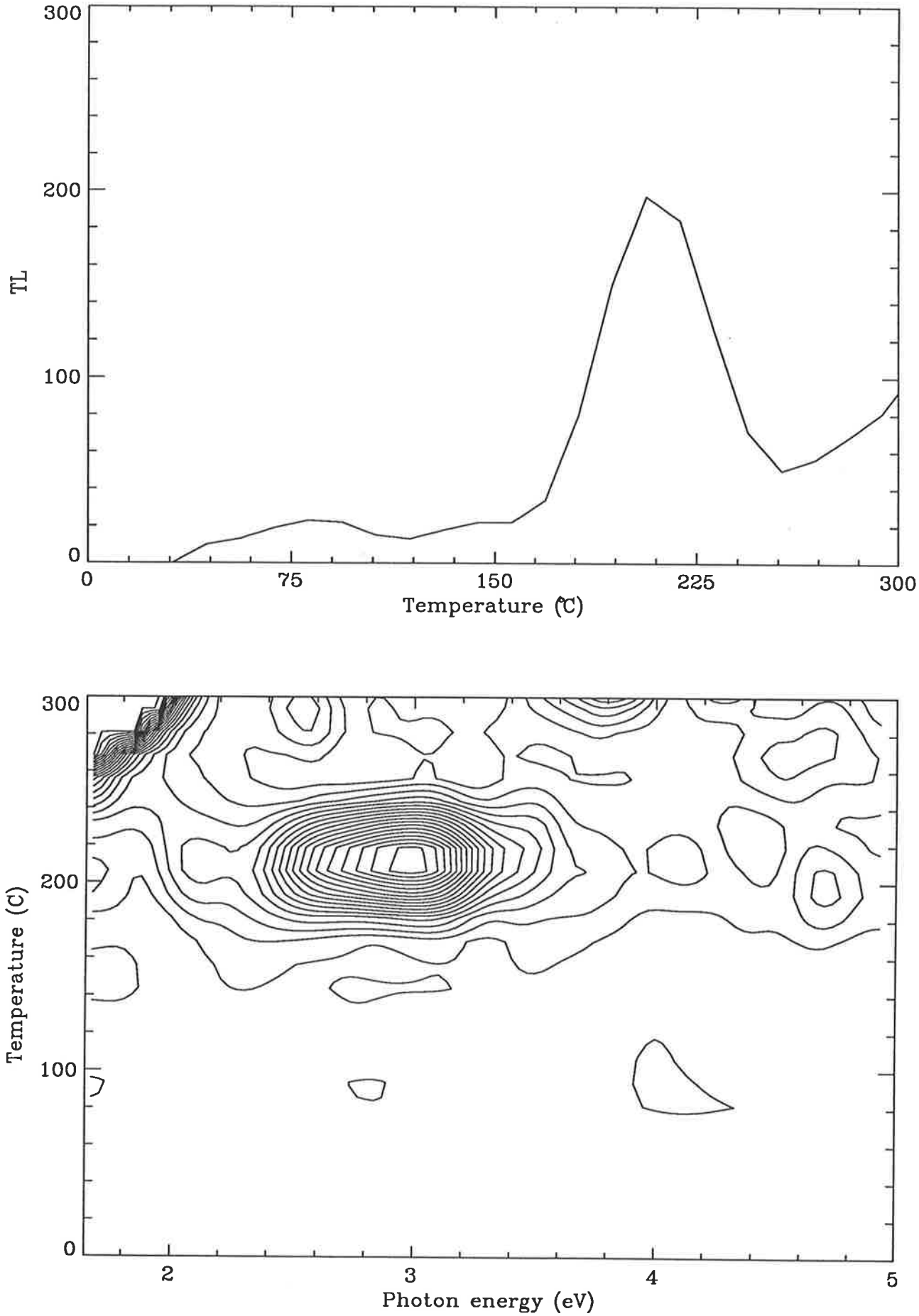

Figure 4.9: LiF for a dose of 30mGy and a wait of about 5 minutes. Above is the 2–D glow curve constructed from the spectral file and below is the contour plot of this spectrum.

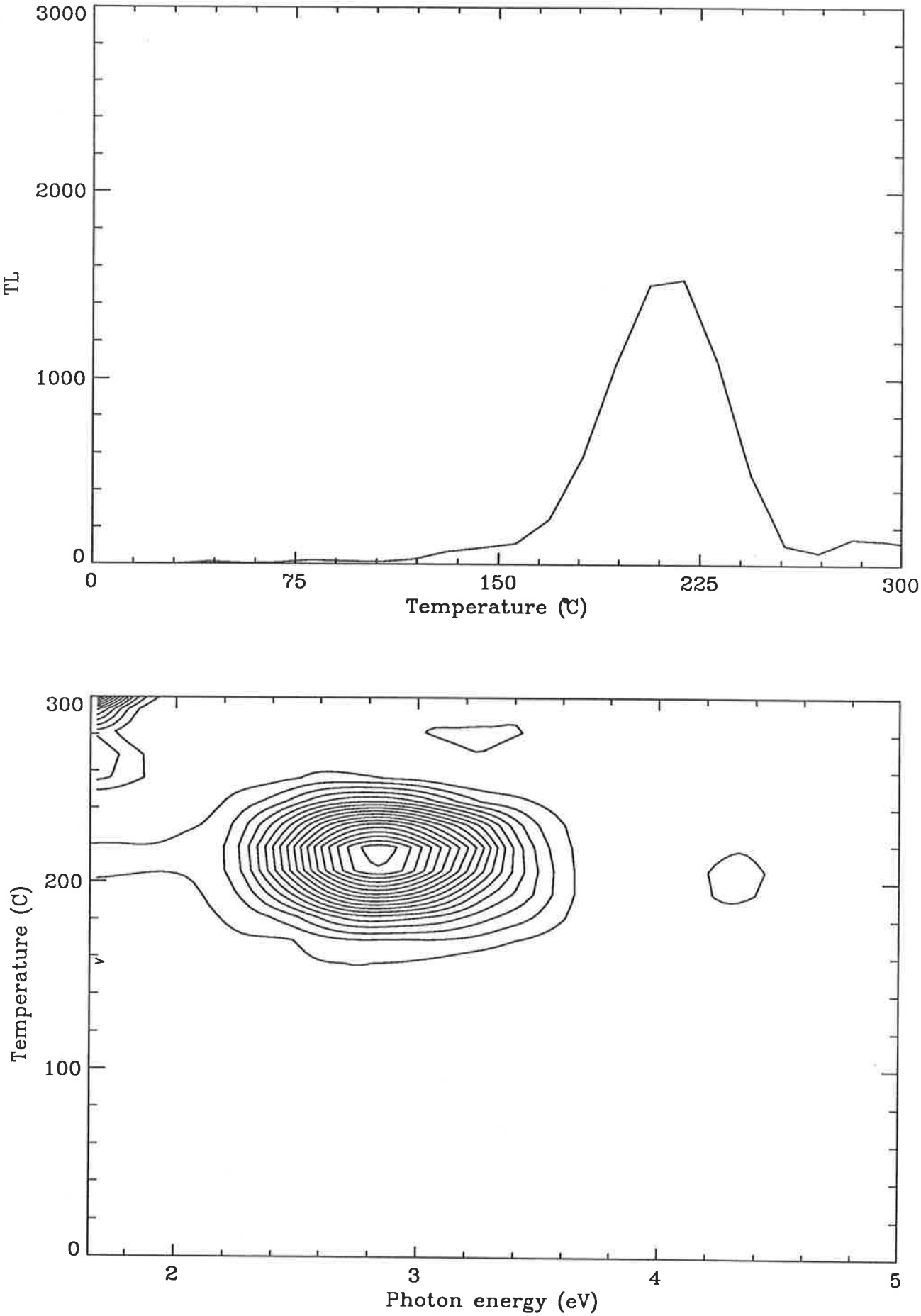

Figure 4.10: LiF for a dose of 1.0Gy and a wait of about 2 days. Above is the 2–D glow curve constructed from the spectral file and below is the contour plot of this spectrum.

ergies. We also observed emission at the high temperature and high photon energy corner of the plot (<400 nm, >300°C) which was relatively more prominent at lower doses. However there was a large difference in the doses for the different cases and undoubtedly the samples had been subjected to differing heat treatments. In spite of the differences in detail, our data were consistent with the interpretation of Townsend *et al* (1983) and McKeever (1984) that the Ti dopant plays an important role in the luminescence centre in emission in the blue. Our results were also consistent with different mechanisms being associated with different peaks, through differing forms of Mg complexes.

AL_2O_3:Ti, Si

The plots shown in figures 4.11 and 4.12 were for doses of 15 mGy and 1.0 Gy, respectively. The dominant peak occurred at a temperature of 250°C (with a smaller peak at about 150°C) and a photon energy of about 1.8 eV (700 nm). This red emission was attributable to Cr^{3+} (Mehta and Sengupta 1979).

Data obtained using the previous design of the apparatus, where the response of the instrument did not extend above 600 nm, showed a complex emission structure around 3.00 eV (410 nm) which has been almost completely swamped out by the red emission (Fox *et al* 1988). Figures 4.13 and 4.14 show the plots for the same doses as for figures 4.11 and 4.12 but instead of the 9558 PMT, the 9635 PMT was used in order to highlight the emission above 2.00 eV (that is, below 600 nm).

These two figures were very similar to one another. The strong peaks were at temperatures of 160, 250 and 310°C. There appeared to be many overlapping, not quite

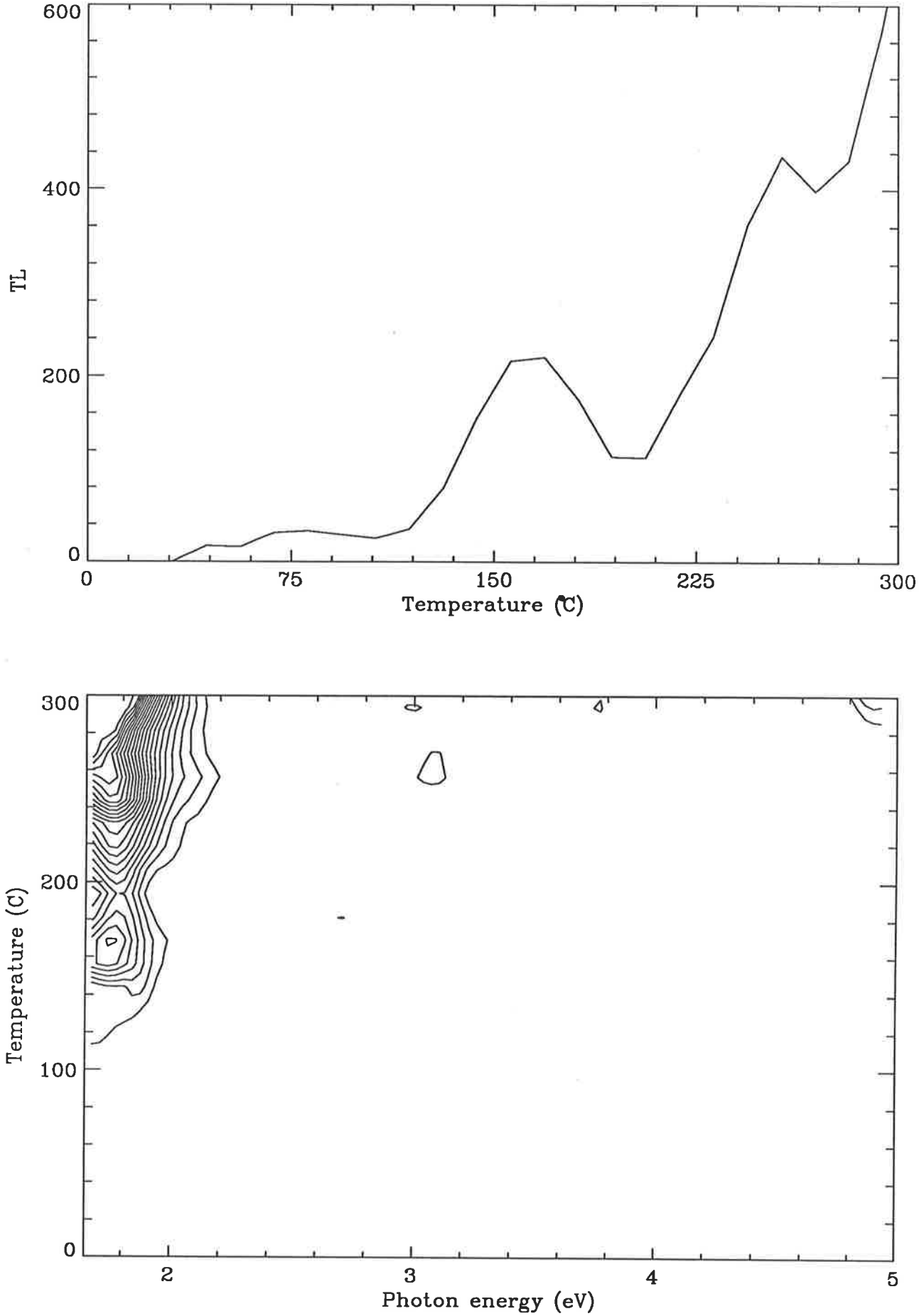

Figure 4.11: Al_2O_3 for a dose of 15mGy and a wait of about 5 minutes. This sample was glowed using an EMI 9558 PMT. Above is the 2–D glow curve constructed from the spectral file and below is the contour plot of this spectrum.

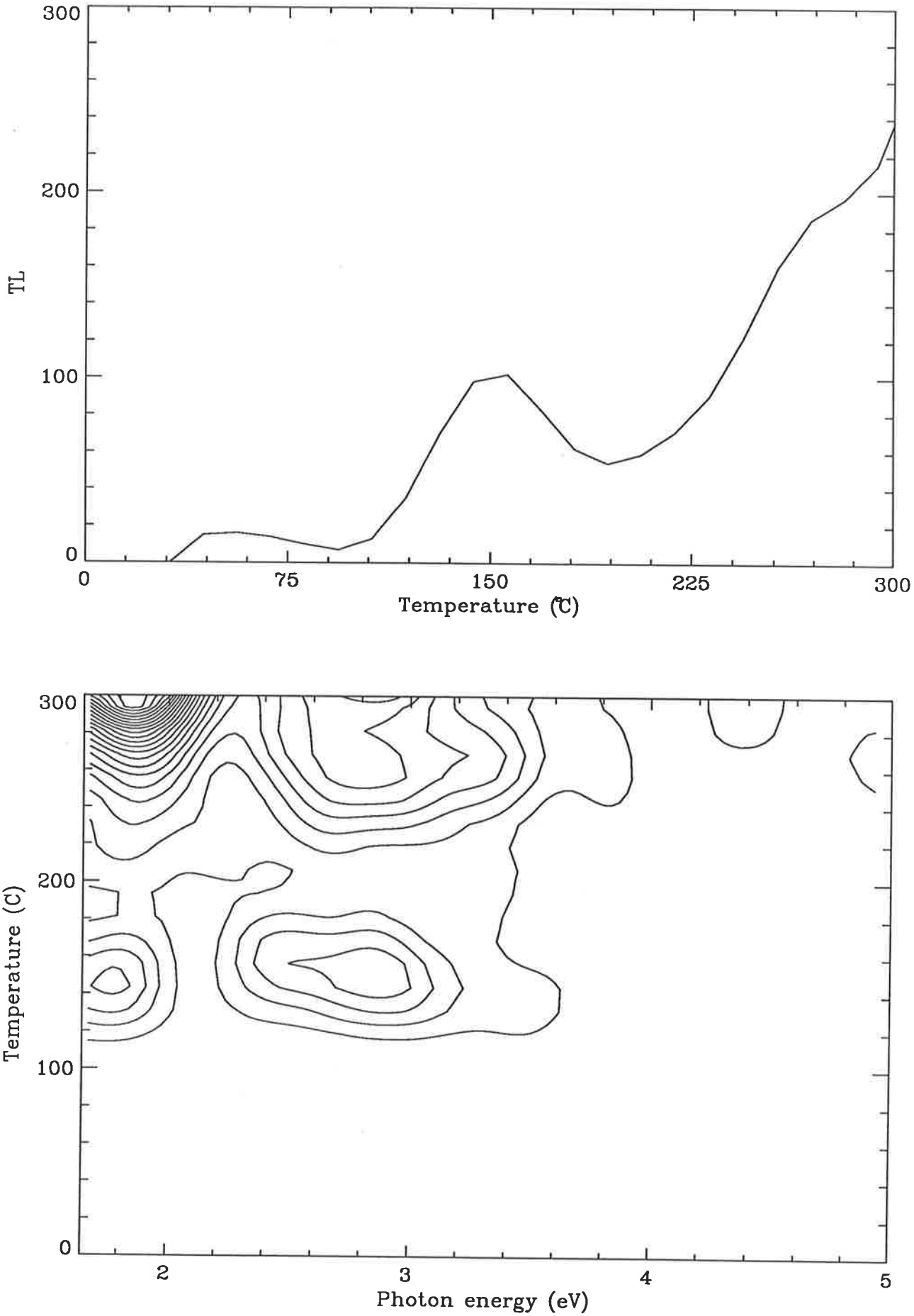

Figure 4.12: Al_2O_3 for a dose of 1.0Gy and a wait of about 2 days. This sample was glowed using an EMI 9558 PMT. Above is the 2–D glow curve constructed from the spectral file and below is the contour plot of this spectrum.

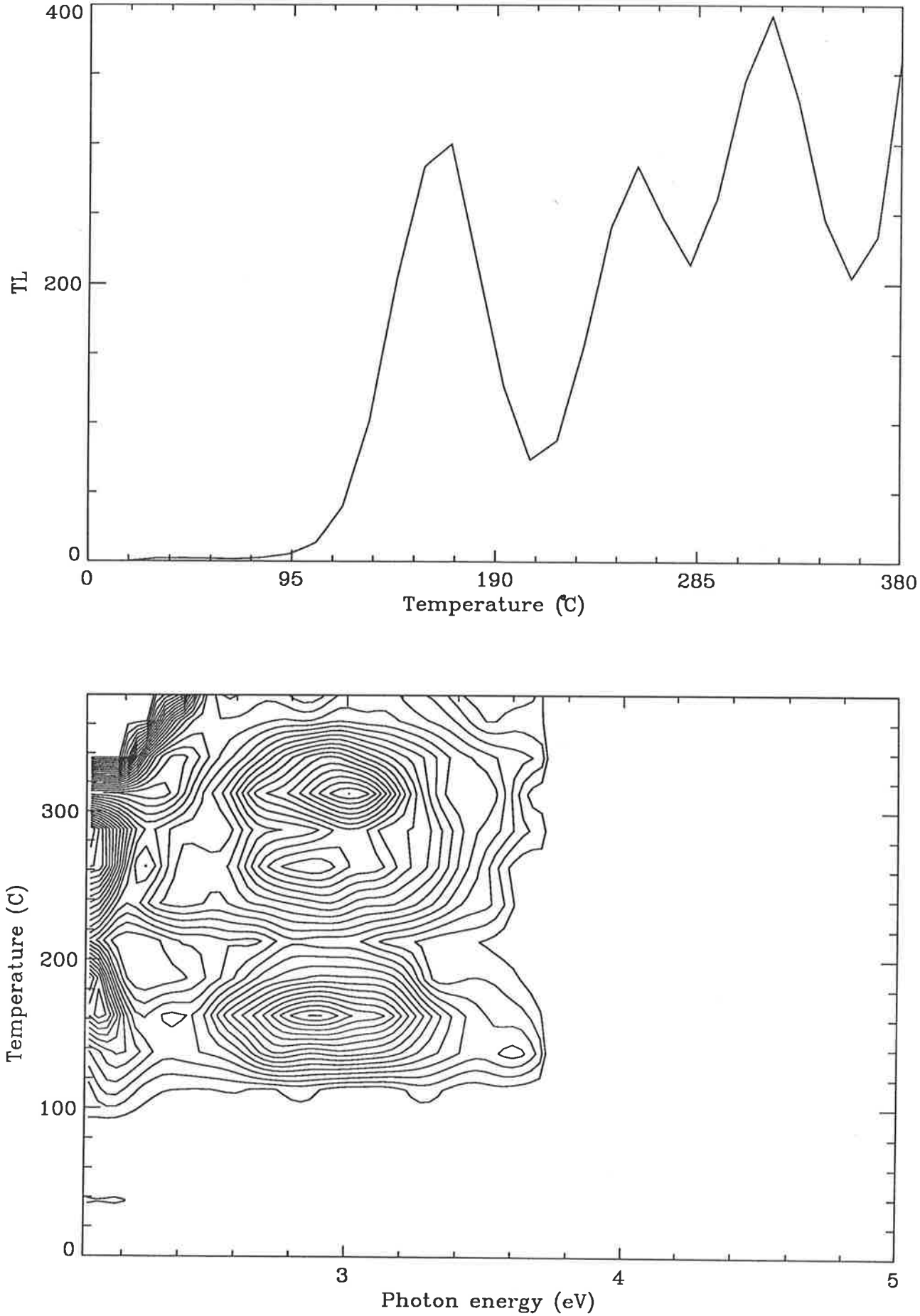

Figure 4.13: Al_2O_3 for a dose of 15mGy and a wait of about 5 minutes. This sample was glowed using an EMI 9635 PMT. Above is the 2–D glow curve constructed from the spectral file and below is the contour plot of this spectrum.

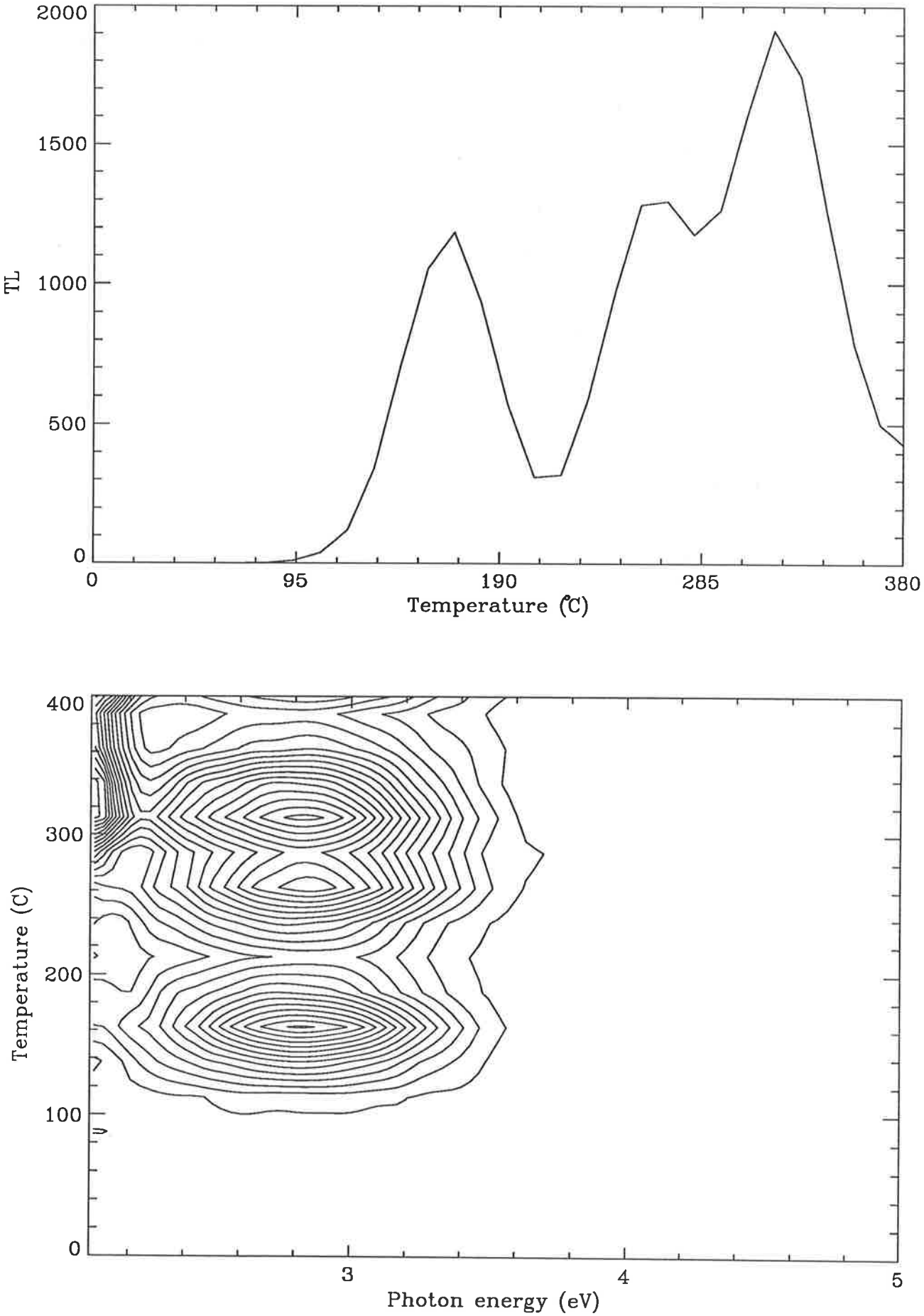

Figure 4.14: Al_2O_3 for a dose of 1.0Gy and a wait of about 2 days. This sample was glowed using an EMI 9635 PMT. Above is the 2–D glow curve constructed from the spectral file and below is the contour plot of this spectrum.

resolved emission bands which showed up consistently at the lower doses although they made a more continuous band at 1.0 Gy. The peak photon energy was between 2.85 (435) and 3.00 eV (410 nm). The 3.00 eV emission has been associated with an F–centre (two electrons trapped at an oxygen vacancy) in pure materials but Mehta and Sengupta (1979) attribute the broad band to recombination of electrons at Ti^{3+} sites. The close similarity of the spectrum to that for LiF which has been identified with Ti (see, for example, McKeever 1984) albeit in a different lattice, lends support to this interpretation.

4.2.3 Discussion

There are two main ways in which the spectra given by Fox *et al* (1988) may be compared with those presented here: calibrated curves should produce spectra whose peak emissions should be almost identical; and the relative peak heights should also be the same. For the spectral region between 2.0 eV and 3.5 eV, figure 4.8.1 shows a comparison of the Mg_2SiO_4 spectra. The energy of the emissions and their relative heights are very close. It also appears that the resolution of the spectrum, recorded with the new apparatus, is slightly lower than with the old equipment.

4.3 TL Emission in Calcites

As mentioned earlier the reason for carrying out this study was to demonstrate the efffectiveness of joint studies involving both TL and electron spin resonance. A greater understanding of the defect state of the materials studied could lead to improved and more reliable dating techniques.

The investigation of the four speleothem calcite samples presented here was part

of a collaboration between the University of Adelaide, the University of Oxford, the University of Bristol and the University of Leicester (Smith *et al* 1990). The aim of the study was to select four samples for an examination of the TL emission spectra and their relationship to the ESR spectra, in particular to try to identify any correlation between the g=2.005 ESR signal and the blue 280°C TL signal. Earlier work (Debenham 1983) had indicated that this would be unlikely but the present work used different sample preparation techniques which it was hoped would remove the unstable ESR signals at g=2.001 and g=2.0020 which can interfere with the ESR signal of interest.

Direct quantitative comparisons between TL and ESR are difficult to make because TL emissions occur after the charge has been released from the traps whereas for ESR the measurements are taken whilst the charge remains trapped. Hence for TL the charge may be retrapped at another deeper trap, or it may recombine at a "killer" centre with no luminescence emitted, or it may recombine at a centre radiatively. This fraction of charge resulting in luminescence varies from sample to sample. However it is still possible to identify trends between TL and ESR measurements in order to identify the origin of the signals.

The contribution of the author to this study was to perform all the TL measurements and to interpret much of the resulting information. The ESR work and its interpretation and the correlation between the TL and ESR data was undertaken by B. Smith.

The four samples chosen for the study were selected mainly because of the variation in their ESR signals and for all the samples the heating rate was 5 Ks^{-1} and they all

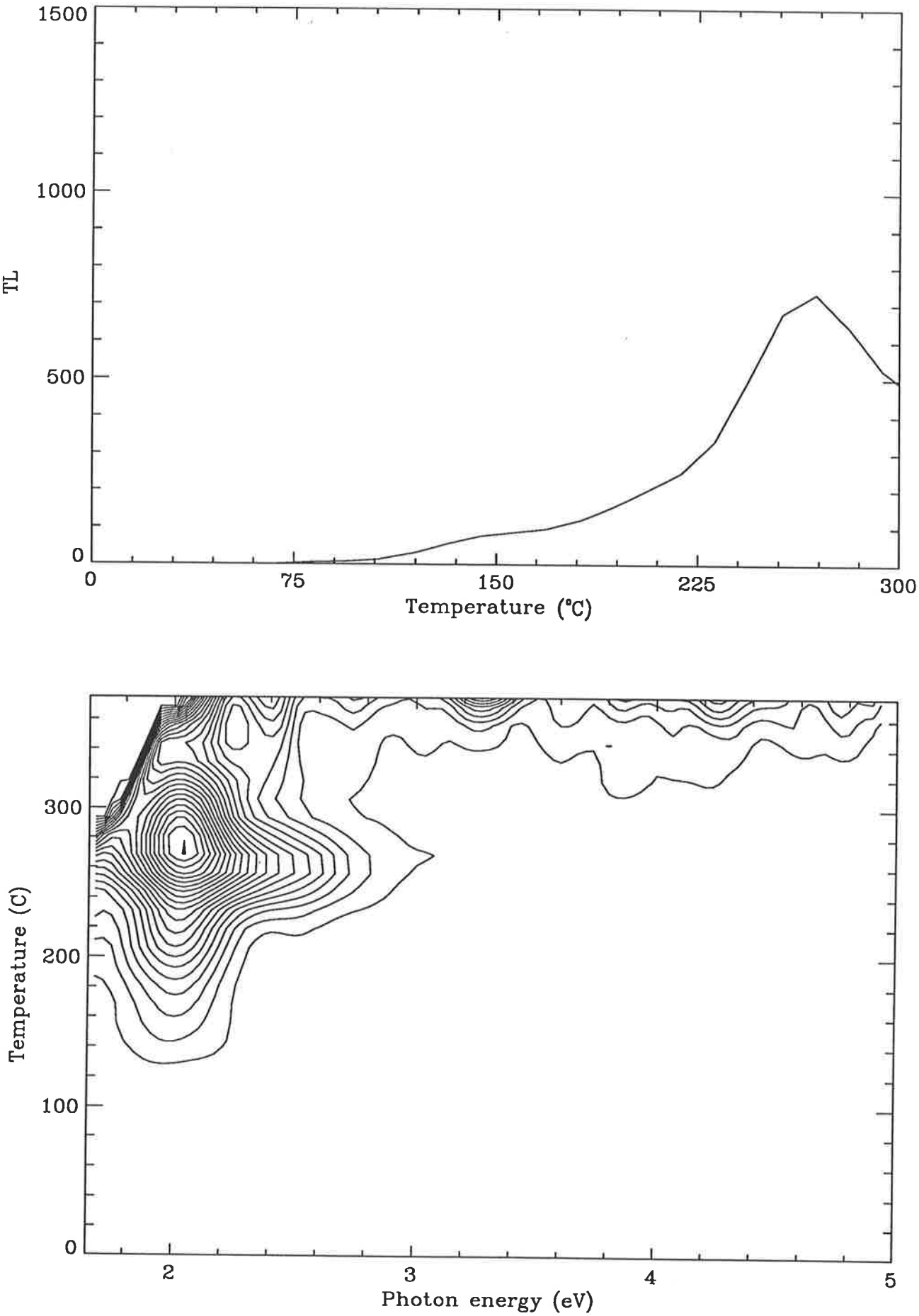

Figure 4.15: Calcite sample KB3B after a dose of 71Gy, showing the 2–D glow curve at the top and the spectral contour diagram below.

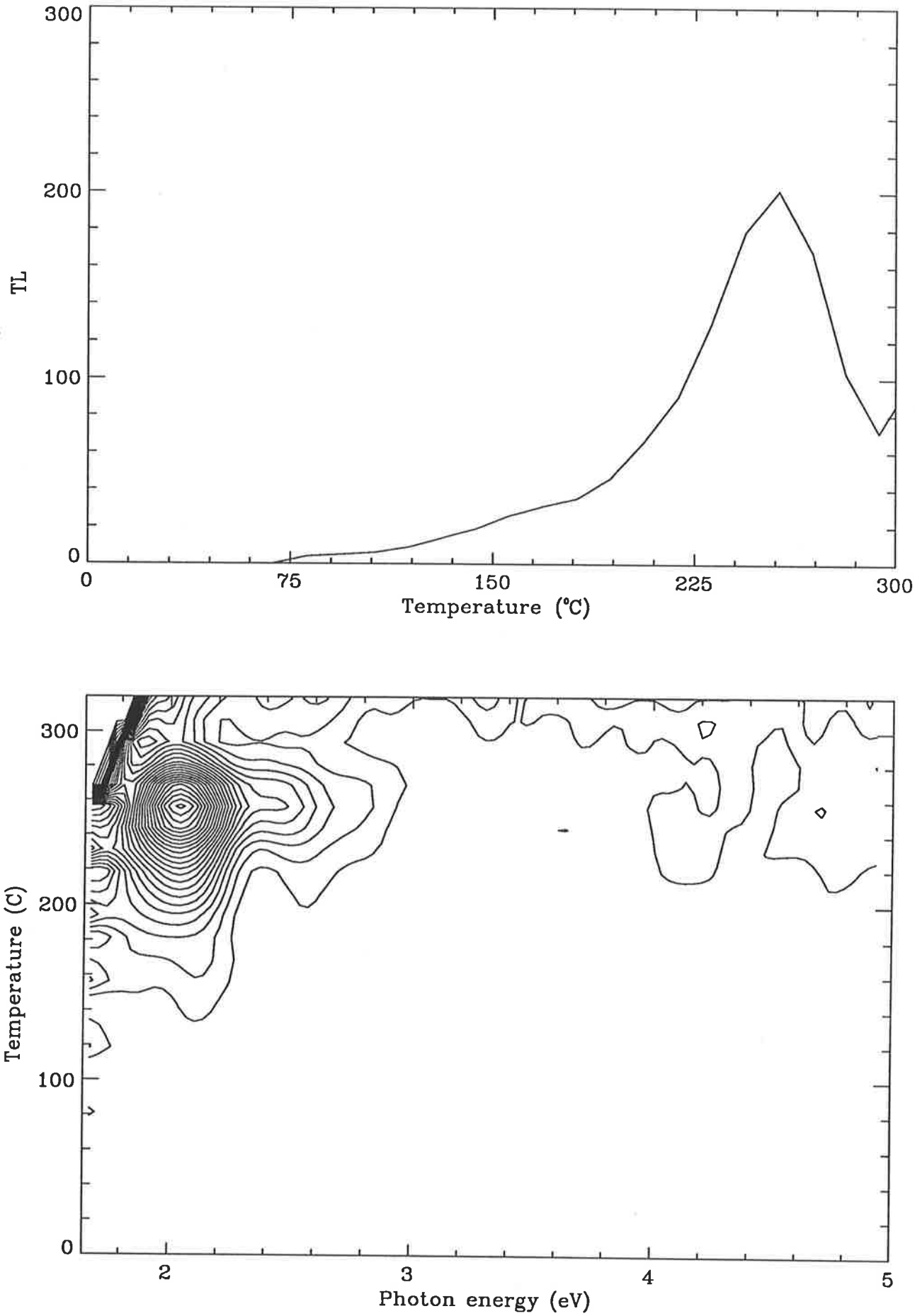

Figure 4.16: Calcite sample T3479C for a dose of 71Gy.

received a laboratory ^{90}Sr β irradiation of 71 Gy.

Sample KB3B was collected from Kaki Bukit, Perlis, Malaysia from pure, white banded flowstone calcite. T34–79C was from Cueva del Agua, Spain as pure white macro–crystalline calcite from a stalagmite column. PH1–82B was from Pickens Hole, Mendips, U.K. as pure densely laminated white–to–buff calcite flowstone. Lastly, GO1B was collected from Great Oones Hole, Mendips, U.K. as impure buff–to–white banded flowstone.

4.3.1 Results

The contour diagram and the 2D glow–curve constructed from it for sample KB3B are shown in figure 4.15. The principal emission from both the 160°C and 270°C TL peaks was at 2.0 eV (610 nm), consistent with the luminescence centres being related to a Mn impurity (Down *et al* 1985). At temperatures above 300°C red incandescence began to obscure the TL signals. The TL contour diagram for sample T34–79C is shown in figure 4.16. The emission was similar to that from KB3B, but the 610 nm peak is significantly narrower (full width at half maximum 120 nm compared with 170 nm). The broader emission of KB3B may be interpreted as being due to increased Mn concentration (Down *et al* 1985), and this was supported by measurements of the Mn^{2+} ESR signal which showed strongly in KB3B but was not visible in T34–79C. However, caution is required when using the Mn^{2+} ESR signal as a measure of the Mn content in the calcite lattice. Measurements on detritally contaminated calcites showed a general trend for larger Mn^{2+} signals in samples with the larger acid insoluble residues (Smith *et al* 1985). This suggested that at least a portion of the Mn^{2+} signal was unrelated to impurities in the calcite lattice itself (Smith *et al*

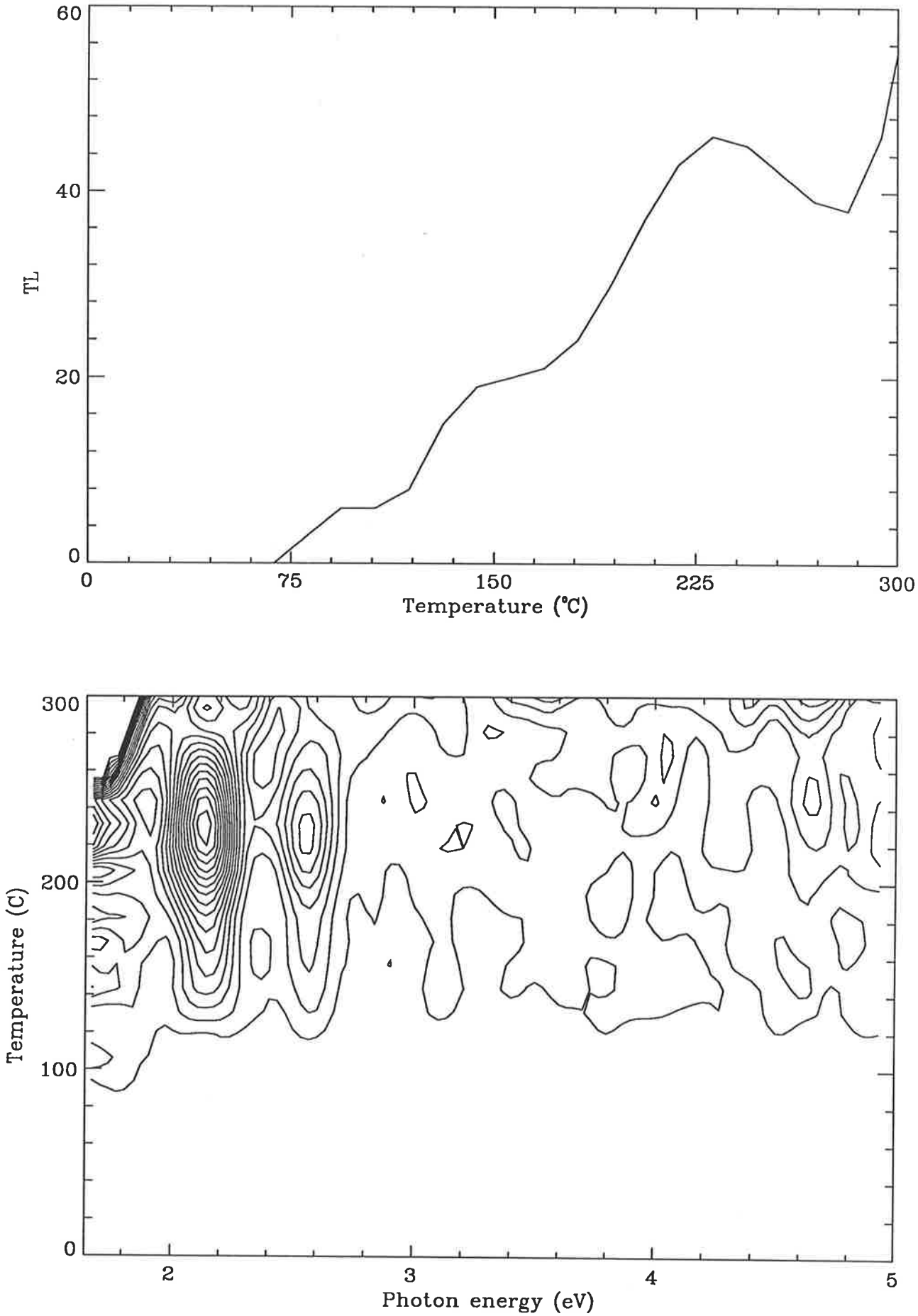

Figure 4.17: Calcite sample PH182B for a dose of 71Gy.

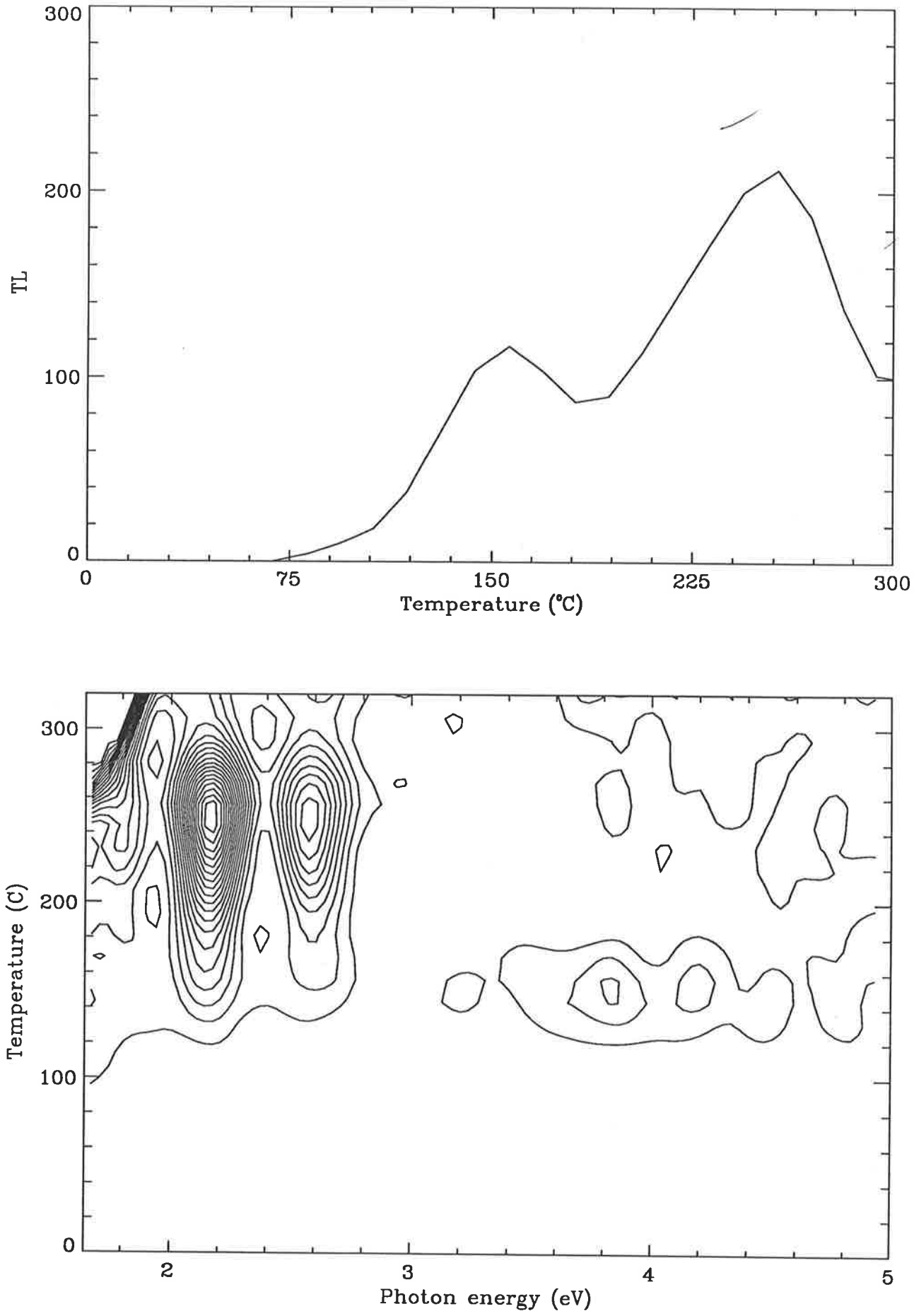

Figure 4.18: Calcite sample GO1B for a dose of 71Gy.

1990).

The other samples: PH1–82B and GO1B gave completely different TL spectra. Figures 4.17 and 4.18 show that the principal emissions were at 2.59 eV (480 nm) and 2.14 eV (580 nm) with the absence of strong 2.03 eV (610 nm) Mn emission, which was consistent with the luminescence centres being related to a Dy impurity (compare with figure 4.1). The 160° TL peak of GO1B also had a very broad emission centred around 3.88 eV (320 nm). These two samples showed TL spectra unlike any previously reported for calcite, contrasting with the spectra reported by Down *et al* (1985), who found Mn- related luminescence centres to be the only significant TL emitters in calcite. It should be noted that they did observe a 480 nm (2.59 eV) emission which was attributed to Mn, but it was present together with a much stronger 600 nm (2.07 eV) emission.

For comparison the conventional 2D plots of TL against temperature are shown with their corresponding spectral contour plot. The high temperature peak in sample T34–79C (and KB3B) was narrower than that of GO1B (and PH1–82B) : the full width at half maximum was 42°C compared to 60°C. The latter sample showed the same peak at 270°C, but also appeared to have a shoulder on the low temperature side, which may have corresponded to the weak 220°C peak evident in the contour plot of KB3B. The significant contribution of this peak in sample GO1B and PH1–82B would explain the broad 200–280°C TL emission observed in their contour diagrams.

The general conclusions that could be drawn from the comparison of ESR and TL spectra were that no conclusive evidence existed for a relationship between the ESR (g=2.0005) and TL (blue 270°C) dating signals. This was primarily due to the

uncertain luminescence efficiency from sample to sample and the possibility that the blue luminescence centres were less stable than the trapped charge responsible for the g=2.0005 signal. If the latter premise was correct, then from the other similarities it seemed likely that the g=2.0005 ESR signal and the 270°C TL emission were indeed related.

The g=2.0036 signal was tentatively correlated with the TL emission at 220°C. If this was the case the broad 270°C TL peaks of samples GO1B and PH1–82B may have been due to an admixture of charge from g=2.0036 and the trap responsible for the 270°C peak. In the samples studied the g=1.9975 ESR signal was consistent with TL emission at 160°C, but there was some indication that it may also have contained a more stable component. The g=2.0055 signal may have been related to the TL emission above 300°C, but this possibility was not investigated. Less stable ESR signals also existed, but they were not considered in this study.

4.4 Gartia Minerals

In this section the results are presented showing the TL emission for several mineral samples which were provided (and which were initially identified) by Prof. R. Gartia of the Physics Department at Manipur University in India.

The minerals were in the form of flat chips which were cleaned and dried with acetone before being glowed. All irradiations were performed using a ^{90}Sr β source with a nominal strength of 1.85×10^{8} Bq, and 10 minutes was allowed to lapse before glowing.

These minerals were thought to have a common TL emission centre: S_2^-. This

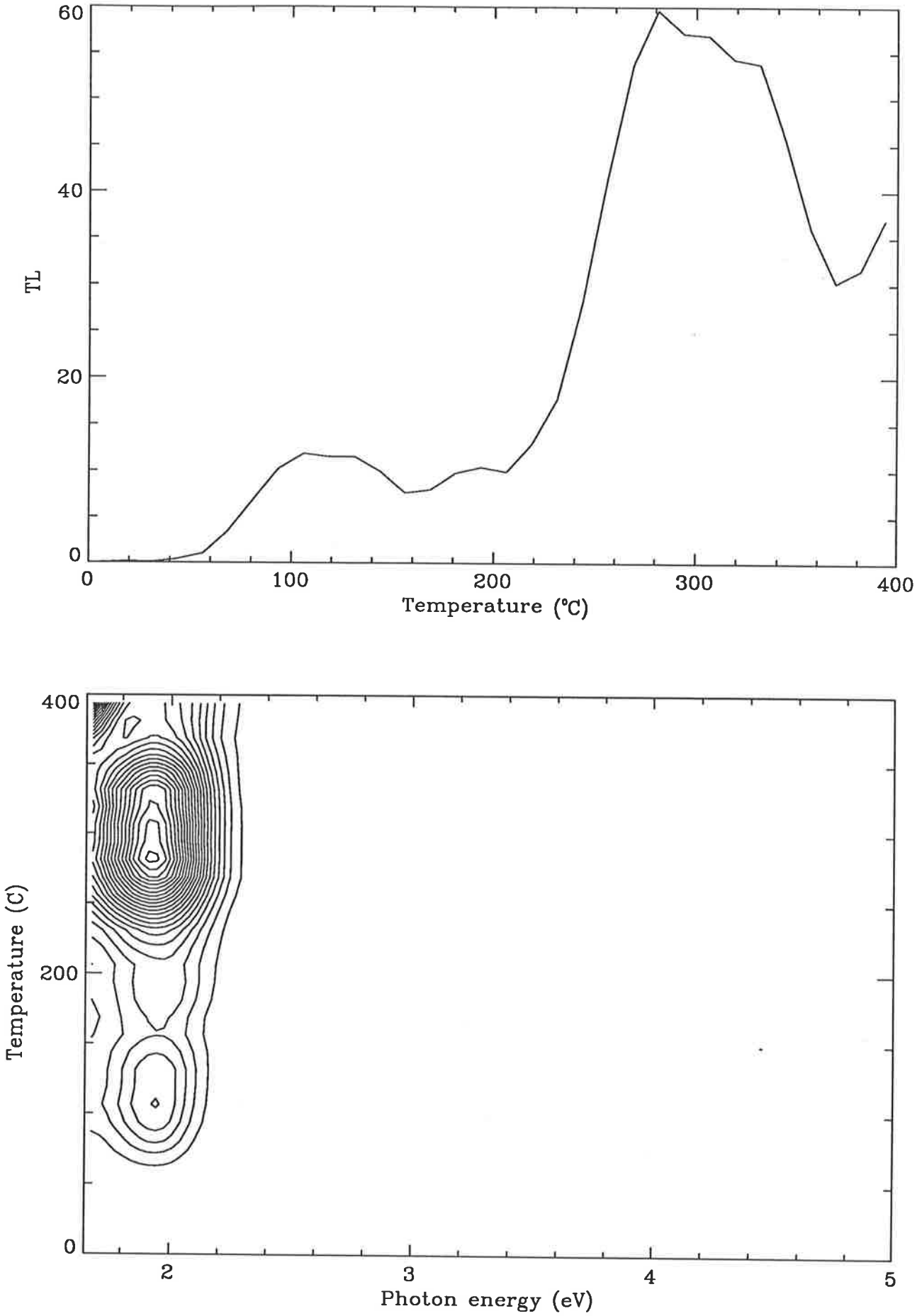

Figure 4.19: Lazurite sample which was given a dose of 6.6Gy followed by a wait of 5 minutes before glowing. The top figure is the 2–D glow curve reconstructed from the spectra and the lower figure is the contour diagram of this sample.

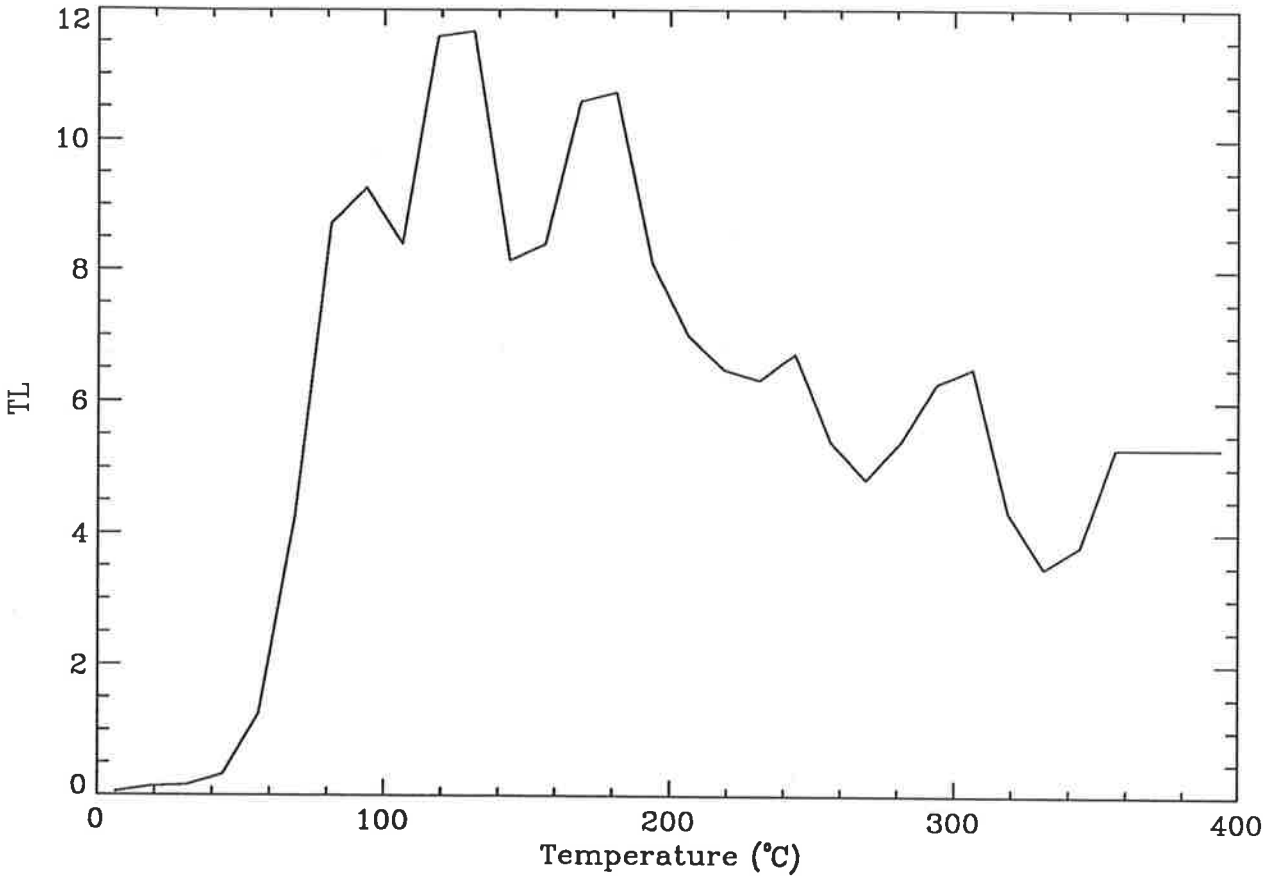

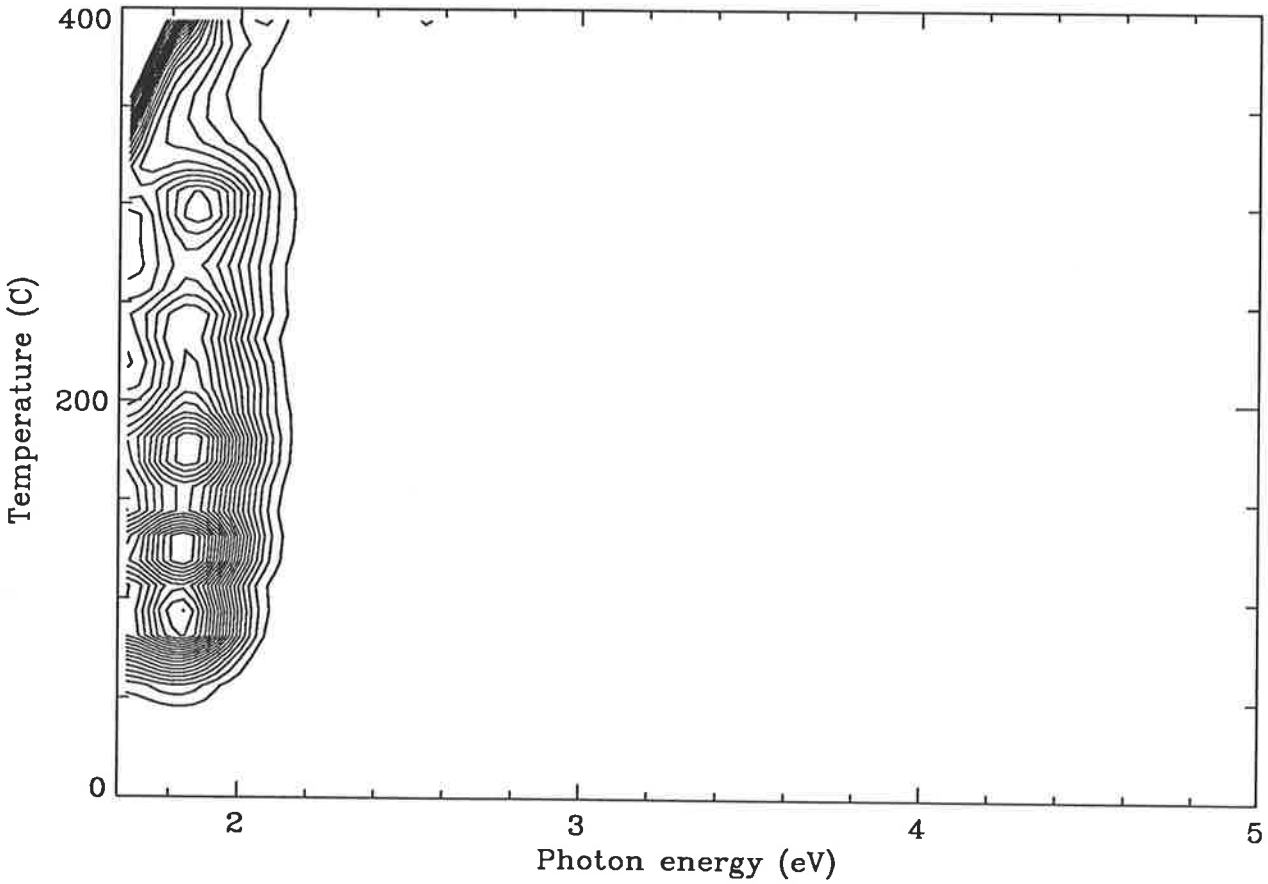

Figure 4.20: Lazurite sample which was heated to 400°C and then given a dose of 2.5Gy followed by a wait of 5 minutes before glowing. The top figure is the 2–D glow curve reconstructed from the spectra and the lower figure is the contour diagram of this sample.

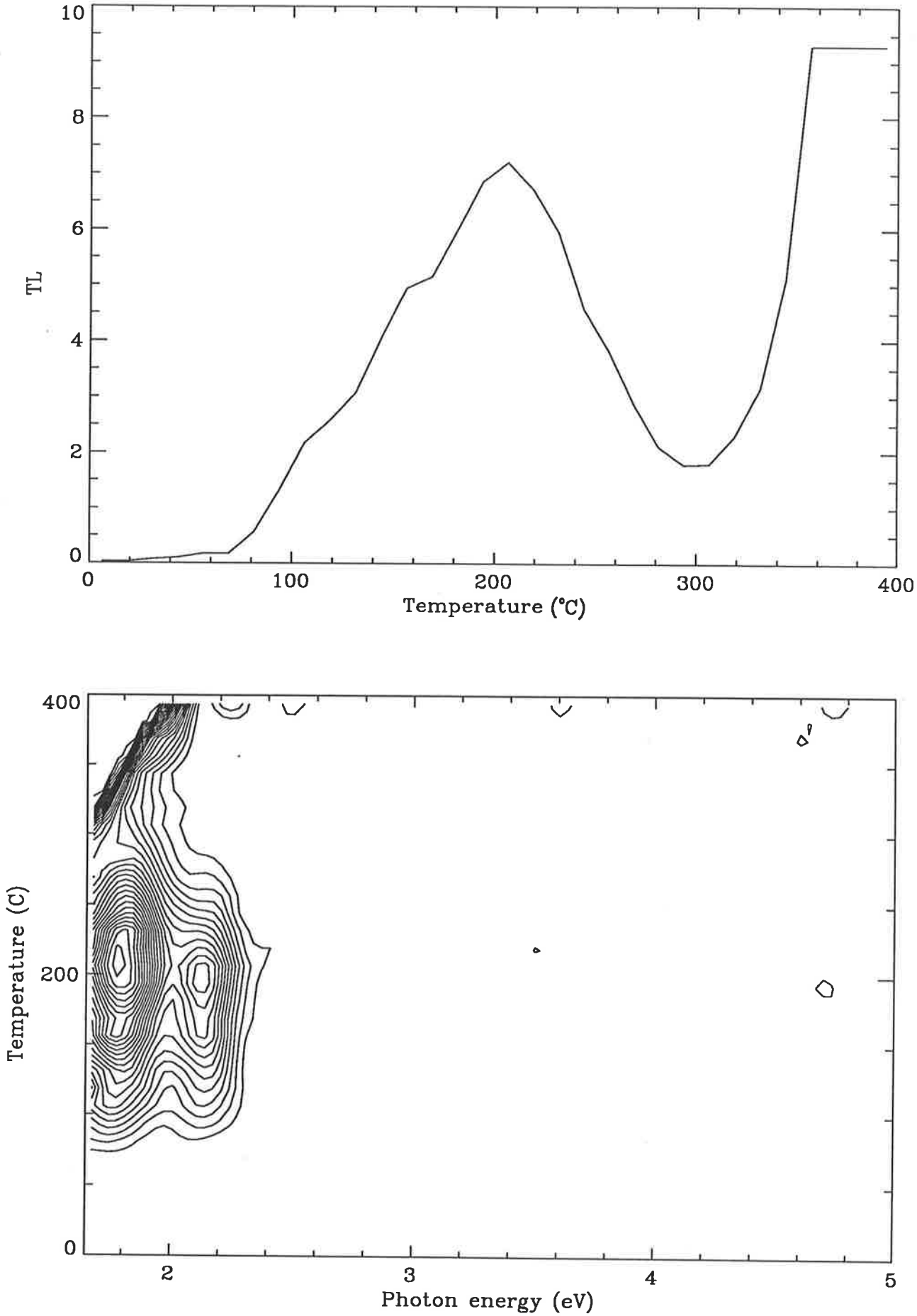

Figure 4.21: Lazurite sample which was heated to 400°C and then given a dose of 6.6Gy followed by a wait of 5 minutes before glowing. The top figure is the 2–D glow curve reconstructed from the spectra and the lower figure is the contour diagram of this sample.

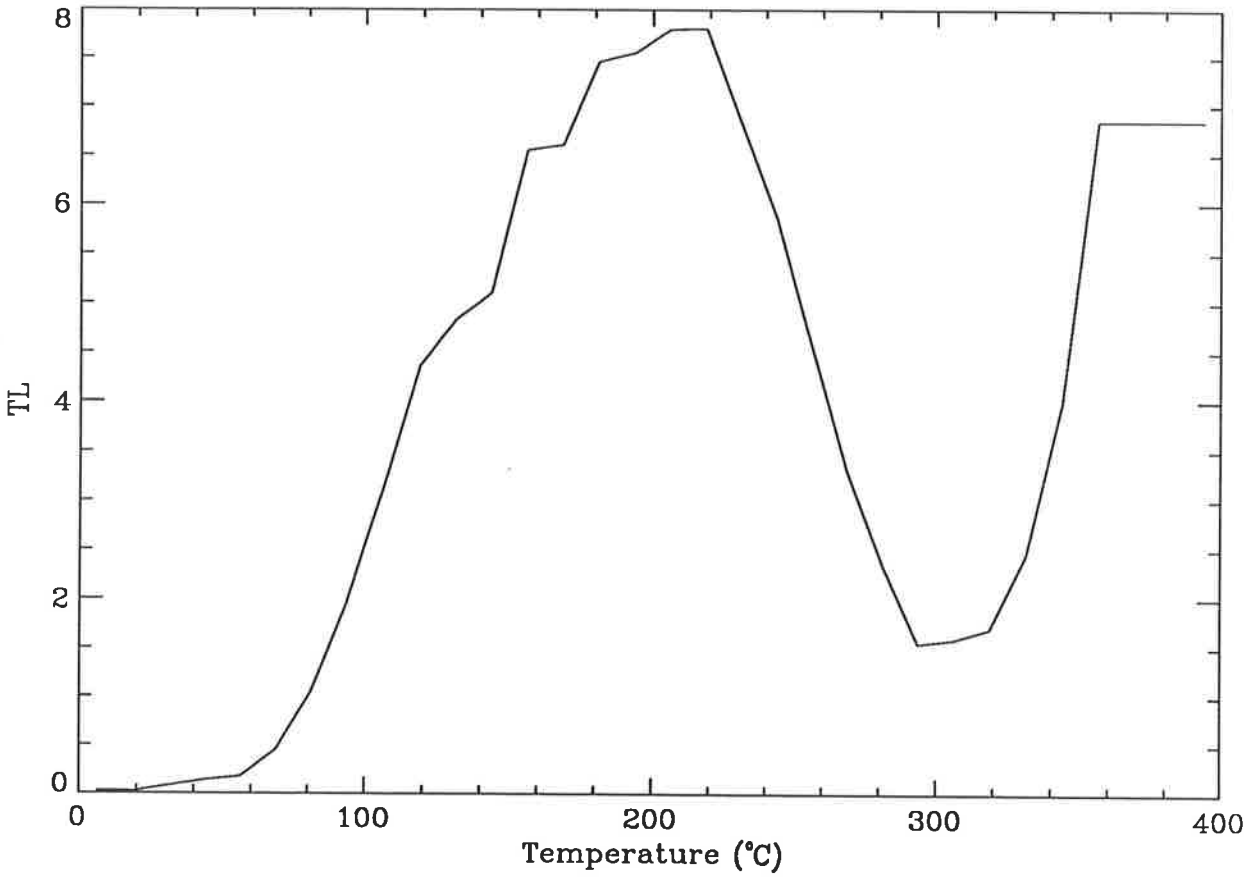

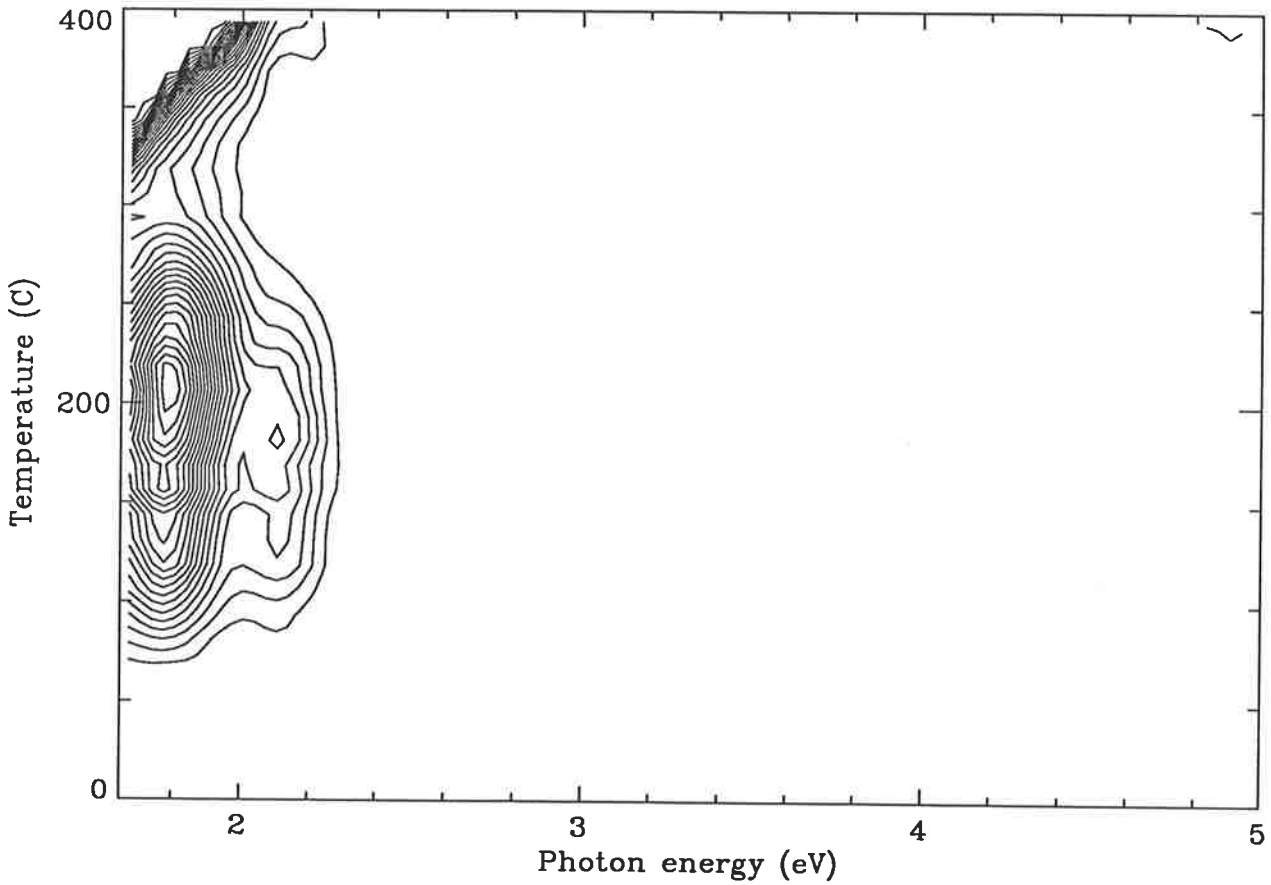

Figure 4.22: Lazurite sample which was heated to 400°C and then given a dose of 5.0Gy followed by a wait of 5 minutes before glowing. The top figure is the 2–D glow curve reconstructed from the spectra and the lower figure is the contour diagram of this sample.

radical is isoelectronic with the O_2^- radical, that is it has the same number of valence electrons as S_2^- (Duke and Holonyak 1973, Marfunin 1979). The nature of this system means that indirect band transitions from the isoelectronic trap (S_2^-) to the hole centre are possible via the O_2^- trap (Duke and Holonyak 1973).

4.4.1 Results

Lazurite

This mineral is one of the sodalite group with a cubic structure and a general formula of:

$$(Na, Ca)_8(Al, Si)_{12}O_{24}(S, SO_4).$$

Figures 4.19, 4.20, 4.21 and 4.22 show the results for 3 lazurite samples. Figure 4.19 received a 40 Gy dose and figure 4.20 a dose of 2.5 Gy after being heated to 400°C. Major peaks occurred at about 100°C and 300°C with an extra peak at about 170°C which was more prominent in figure 4.20.

In figure 4.19 the emission was at a photon energy of 1.93 eV (642 nm) and in figure 4.20 at 1.85 eV (670 nm).

Figures 4.21 and 4.22 show the data for the other two lazurite samples which exhibited markedly different emission. Both had broad TL peaks at about 210°C and emission at 1.80 eV (690 nm) and 2.12 eV (585 nm).

Lazurite is one of a class of aluminosilicates whose emission spectra is mainly due to S_2^- and O_2^- (Marfunin 1979). For S_2^- the maximum of the emission occurs at about 660 nm in lazurite and between 450 and 550 nm for O_2^- (Tarashchan 1978). For figures 4.21 and 4.22 the emission was consistent with S_2^- being the luminescence

centre at 1.80 eV with the lower intensity emission at 2.12 eV being due to an O_2^- centre.

The lazurite sample shown in figures 4.19 and 4.20 differed significantly from the samples shown in figures 4.21 and 4.22, both at the temperature at which the emission occurred and at the photon energy and number of the emission centres. The main glow peak in figures 4.21 and 4.22 is about 100°C lower than for figure 4.19 and is much broader. In figures 4.19 and 4.20 the 1.93 eV and 1.85 eV emissions could have been due to an S_2^- impurity although no O_2^- emission was observed. This emission is also much broader than for figures 4.21 and 4.22 (about 0.4 eV in figure 4.19 as opposed to about 0.2 eV in figure 4.21). The physical appearance of this sample was a deep blue in comparison with the other samples which were a much lighter colour of blue. Possibly this may have indicated the presence of much more sulphur in this first lazurite sample (hence the dominant emission around 1.9 eV) since the optical absorption which causes this blue colour is due to a S_3^- centre (Marfunin 1979).

Scapolite

Scapolite has a tetragonal structure and has the general formula:

$$(Na, Ca, K)_4 Al_3 (Al, Si)_3 Si_6 O_{24} (Cl, F, OH, CO_3, SO_4).$$

Figures 4.23 and 4.24 show the glow curves and emission spectra for a scapolite sample that had received a dose of 5.0 Gy. These two figures were for the same sample but plotted for different contour ranges. The glow peaks occurred at temperatures of 100°C and a broad peak centred at about 210°C. There was also a peak above 350°C which was, to a large extent, obscured by the incandescent glow.

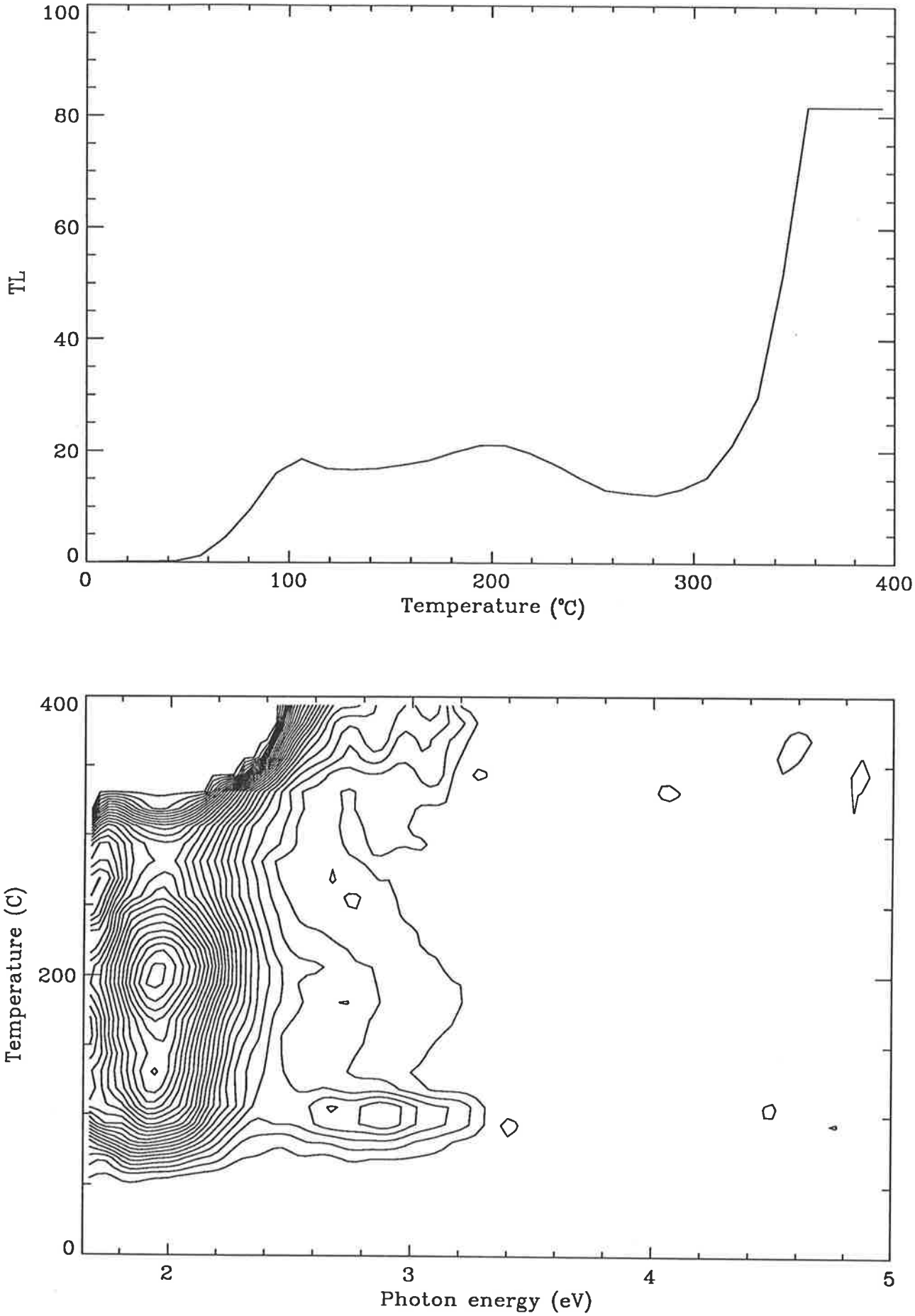

Figure 4.23: Scapolite sample which was heated to 400°C and then given a dose of 5.0Gy followed by a wait of 5 minutes before glowing. The top figure is the 2–D glow curve reconstructed from the spectra and the lower figure is the contour diagram of this sample.

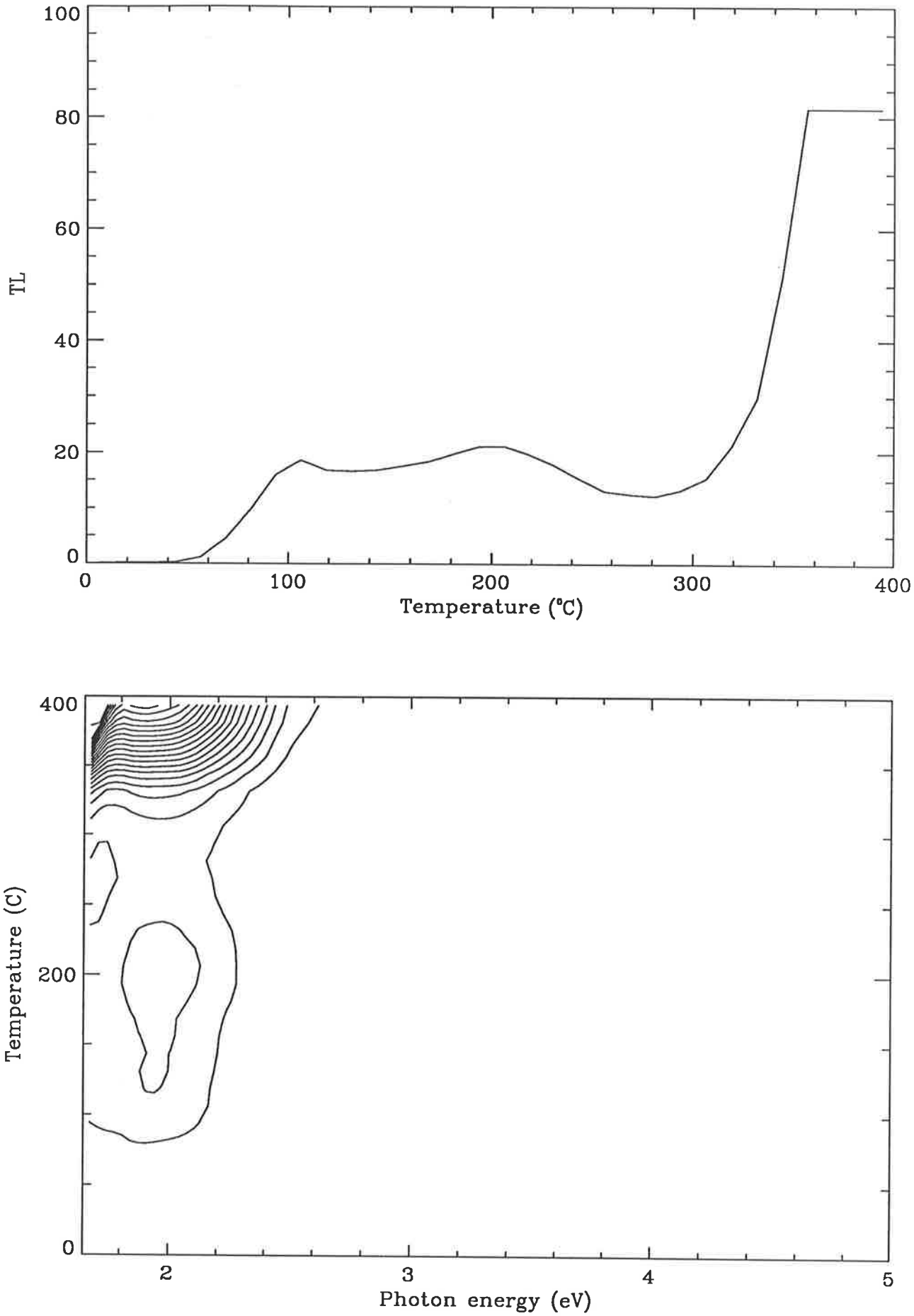

Figure 4.24: Scapolite sample which was heated to 400°C and then given a dose of 5.0Gy followed by a wait of 5 minutes before glowing. The top figure is the 2–D glow curve reconstructed from the spectra and the lower figure is the contour diagram of this sample.

The main emission at 100°C was at 1.93 eV (643 nm) and a less intense component between 2.66 eV (466 nm) and 2.88 eV (430 nm). The emission due to the S_2^- centre in scapolite (in contrast to lazurite) has been observed to be shifted to higher photon energies (Tarashchan 1978) and this was indeed observed in comparison to figures 4.21 and 4.22. The emission between 2.66 and 2.88 eV was also consistent with an O_2^- centre.

Spodumene

This mineral has a monoclinic crystal system with a formula:

$$LiAlSi_2O_6.$$

Figure 4.25 shows a spodumene sample that had been given a dose of 5.0 Gy. There are several glow peaks occurring at about 80, 140, 170 and 240°C with a shoulder on the high temperature side of the 240°C peak. From the contour plot there is also evidence for a peak around 400°C but this is obscured by the incandescent glow. TL peaks between 220 and 240^{O}C have been reported previously by Daniels and Saunders (1951) in "green" spodumene.

The emission occurred at an energy of 2.05 eV (605 nm). This emission may also have been due to an S_2^- centre, but a more likely candidate may have been Mn^{2+} although this is tentative since the Mn^{2+} luminescence is highly dependent on its coordination within the crystal lattice (Marfunin 1979).

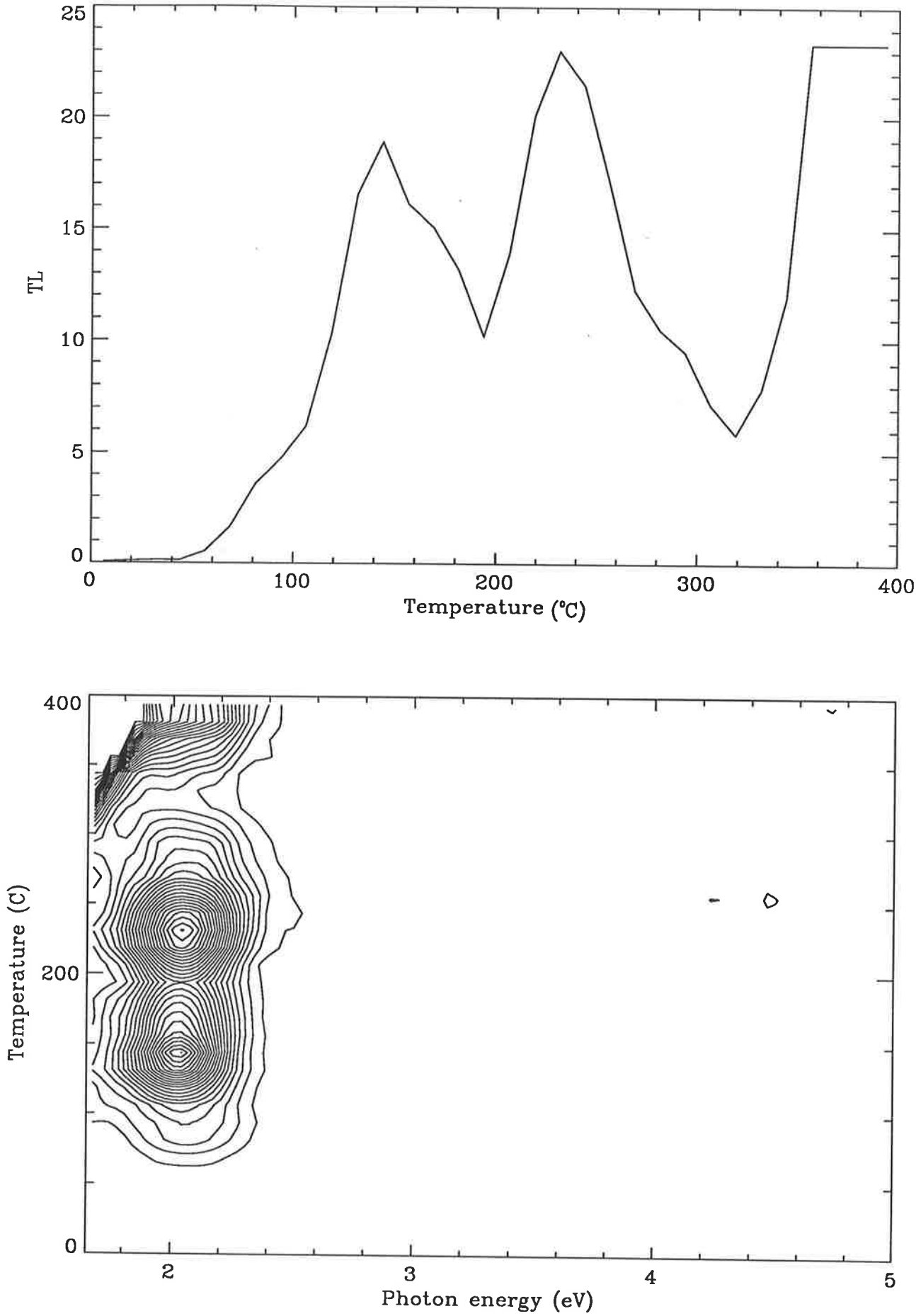

Figure 4.25: Spodumene sample which was given a dose of 5.0Gy followed by a wait of 5 minutes before glowing. The top figure is the 2–D glow curve reconstructed from the spectra and the lower figure is the contour diagram of this sample.

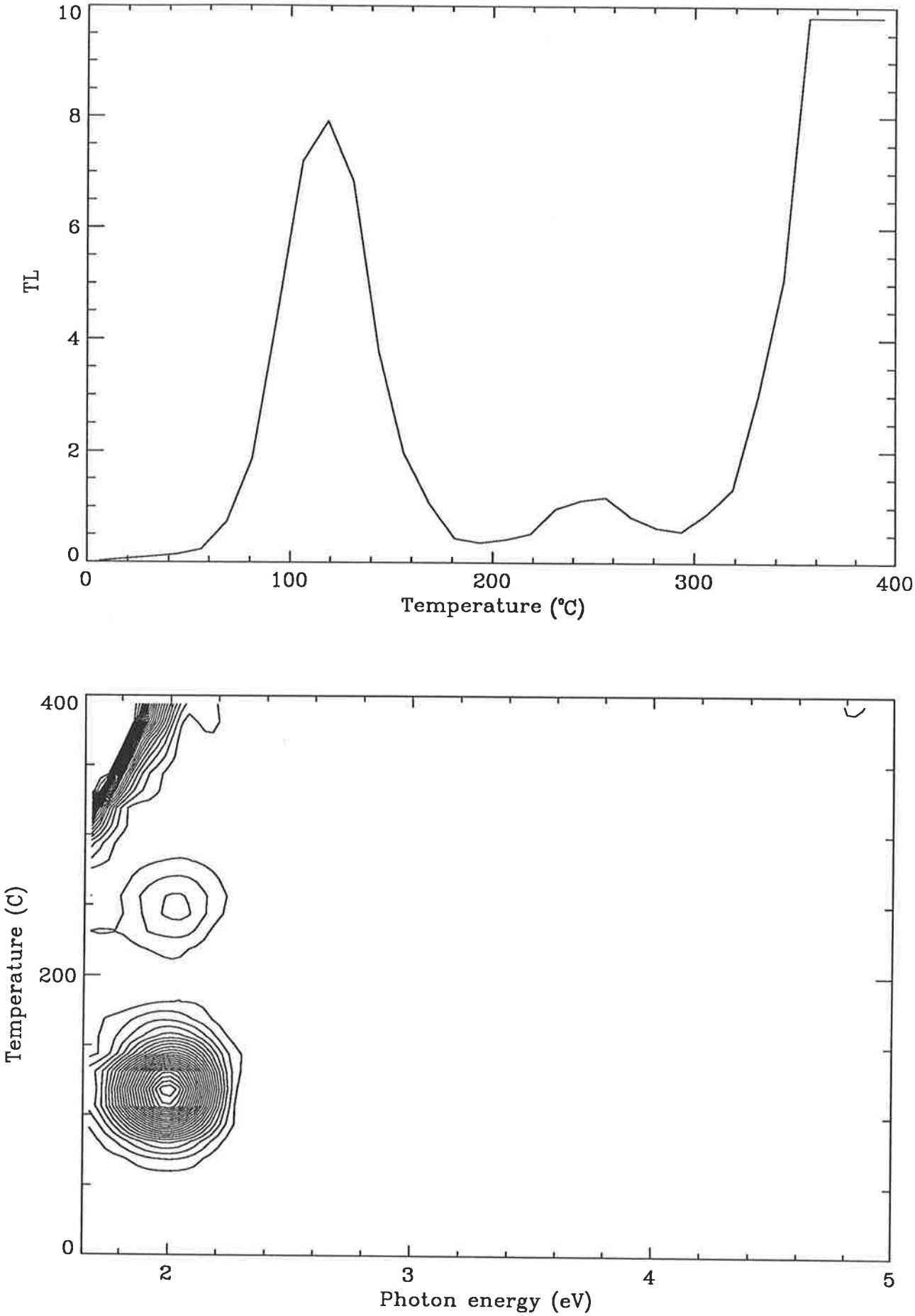

Figure 4.26: Tremolite sample which was given a dose of 6.6Gy followed by a wait of 5 minutes before glowing. The top figure is the 2–D glow curve reconstructed from the spectra and the lower figure is the contour diagram of this sample.

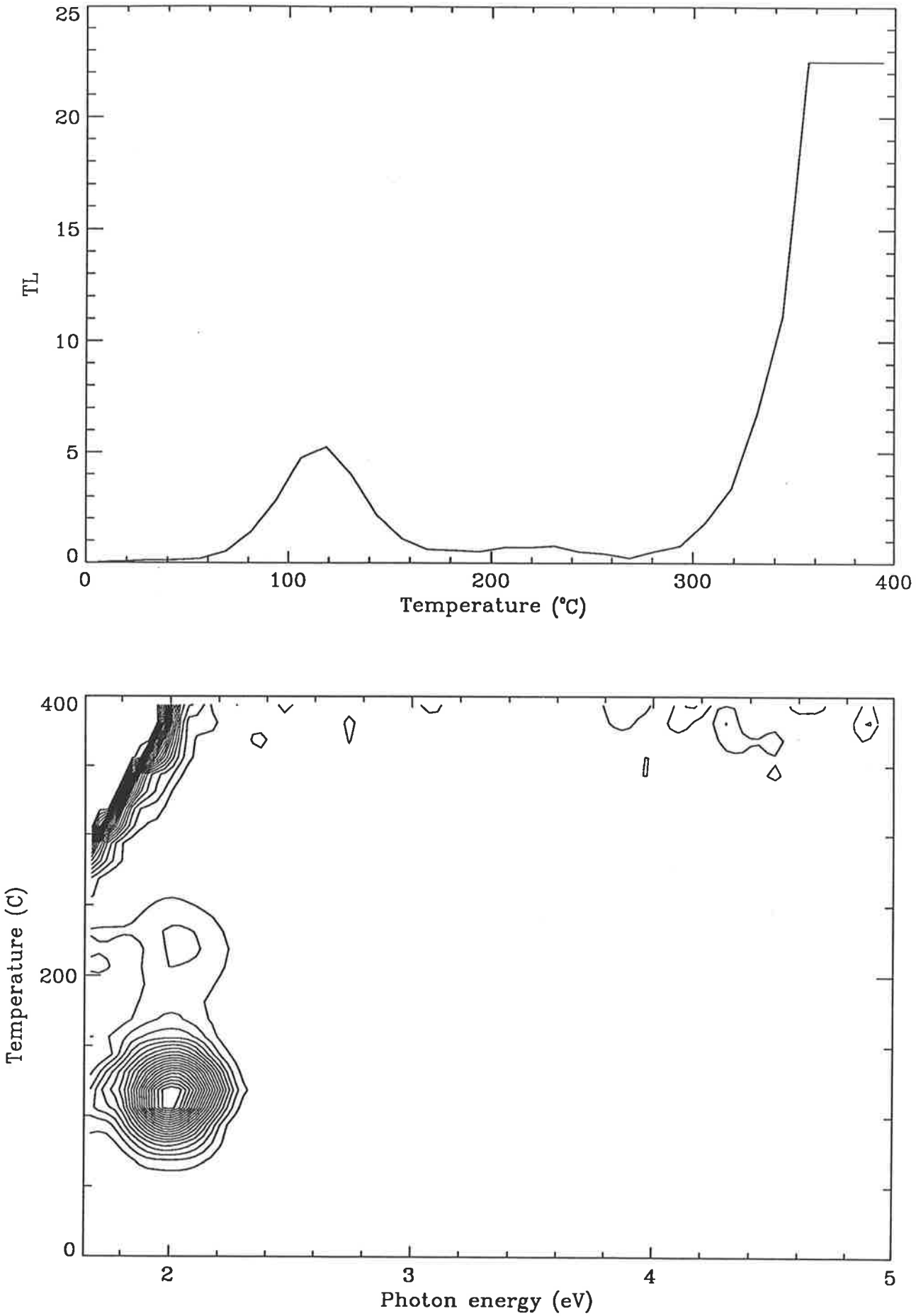

Figure 4.27: Actinolite sample which was given a dose of 5.0Gy followed by a wait of 5 minutes before glowing. The top figure is the 2–D glow curve reconstructed from the spectra and the lower figure is the contour diagram of this sample.

Tremolite and Actinolite

Both these minerals have a monoclinic crystal system with formulae:

$$tremolite: \ Ca_2Mg_5Si_8O_{22}(OH)_2,$$

$$actinolite: \ Ca_2(Mg,Fe)_5Si_8O_{22}(OH)_2^-.$$

These two samples are treated together since they both have a similar structure based on Si_4O_{11} strips connected together by Mg atoms (Bakhtin 1976). Figures 4.26 and 4.27 show the 2–D glow curves and contour diagrams for the tremolite and actinolite samples respectively. Both received a 5.0 Gy dose and both had a main TL peak at 115°C with less intense peaks at 250 and 220°C for the tremolite and actinolite samples respectively.

The TL emissions for both the samples are practically identical – at 2.00 eV (620 nm). Bakhtin (1976) has studied tremolite and actinolite with both manganese and chromium centres. The absence of any significant emission at 1.78 eV (698 nm) would seem to indicate that there was relatively little Cr present with the emission being due mainly to the $^4G \rightarrow {}^6S$ transition in Mn^{2+}, although this emission occurred at 2.13 eV (582 nm) in the samples studied by Bakhtin (1976).

4.4.2 Discussion

While the purpose of this study was to measure spectra for a selected group of minerals, they were also useful in evaluating the performance of the spectrometer in the red. An incorrect calibration would result in significant shifts in the positions of the emission peaks compared with the expected emission peaks. The close correlations of

the peak emission observed with those reported by other workers has demonstrated that no significant shifts occured and hence the calibration in the red is accurate.

4.5 Feldspars

The use of feldspars in dating has great potential in dating sediments because of their high TL brightness (10–50 times that of quartz) and their large dose range (Aitken 1985). Studies of the emission spectra of feldspars may help to improve techniques for obtaining more reliable dates, for example by an understanding of some of its problems, such as anomalous fading (Aitken 1985).

In this section the results from some investigations into four feldspar samples are presented. The samples were provided by Prof. K. Nambi of the Bhabha Atomic Research Centre, Bombay in India.

The samples studied here were collected from different layers of a mine in Singhbhum, Bihar State, India and were provided in the form of very fine grains. In addition Prof. Nambi subsequently provided corrected spectral emission curves for sample 1 which showed the existence of a peak at about 4.43 eV (280 nm). These samples were said to have exceptional sensitivity to radiation and it was hoped that by studying the emission spectra a reason for this could be found.

Also this work continues on from earlier work done in this department, particularly by Akber (1986), but for a more restricted spectral region.

Feldspar minerals are aluminosilicates classified according to the percentage of three different end–members, namely: potassium (orthoclase), sodium (albite), calcium (anorthite). Barium may substitute for calcium in celsian (Akber 1986). The

TL peaks have been associated with Al–O–Al centres, oxygen hole centres and Ti^{3+} centres, and the emission at 280, 580 and 750 nm to be due to Pb^{2+},Mn^{2+} and Fe^{3+} respectively (Marfunin 1979). For a detailed review of the defects responsible for the TL in feldspars, see for example Marfunin (1979) and Akber (1986).

Akber (1986) studied 28 feldspar samples with a compositional distribution covering the whole range – from orthoclase through albite to anorthite. He found that high sodic and potassium feldspars show an emission band in the 380–400 nm region and high sodic plagioclases exhibited another band near 540 nm. Intermediate compositional feldspars and high calcic feldspars show a broad emission between 430 nm and 450 nm. The TL intensity was found to vary systematically, by many orders of magnitude, between the albite and the anorthite feldspars which could explain the difficulties in dating high calcic feldspars (Akber 1986).

Huntley *et al* (1988a) have also recorded the emission spectra for a range of alkali and plagioclase feldspar samples which were in agreement with Akber (1988). Emission bands were observed at about 400 nm, 450 nm and 570 nm for their samples in addition there was emission below 350 nm and in the infra–red. The 570 nm emission was only found in the plagioclase feldspars and was thought to be due to Mn^{2+} substituting for Ca^{2+} (Huntley *et al* 1988a).

As for Prof. Gartia's samples all the discs received doses using a ^{90}Sr β source. The samples were received in the form of fine grains with a size of about 50μm and were glowed on aluminium sample holder discs.

Each sample received a dose which depended on its sensitivity and two sets of data are presented – firstly with a long wait between the irradiation and the glow

(of several days) and secondly with only a short wait (about 10 minutes). The first figure for each sample in the results section is for the long wait and the second figure is for the short wait.

4.5.1 Results

Sample 1

Figures 4.28 and 4.29 show the 2–D curves and contour diagrams for sample 1 for doses of 5.0 Gy and 2.5 Gy respectively. Both exhibit similar 2–D glow curves with broad peaks centred at about 170°C and shoulders at about 250°C. In addition, in figure 4.29 there is a shoulder at around 100°C.

For both cases the emission was almost identical. The 4.43 eV (280 nm) emission occurs at 155°C, the 3.10 eV (400 nm) emission at 260°C and the 2.18 eV (570 nm) emission at 195°C. There was also some weak emission at 3.10 eV (400 nm) at about 100°C in figure 4.29 (the short wait case). This sample resembles a sample of orthoclase studied by Akber (1986).

The 4.43 eV emission is consistent with a Pb^{2+} impurity, the 3.10 eV emission with a Eu^{2+} impurity and the 2.18 eV emission with a Mn^{2+} impurity (Tarashchan 1978, Marfunin 1979).

Prof. Nambi subsequently supplied calibrated emission spectra of this sample. The ratio of the emission at 4.43 eV to the emission at 3.10 eV from these data was 1.6±0.1. The corresponding ratio averaged between the emission peaks in figures 4.28 and 4.29 gives 1.5±0.1.

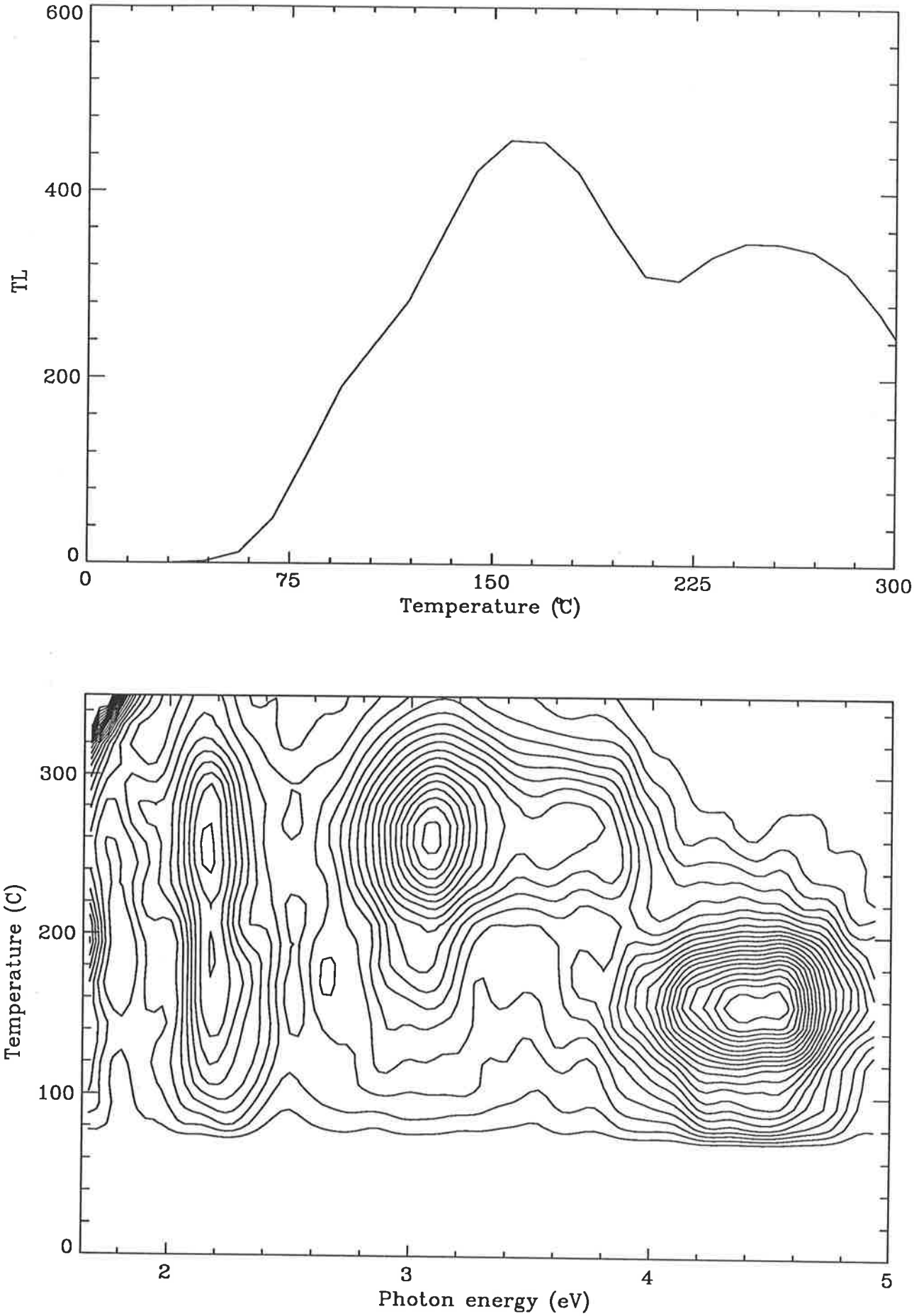

Figure 4.28: Feldspar sample 1 for a dose of 5.0Gy and a wait of several days.

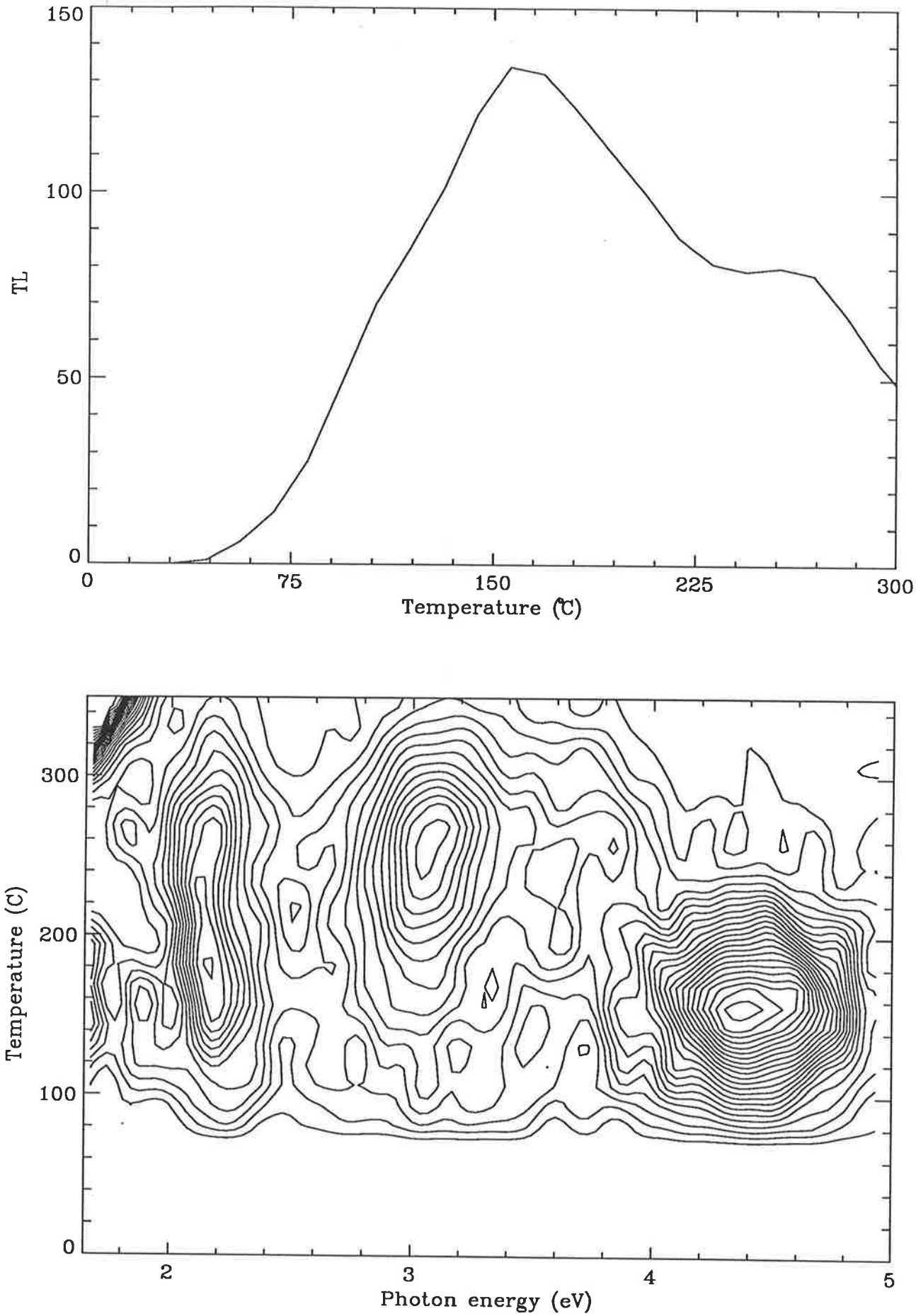

Figure 4.29: Feldspar sample 1 for a dose of 2.5Gy and a wait of several minutes.

Sample 2

Figures 4.30 and 4.31 show the data for sample 2 for doses of 680 Gy and 1.0 Gy. The peaks in figure 4.30 are at 195°C and the emission energies were at 2.53 eV (490 nm) and about 1.91 eV (650 nm). The 2.53 eV emission does not correspond to the energy of the Eu centre observed for the previous sample, since the rare earth emission would be unaffected by the crystal field. Mariano *et al* (1973) matched their 450 nm (2.76 eV) emission with that from a synthetic plagioclase doped with Ti^{4+}, so possibly Ti could be responsible for this emission. Tarashchan (1978) also reports feldspar emission at 2.70 eV (460 nm) which was associated with an AlO_4^{5-} centre. The most likely candidate for the red emission is a Mn^{2+} impurity. In addition there also seemed to be some weak emission at about 4.5 eV (275 nm), consistent with a Pb^{2+} impurity.

The emission shown in figure 4.31 was at a temperature of 105°C and a photon energy of 3.45 eV (360 nm). The shape of the glow curve and its emission, indicated that this peak corresponds to the 110°C peak of quartz. The dominance of this peak in figure 4.31 indicates that there is a considerable amount of quartz in the sample provided by Prof. Nambi and this may be the reason for the high sensitivity of these samples.

Sample 3

Figures 4.32 and 4.33 are the diagrams for sample 3 for doses of 680 Gy and 1.0 Gy respectively. The TL peaks in figure 4.32 are at 180°C with a shoulder at a temperature between 250 and 300°C. The emission is at 4.43 eV (280 nm), 3.70 eV

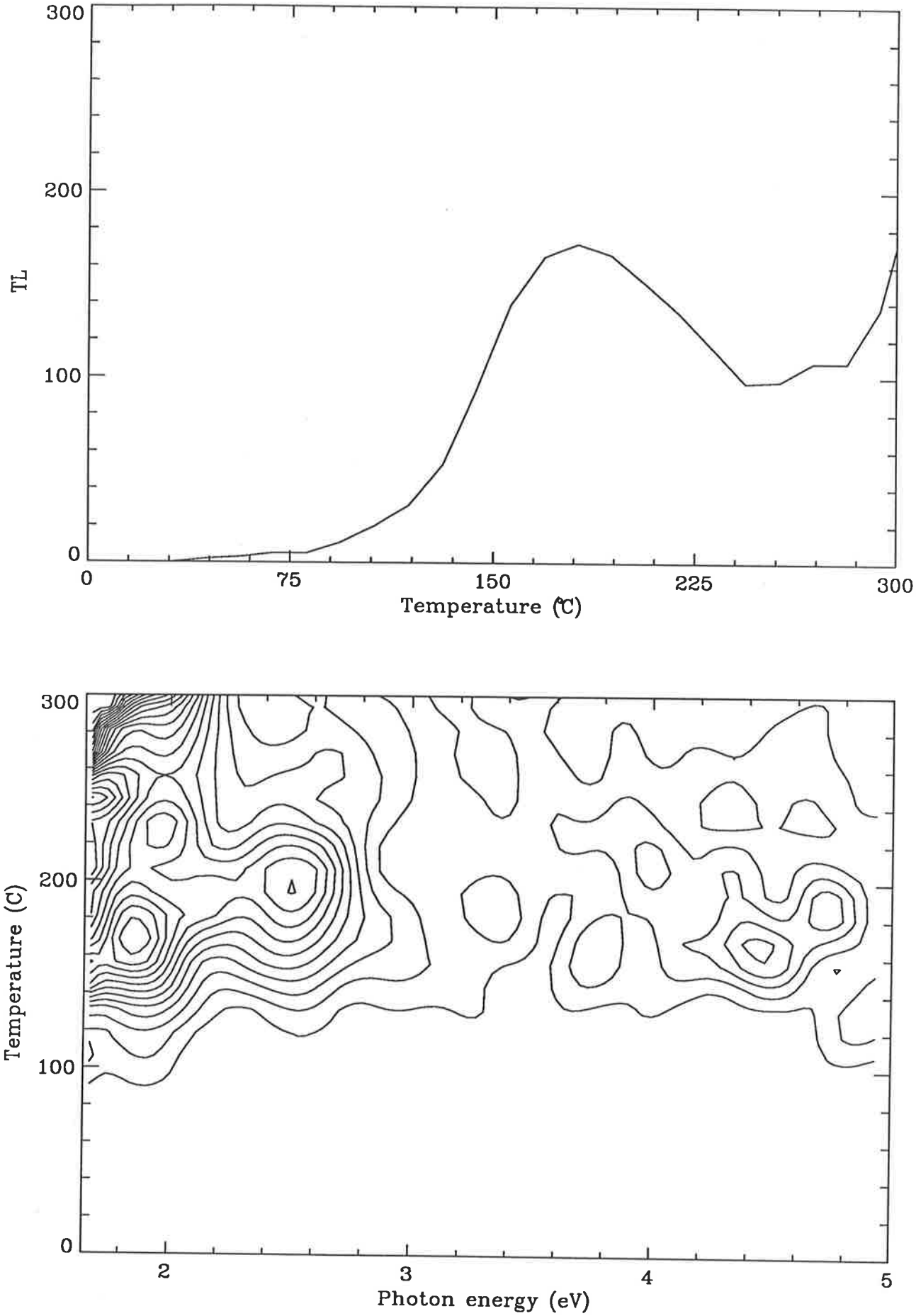

Figure 4.30: Feldspar sample 2 for a dose of 680Gy and a wait of several days.

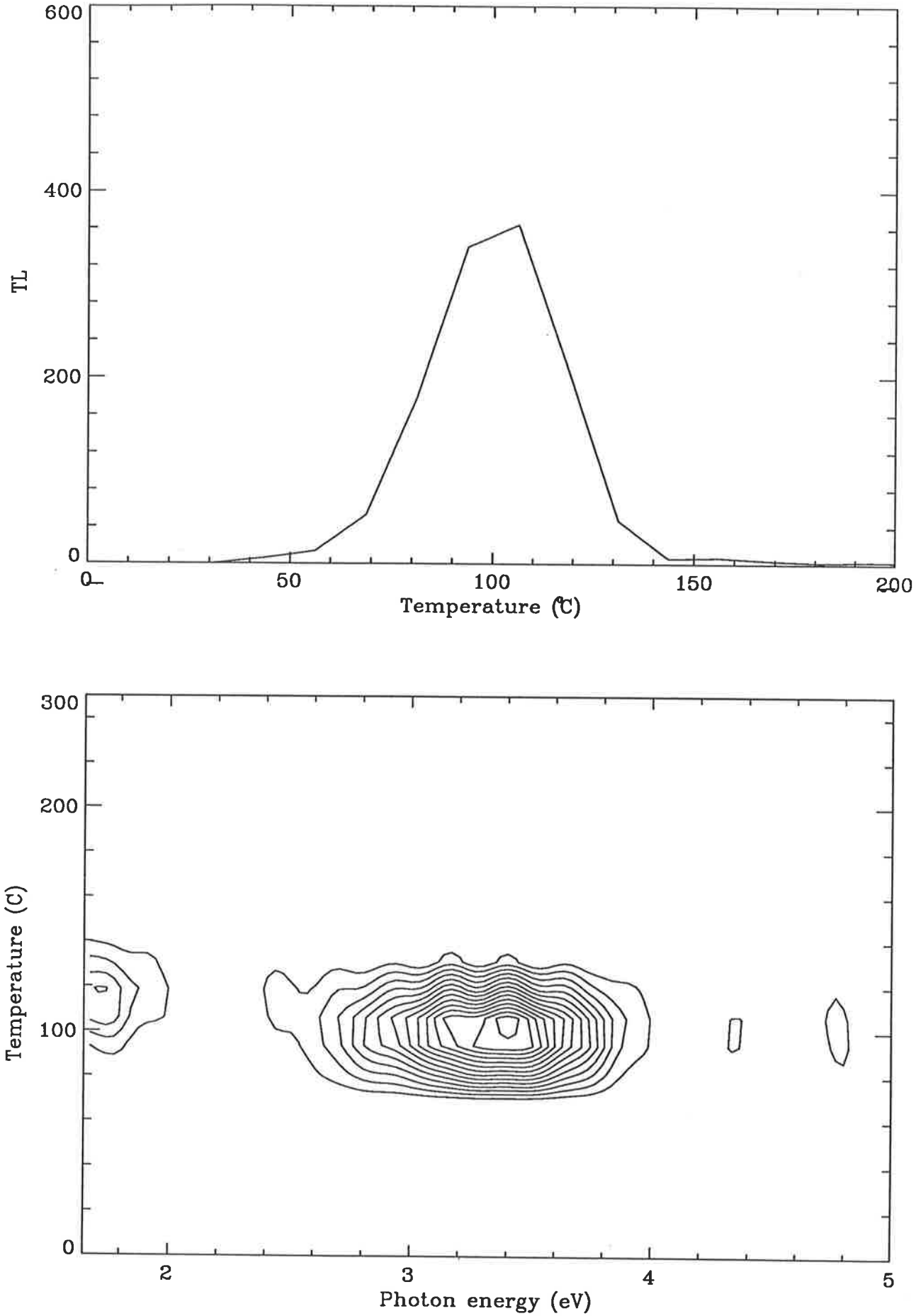

Figure 4.31: Feldspar sample 2 for a dose of 1.0Gy and a wait of several minutes.

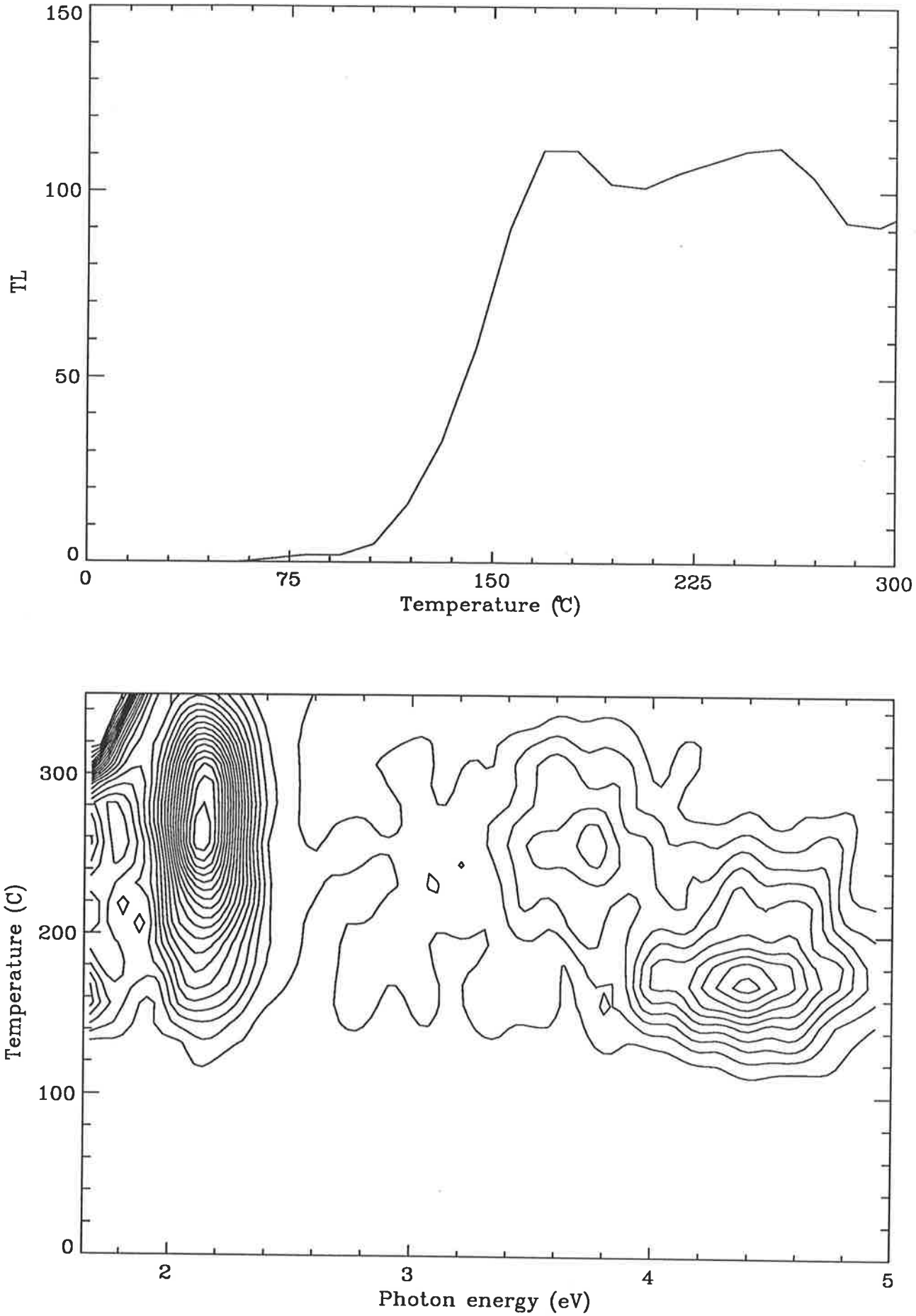

Figure 4.32: Feldspar sample 3 for a dose of 680Gy and a wait of several days.

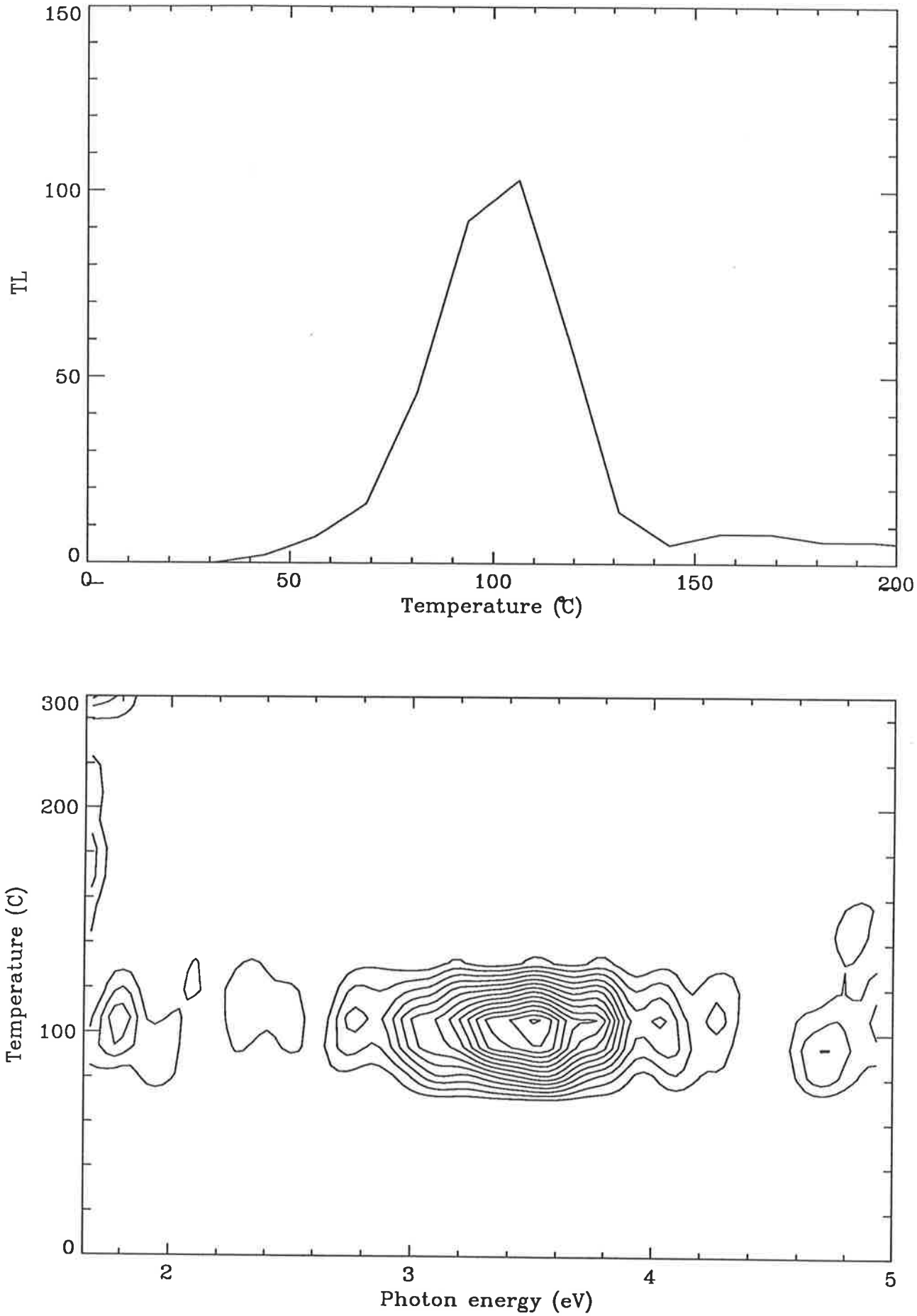

Figure 4.33: Feldspar sample 3 for a dose of 1.0Gy and a wait of several minutes.

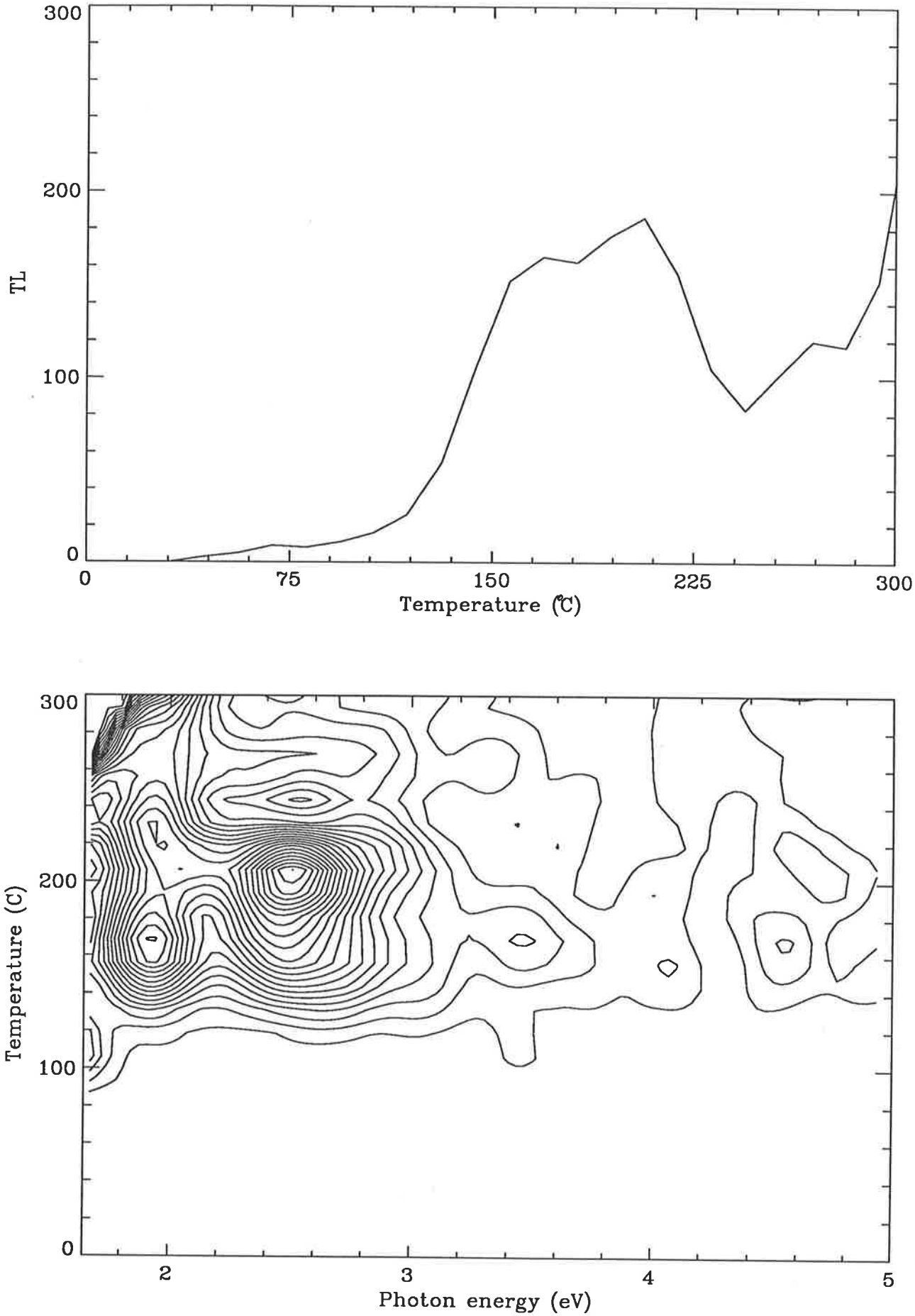

Figure 4.34: Feldspar sample 4 for a dose of 680Gy and a wait of several days.

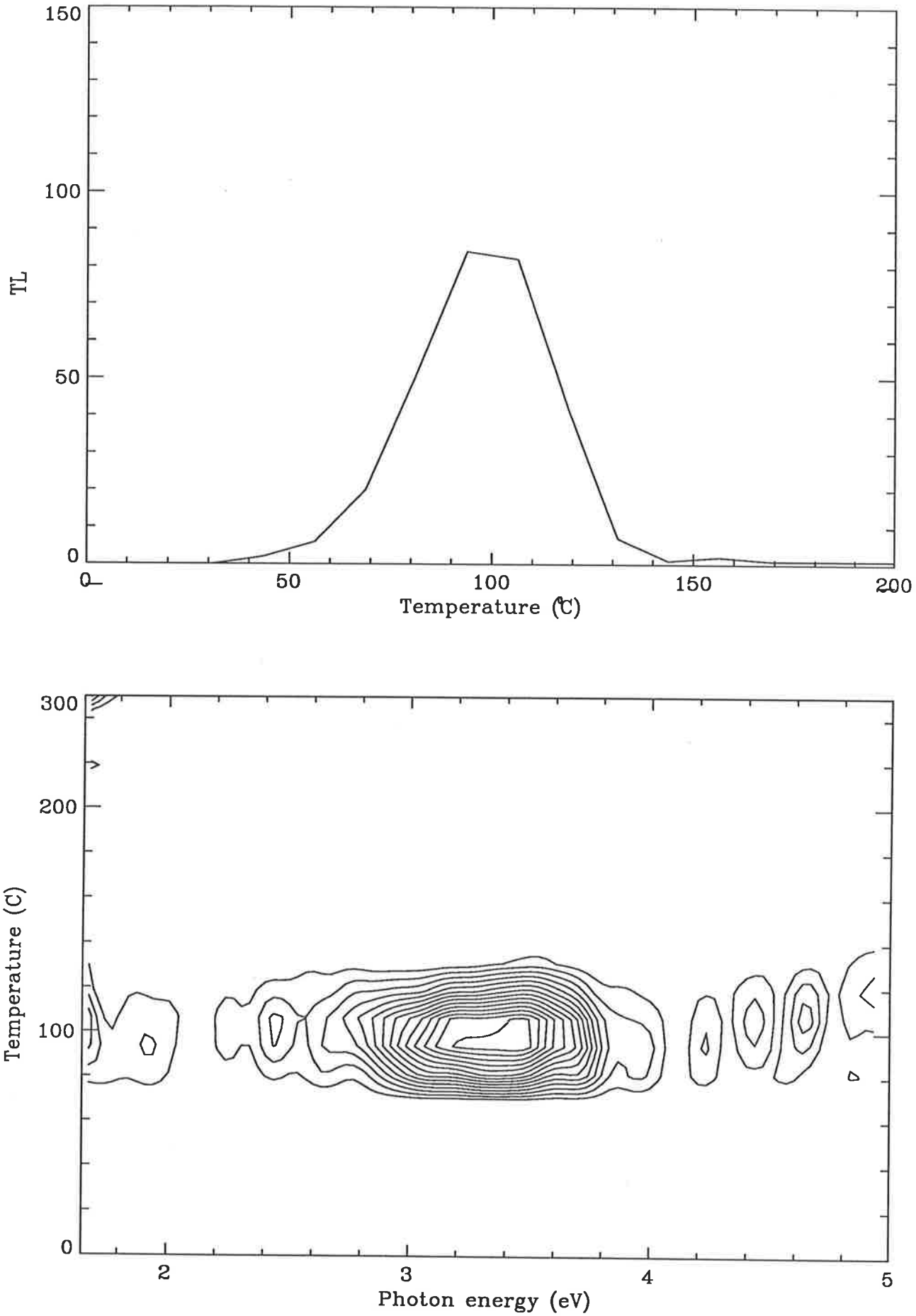

Figure 4.35: Feldspar sample 4 for a dose of 1.0Gy and a wait of several minutes.

(335 nm) and at 2.14 eV (580 nm) at temperature of 170, 265 and 285°C respectively and appears to be a sample of albite (Akber 1986).

Compared to sample 1 there appeared to be little Eu, otherwise the emissions matched those of sample 1. The 3.70 eV emission may have been due to Ce^{3+} (Marfunin 1979).

The emission shown in figure 4.33 was at a temperature of 105°C and a photon energy of 3.45 eV (360 nm) and is identical to the emission in figure 4.31 Consequently it appears that quartz is also present in this sample.

Sample 4

The data for sample 4 is shown in figures 4.34 and 4.35 for doses of 680 Gy and 1.0 Gy respectively. In figure 4.34 the peak is at 205°C with a shoulder between 150 and 200°C. The emission centres for this sample are almost identical to those of sample 2 except for even weaker emission below 4.0 eV (300 nm) As before, for figure 4.35, the narrow 105°C peak is probably due to quartz.

4.5.2 Discussion of Feldspar Samples

The feldspar samples studied here have emission spectra similar to those reported by Akber (1986) and Huntley *et al* (1988a). In addition samples 1 and 3 show a large emission peak at around 4.43 eV (280 nm) which was not observed by either of these other studies. This was due to the limited spectral response of their instruments.

Samples 2,3 and 4 showed a dominant emission band at 105°C and 3.45 eV (360 nm). This was compared with quartz emission spectra reported by Akber *et al* (1987) and found to be identical. Subsequent x–ray fluorescence studies (J. Hutton personal

communication) showed that these samples had, in fact, a large component of SiO_2, consistent with the emission spectra.

4.6 Conclusion

This chapter has demonstrated that the modifications to the spectrometer, described in chapter 3, were successful in extending its spectral range into the red and ultra–violet. Also demonstrated were the usefulness of TL emission spectra in characterising mineral samples and how they can be used with electron spin resonance to study the defect state of a particular mineral, in this case calcite.

In the next chapter this spectrometer will be used to examine the emission spectra of several quartz samples both before and after their illumination with several selected wavelengths of light.

Chapter 5

Spectra of Bleached Quartz

5.1 Introduction

One of the major projects of this thesis concerned the changes in the emission spectra of quartz with bleaching. This study was intended as a general investigation of the emission spectra of several bleached quartz samples, so that obvious trends could be identified which may indicate fruitful directions for further, more detailed research. It was also intended that the results should be used in chapter 7 to aid in the development of realistic theoretical models describing the decay mechanism of quartz. Before discussing the present work it is appropriate to review the structure of quartz, its defect state and earlier work on this material.

5.2 Quartz

5.2.1 Structure

α–quartz or crystalline SiO_2 has been the object of scientific study for over 2000 years (Evans 1966). More recently the observation that quartz crystals, extracted from ancient pottery samples, exhibit TL has spurred the development, not only of dating techniques, but also research into the mechanisms involved in the production

of TL. In addition α–quartz is a vital component in many electronic devices such as high–precision oscillators, filters, accelerometers etc., and an understanding of the effects radiation has on its properties and especially the role impurities play is important in determining under what conditions such devices may be operated and in designing new devices for novel situations (Halliburton *et al* 1981).

Below 573°C the stable modification of quartz is called α–quartz and has a rhombohedral structure (McKeever 1984). Each silicon atom is tetragonally bonded to four oxygen atoms with two of the bonds making an angle of 66° with the optical axis (which is also called the c–channel) and the other two bonds making an angle of 44°. The nature of the bonds is about 40% ionic and about 60% covalent (Evans 1966). The tetrahedron of oxygen about a silicon atom is almost regular with the Si–O distance about 16.1 nm and each oxygen also has six adjacent oxygen atoms at distances ranging from 22.7 to 26.0 nm (Wyckoff 1960). Figure 5.1 shows the six fold symmetry of α–quartz projected onto a plane perpendicular to the c-axis channel and also a packing drawing viewed almost down the c-axis.

5.2.2 Defects

Several different techniques have helped to elucidate the role that defects play in the quartz lattice. Probably the most widely studied defects are those due to oxygen vacancies. One of the earliest studies was of the optical absorption of neutron irradiated quartz (Mitchell and Paige 1956). They associated the absorption bands at 5.7eV and 7.6eV with an electron trapped at an O^{2-} vacancy and an electron missing from an O^{2-} defect respectively. Also important is the role broken silicon and oxygen bonds play since they can act as possible hole traps (Staplebroek *et al* 1976).

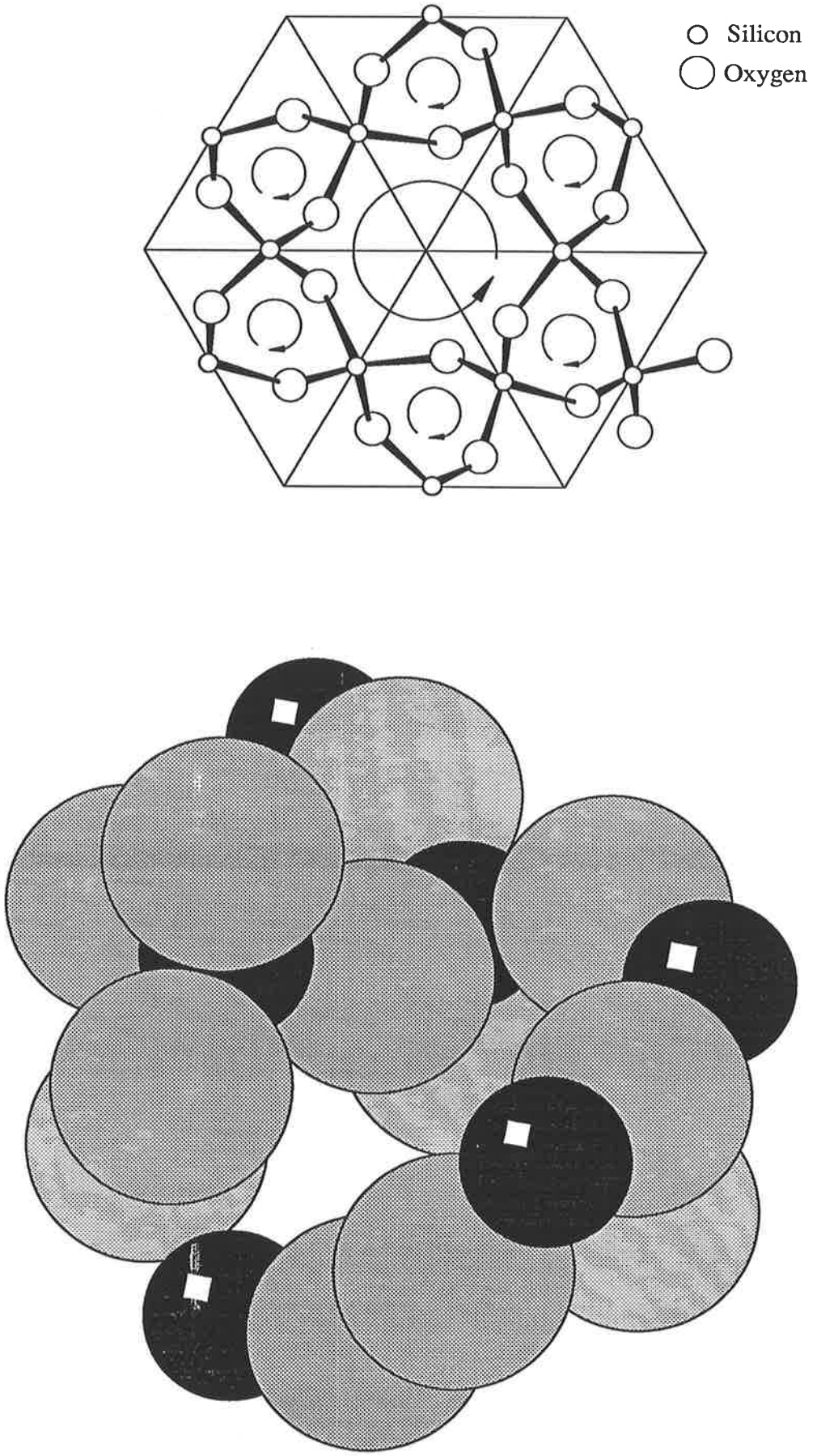

Figure 5.1: Above is the quartz structure projected onto a plane perpendicular to the c-axis channel (after Weil 1984). Below is a packing diagram viewed almost down the c-axis. The all–black spheres are the silicon atoms (after Wyckoff 1960).

Impurity atoms modify the quartz lattice and can give rise to new optical absorption bands, electron spin resonance (ESR or equvalently electron paramagnetic resonance) and TL features (McKeever 1984). O'Brien (1955) and Griffiths *et al* (1954) were the first to propose a model to account for some of the properties of the colour centres in quartz, which involved aluminium atoms substituting for silicon. Since Al atoms are trivalent and Si tetravalent, the Al can be charge compensated by monovalent atoms such as alkali and hydrogen ions which easily diffuse along the c-axis channels. Hence, depending upon the compensating ion, various aluminium centres can exist (McKeever 1984).

Other seemingly less important impurity atoms include Germanium which substitutes tetragonally for Si and acts as a strong electron trap (MacKey 1963) and possibly Titanium which is also tetravalent (Weil 1984). Weil (1984) has given a review of the EPR studies of the defects in α–quartz arising from Al, H, Cu, Ag, Ge, P, Ti and Fe impurities.

5.2.3 Thermoluminescence

One of the first people to study the TL properties of quartz was Medlin (1963), who studied x-ray and UV excited TL in natural and synthetic quartz doped with a wide variety of impurities. The conclusion drawn from this study was that, below room temperature, of the four main glow peaks, one was associated with the Ti^{4+} impurity and the others with a defect centre. Apparently the other impurities play no role in the production of the TL studied. The emission spectrum associated with the Ti^{4+} impurity was rather broad-band extending from around 350 nm to 750 nm, whereas for the other peaks the spectra were much narrower, falling between 330 nm and 500

nm and centred on 380 nm.

Above room temperature, Levy (1979) has shown isometric plots of optical grade natural quartz for ^{60}Co irradiations ranging from 2000Gy to 50,000 Gy and he observed a single broad-band emission at 500 nm. Other reported spectral measurements (Schlesinger 1964, Malik *et al* 1981 and Durrani *et al* 1977) have described emission between 450 nm and 470 nm with an increase in the glow peak intensity upon irradiating at high temperatures. This is interpreted as the diffusion of the charge compensating ions away from an Al site, thus forming an $(Al^{3+})^0$ centre (McKeever 1984). Other emission bands have also been reported at 410 nm (Huntley *et al* 1988b), 630 nm (Serebrennikov *et al* 1982, Huntley *et al* 1988b) and at 360 nm (Serebrennikov 1982, Hashimoto *et al* 1986 and Akber *et al* 1988).

Using a combination of TL and ESR, the emission at 470 nm has been assigned to the recombination of electrons (trapped at a Ge^{4+} site) at Al^{3+} - $hole^{+}$ centres (McKeever *et al* 1985). However, the centre responsible for the observed 380 nm emission which is the major emission wavelength for the 110°C peak, was unidentified.

The impurities responsible for most of the TL peaks observed still remain unknown (McKeever 1984) although as mentioned earlier H^+, Na^+ and Li^+ seem to be important. Ge, too, appears to be crucial for TL close to 300°C (Schlesinger 1964 and McMorris 1971).

5.2.4 Bleaching

The motivation for this research has its genesis in a series of papers by Wintle and Huntley (Wintle and Huntley 1979, 1980, 1982 and Huntley 1985) where they describe a procedure for dating sediments that had been exposed to sunlight prior to being

deposited. The crucial fact that enabled dates to be found was that the sunlight exposure acted as the zeroing mechanism, although the remaining TL was not reduced totally to zero and the different traps were emptied at different rates (Huntley 1985). In order further to understand the behaviour of quartz when exposed to sunlight, Spooner (1987) studied the relative efficiencies of different narrow band fractions of the solar spectrum, between 320 nm and 750 nm, in reducing the TL of several glow peaks above 300°C. Figure 5.2, taken from Spooner (1987), shows the effects that different wavelengths had on the 325 and the 370°C peaks of Lake Woods quartz. The original figure was the total energy required to completely remove the 325°C TL peak plotted against the bleaching wavelength but here it is reproduced in a slightly different way, with the total number of photons required to remove the peak against the wavelength. Plotted this way the data is more representative of the relative bleaching efficiencies of the various wavelengths. These results have been partially confirmed by an independent study of Berger (1988), who also presents a graph of the reduction in the TL of quartz following its exposure to different wavelengths showing essentially the same effect, although no information is provided concerning which peaks were being investigated. Clearly, the 325°C peak is considerably more sensitive to bleaching than the 370°C peak, even though their kinetically determined trap depths are practically the same (Spooner 1987).

It can be somewhat misleading to compare the thermal and optical activation energies if the effect of the Franck–Condon principle has been ignored (Mott and Gurney 1940). This effect states that the thermal activation energy is always less than the optical activation energy (de Boer and van Geel 1935). The reason for this

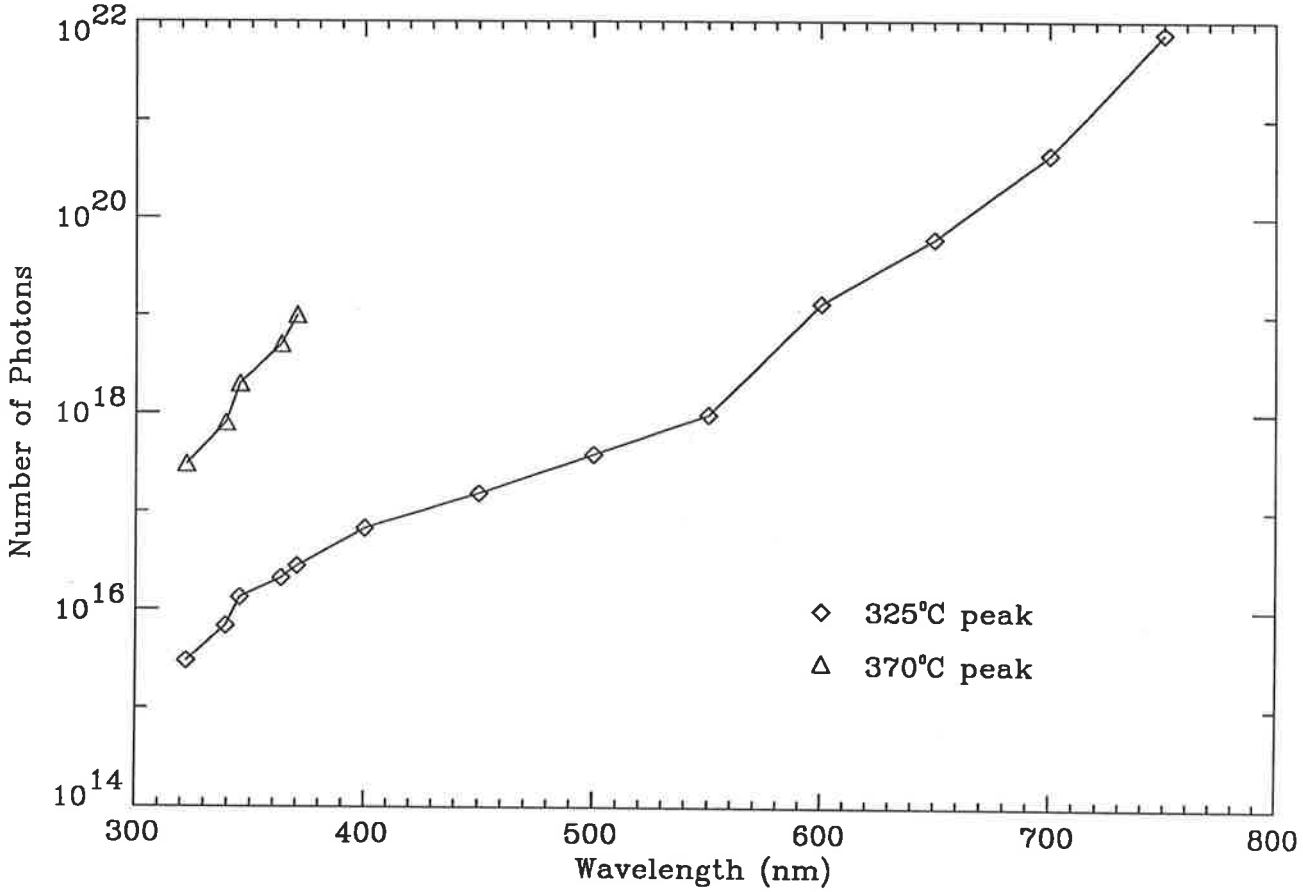

Figure 5.2: Graph of the number of photons against the bleaching wavelength required to completely remove the 325°C TL peak of Lake Woods quartz (after Spooner 1987).

is that the ions surrounding a trapped electron remain stationary when the electron is removed optically, hence they are no longer in equilibrium. They will then rearrange themselves into a new equilibrium configuration and in the process give out energy, U. The thermal activation energy, E, where the ions are always in equilibrium, is then the difference between, $h\nu$, the energy of the photon and U. Mott and Gurney (1940) calculate the ratio of $h\nu$ and E. U is given by

$$U = \frac{e^2}{8\pi\epsilon_0 R}\left(\frac{1}{k_0} + \frac{1}{k}\right), \tag{5.1}$$

where k_o and k are the high frequency and static field dielectric constants respectively, and R is the radius of the impurity centre. Since the depth of the potential hole is $e^2/k_o R$, we have

$$h\nu \sim \frac{e^2}{8\pi\epsilon_0 k_0 R}, \tag{5.2}$$

and hence

$$E \sim \frac{e^2}{8\pi\epsilon_0 k R}. \tag{5.3}$$

For quartz k_0 is about 2.1 and k is about 4.3 (C.R.C. Handbook 52^{nd} Edition 1971) and so from equations 5.2 and 5.3, E is of the order $\frac{1}{2}h\nu$. The trap depths of the 325°C and 370°C peaks are 1.69 eV and 1.66 eV respectively (Aitken 1985), which correspond to optical excitation wavelengths of 370 nm and 375 nm. In fact, figure 5.2 does show possible evidence for an increase in bleaching efficiency which is in operation below about 400 nm for both the 325°C and 375°C peaks. However for the 325°C peak there is clearly a special bleaching mechanism involved for wavelengths above 400 nm.

The effect of UV bleaching of quartz has been studied extensively. Nelson and

Weeks (1960) bleached irradiated quartz at various UV wavelengths at 78°K and at room temperature and found that it was easier to transfer electrons from one trap to another than it was to stimulate electron–hole recombination. This was interpreted as either a concentration effect or that the electron–hole capture cross-section was much smaller than for the electron traps. David and Sunta (1981) performed a systematic bleaching study on a pink variety of quartz, using 250 nm light and showed a number of decay curves (graphs of the TL against the UV exposure time) for different TL peaks, after different sample preparations. Essentially, their results show that the low temperature TL peaks were generated at the expense of the residual high temperature peak. Kristianpoller (1983) used a double monochromator to measure the photoluminescence (PL) spectra emitted from natural quartz crystals when they were excited with UV light at temperatures from liquid nitrogen up to 500°C. Two main emission bands were observed at 370 nm and 440 nm which varied with temperature and thermal pretreatment. The changes were attributed to competition between the emission centres and possibly also to a phase transition during the high temperature anneals.

Using selected filters, Huntley (unpublished data) has also measured a PL emission spectrum of quartz, centered around 370 nm, when the samples were excited by optical wavelengths.

5.3 Experimental Details

Four samples of natural quartz were used in this study, collected in Australia from various locations (see map 5.1). The collection sites were Lake Woods (Northern Ter-

Map 5.1: Map of Australia showing the locations where the various quartz samples were collected.

ritory), East Bank – Roonka (Murray River Valley), Wokewine (Southeast of South Australia) and at Puritjarra (Central Australia). Each sample will be designated: LW, EB, WK and PJ respectively.

Each sample was prepared in the same way by a combination of mechanical, chemical and magnetic processes. These included the removal of carbonates and sulphides with hydrochloric acid, sieving to extract the 90–125μm grain fraction and magnetic separation. Finally the grains were chemically etched in hydrofluoric acid for about 40 minutes to remove the outer α–irradiated layer of the grains and any feldspar contaminants. Each process was accompanied by several rinses in distilled water followed by drying with methanol and acetone.

During each phase of the sample preparation and subsequent treatment, the laboratory illumination was orange (Spooner 1987).

For the purposes of bleaching and glowing, the quartz samples were loaded onto 0.97 cm diameter, 0.5 mm thick aluminium discs which had been pre–sprayed with a small amount of silicone oil. Using a loading technique described in great detail by Spooner (1987), a monolayer of grains could be easily packed onto the discs. During the loading procedure the sample weight was also recorded.

All laboratory irradiations were performed using a ^{90}Sr – ^{90}Y β source of nominal strength 1.48×10^{9} Bq to deliver a total dose of (41.3 ± 0.2) Gy. Large batches of discs were irradiated automatically with an Oxford Instruments Automatic Irradiator.

The bleaching was done with an Oriel Corporation 1000 W Solar Simulator. This allowed the conditions under which the bleaching was performed to be highly controlled and also very convenient. This particular solar simulator also offered short

and long term output stability. Up to seven discs could be bleached simultaneously for a given filter, in light tight conditions (Spooner 1987). Before commencing any bleaching run, the simulator was calibrated with an Oriel radiometer and the radiant flux reaching the samples could be then adjusted by raising or lowering the table upon which the sample holder rested (Spooner 1987).

For this study three wavelengths were used to bleach the quartz samples, selected using Corion interference filters. The wavelengths were at 650 nm ($\pm$ 20 nm), 550 nm ($\pm$ 20 nm) and 350 nm ($\pm$ 12 nm). The transmission curves of these three filters is shown in figure 5.3. The three wavelengths were chosen with reference to figure 5.2, in order to reflect any possible structure in this graph and to examine if widely different wavelengths have an appreciably different bleaching effect on the quartz samples.

The data presented on samples that have received no bleaching at all are averages of five weight–normalised discs, and the rest are averages of two discs. The reason for five disc averages in some of the cases is that they were used as a comparison for all subsequent wavelength bleaches, so providing reference spectra.

The quartz sample receiving the most detailed study was LW. A succession of four bleach times was performed, whereas for the WK, EB and PJ samples the bleach times corresponded to complete removal of the 325°C peak and one third of this time.

In general the TL peaks which are of greatest interest are above about 250°C which means that the incandescent radiation would swamp the TL signal from the samples. The EMI 9635QA PMT was used for these experiments which necessarily restricted the spectral range of the spectrometer to above 2.0 eV.

All the spectra have been corrected for the spectral response of the interferometer

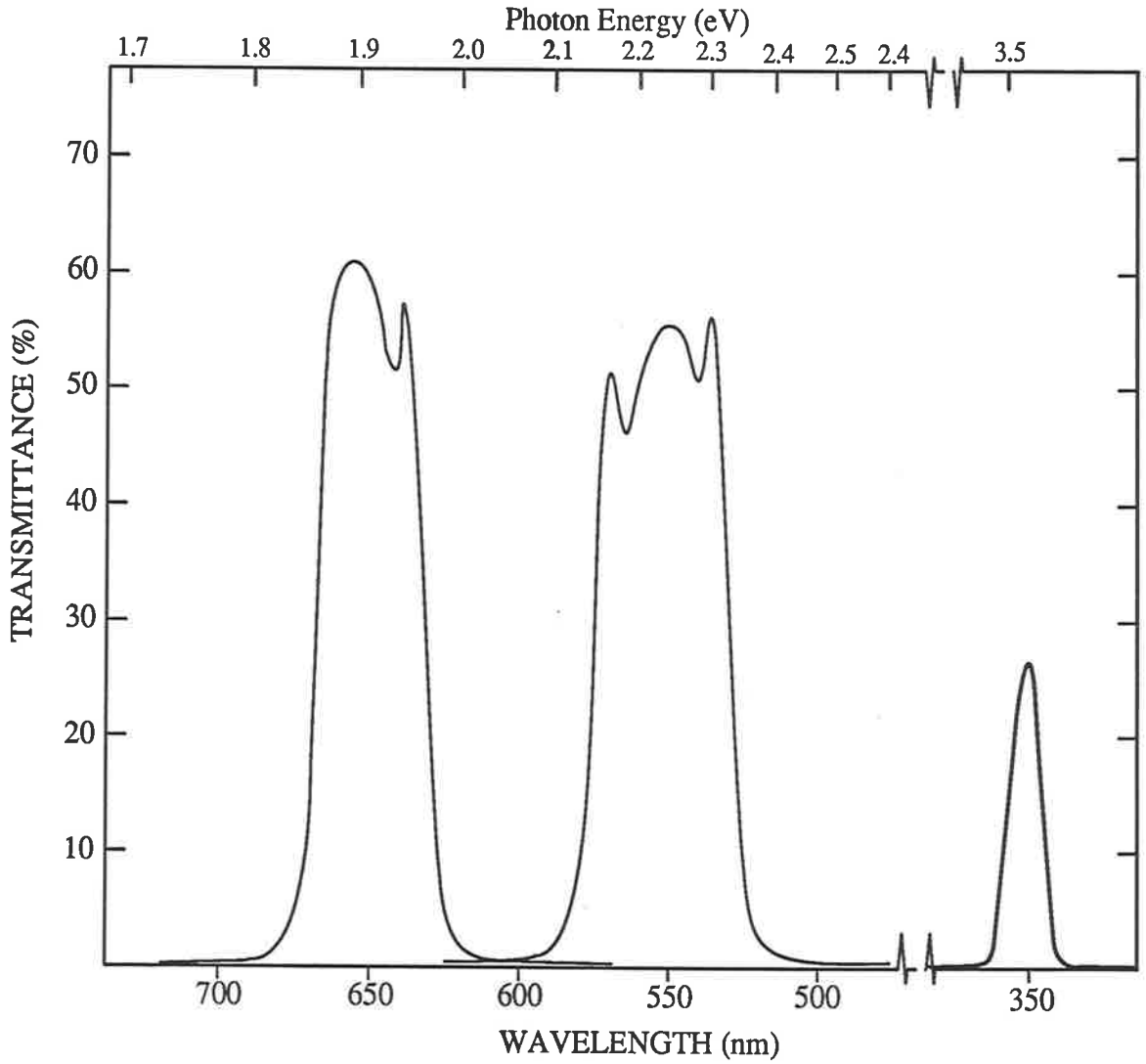

Figure 5.3: Graph showing the transmission curves for the 650, 550 and 350 nm band pass interference filters used for the bleaching experiments.

(see figure 3.16). One of the effects of this correction was to amplify the data near 2.0 eV and 5.0 eV, since the response is least at these photon energies. This means that smoothed noise fluctuations, especially just above 2.0 eV, may appear to be more significant than they warrant. Accordingly, only systematic changes in the bleached spectral sequences should be viewed as significant.

Also, 2–D glow curves have been plotted from the corrected spectra data which has resulted in glow curves with a temperature resolution of only about 10 K. No smoothing of these curves has been done.

Spooner (1987) presents data on the amount of energy at different wavelengths which was required to completely remove the 325°C peak. These energy values have been used here as a guideline in determining the length of time, at each wavelength, that each sample was bleached. This means that comparisons can be made between this work and that of Spooner (1987), however it should be realised that the TL measured by Spooner was for a spectral range limited by the 7–59 glass filter used in his apparatus and hence the glow curves may appear somewhat different in shape.

5.4 Results

5.4.1 Natural LW Quartz

Figure 5.4 shows the contour diagram for natural unbleached LW quartz. This diagram shows a broad emission band peaking near 2.1 eV (590 nm) extending into the near ultra–violet, to about 3.8 eV (325 nm). Probably the most noticeable feature of this plot is the fact that the peak of the emission at the higher photon energies occurs at a lower temperature than the lower (2.1 eV) energy emission peak. This is

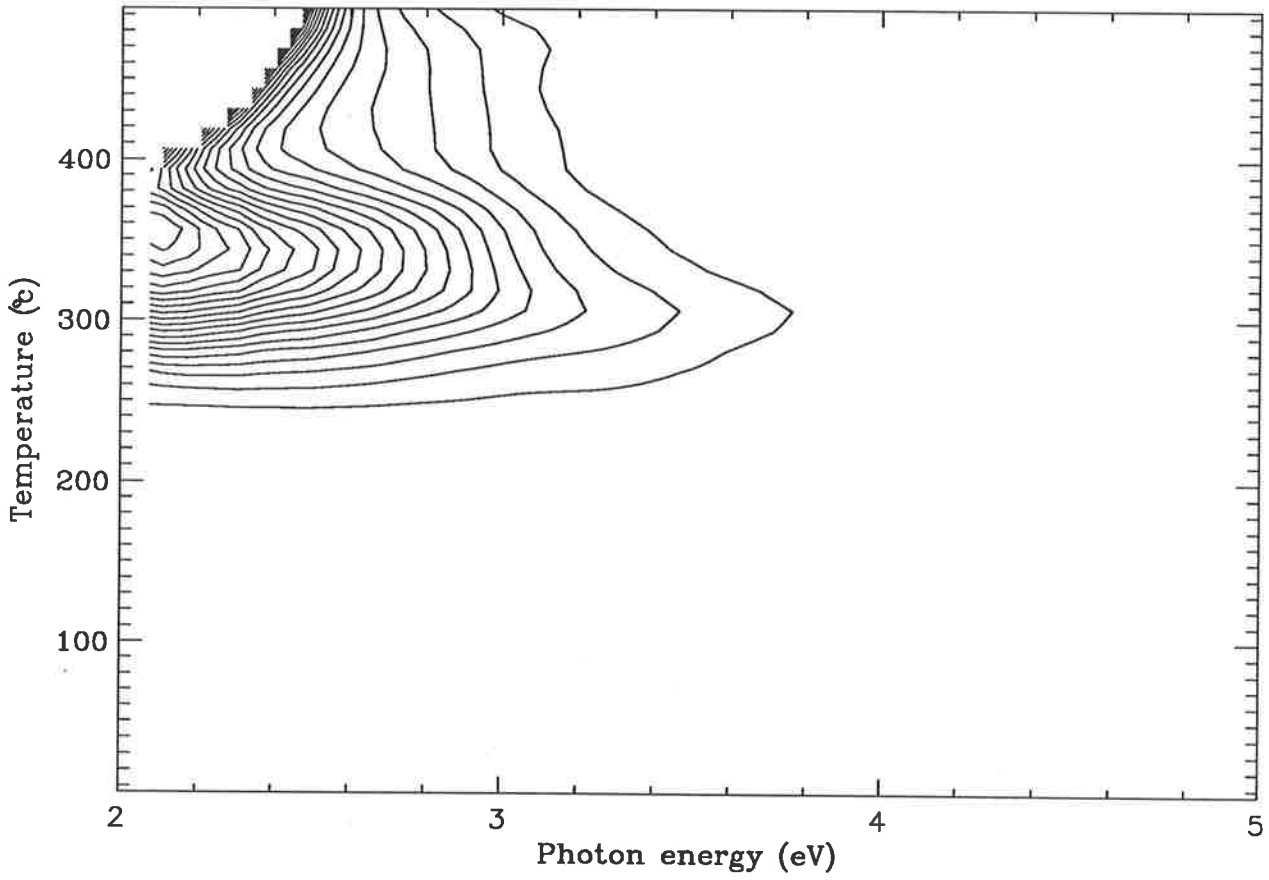

Figure 5.4: Contour diagram of natural LW quartz.

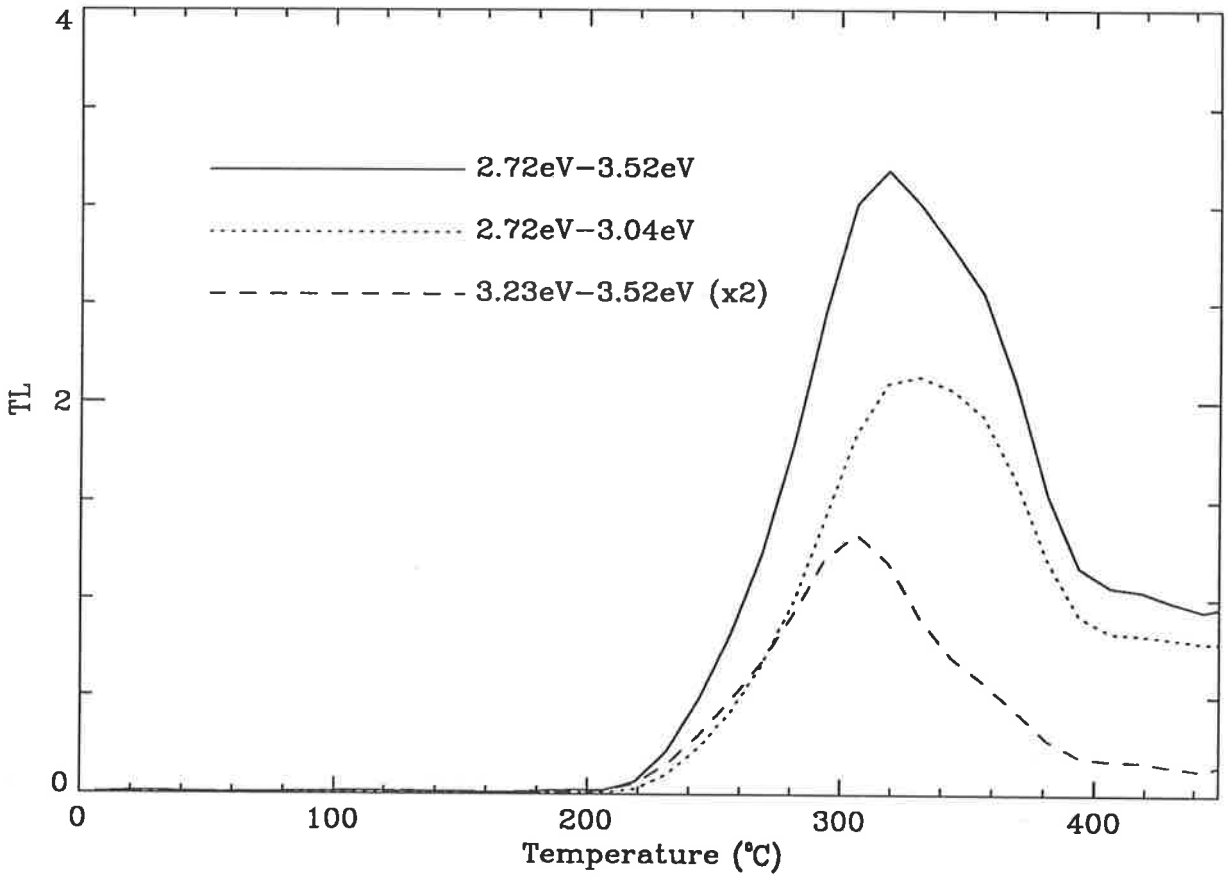

Figure 5.5: Glow curves obtained by summing through different photon energy regions (shown on the plot) for natural LW.

demonstrated more clearly in figure 5.5 which shows the 2–D glow curve (solid line) for a spectral range of 2.72–3.52 eV (350–456 nm). Also plotted (broken lines) are the glow curves for two other spectral ranges: 2.72–3.04 eV (408–456 nm) and 3.23–3.52 eV (353–384 nm). In this latter case the curve has been scaled up by a factor of two in order to make the lines easier to compare. The curve for the higher photon energy region has its peak at a significantly lower temperature (about 305°C) than for the other broken curve whose peak is at about 335°C. Both peaks also have components on the high and low temperature sides of their respective peaks.

The unbroken line resembles glow–curves presented by Spooner (1987) for LW because the curve in figure 5.5 was for a restricted energy range used to highlight the higher photon energy region. In later figures the full glow curves of the natural and bleached samples are shown. In these figures the 340°C TL emission clearly dominates. Also evident from these glow curves is emission at about 430°C.

Bleaching by 350 nm Light

Figure 5.6.1 shows the contour diagrams for natural LW samples (a), b), c) and d)) that were successively bleached with 0.5, 1.0, 1.5 and 2.0 minutes of 350 nm light. These times correspond to energy fluxes of 0.93, 1.85, 2.78 and 3.70 mJ cm^{-2} respectively. Apart from plots b) and c) which show remnants of the 305°C high energy emission, the plots resemble one another, that is they appear to be the same as figure 5.4 minus the high energy emission. Further, this removal appears to have taken place quite rapidly, within the first 30 s of the bleach. Figure 5.6.2 and 5.6.3 show the bleaching sequences for the individual spectra at given temperatures (shown

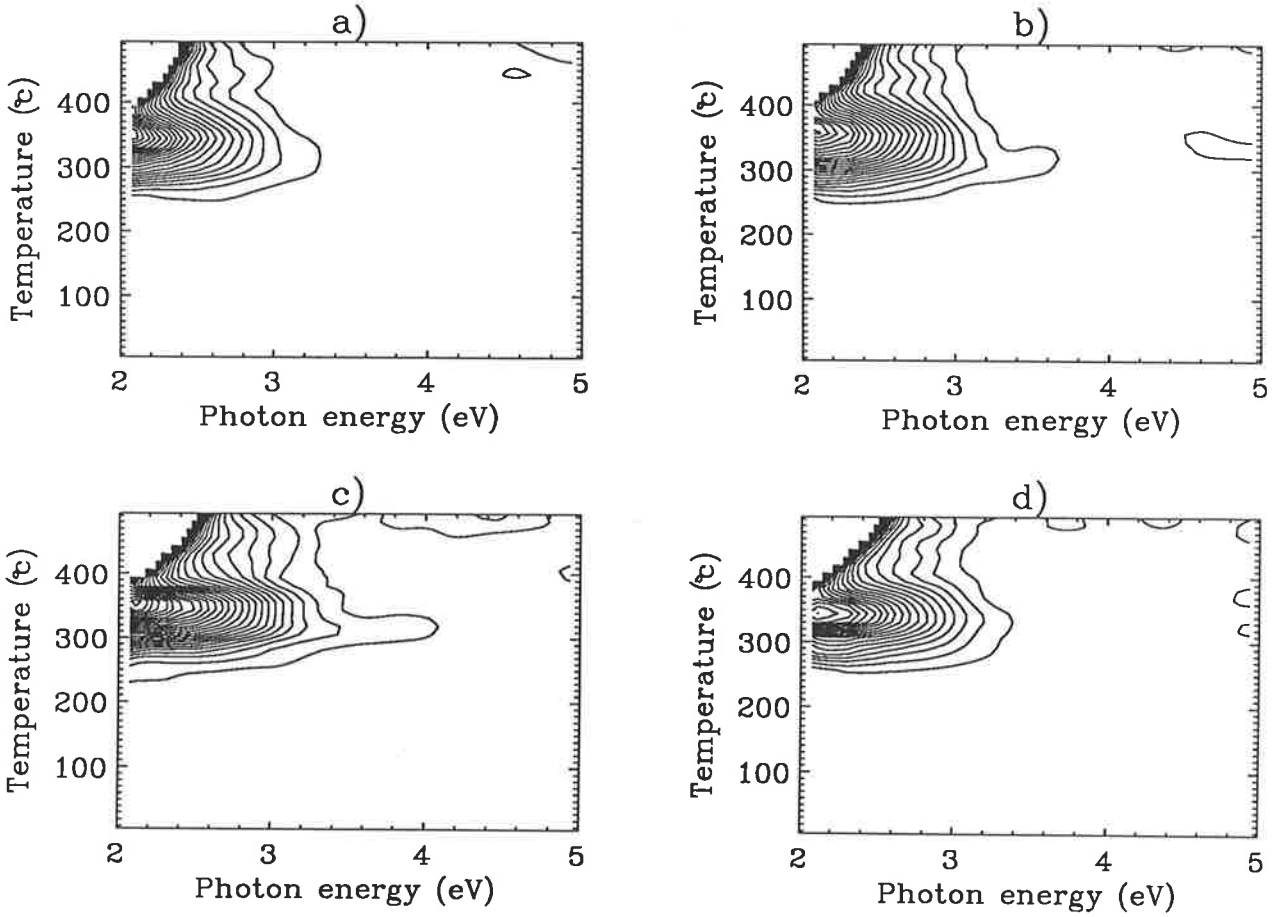

Figure 5.6.1: Contour diagrams of natural LW quartz for a) 0.5, b) 1.0, c) 1.5 and d) 2.0 minutes of bleaching by 350 nm light.

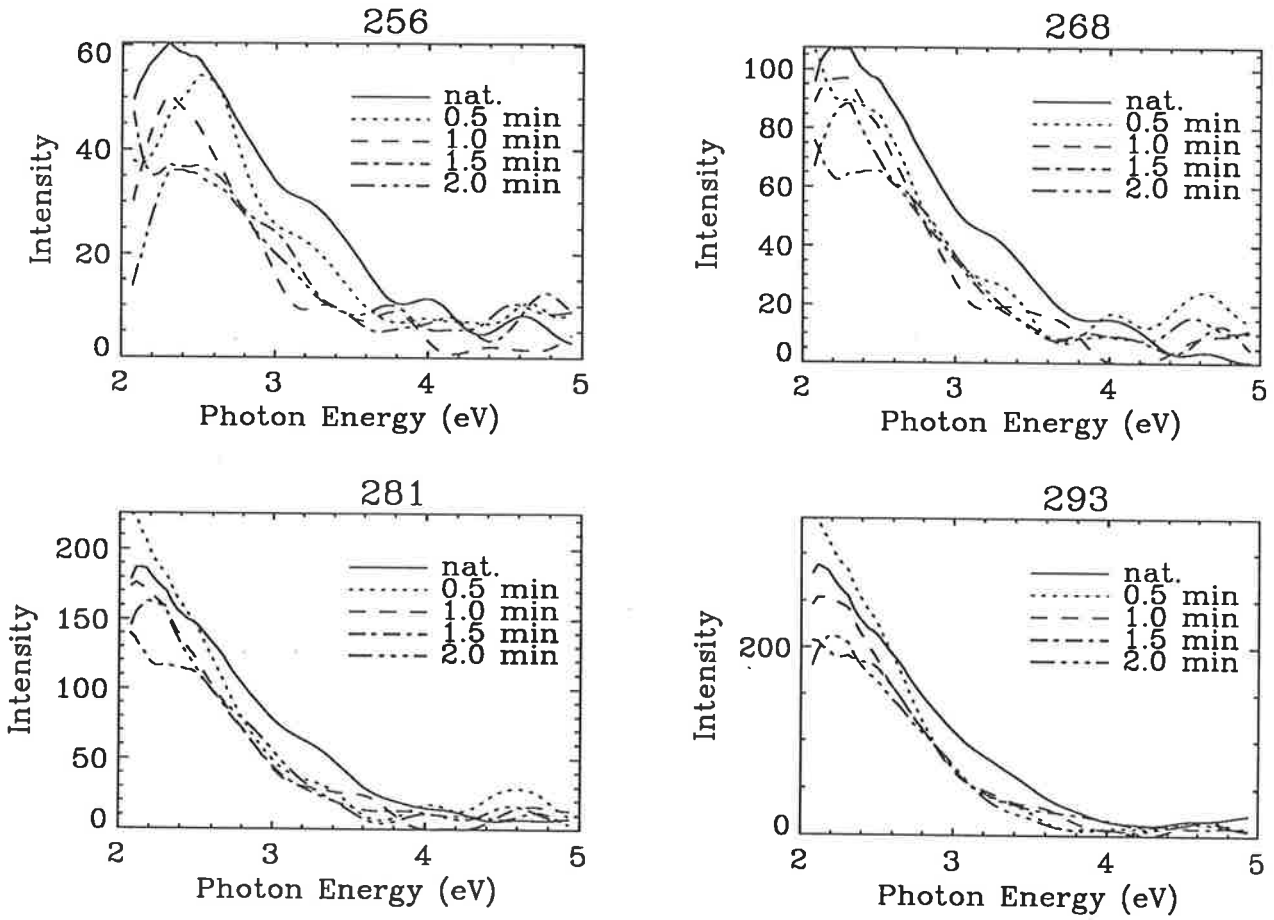

Figure 5.6.2: Individual spectra for natural LW showing the sequence from no bleach to full bleach at temperatures (in Celsius) shown above each plot.

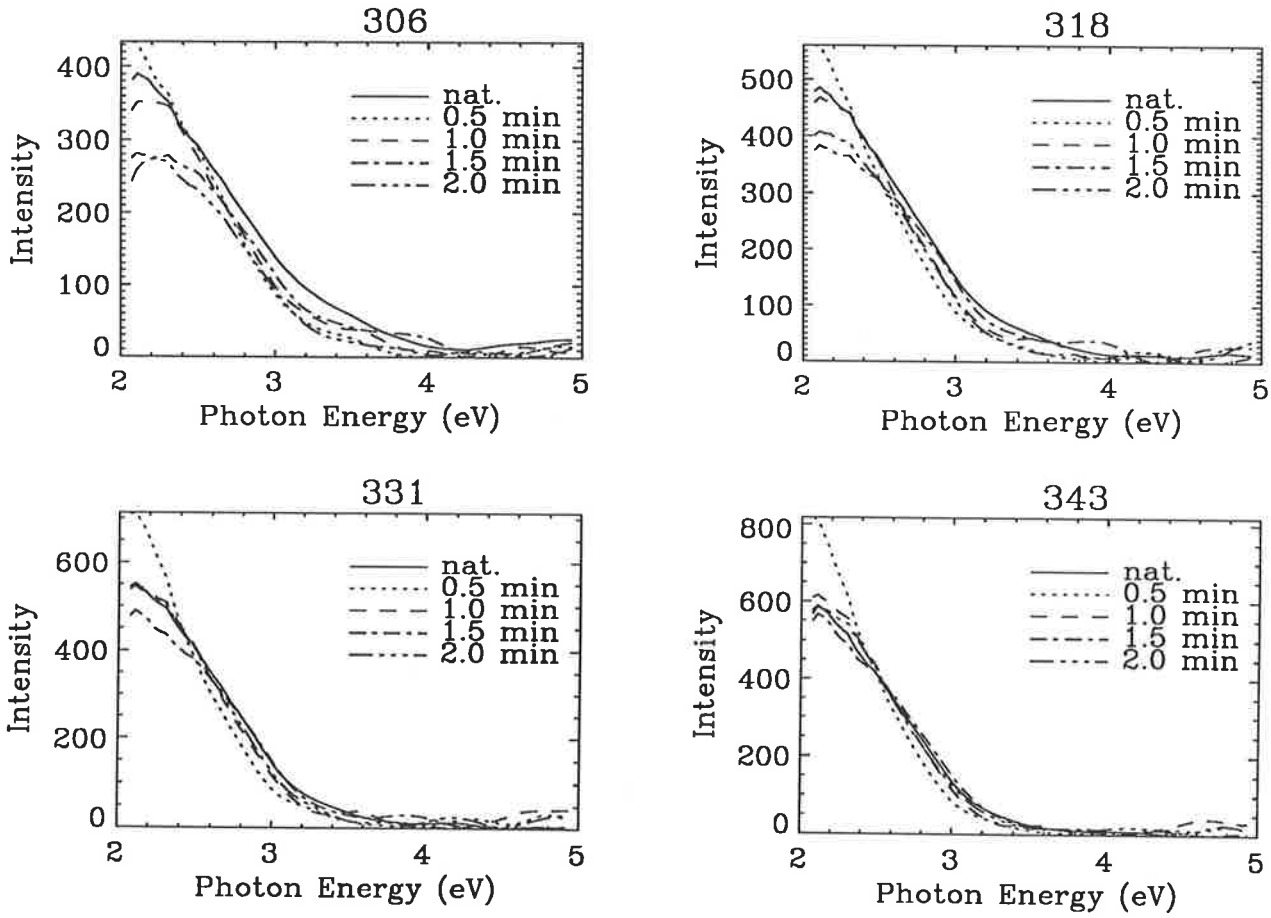

Figure 5.6.3: Individual spectra for natural LW showing the sequence from no bleach to full bleach at temperatures (in Celsius) shown above each plot.

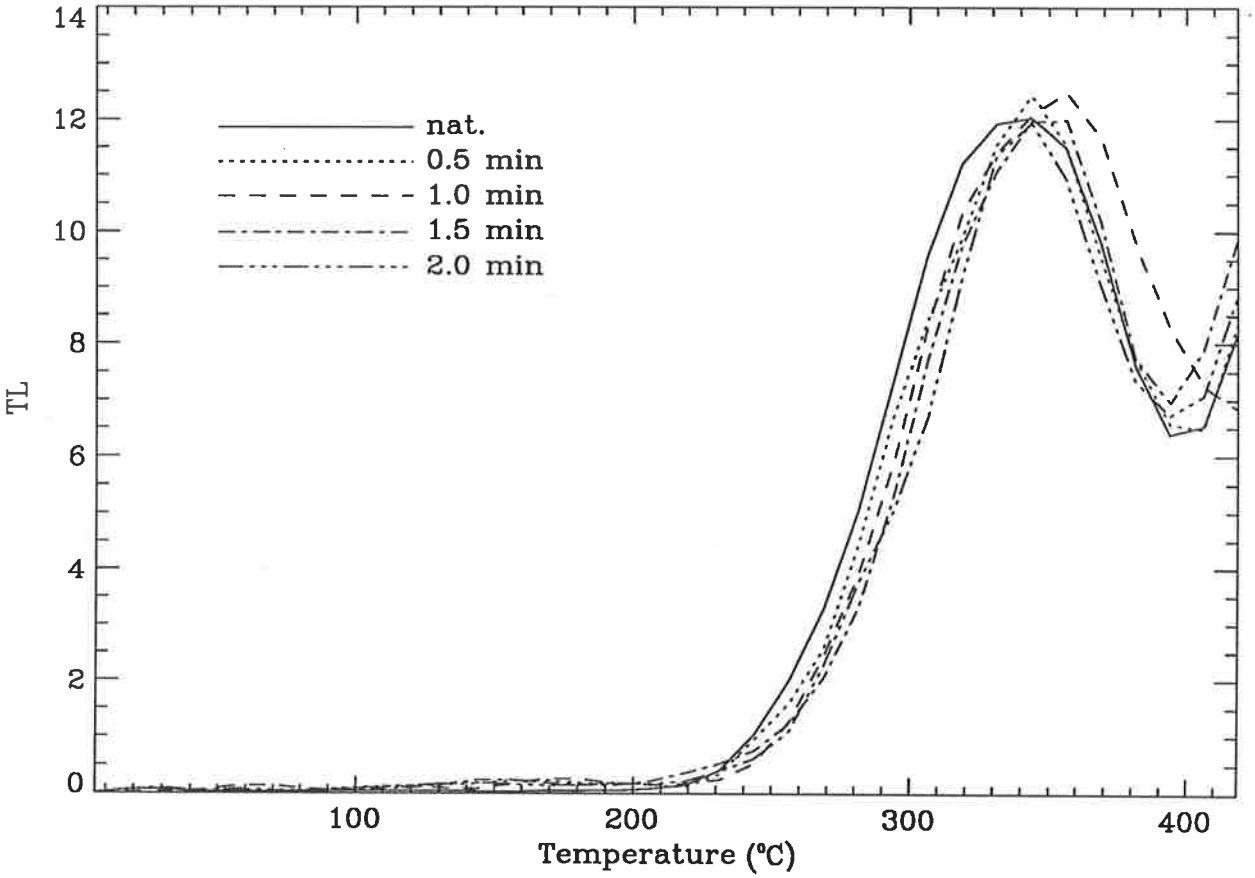

Figure 5.7.1: Full glow curves for the 350 nm bleaching sequence for natural LW.

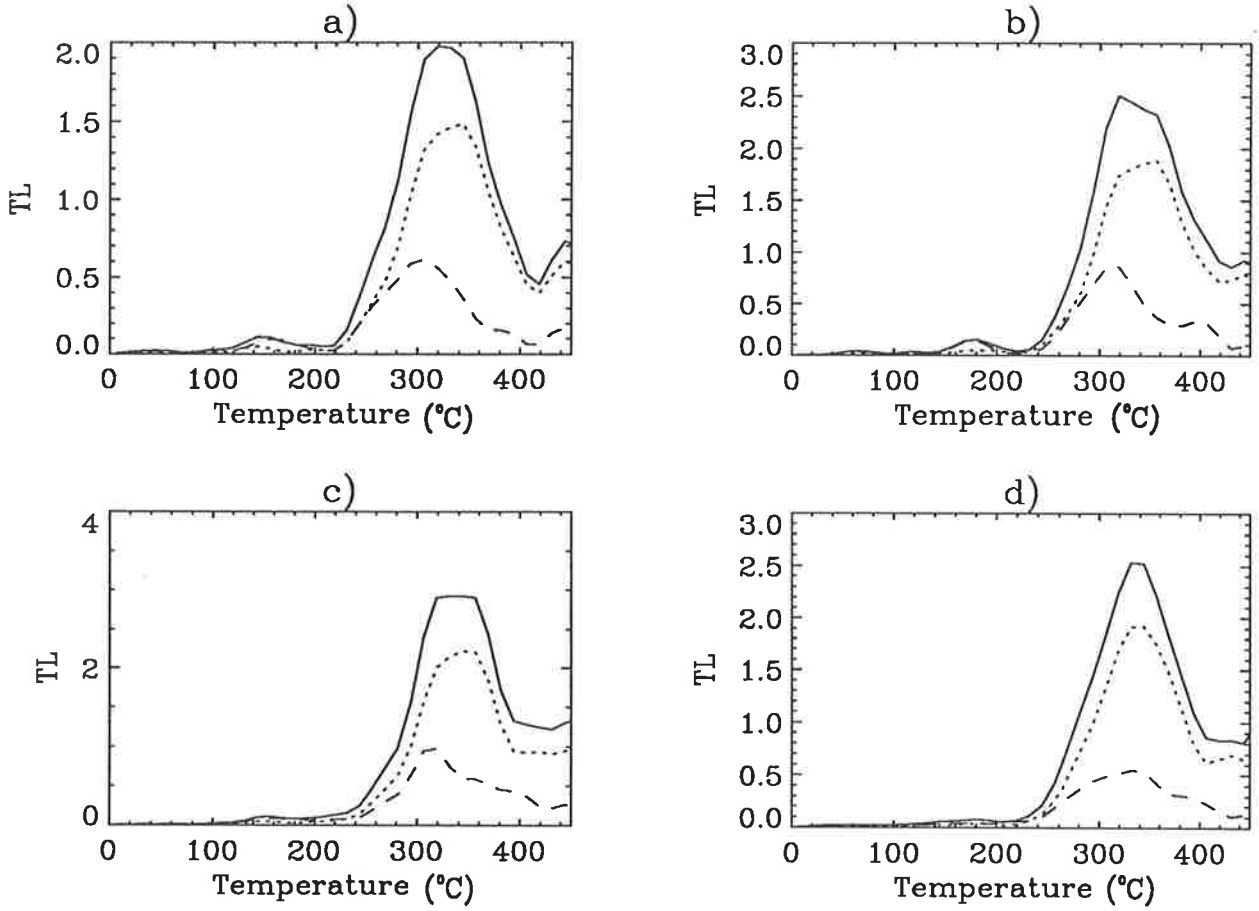

Figure 5.7.2: Glow curves for natural LW obtained by summing through different photon energy regions for a) 0.5, b) 1.0, c) 1.5 and d) 2.0 minutes of bleaching by 350 nm light.

above each plot). Below about 305°C there appears to be a component of the emission spectrum between about 3.0 and 3.6 eV which is preferentially bleached. At the lower photon energies (below about 2.5 eV) it is difficult to say whether the emission spectrum has been affected in a systematic way. Above about 320°C, though, the spectra are all very similar to each other except for the "0.5 min" bleach curve, and so one can say that these spectra were unaffected by the bleach.

Figure 5.7.1 shows the glow curves generated from the above spectra (by summing through the whole spectral range) all plotted together for comparison. The main peak is at about 345°C and there is some suggestion of a systematic decrease in the low temperature side of the curves as the bleach time is increased but the effect is small. Figure 5.7.2 shows the glow curves (as in figure 5.5) for the bleached samples. The relative magnitude of the curve for the high energy region, with respect to the lower energy region, has decreased rapidly to what appears to be a constant value and there is less distinction between the 305 and 345°C peaks. However there is still evidence of a distinct peak or component at about 300°C which appears to be unaffected by the bleaching.

Bleaching by 550 nm Light

Figure 5.8.1, 5.8.2 and 5.8.3 show the contour diagrams and individual spectral sequences for bleach times of 2, 4, 6 and 8 minutes of 550 nm light (corresponding to 340, 680, 1020 and 1360 mJ cm^{-2} respectively).

As for the 350 nm bleach, the sequence of contour diagrams show a rapid initial bleach of the high energy emission down to a less sensitive remnant. The individual

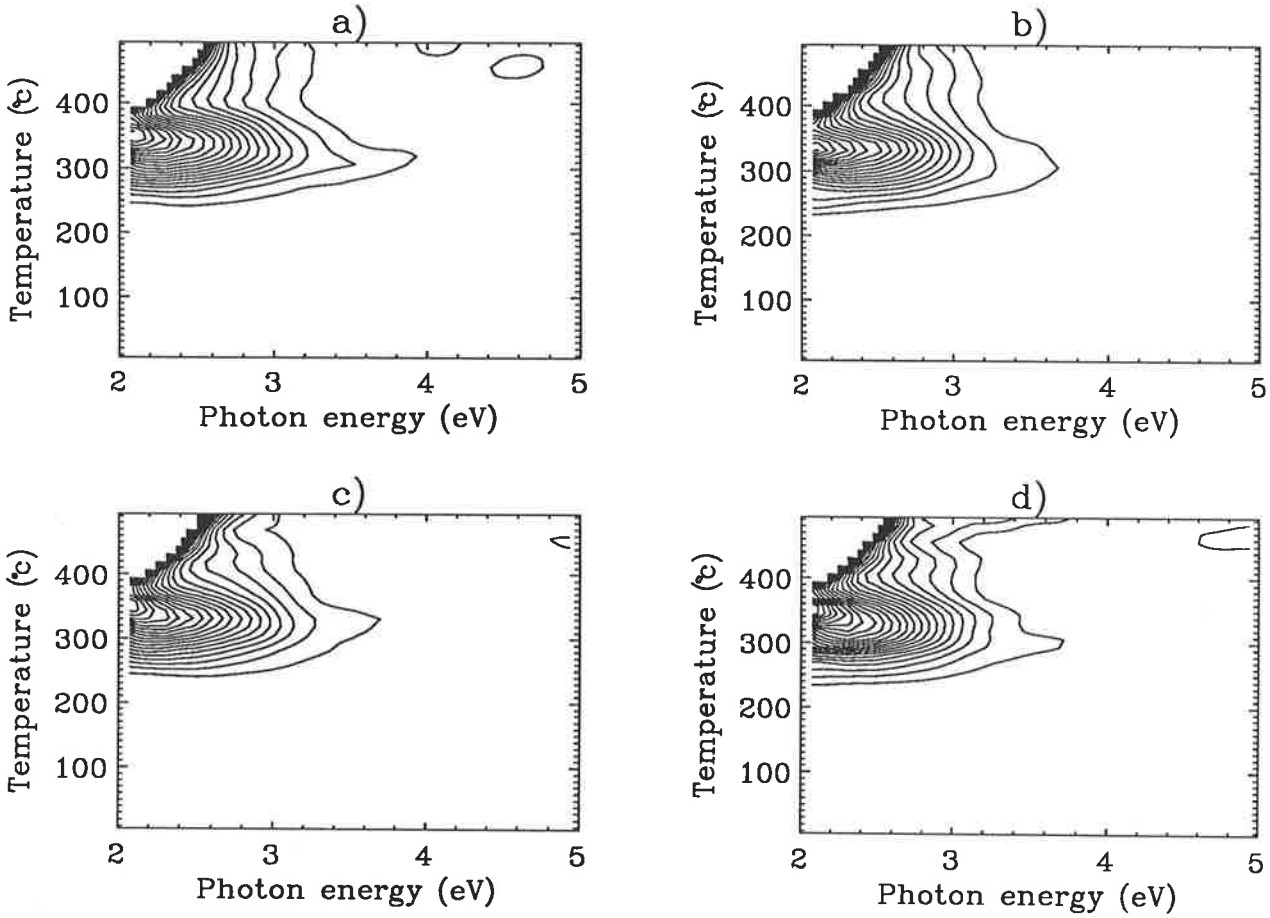

Figure 5.8.1: Contour diagrams of natural LW quartz for a) 2, b) 4, c) 6 and d) 8 minutes of bleaching by 550 nm light.

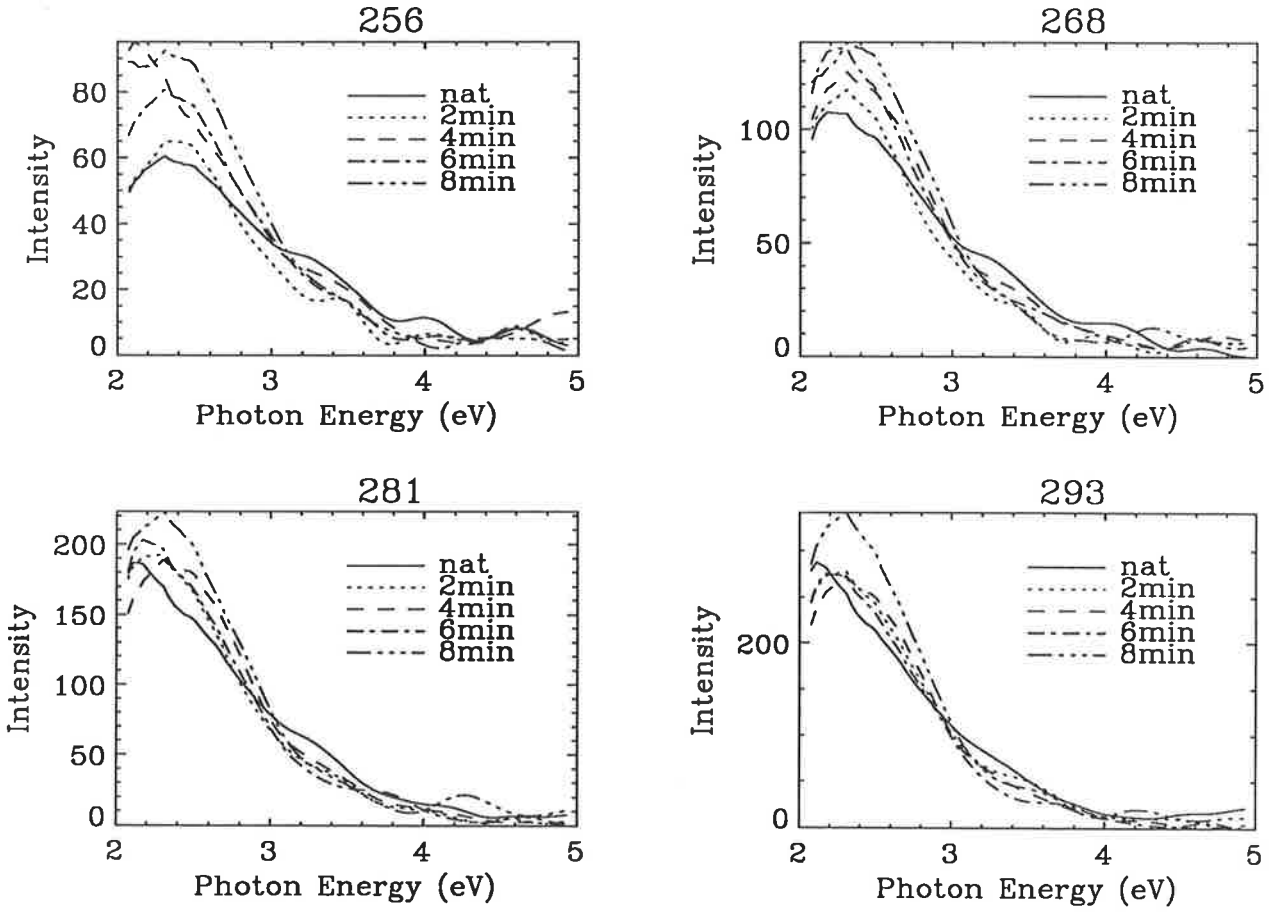

Figure 5.8.2: Individual spectra for natural LW showing the sequence from no bleach to full 550 nm bleach at temperatures (in Celsius) shown above each plot.

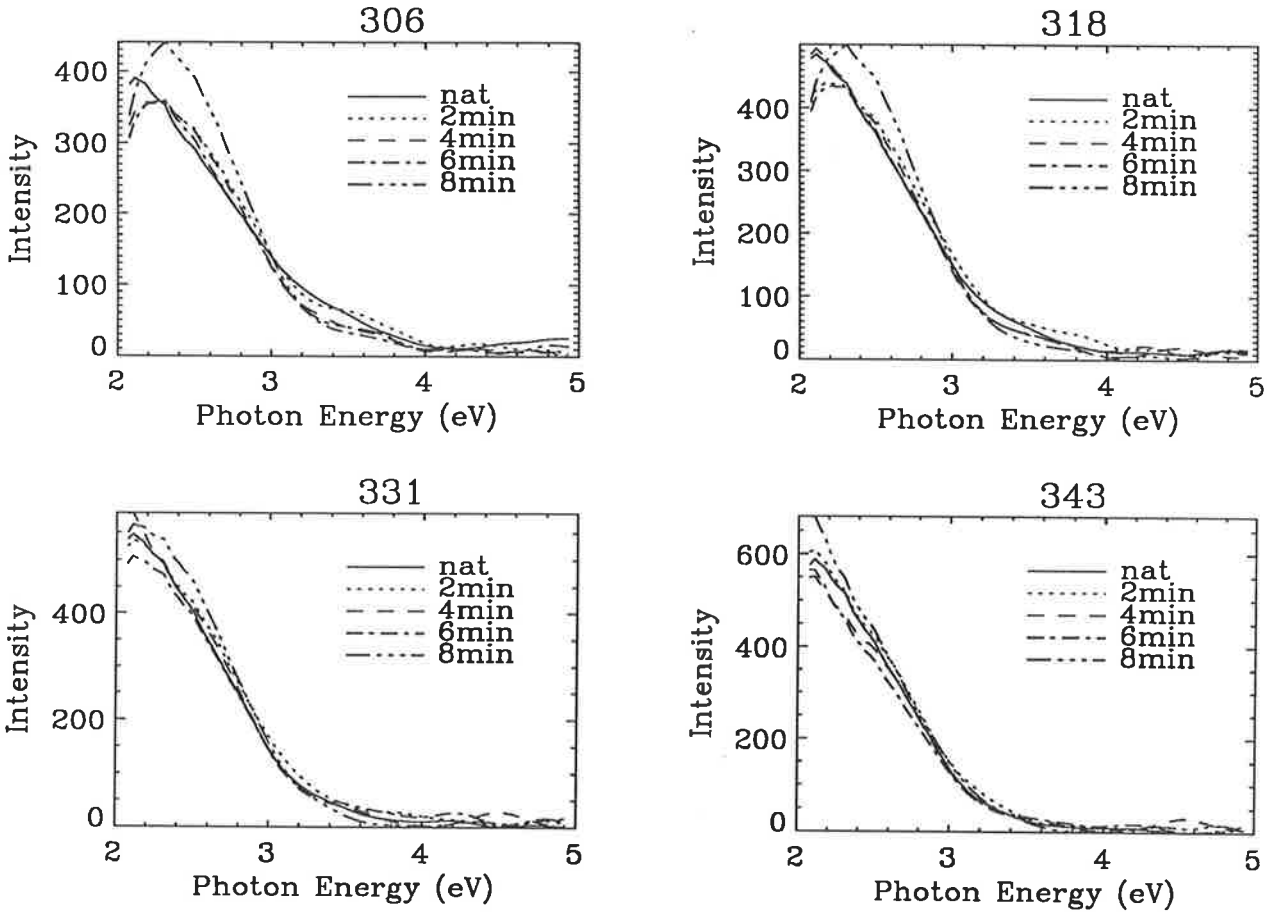

Figure 5.8.3: Individual spectra for natural LW showing the sequence from no bleach to full 550 nm bleach at temperatures (in Celsius) shown above each plot.

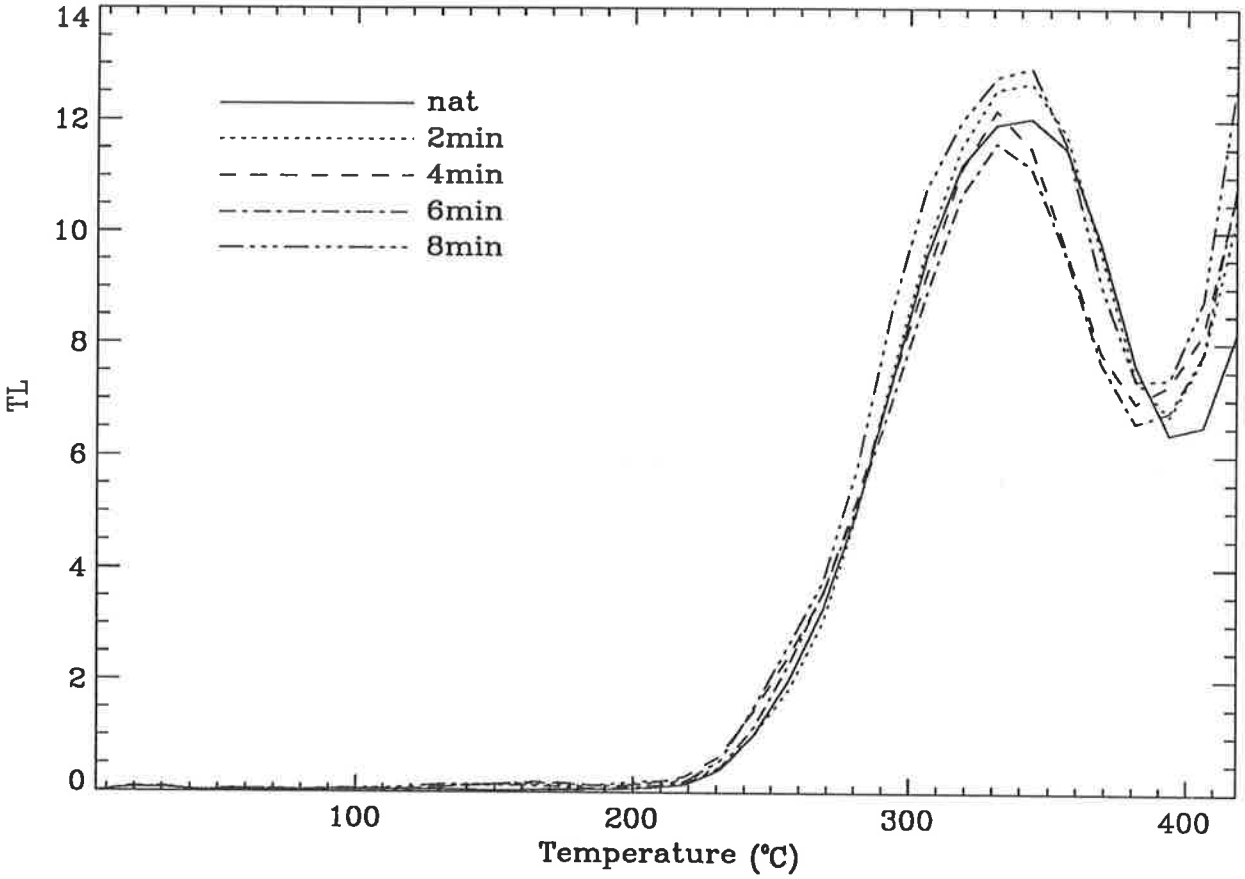

Figure 5.9.1: Full glow curves for the 550 nm bleaching sequence for natural LW.

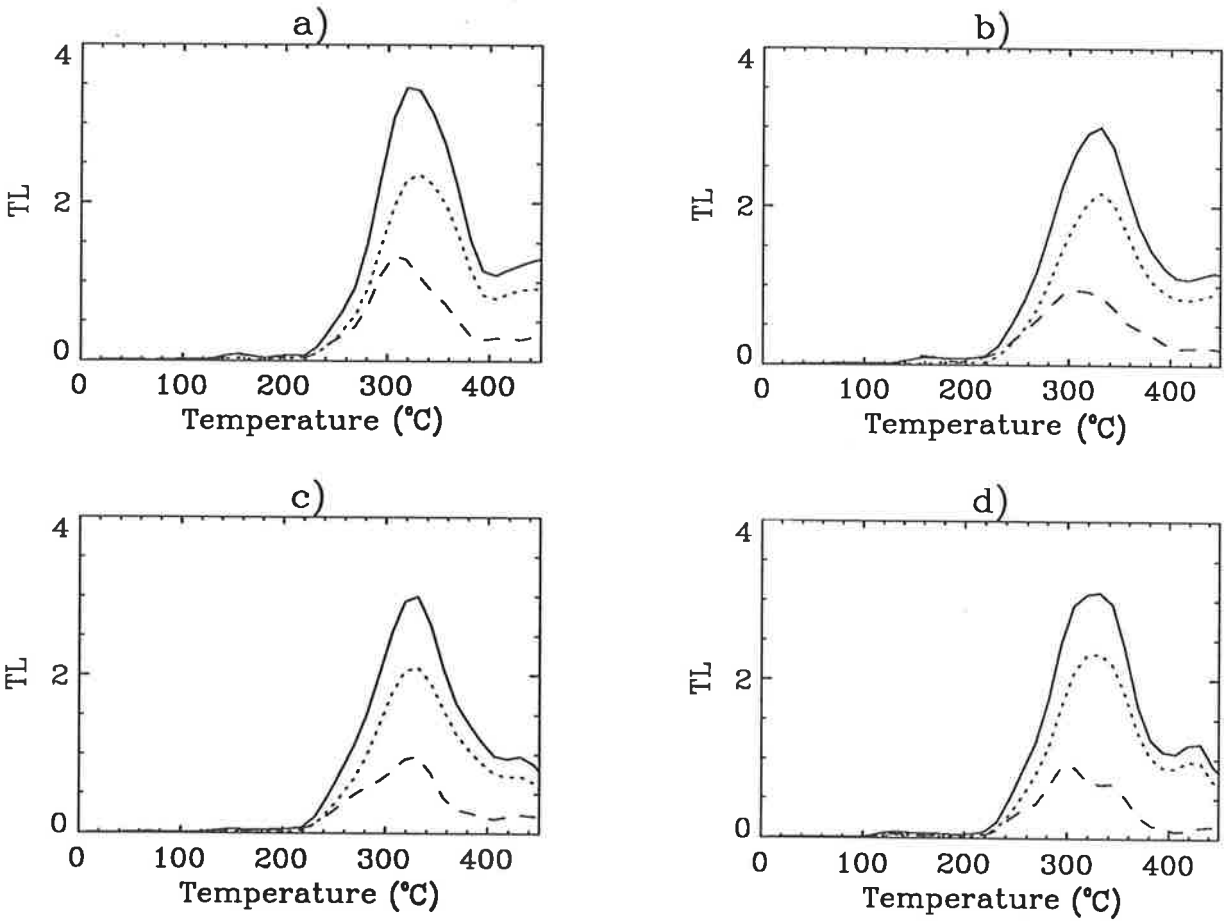

Figure 5.9.2: Glow curves for natural LW obtained by summing through different photon energy regions for a) 2, b) 4, c) 6 and d) 8 minutes of bleaching by 550 nm light.

spectra of figures 5.8.2 and 5.8.3 show this component to be between about 3.0 and 3.5 eV as before, also the higher temperature spectra are unaffected by the bleach.

Figure 5.9.1 shows the glow curves for this sequence and there is no significant difference between them. Figure 5.9.2 shows the individual glow curves and their components. The effect of the 550 nm bleach appears to be very similar to that of the 350 nm bleach and these glow curves do not differ significantly from those of figure 5.7.2.

Bleaching by 650 nm Light

Figures 5.10 and 5.11 are the equivalent diagrams to those above for the bleach sequence of 20, 40, 60 and 80 minutes of 650 nm light. These times correspond to 3, 6, 9 and 12 J cm^{-2} respectively.

The bleaching does not appear to have been quite so rapid using the 650 nm light as for the other wavelengths. This shows up in figures 5.10.1, 5.10.2 and 5.10.3. In figure 5.10.1 there is still evidence of the high energy component even after the longest bleach time although from figures 5.10.2 and 5.10.3 it still appears as though the same component as above is being removed

Once again there is very little difference between the glow curves (figure 5.11.1) that could not be explained by the sample to sample scatter inherent in any quartz. The glow curve component curves in figure 5.11.2 would seem to support the observation of the greater persistence of the high photon energy component during bleaching. The high photon energy curves are more prominent than for either the 350 or 550 nm bleaches.

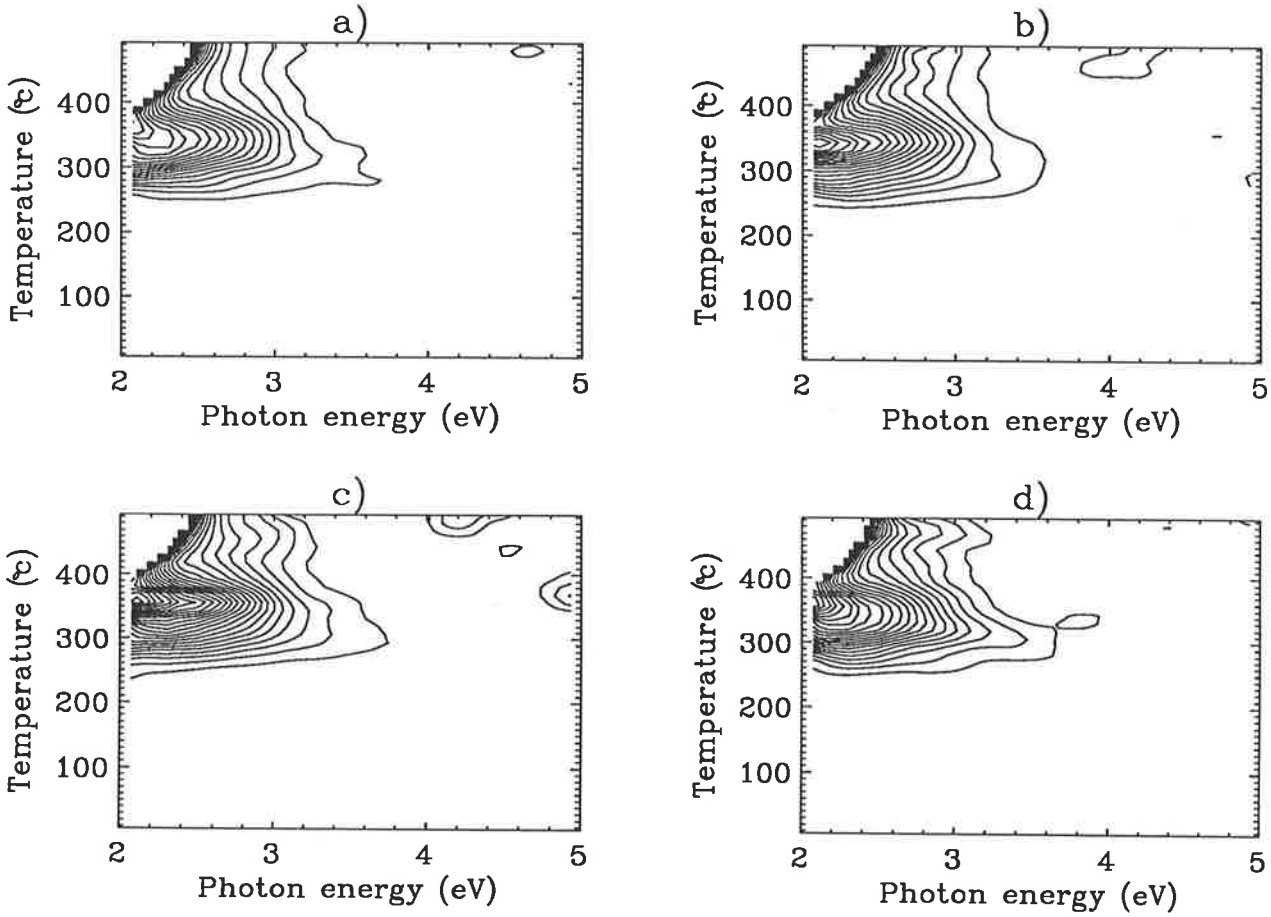

Figure 5.10.1: Contour diagrams of natural LW quartz for a) 20, b) 40, c) 60 and d) 80 minutes of bleaching by 650 nm light.

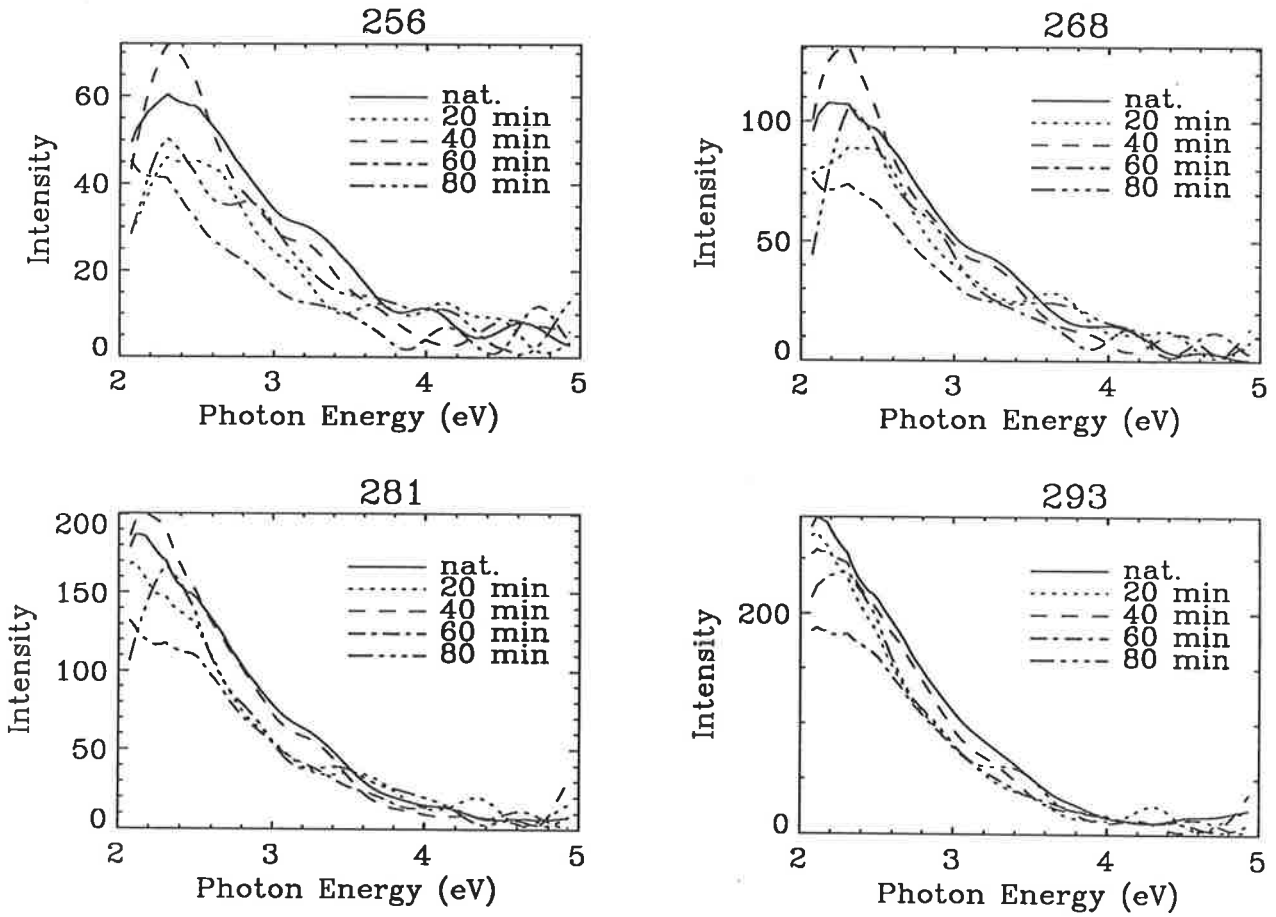

Figure 5.10.2: Individual spectra for natural LW showing the sequence from no bleach to full 650 nm bleach at temperatures (in Celsius) shown above each plot.

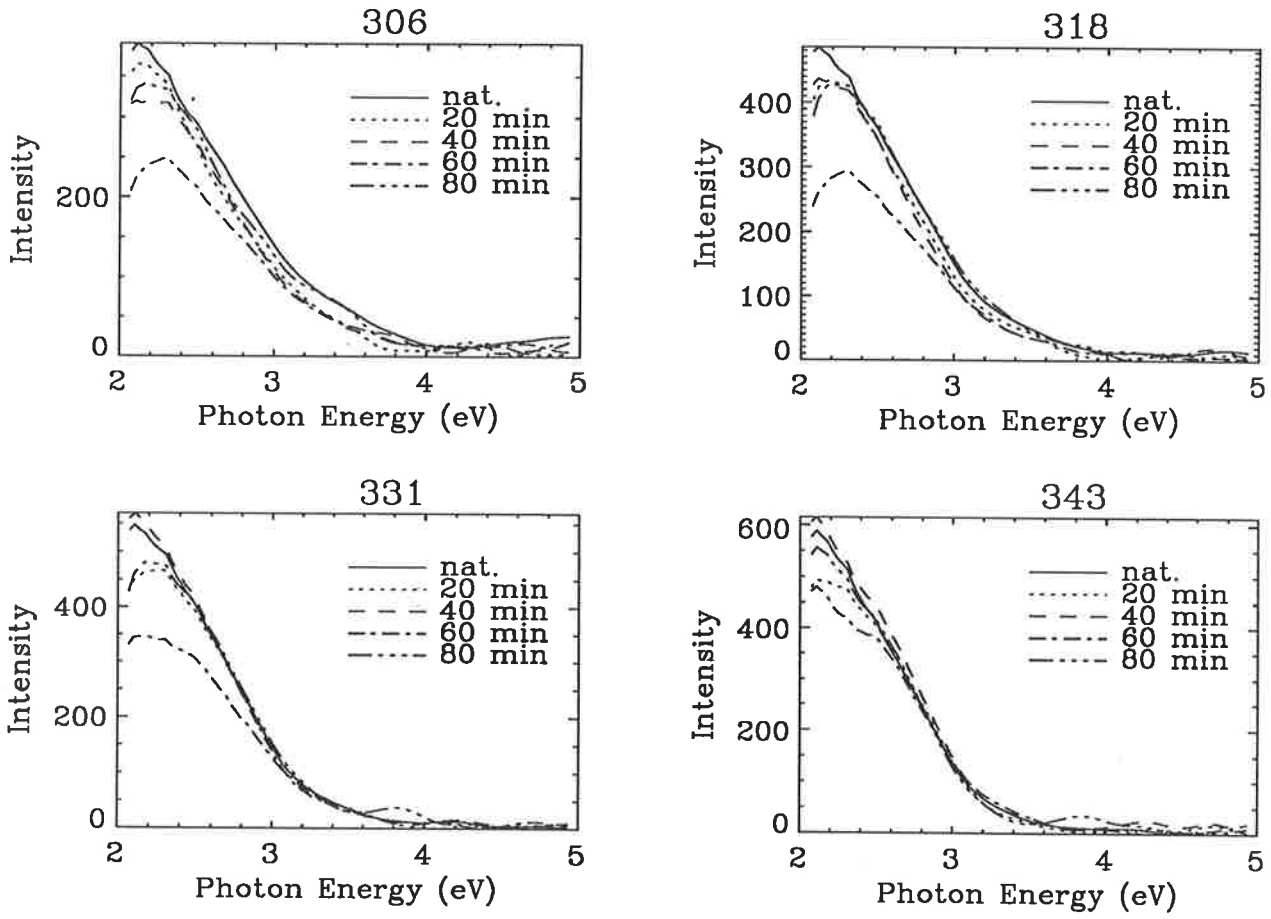

Figure 5.10.3: Individual spectra for natural LW showing the sequence from no bleach to full 650 nm bleach at temperatures (in Celsius) shown above each plot.

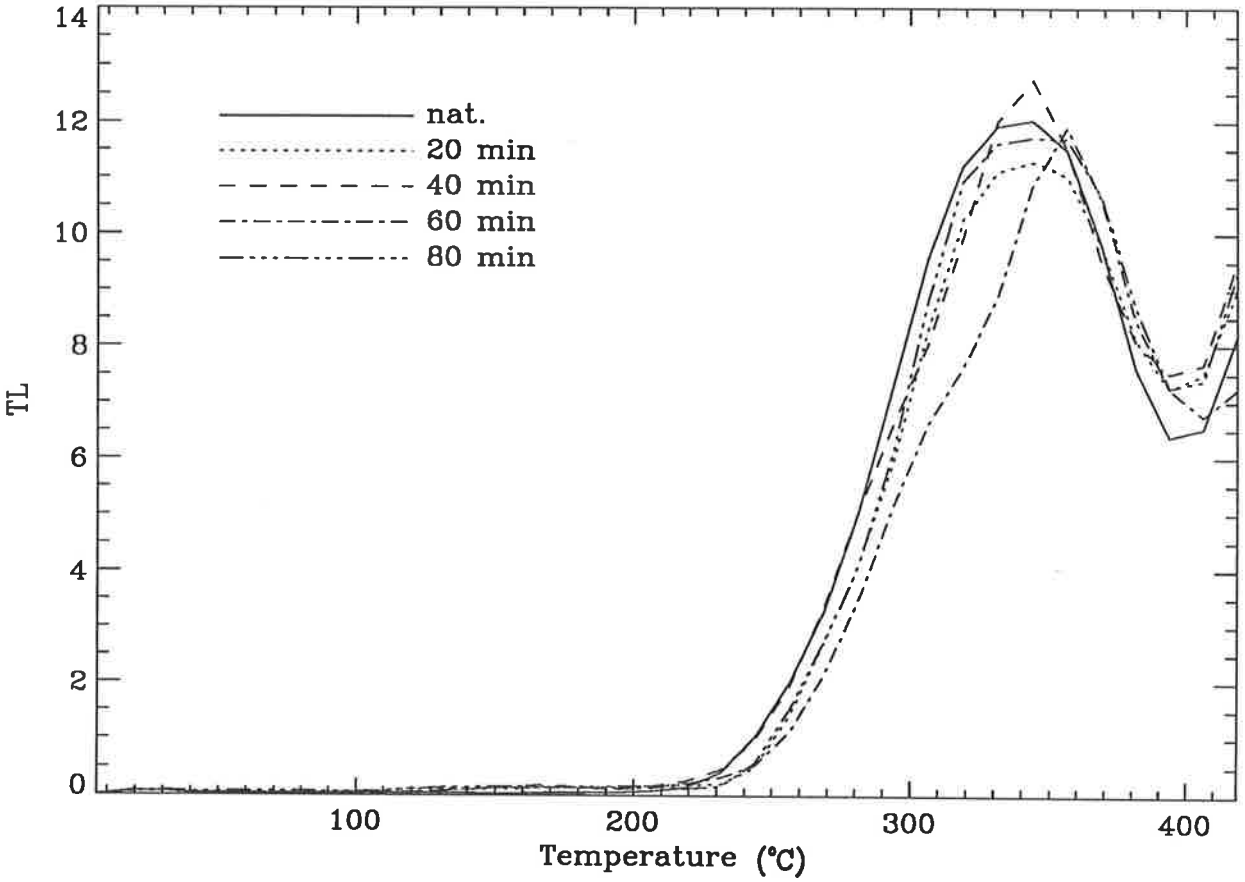

Figure 5.11.1: Full glow curves for the 650 nm bleaching sequence for natural LW.

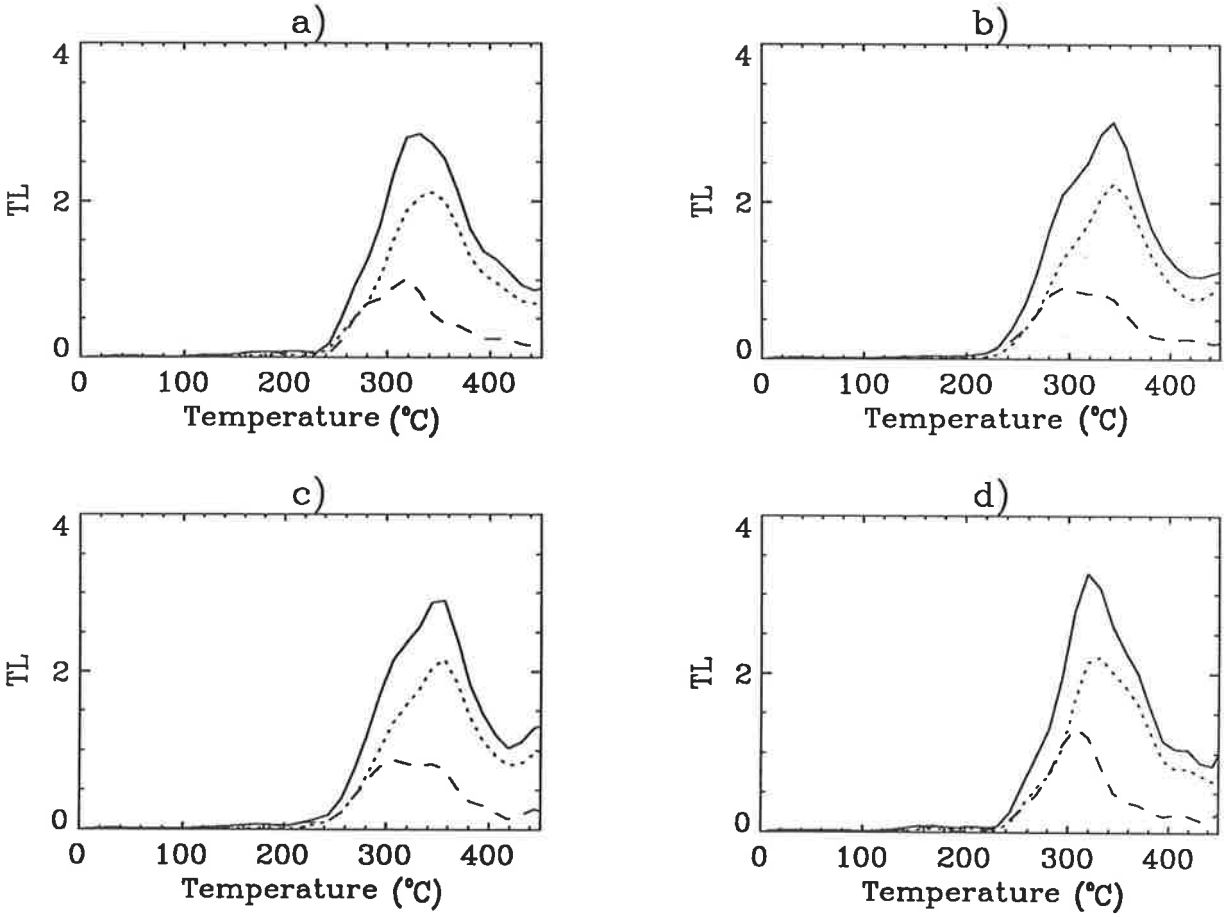

Figure 5.11.2: Glow curves for natural LW obtained by summing through different photon energy regions for a) 20, b) 40, c) 60 and d) 80 minutes of bleaching by 650 nm light.

5.4.2 Irradiated LW Quartz

Figures 5.12 and 5.13 are the contour and glow curve component diagrams for LW that had received a dose of about 41 Gy after being heated to about 500°C.

At temperatures above about 250°C the features are essentially the same as for natural LW. The high energy emission region near to 300°C has been regenerated along with the lower energy emission at about 350°C. This high energy component seems to be slightly more prominent than for the natural LW case (conceivably this component may be subject to pre–dosing). In addition there are now peaks at about 150 and 180°C, both with peak emission at about 3.3 eV (375 nm) and which extends down to below about 2.4 eV (520 nm). Figure 5.13 shows the glow curve components which show essentially these same features. At the lower temperatures the higher energy emission is proportionally greater than the low energy region in contrast to the case at the higher temperatures.

Bleaching by 350 nm Light

Figures 5.14 and 5.15 are the equivalent diagrams as for the natural LW case. The contour diagrams and individual spectra of figures 5.14 once more show the rapid bleaching of the 3.0–3.5 eV emission component whose increased prominence is clearly visible in figure 5.14.1. This bleaching is confined to temperatures below about 310°C

Figures 5.15.1 and 5.15.2 show that of all the peaks present it is predominantly the 300°C peak that has bleached by any significant amount. This is demonstrated clearly in figure 5.15.2. The peaks below 250°C are unaffected by this degree of 350 nm bleaching.

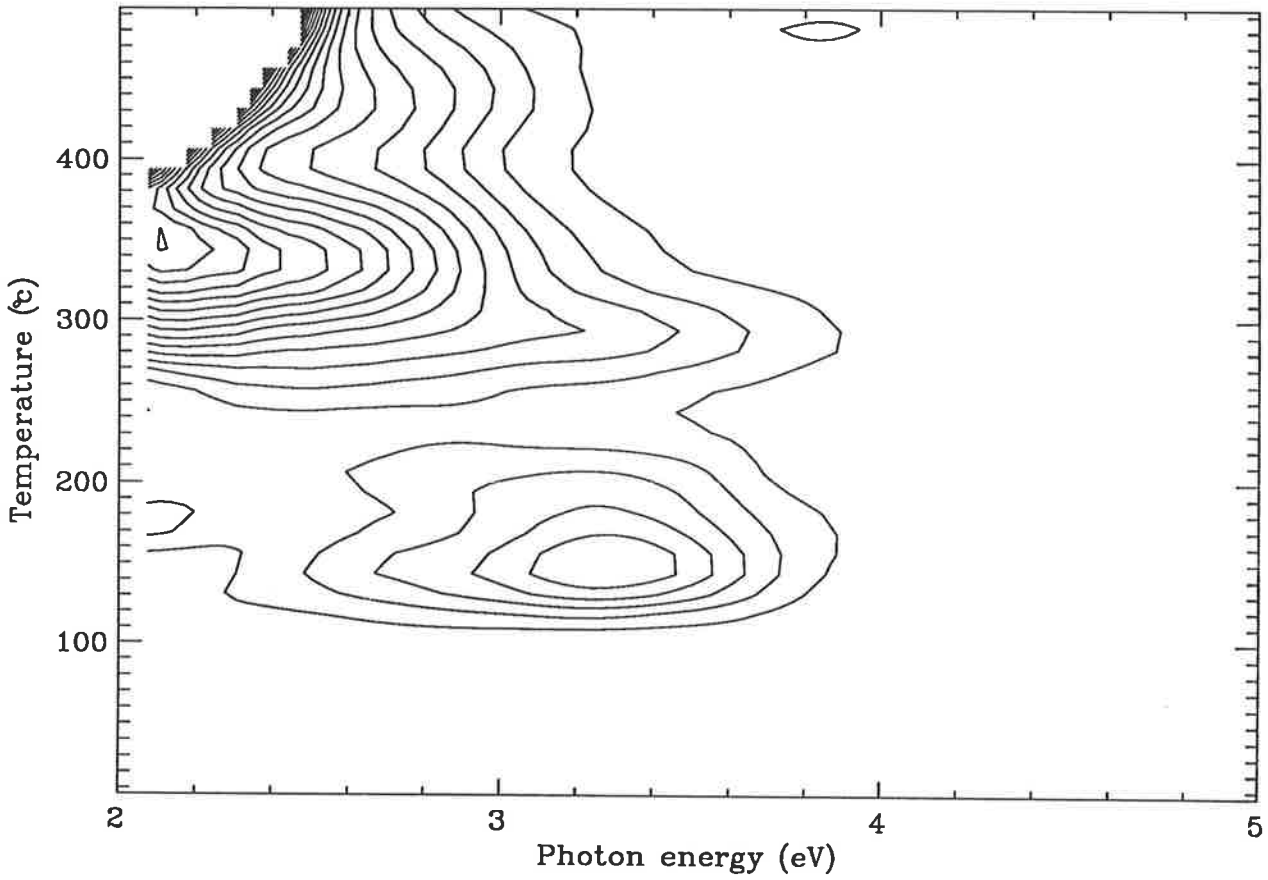

Figure 5.12: Contour diagram of irradiated LW quartz.

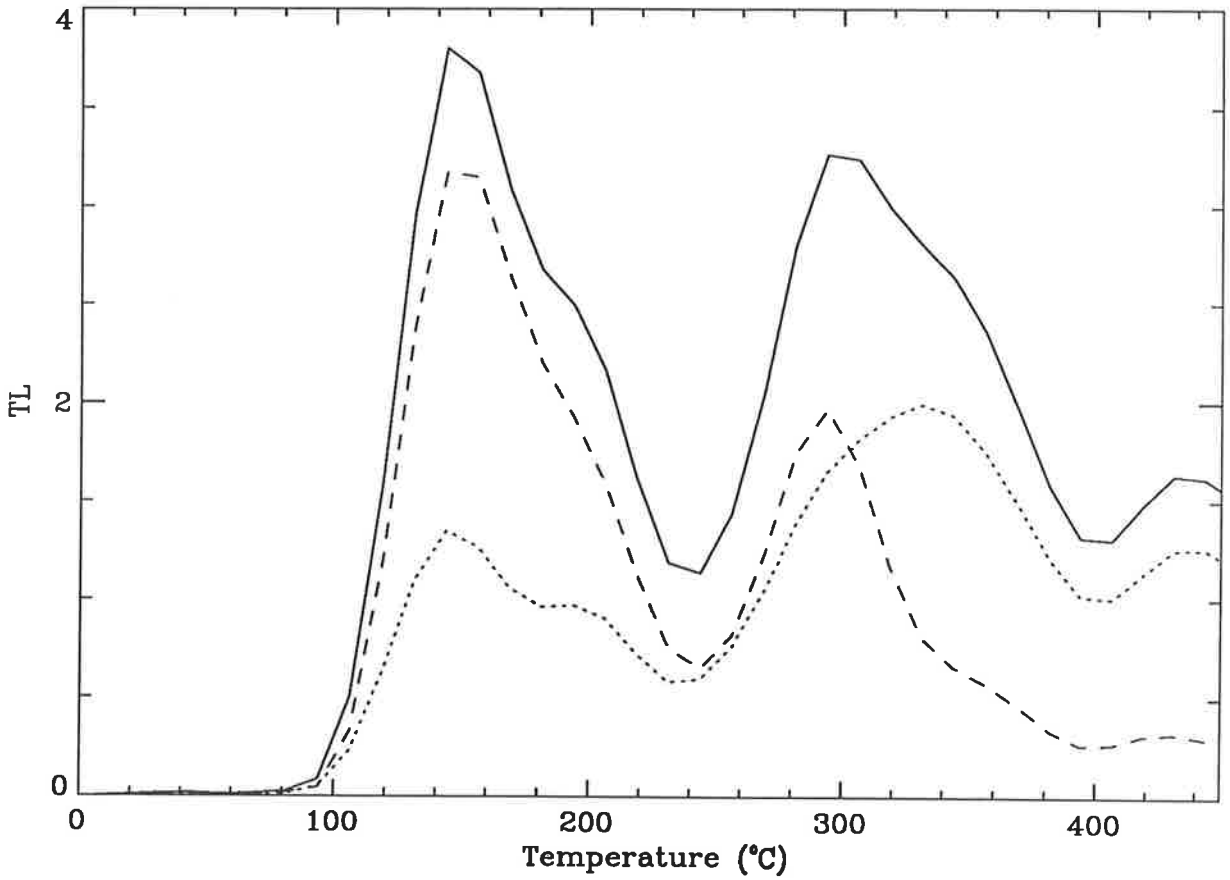

Figure 5.13: Glow curves obtained by summing through different photon energy regions (shown in figure 5.5) for irradiated LW.

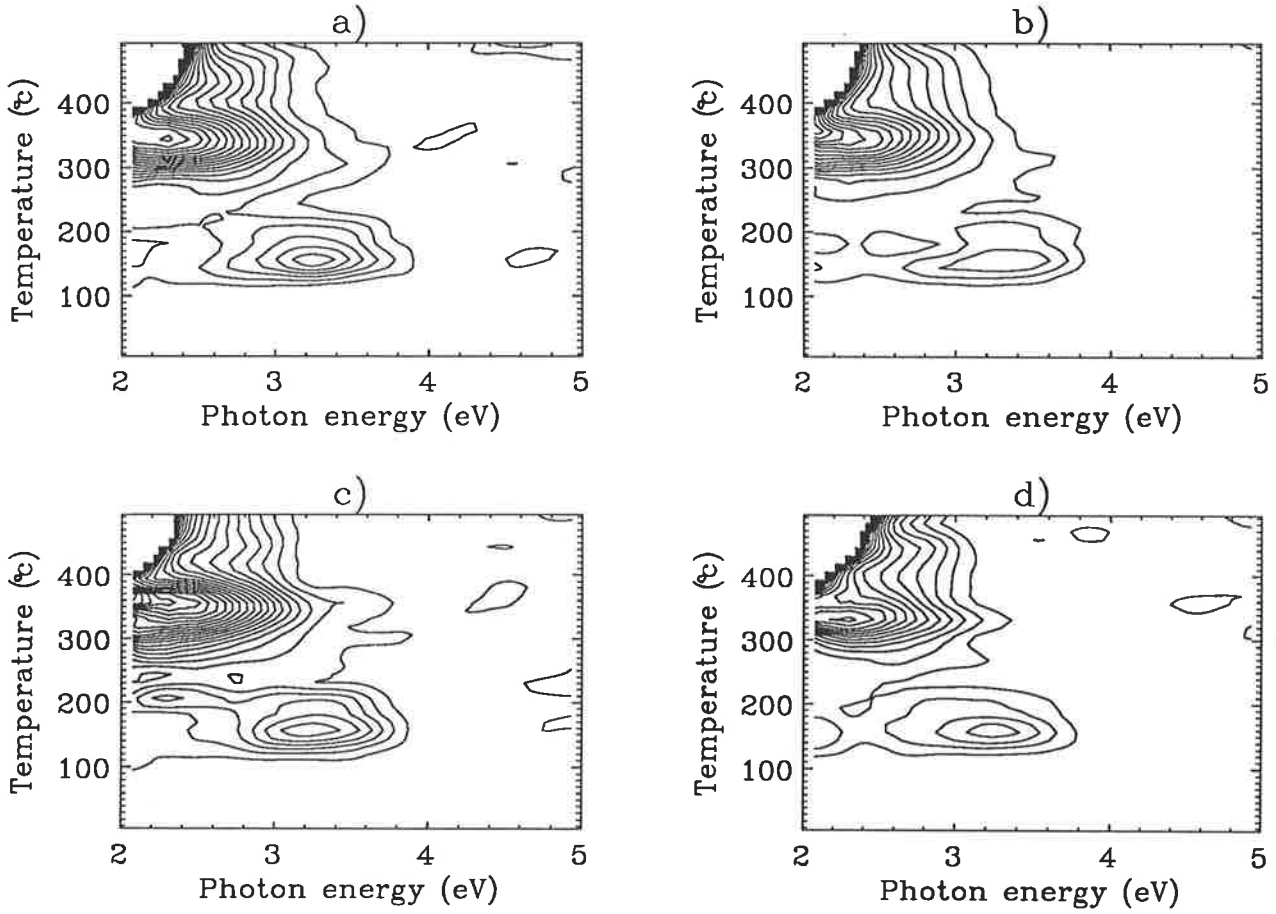

Figure 5.14.1: Contour diagrams of irradiated LW quartz for a) 0.5, b) 1.0, c) 1.5 and d) 2.0 minutes of bleaching by 350 nm light.

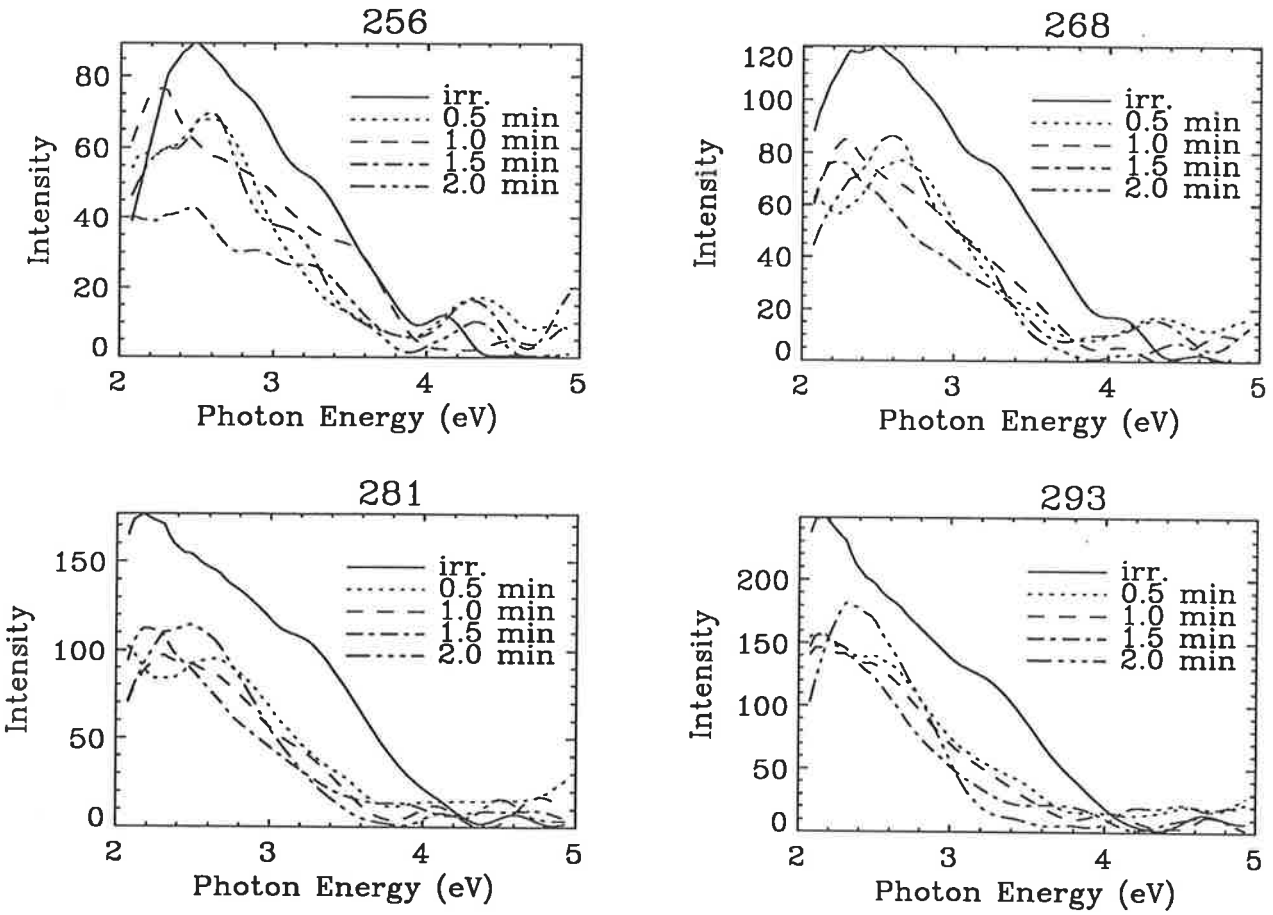

Figure 5.14.2: Individual spectra for irradiated LW showing the sequence from no bleach to full bleach at temperatures (in Celsius) shown above each plot.

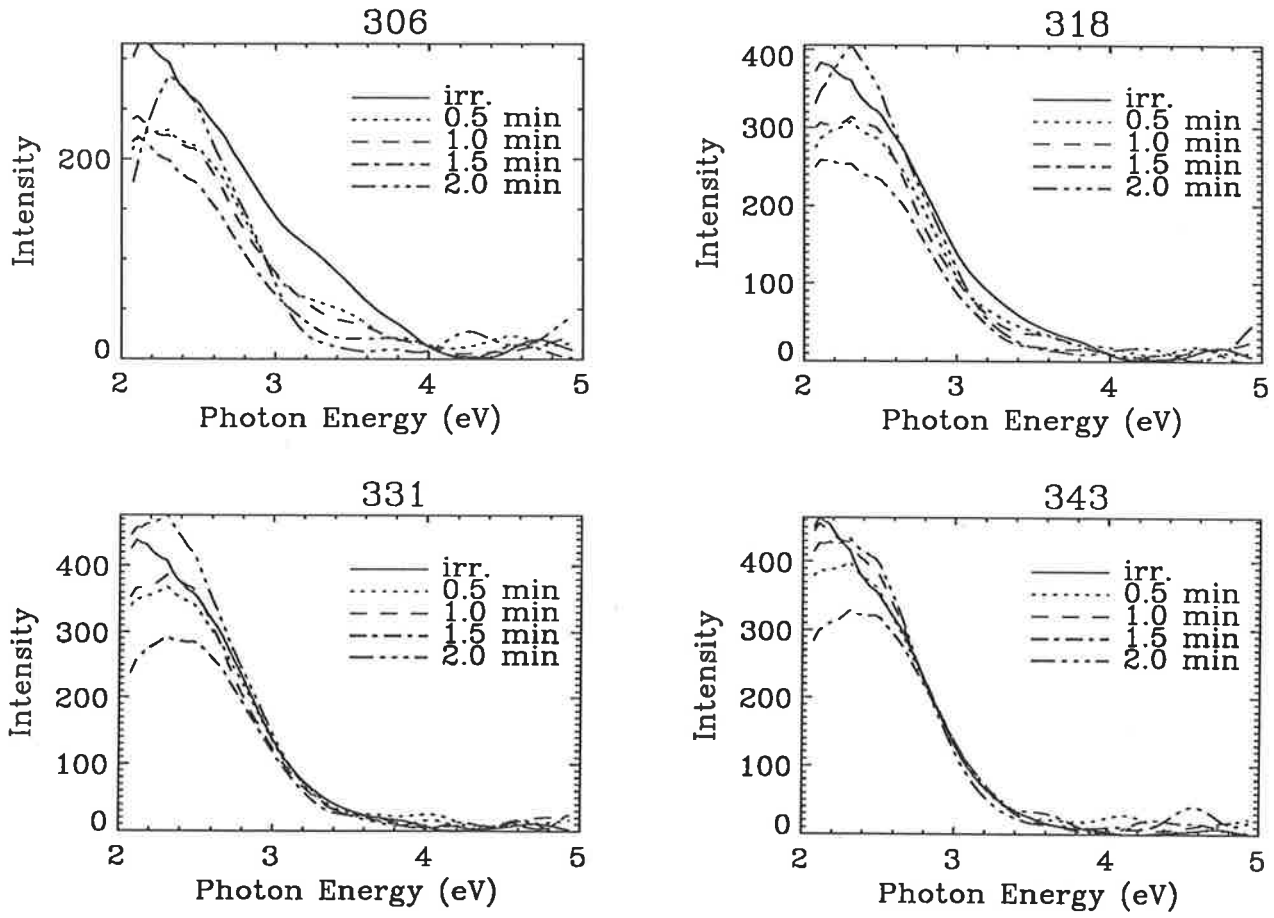

Figure 5.14.3: Individual spectra for irradiated LW showing the sequence from no bleach to full bleach at temperatures (in Celsius) shown above each plot.

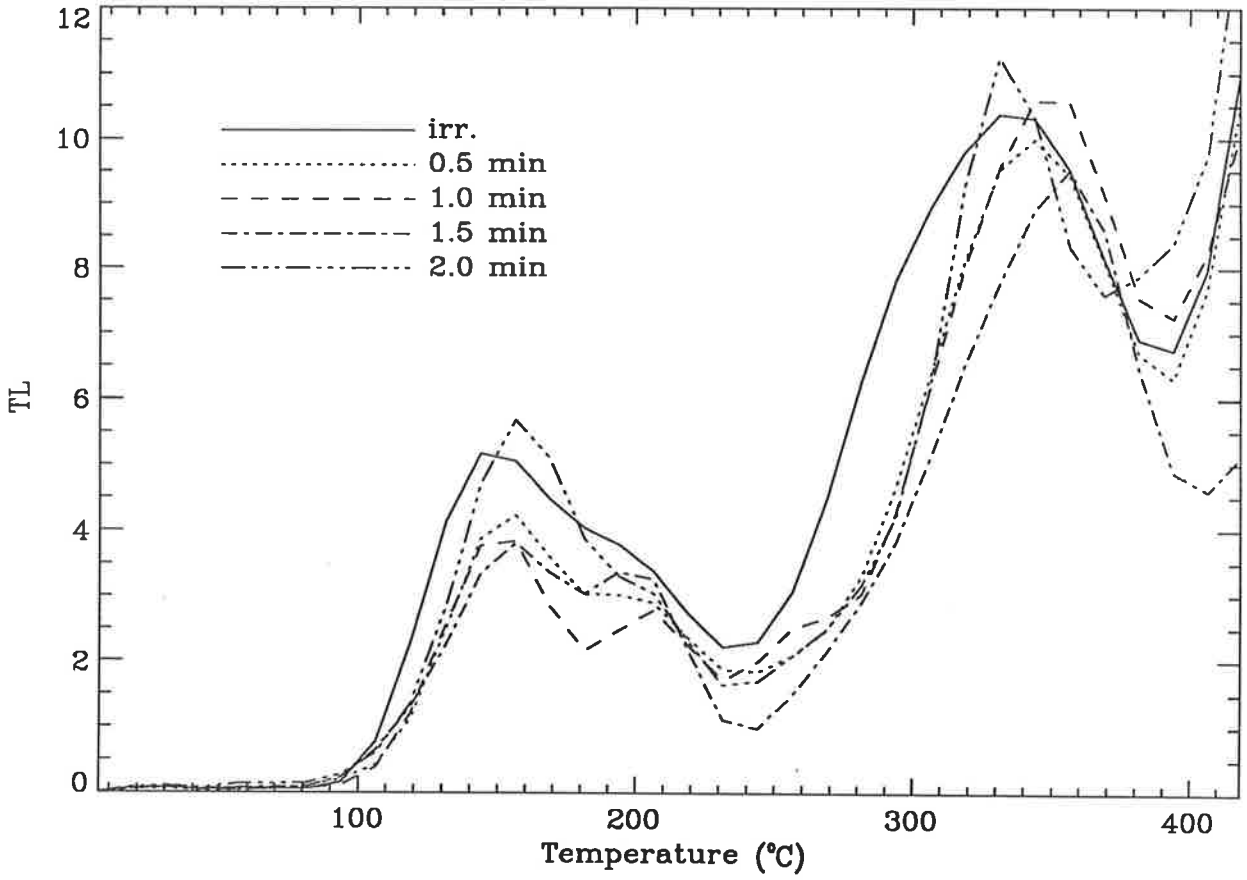

Figure 5.15.1: Full glow curves for the 350 nm bleaching sequence for irradiated LW.

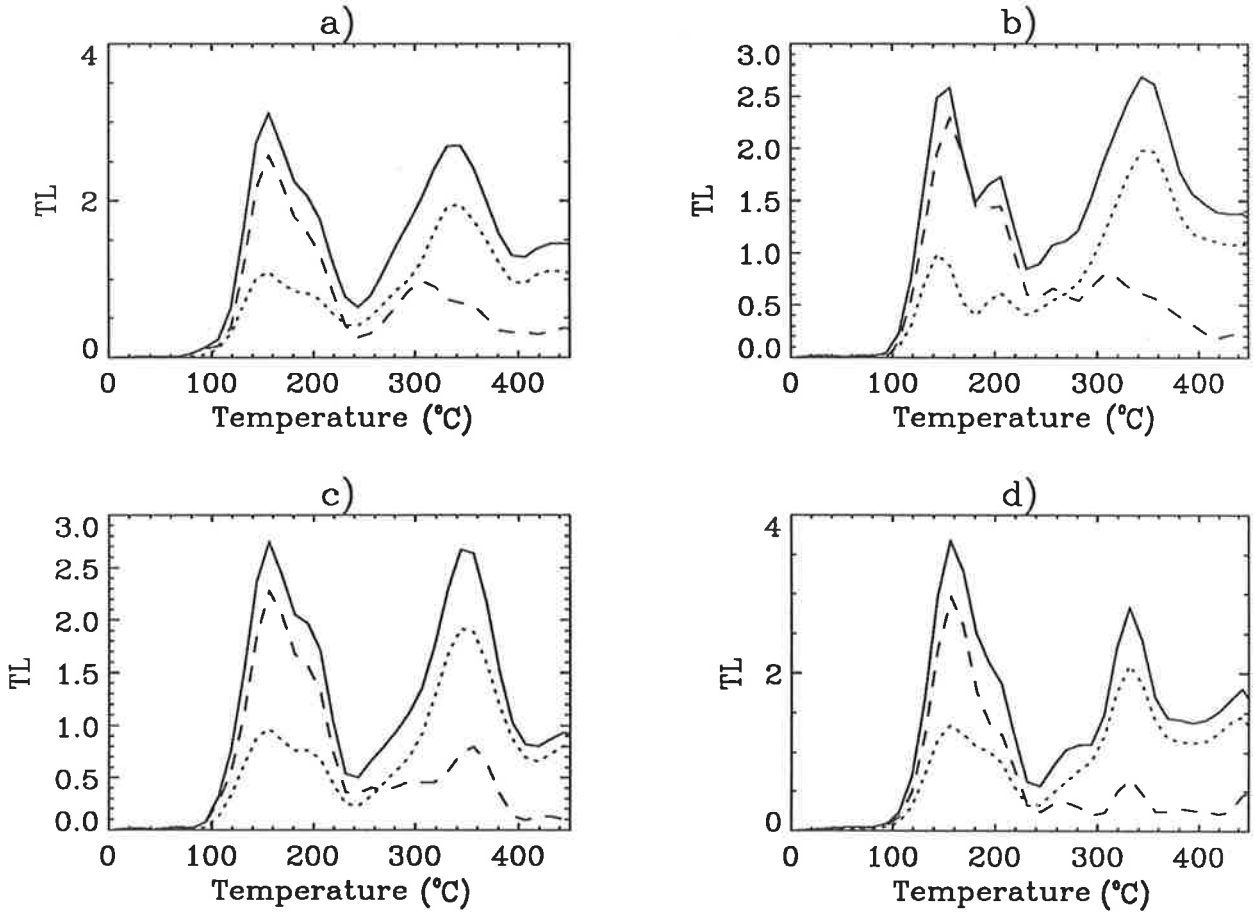

Figure 5.15.2: Glow curves for irradiated LW obtained by summing through different photon energy regions (shown in figure 5.5) for a) 0.5, b) 1.0, c) 1.5 and d) 2.0 minutes of bleaching by 350 nm light.

Bleaching by 550 nm Light

The data in figures 5.16 and 5.17 show essentially that the 550 nm bleaching has had the same effect as for 350 nm bleaching and confirm (especially in figures 5.16.2 and 5.17.2) that it is only the high energy components at 300°C which are affected by the bleach.

Bleaching by 650 nm Light

The data are shown in figures 5.18 and 5.19. For this bleaching wavelength there is far more evidence of a true bleaching sequence, that is, the bleaching takes place over a more prolonged time and the bleaching times chosen show this up. This is especially prominent in figures 5.18.2 and 5.19.1 where there is clearly a systematic decrease (proportional to the bleach time) in the same emission component as before.

As for the 350 and 550 nm bleach, only the one emission component has been removed by the illumination of 650 nm light.

5.4.3 Natural WK Quartz

The contour diagram and glow curve components for natural WK quartz are shown in figure 5.20 and 5.21 respectively. The details of these figures are essentially the same as for LW quartz.

Bleaching of Natural WK

Figures 5.22 to 5.23 show the sequence of diagrams for WK bleached by 350 (1.24 and 3.7 mJ cm^{-2}), 550 (425 and 1275 mJ cm^{-2}) and 650 nm (7.4 and 22 J cm^{-2}) light.

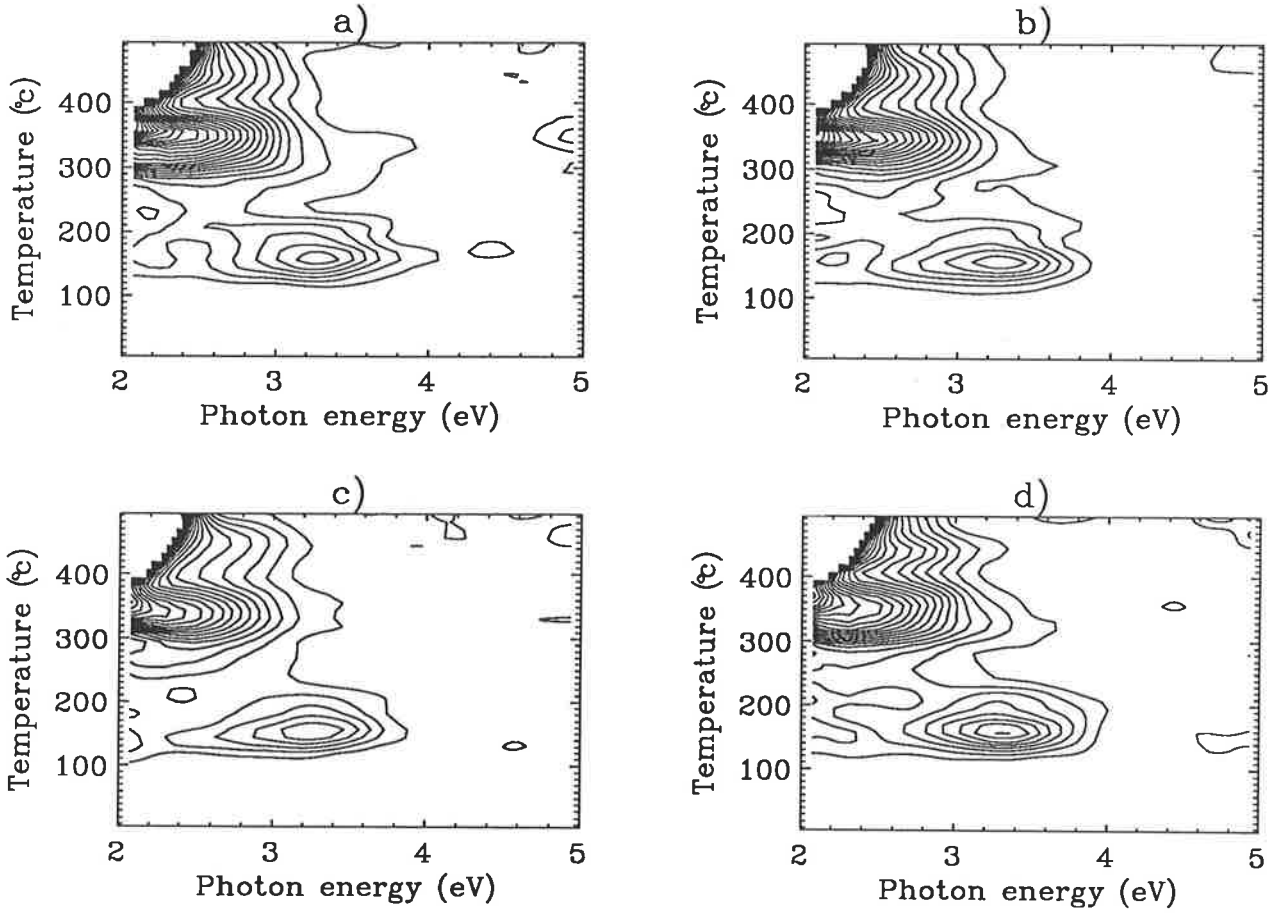

Figure 5.16.1: Contour diagrams of irradiated LW quartz for a) 2, b) 4, c) 6 and d) 8 minutes of bleaching by 550 nm light.

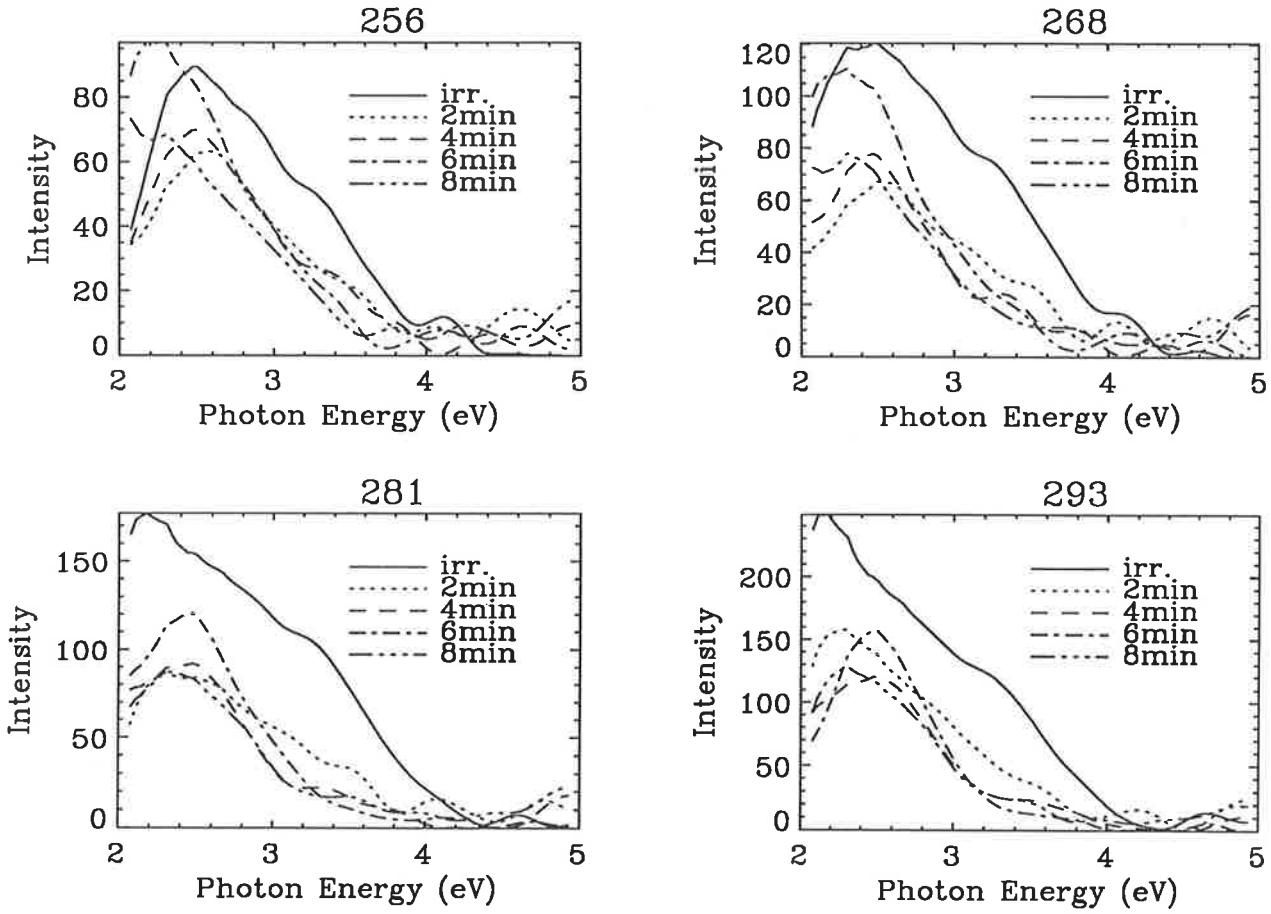

Figure 5.16.2: Individual spectra for irradiated LW showing the sequence from no bleach to full 550 nm bleach at temperatures (in Celsius) shown above each plot.

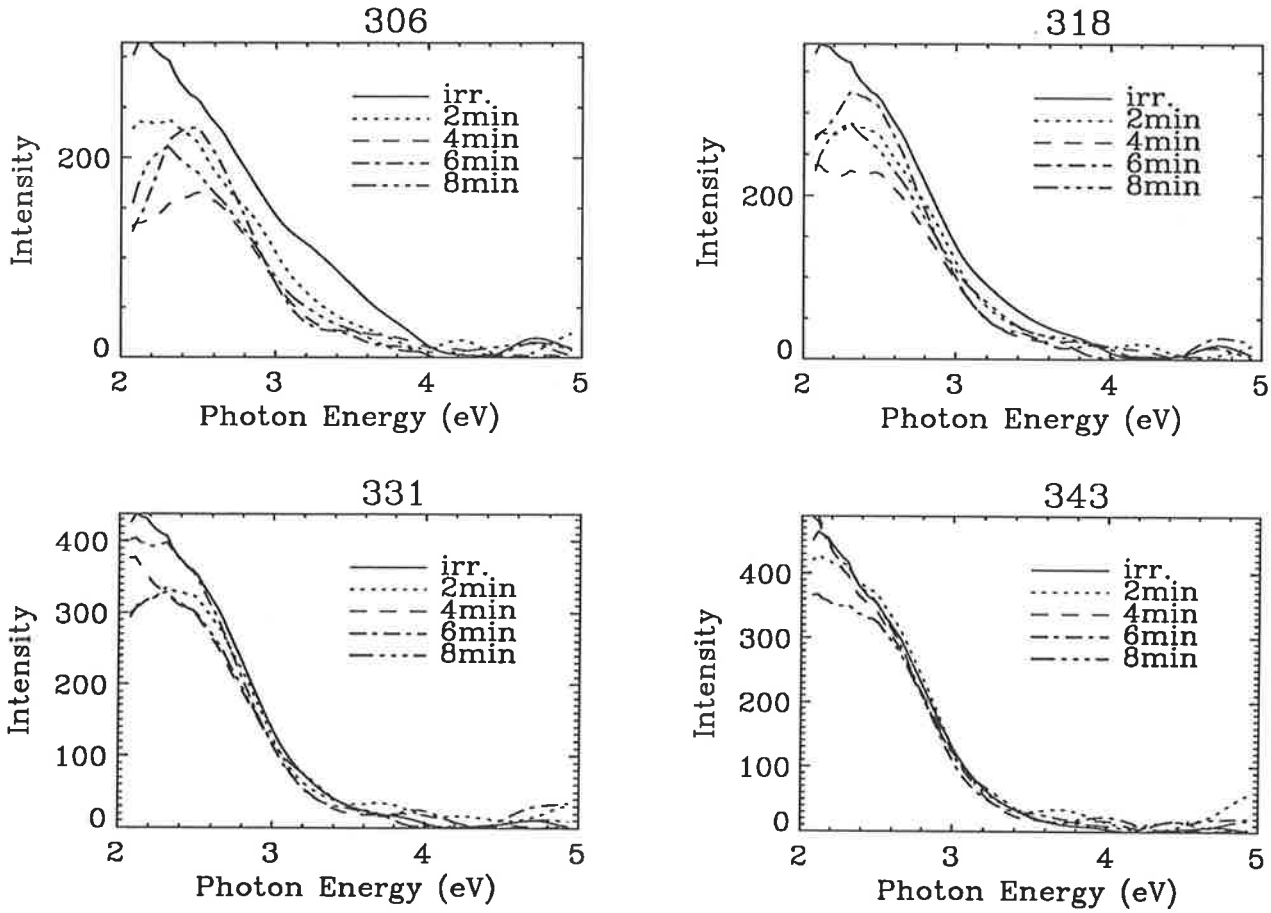

Figure 5.16.3: Individual spectra for irradiated LW showing the sequence from no bleach to full 550 nm bleach at temperatures (in Celsius) shown above each plot.

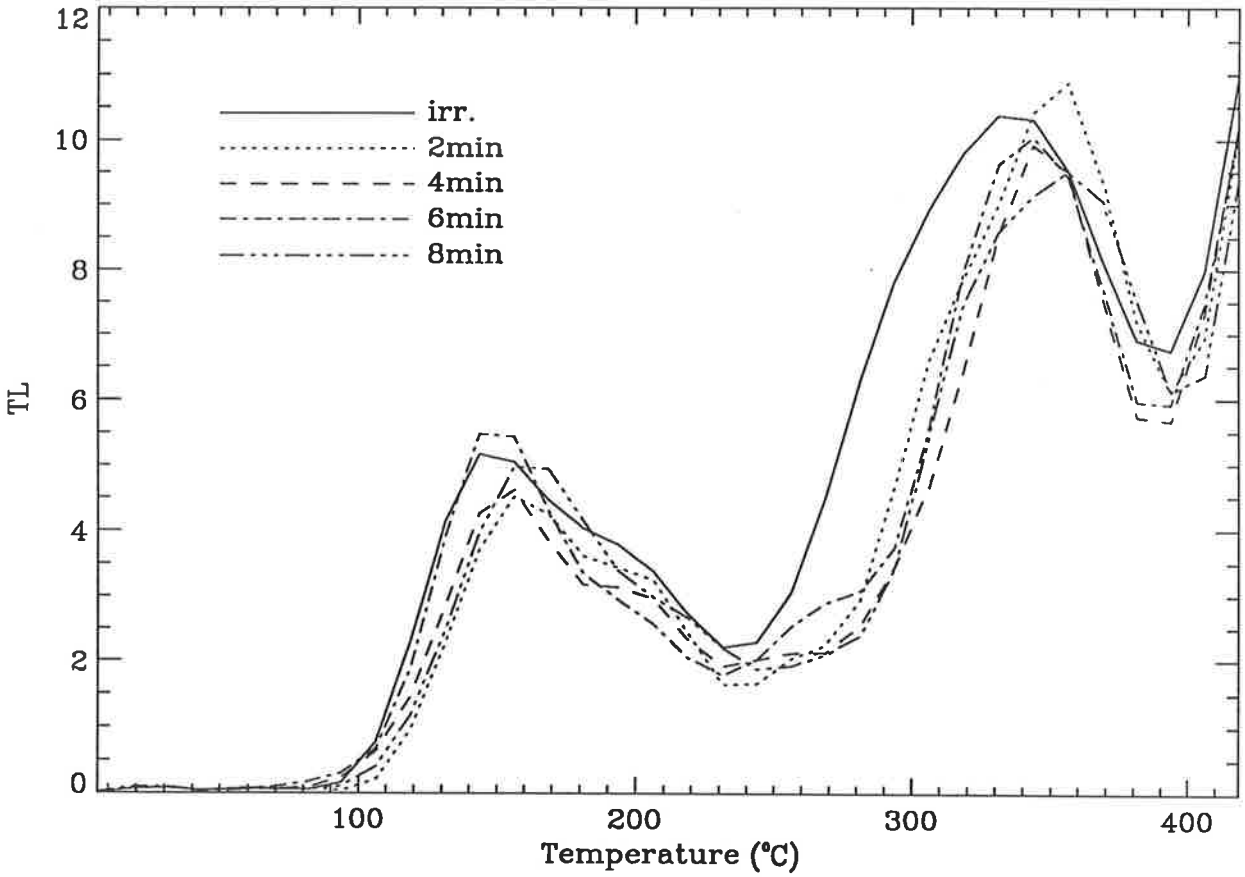

Figure 5.17.1: Full glow curves for the 550 nm bleaching sequence for irradiated LW.

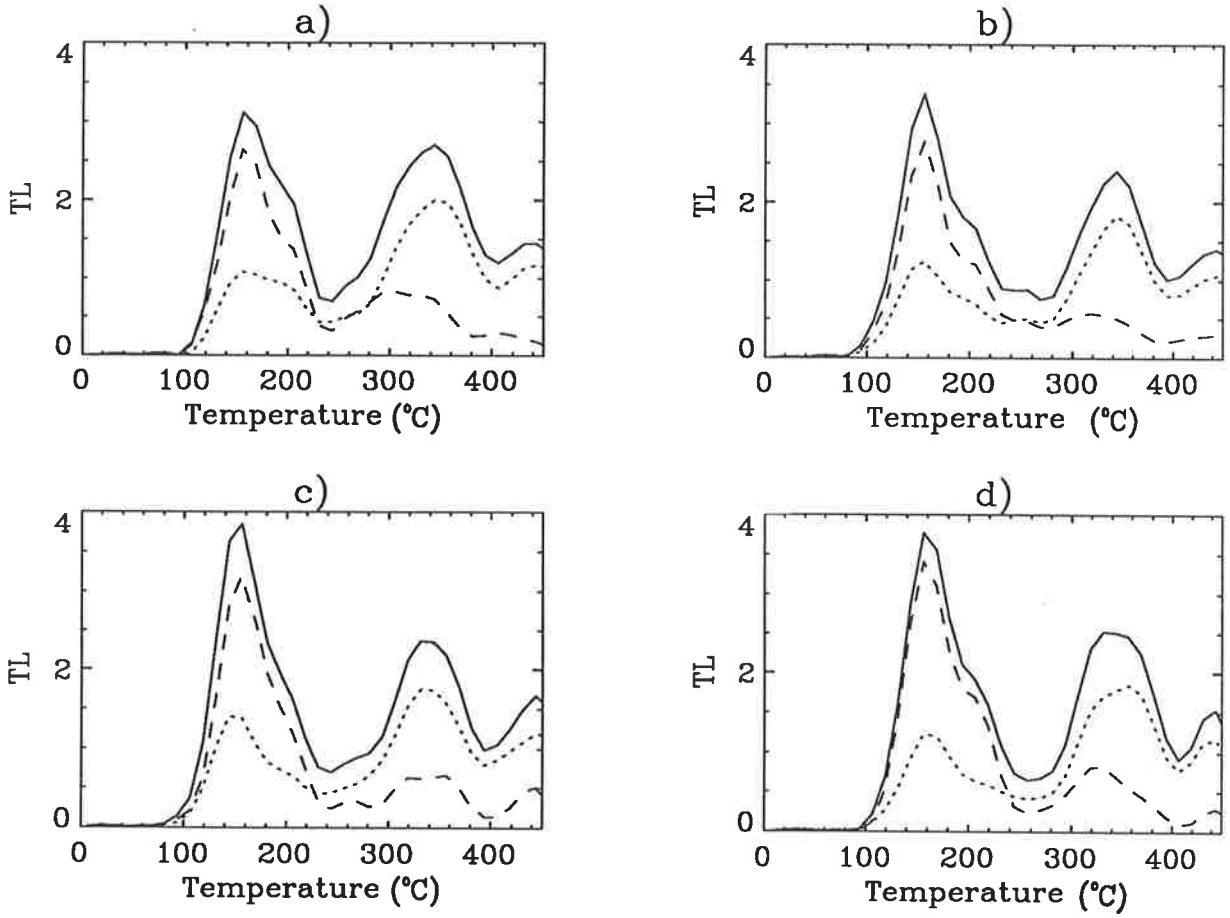

Figure 5.17.2: Glow curves for irradiated LW obtained by summing through different photon energy regions (shown in figure 5.5) for a) 2, b) 4, c) 6 and d) 8 minutes of bleaching by 550 nm light.

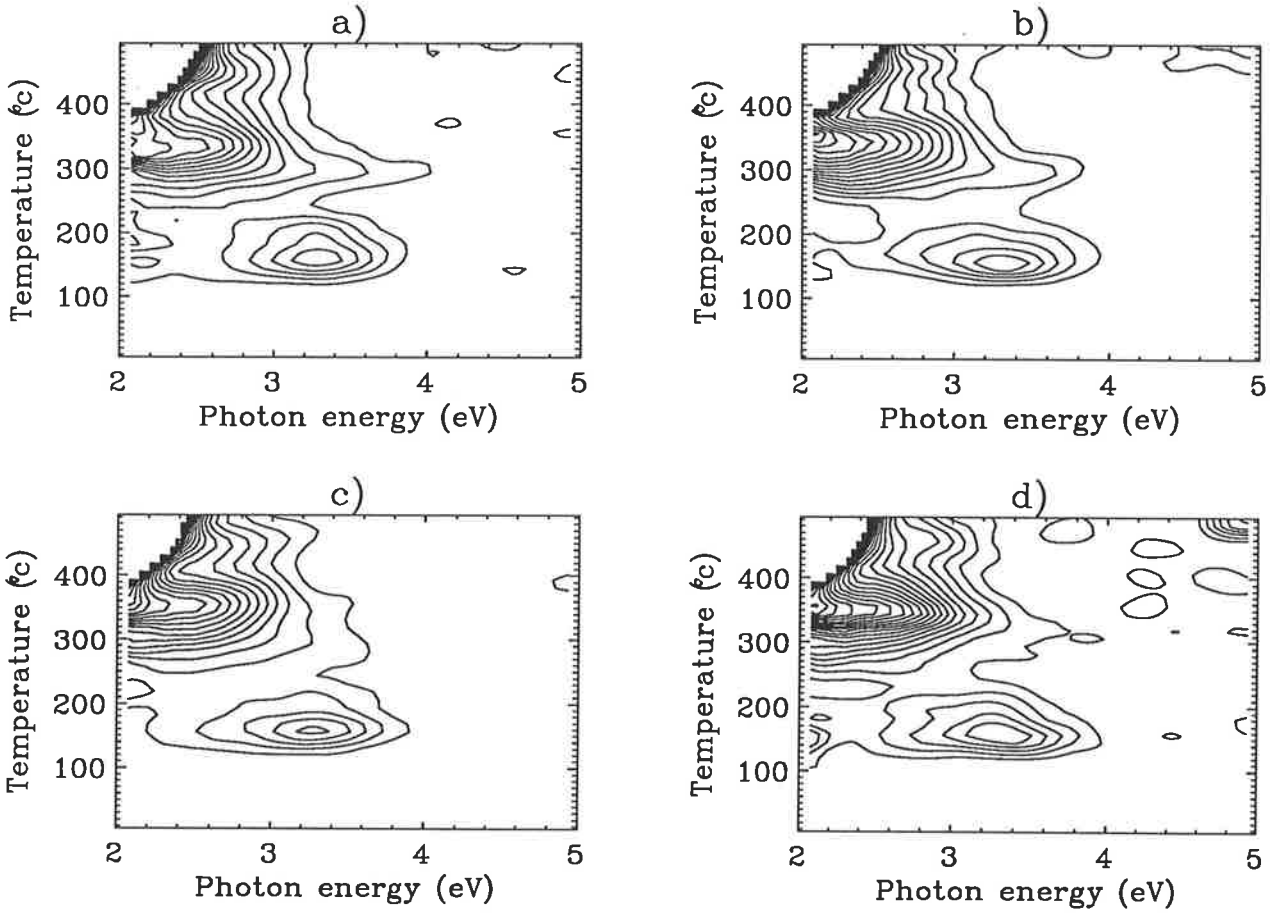

Figure 5.18.1: Contour diagrams of irradiated LW quartz for a) 20, b) 40, c) 60 and d) 80 minutes of bleaching by 650 nm light.

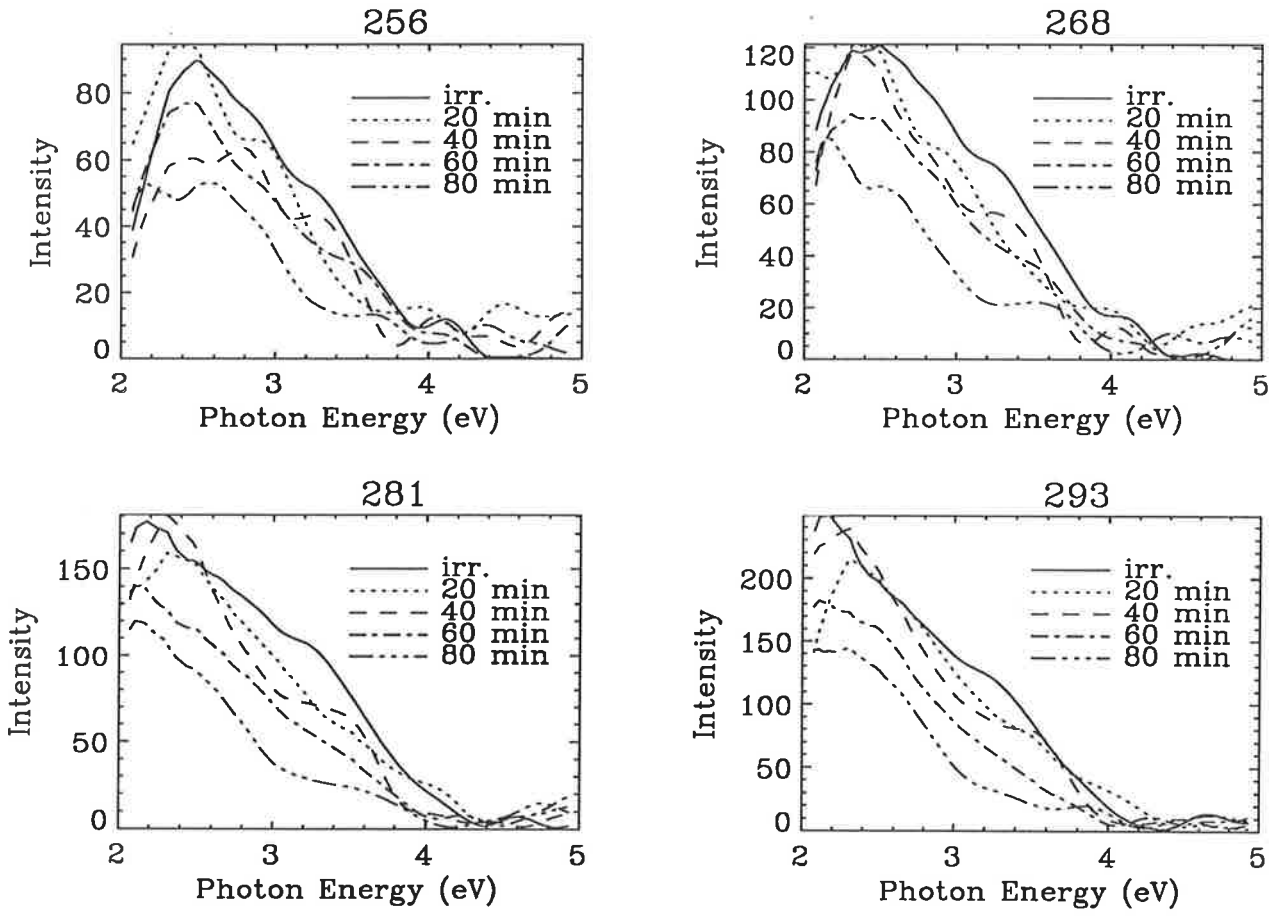

Figure 5.18.2: Individual spectra for irradiated LW showing the sequence from no bleach to full 650 nm bleach at temperatures (in Celsius) shown above each plot.

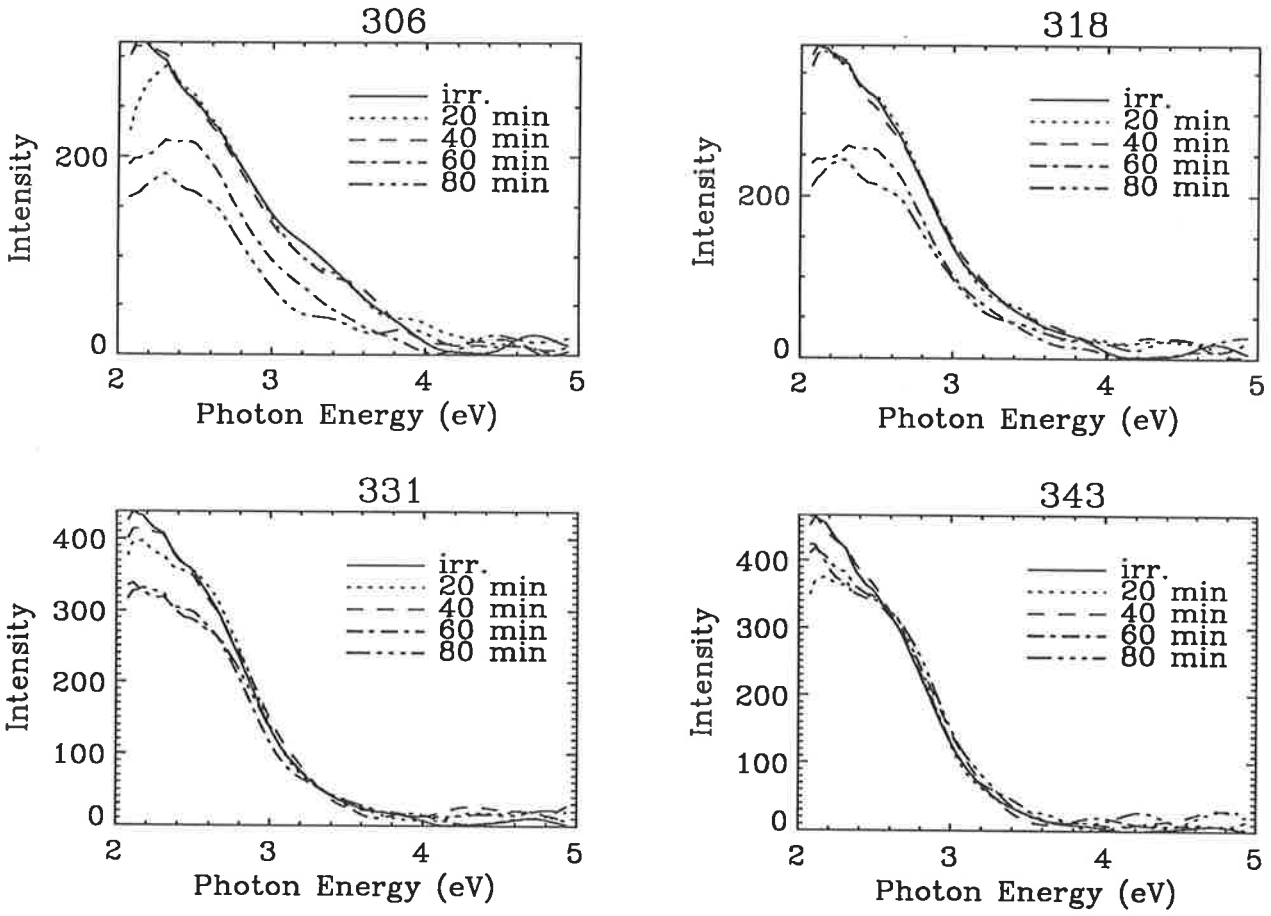

Figure 5.18.3: Individual spectra for irradiated LW showing the sequence from no bleach to full 650 nm bleach at temperatures (in Celsius) shown above each plot.

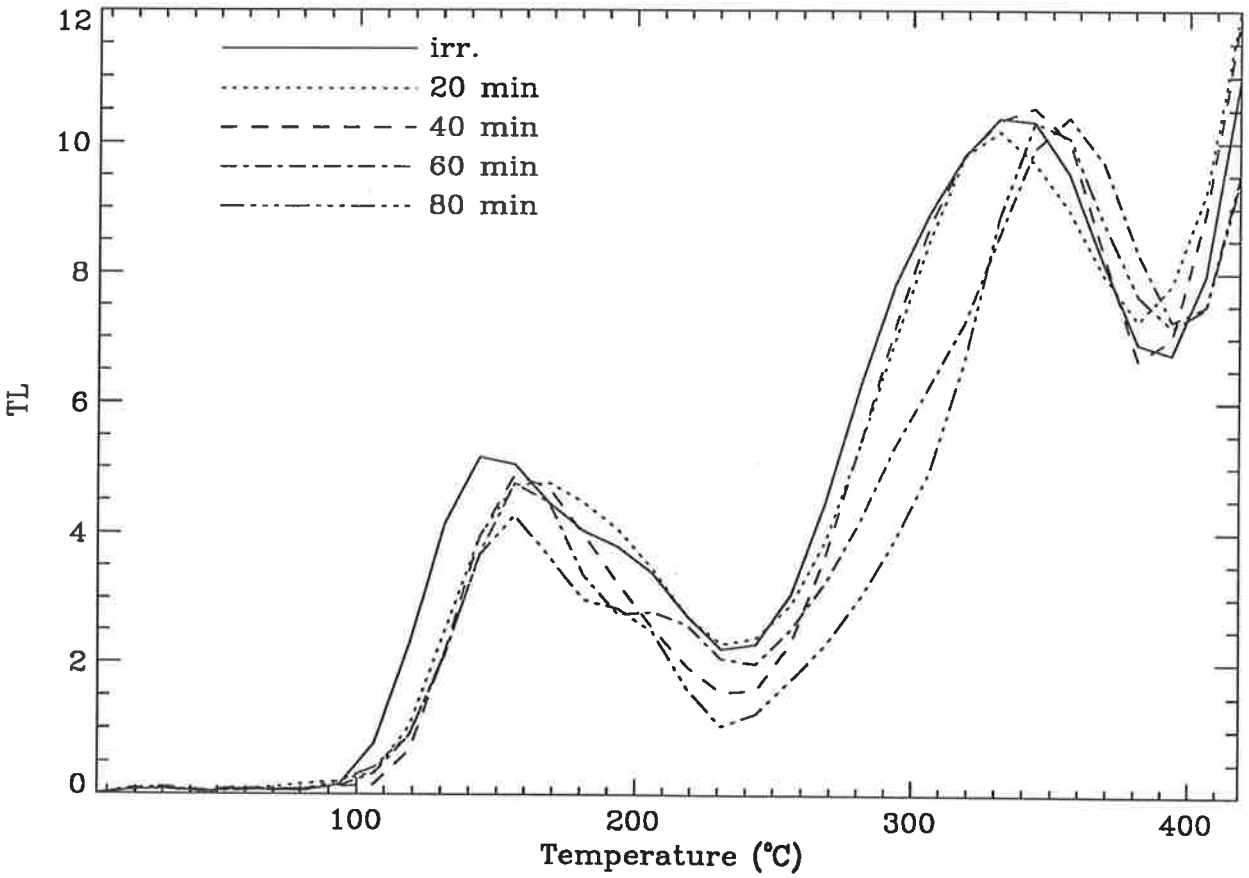

Figure 5.19.1: Full glow curves for the 650 nm bleaching sequence for irradiated LW.

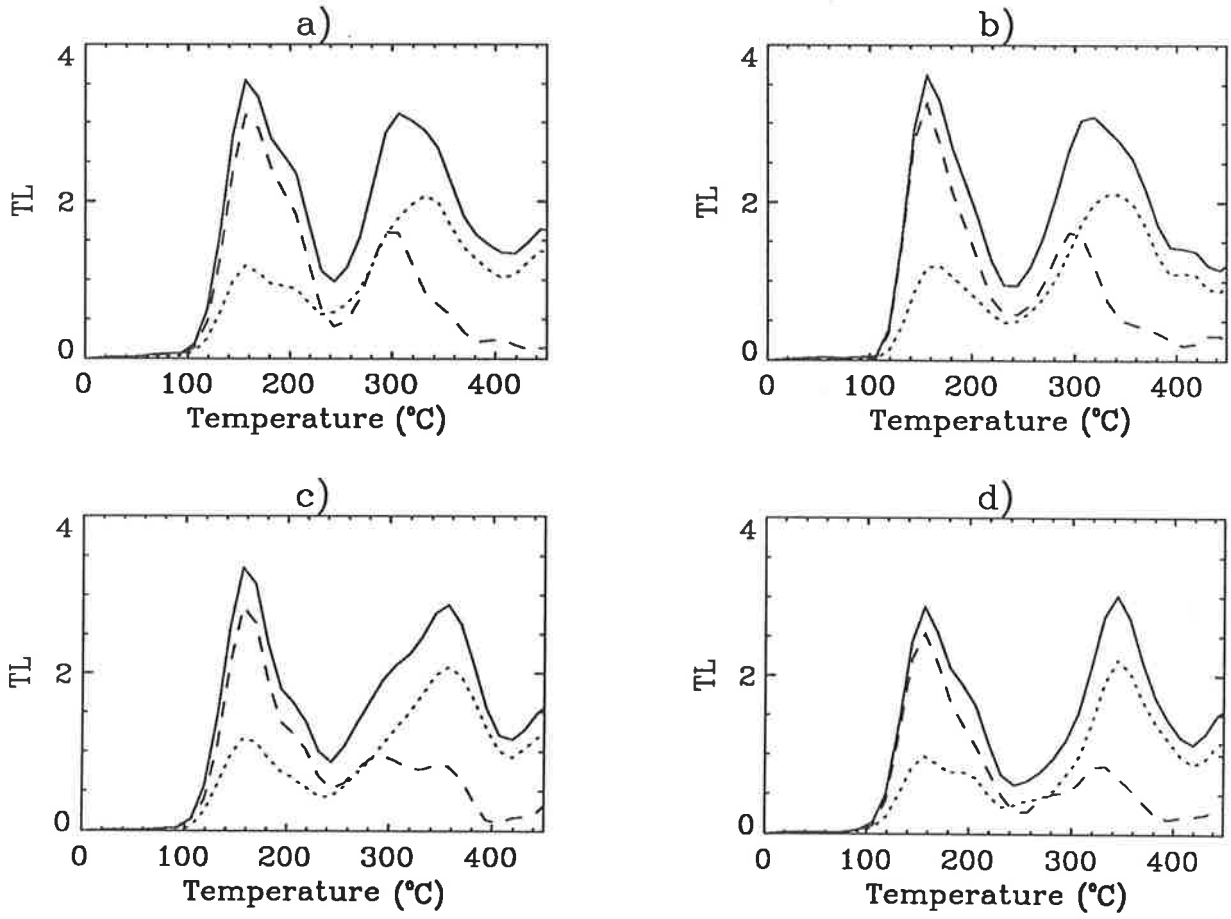

Figure 5.19.2: Glow curves for irradiated LW obtained by summing through different photon energy regions (shown in figure 5.5) for a) 20, b) 40, c) 60 and d) 80 minutes of bleaching by 650 nm light.

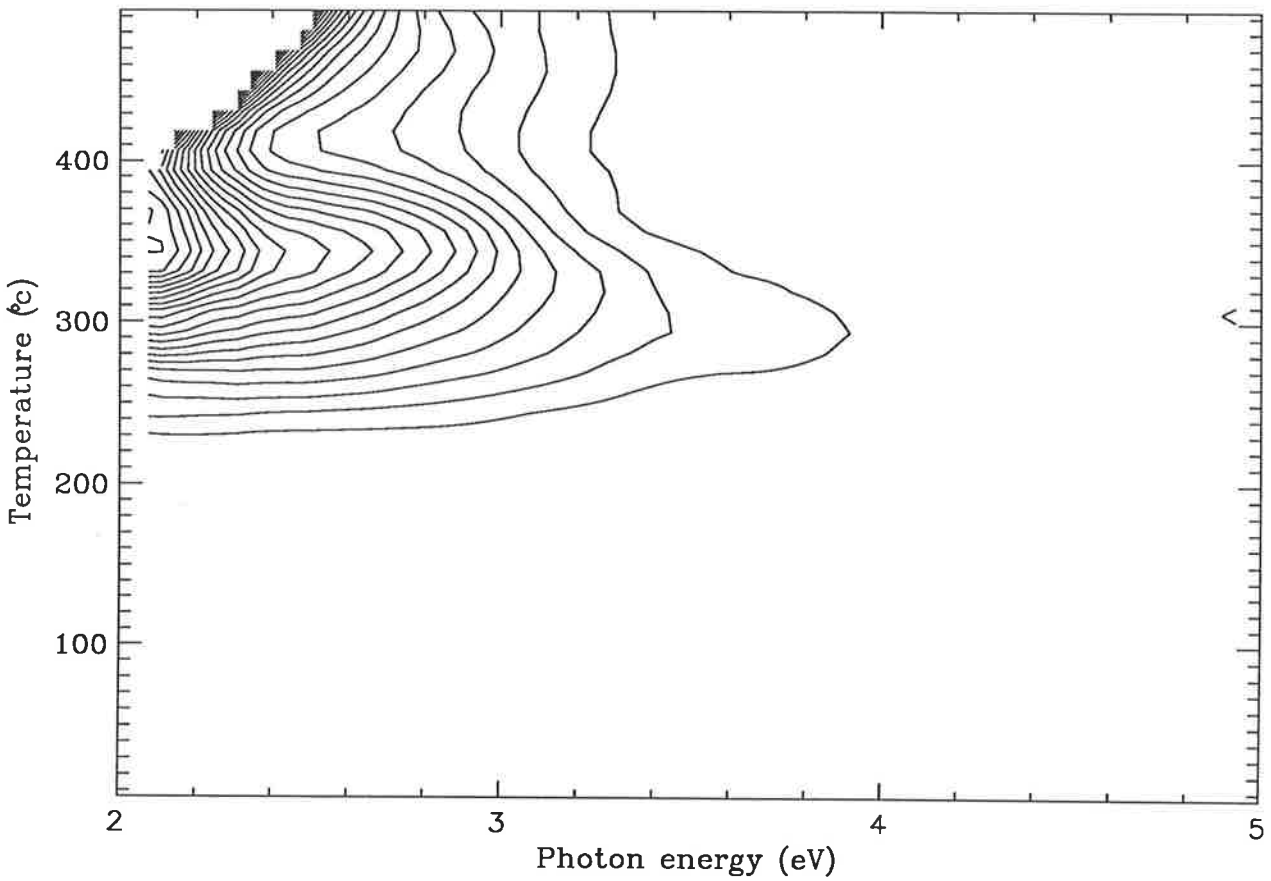

Figure 5.20: Contour diagram of natural WK quartz.

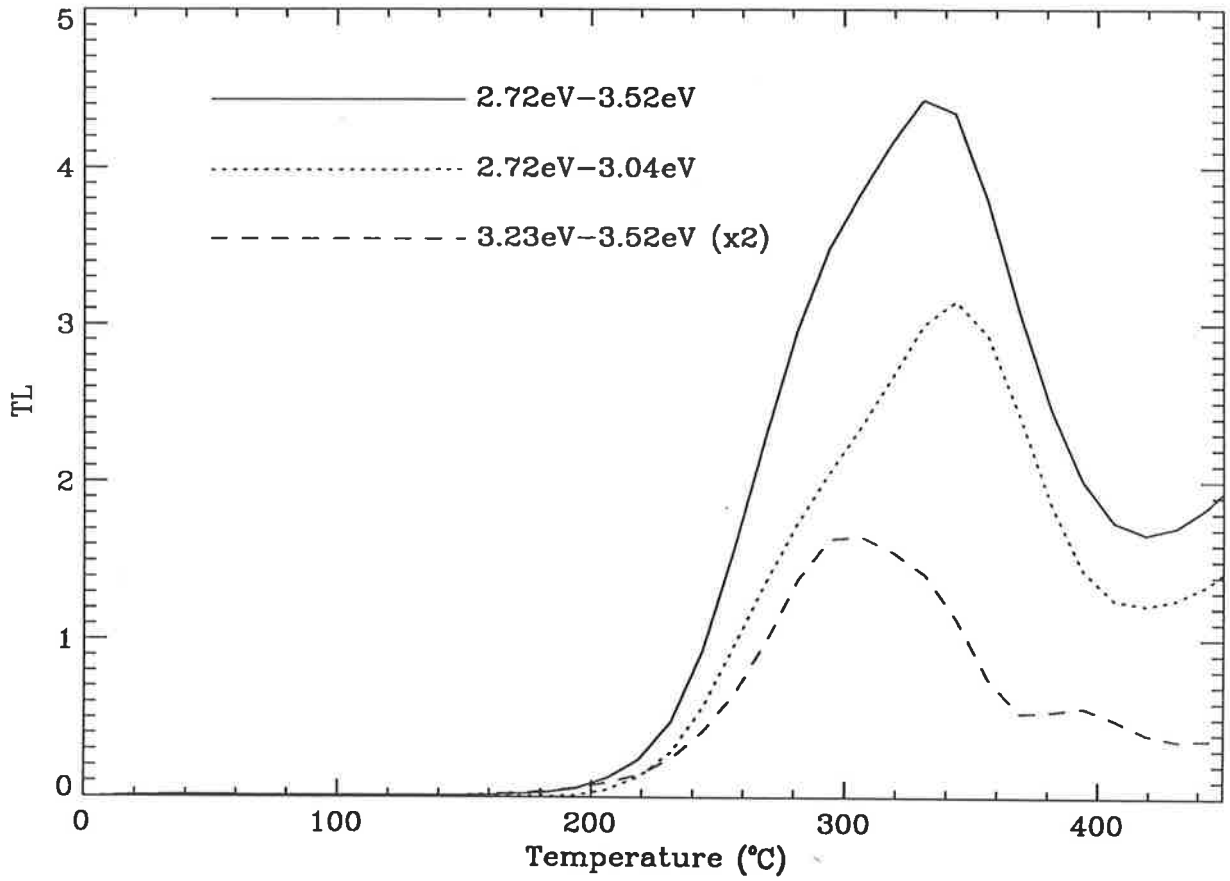

Figure 5.21: Glow curves obtained by summing through different photon energy regions (shown on the plot) for natural WK.

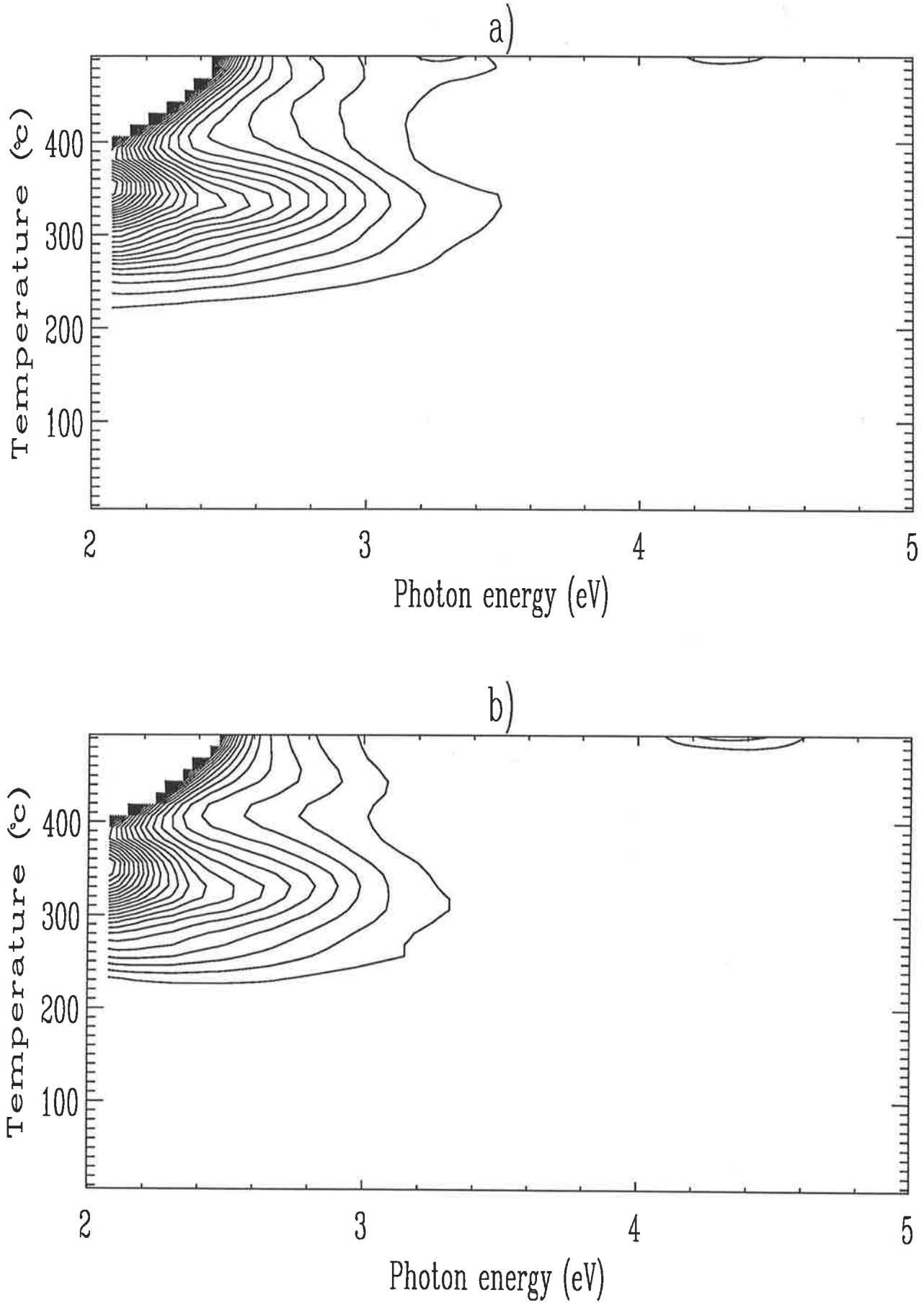

Figure 5.22: Contour diagrams of natural WK quartz for a) 40 s and b) 2.0 minutes of bleaching by 350 nm light.

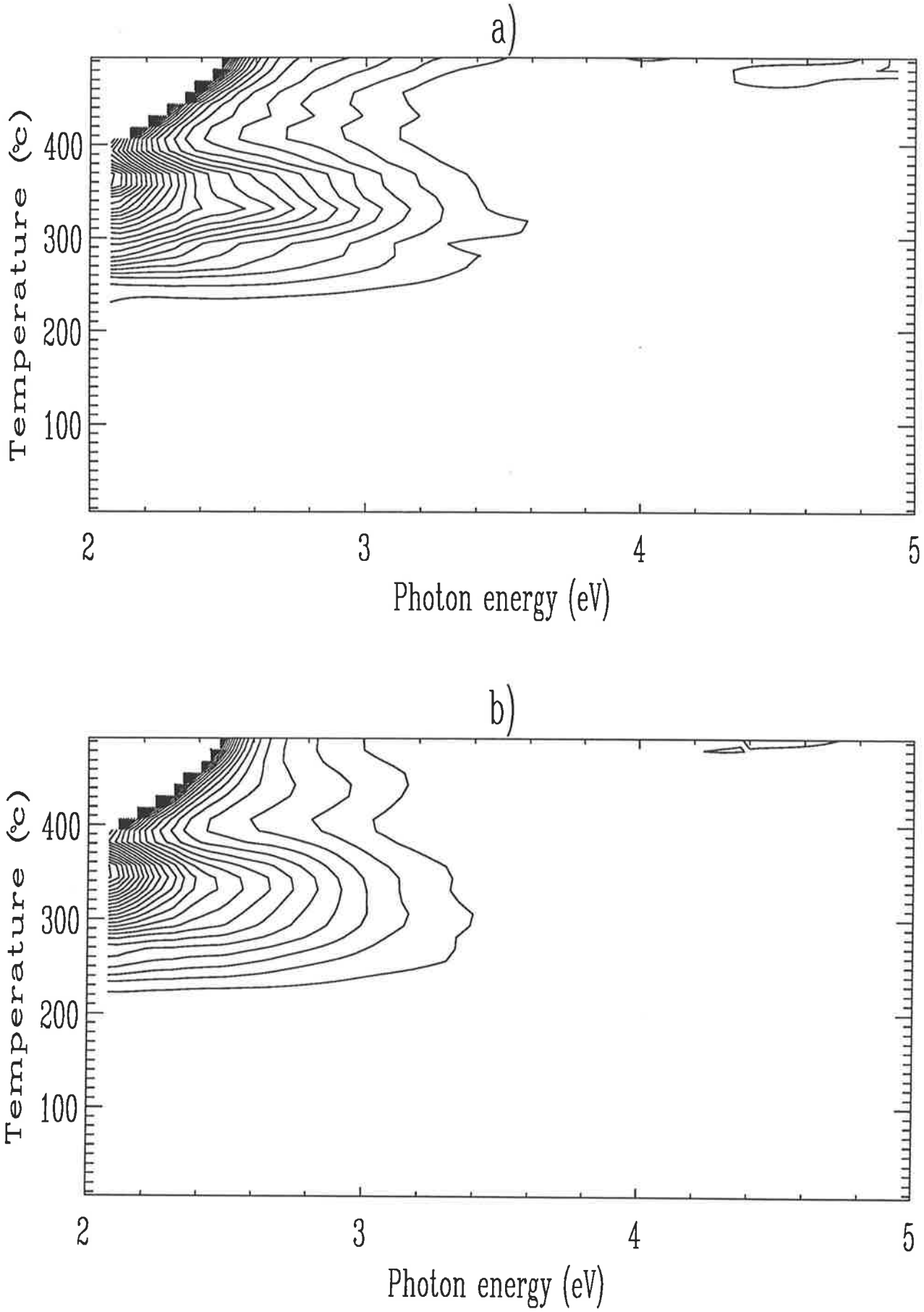

Figure 5.23: Contour diagrams of natural WK quartz for a) 2.5 and b) 8.0 minutes of bleaching by 550 nm light.

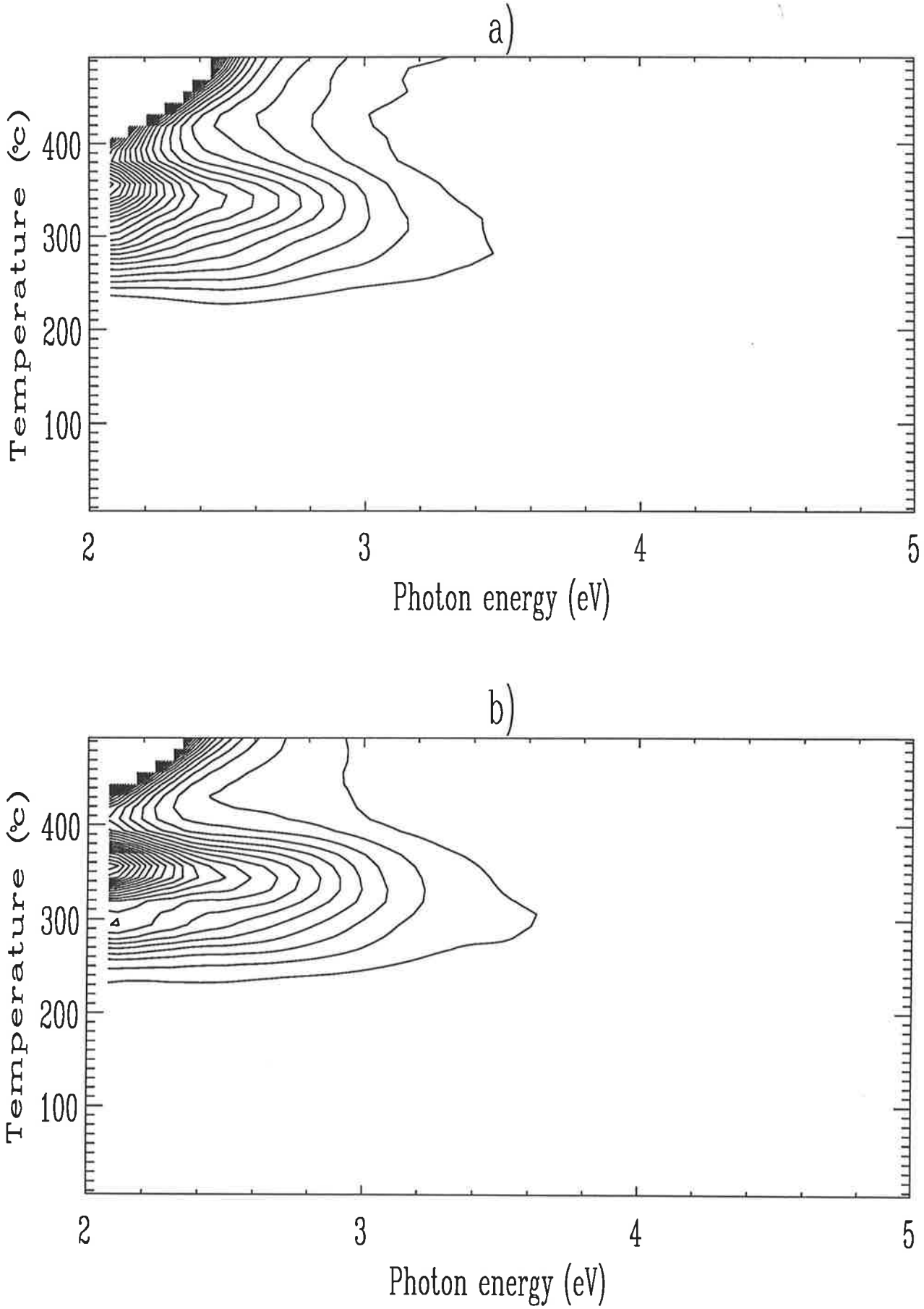

Figure 5.24: Contour diagrams of natural WK quartz for a) 49 and b) 146 minutes of bleaching by 650 nm light.

The results for natural WK are essentially the same as for the equivalent diagrams for LW. It is only the high photon energy component that is removed. This is best seen by comparing figure 5.20 with figures 5.22, 5.23 and 5.24. A complete set of data measurements identical with that already described for LW was carried out for WK. The two samples differ only in detail, with the high energy component being perhaps a little smaller in proportion for WK. Only a selection of data are shown.

5.4.4 Irradiated WK Quartz

Figures 5.25 and 5.26 give the contour and glow curve component diagrams for irradiated WK quartz.

As for LW new peaks with emission around 3.3 eV and at temperatures of 150 and 180°C have been generated in addition to the higher temperature peaks above 250°C. These higher temperature peaks differ somewhat from those in the natural samples in that the higher energy emission occurs at a lower temperature (about 280°C) than for the natural WK case and the "300" and "340°C" peaks are now clearly separate, resolved peaks.

Bleaching of Irradiated WK

The data for the bleaching of irradiated WK quartz is presented in figures 5.27, 5.28 and 5.29 for the same bleach times as for the natural case. For the high temperature peaks the bleaching by the 350, 550 and 650 nm light is the same as for the natural case – with the rapid removal of the high energy component only.

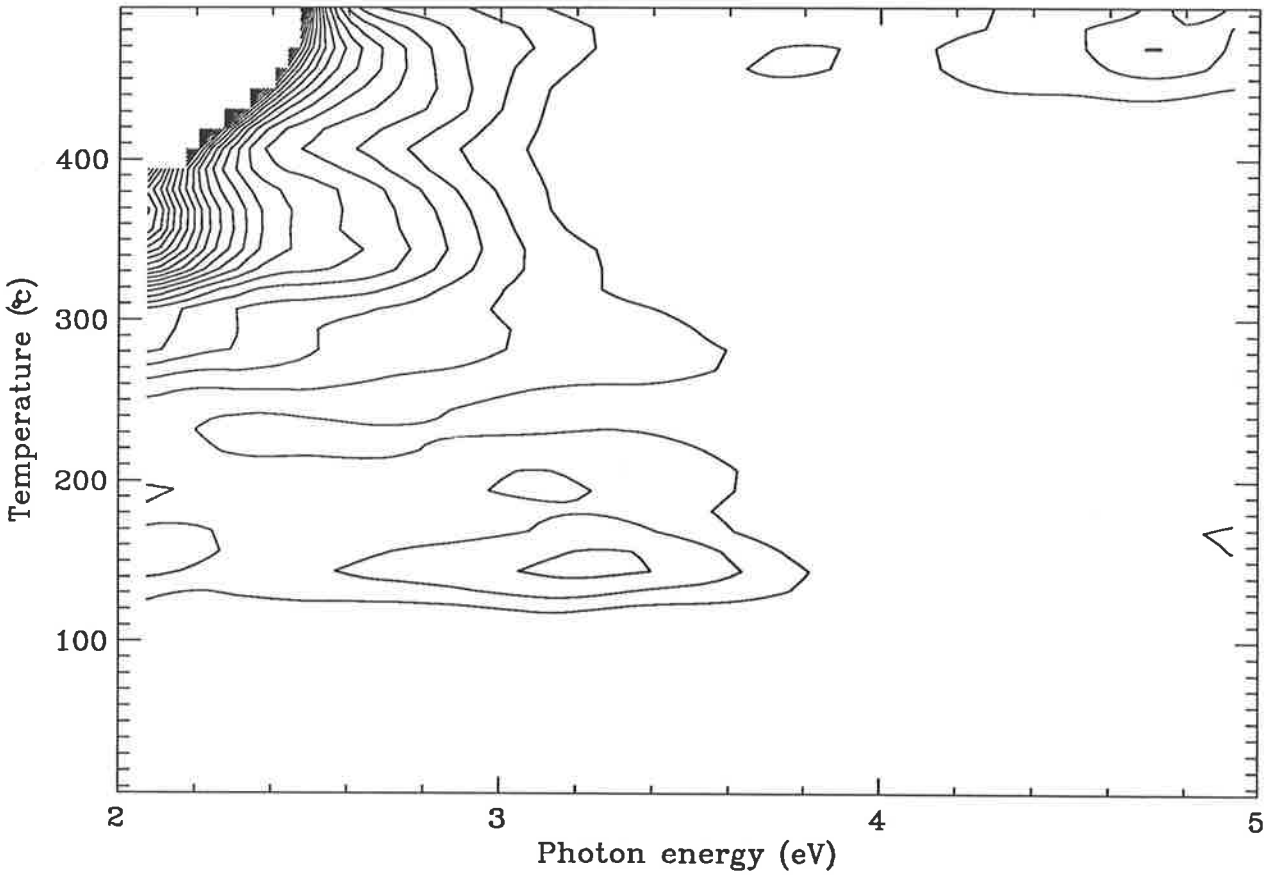

Figure 5.25: Contour diagram of irradiated WK quartz.

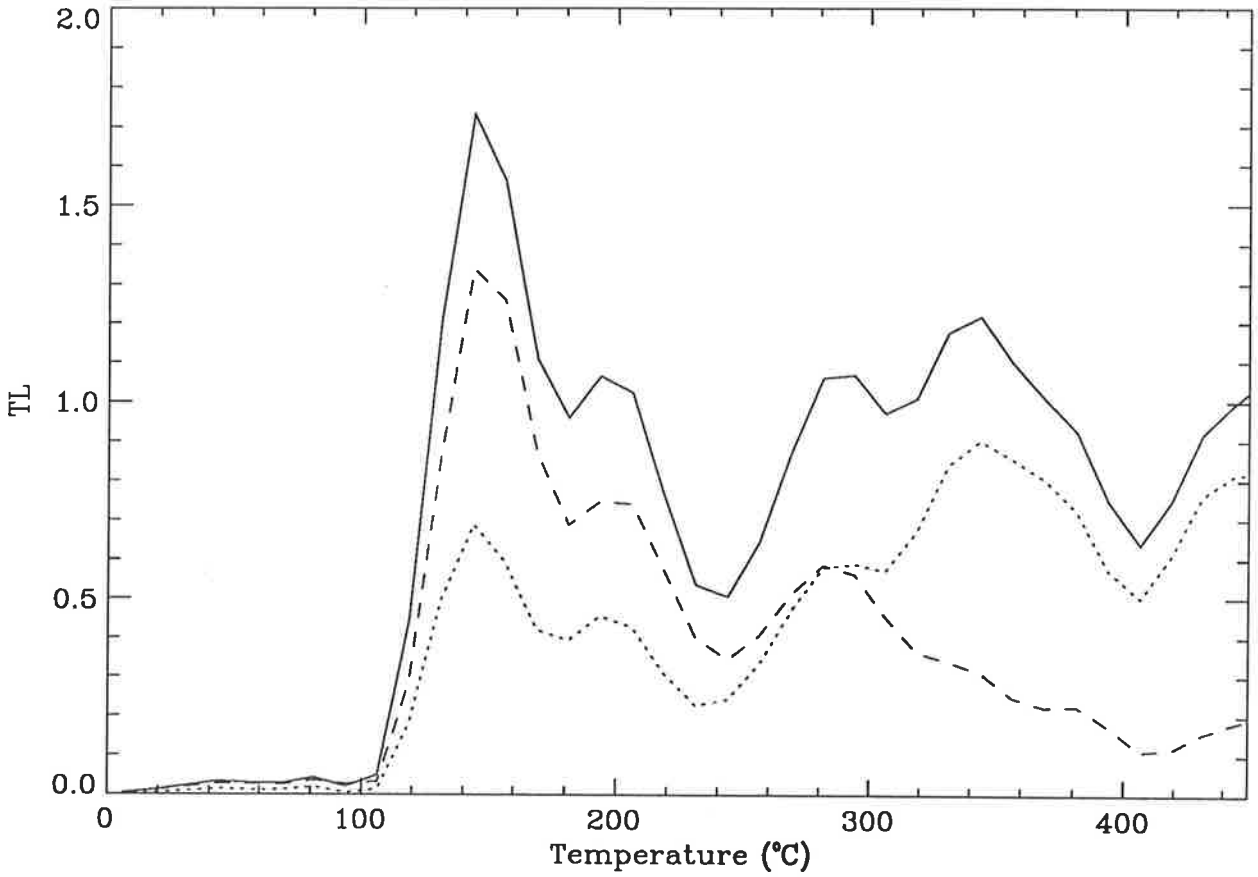

Figure 5.26: Glow curves obtained by summing through different photon energy regions (shown in figure 5.21) for irradiated WK.

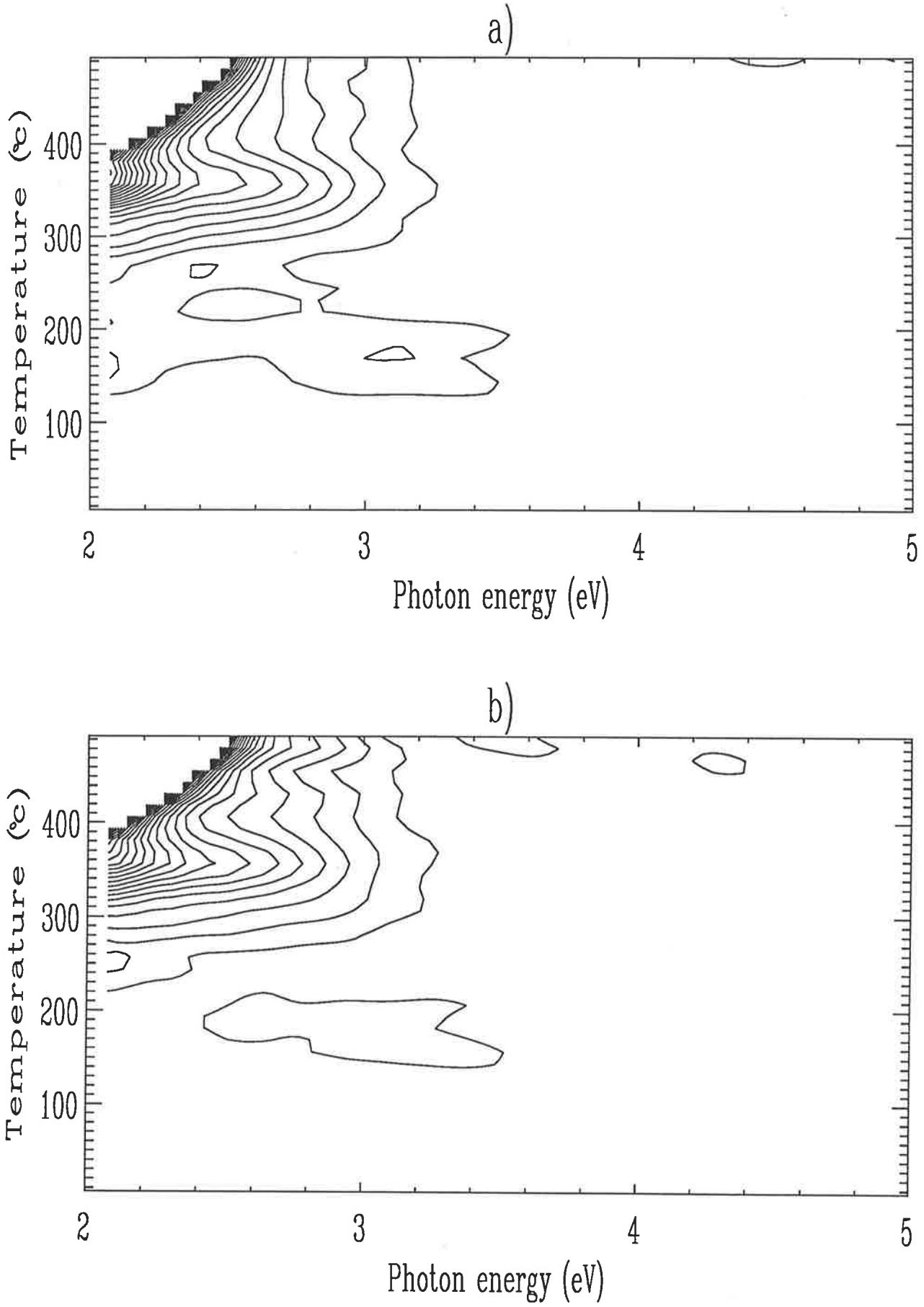

Figure 5.27: Contour diagrams of irradiated WK quartz for a) 40 s and b) 2.0 minutes of bleaching by 350 nm light.

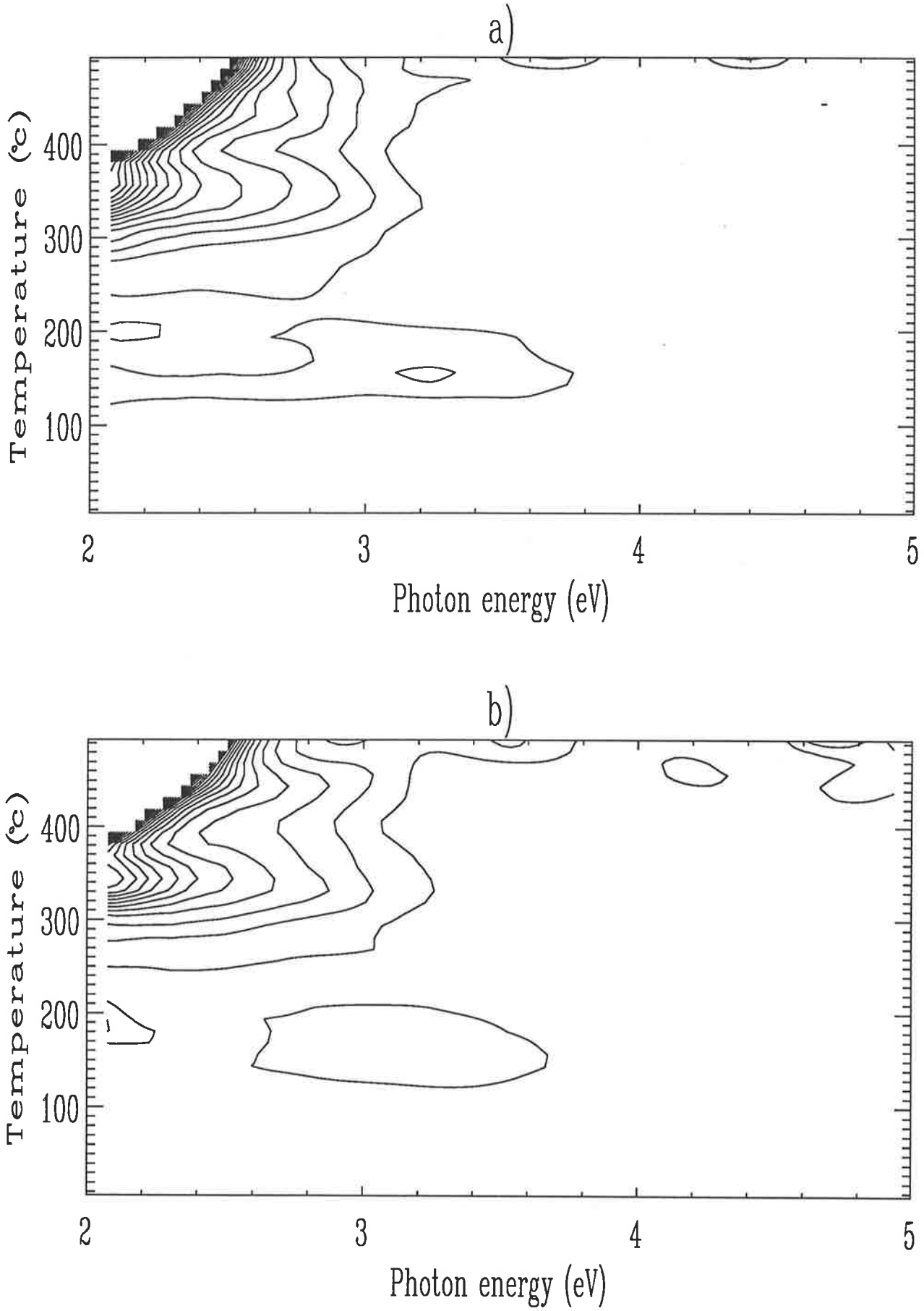

Figure 5.28: Contour diagrams of irradiated WK quartz for a) 2.5 and b) 8.0 minutes of bleaching by 550 nm light.

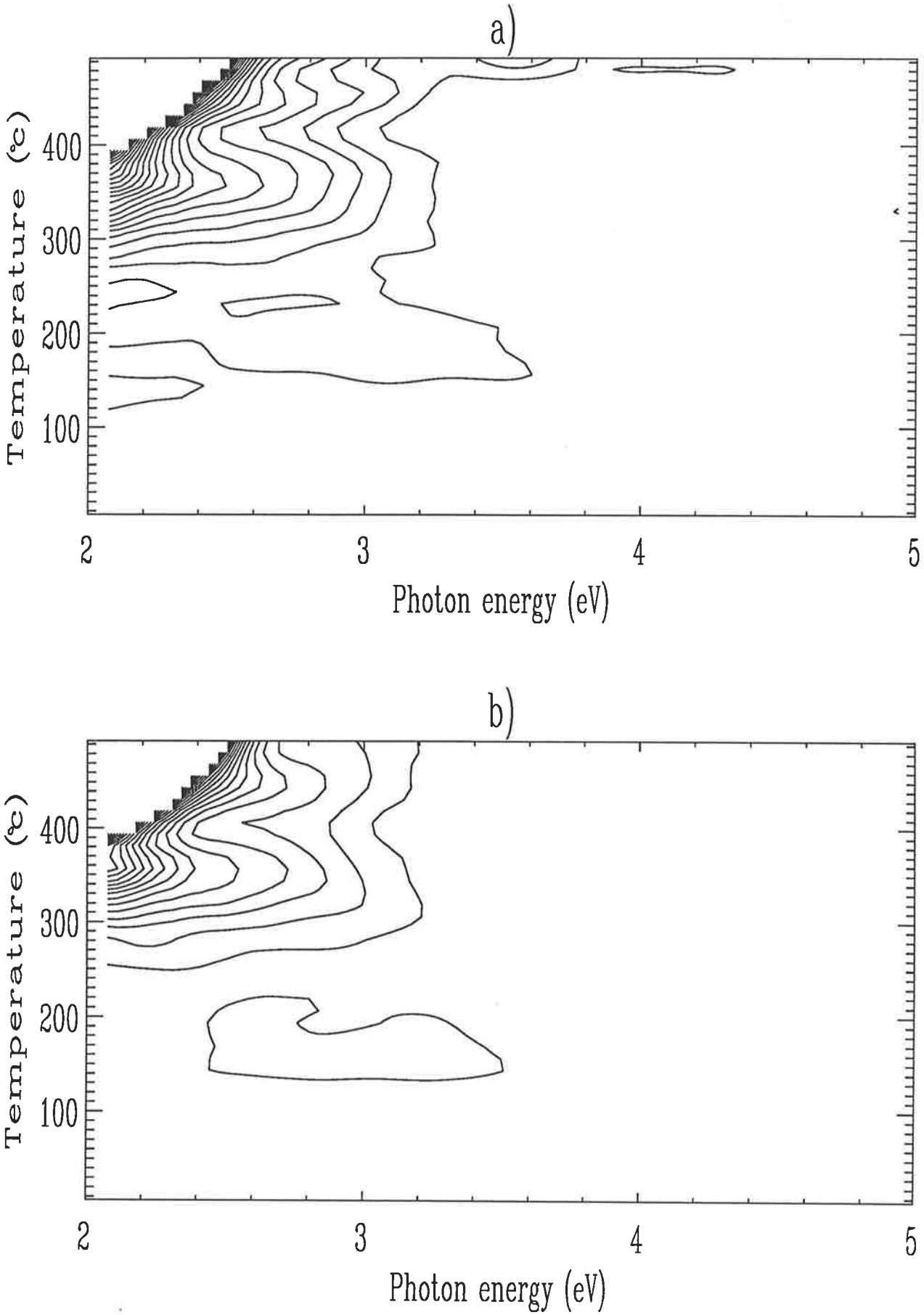

Figure 5.29: Contour diagrams of irradiated WK quartz for a) 49 and b) 146 minutes of bleaching by 650 nm light.

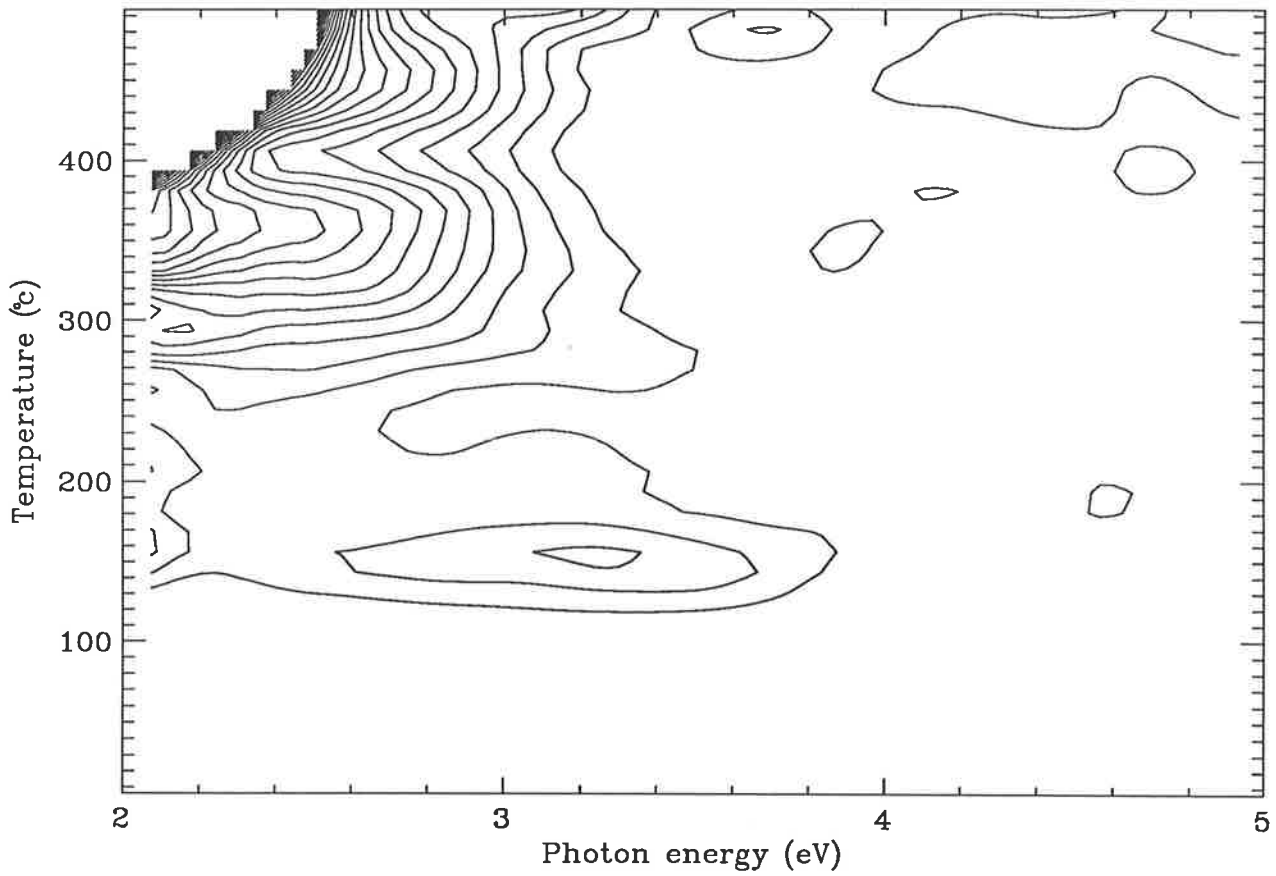

Figure 5.30: Contour diagram of irradiated EB quartz.

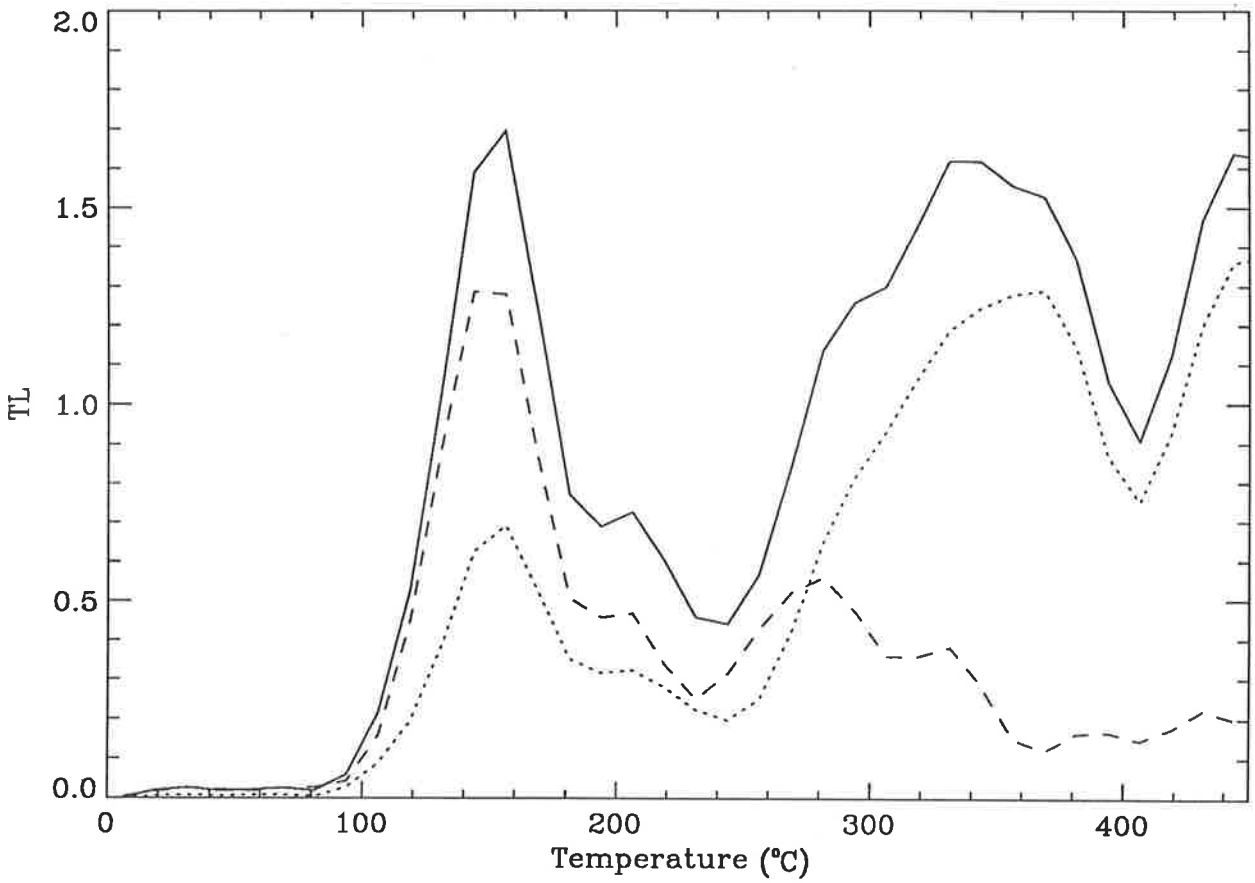

Figure 5.31: Glow curves obtained by summing through different photon energy regions (shown in figure 5.21) for irradiated EB.

5.4.5 Irradiated EB Quartz

Figures 5.30 and 5.31 are the unbleached contour and glow curve component diagrams for irradiated EB quartz. As for WK quartz the essential details are the same except that for EB quartz the level of the high energy emission (near to 300°C) is much lower than for irradiated LW and also the TL peak above 400°C is much more prominent.

Bleaching of Irradiated EB

Figures 5.32, 5.33 and 5.34 are the equivalent diagrams for the bleaching of irradiated EB quartz for the same bleach energies as for WK quartz.

The effect of the bleaching was practically identical to that upon WK quartz.

5.4.6 Irradiated PJ Quartz

The contour plot and glow curve components for irradiated PJ quartz are given in figures 5.35 and 5.36. In terms of the peak temperatures and emission energies, PJ is essentially the same as for the other quartz samples studied. However the intensity of the emission component above 3.0 eV is much greater than for the other samples and hence the bleaching effect is more dramatic. The prominence of this component means that a difference spectrum can be obtained, that is the difference between an unbleached spectrum and a bleached spectrum

Bleaching of Irradiated PJ

Figures 5.37, 5.38 and 5.39 show the plots of the bleached PJ data for the same illuminating energy fluxes as for WK and EB.

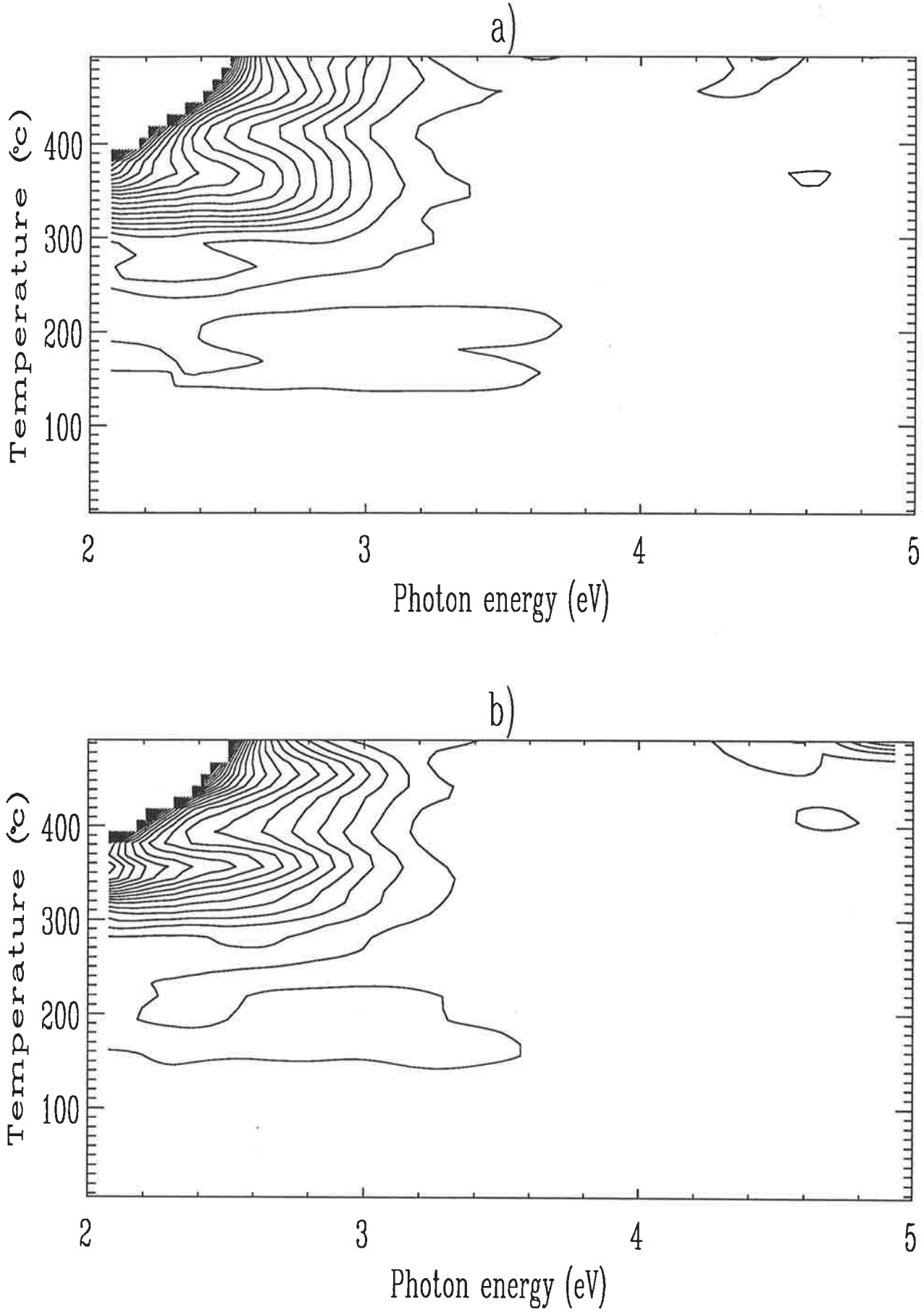

Figure 5.32: Contour diagrams of irradiated EB quartz for a) 40 s and b) 2.0 minutes of bleaching by 350 nm light.

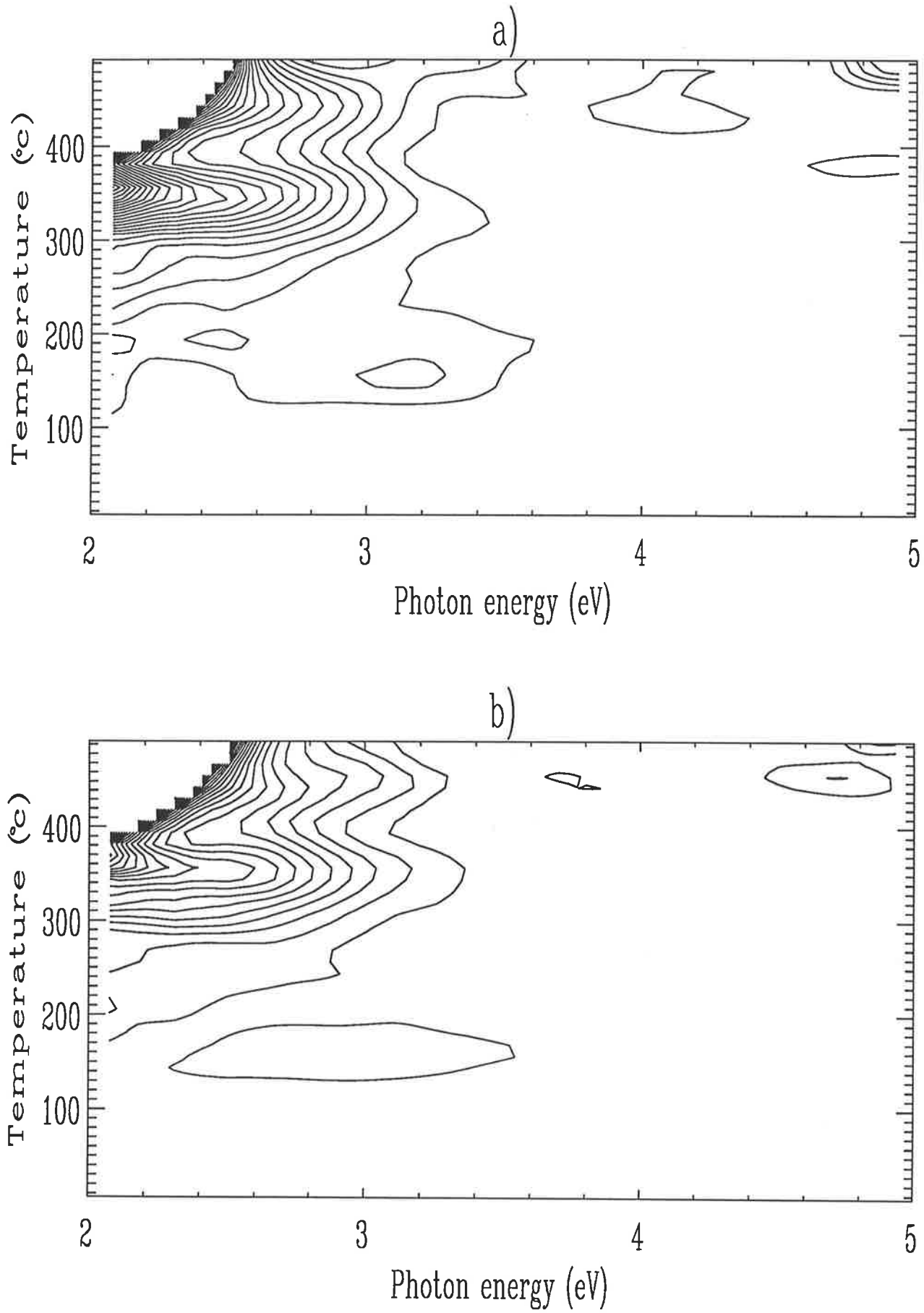

Figure 5.33: Contour diagrams of irradiated EB quartz for a) 2.5 and b) 8.0 minutes of bleaching by 550 nm light.

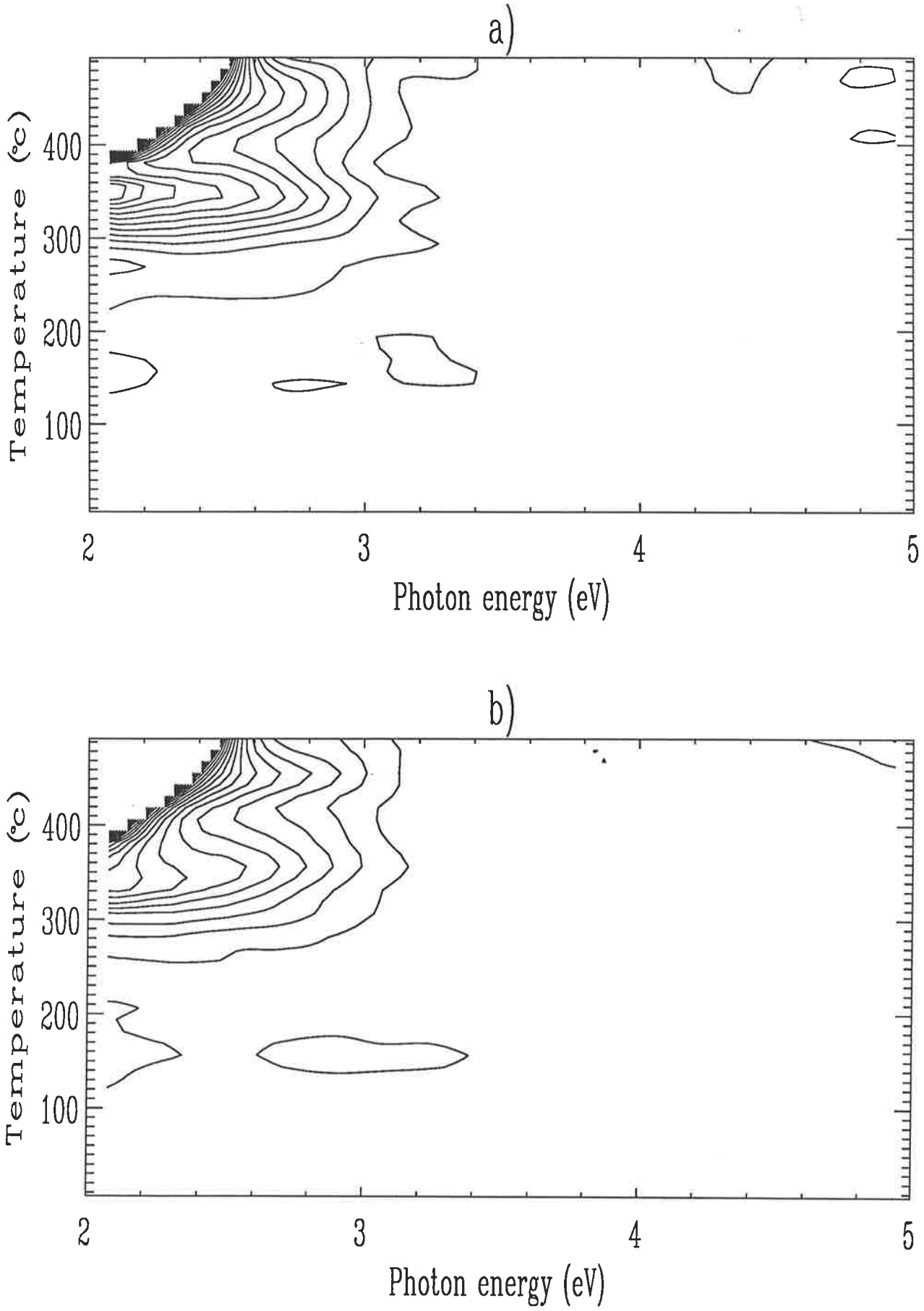

Figure 5.34: Contour diagrams of irradiated EB quartz for a) 49 and b) 146 minutes of bleaching by 650 nm light.

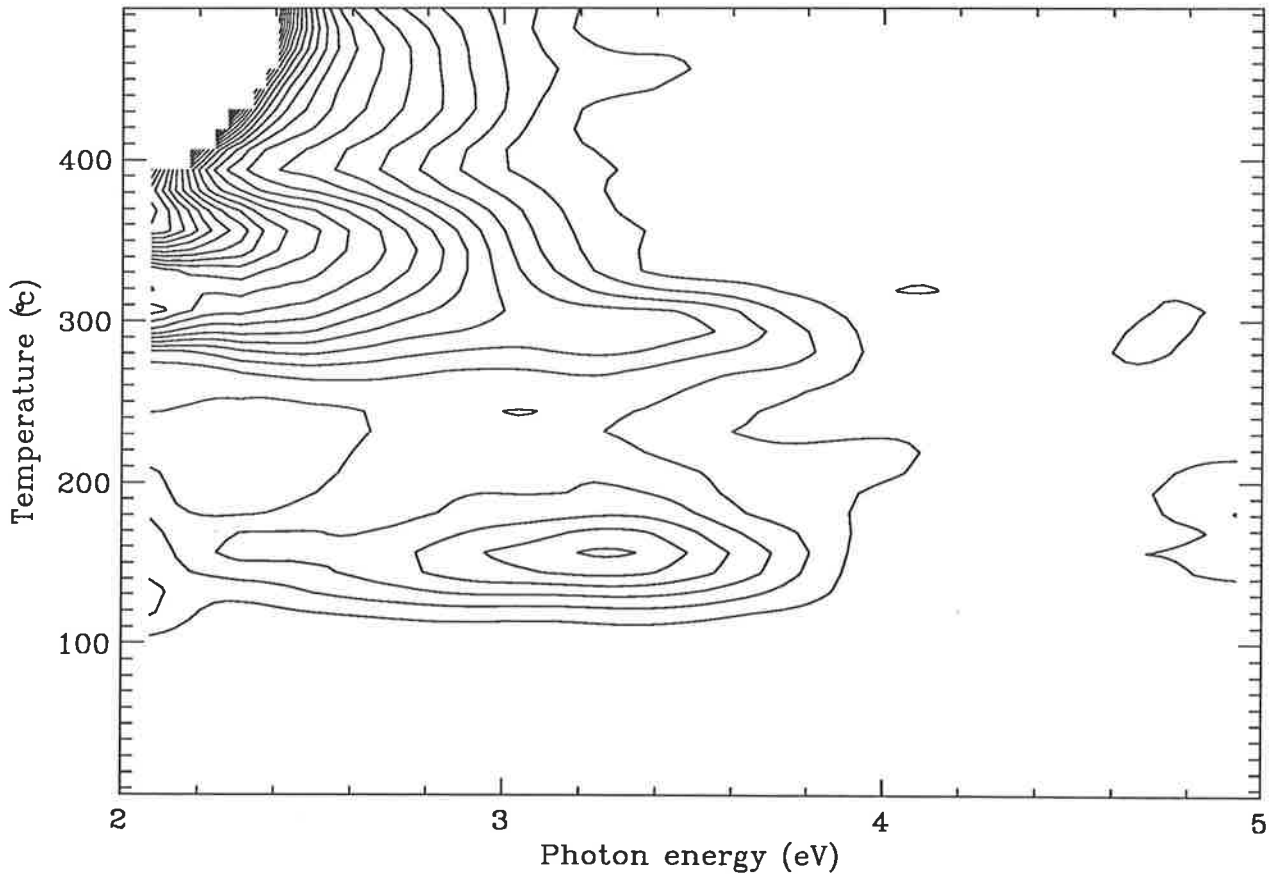

Figure 5.35: Contour diagram of irradiated PJ quartz.

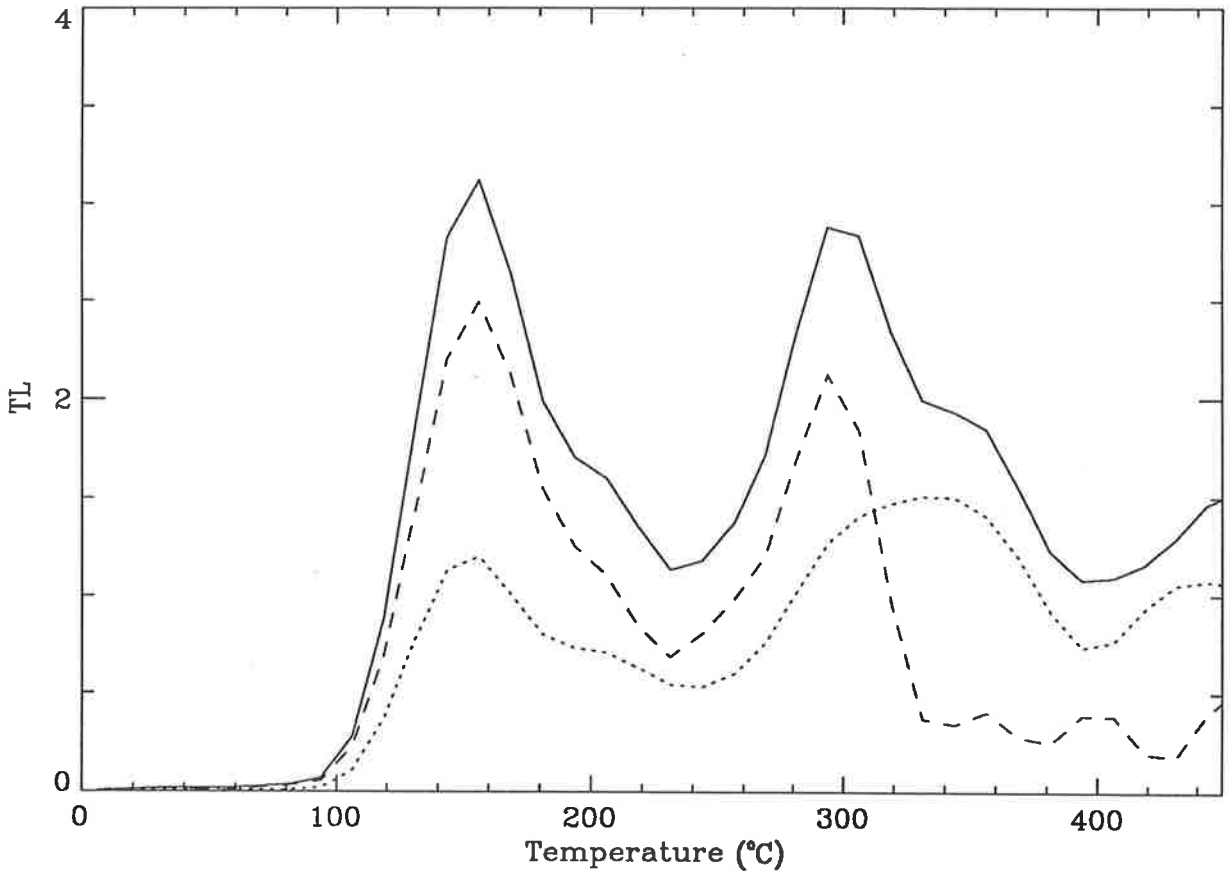

Figure 5.36: Glow curves obtained by summing through different photon energy regions (shown in figure 5.21) for irradiated PJ.

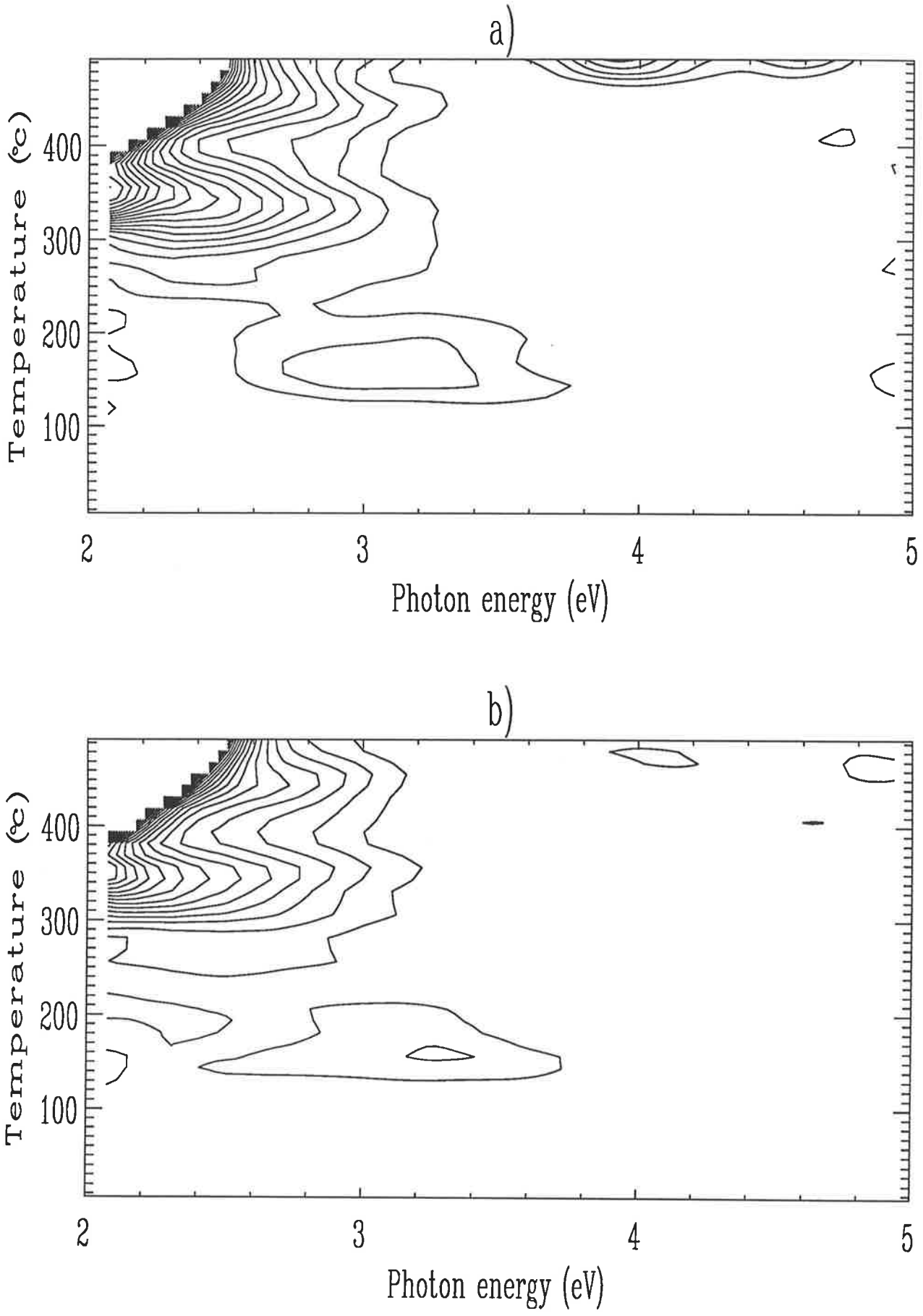

Figure 5.37: Contour diagrams of irradiated PJ quartz for a) 40 s and b) 2.0 minutes of bleaching by 350 nm light.

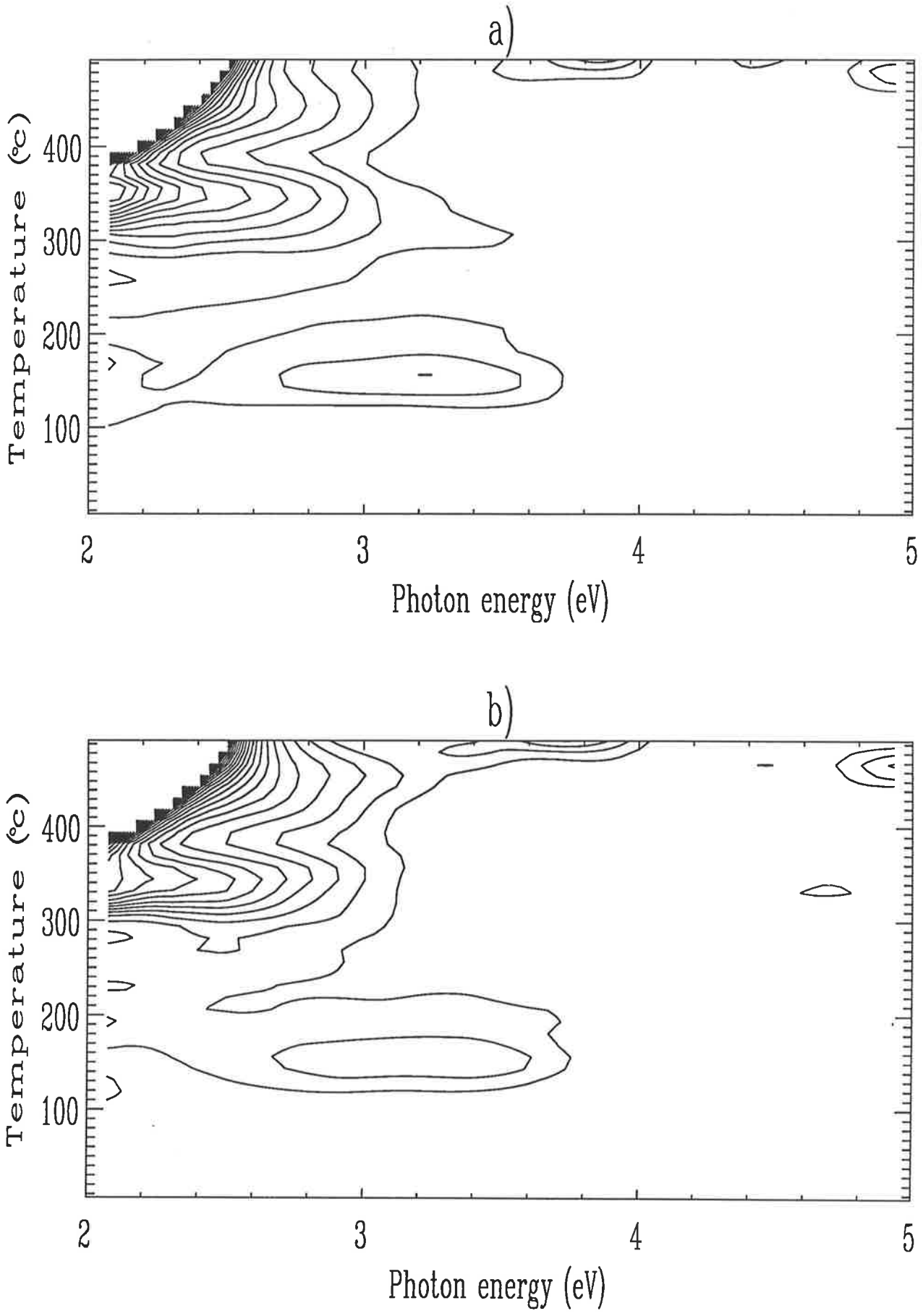

Figure 5.38: Contour diagrams of irradiated PJ quartz for a) 2.5 and b) 8.0 minutes of bleaching by 550 nm light.

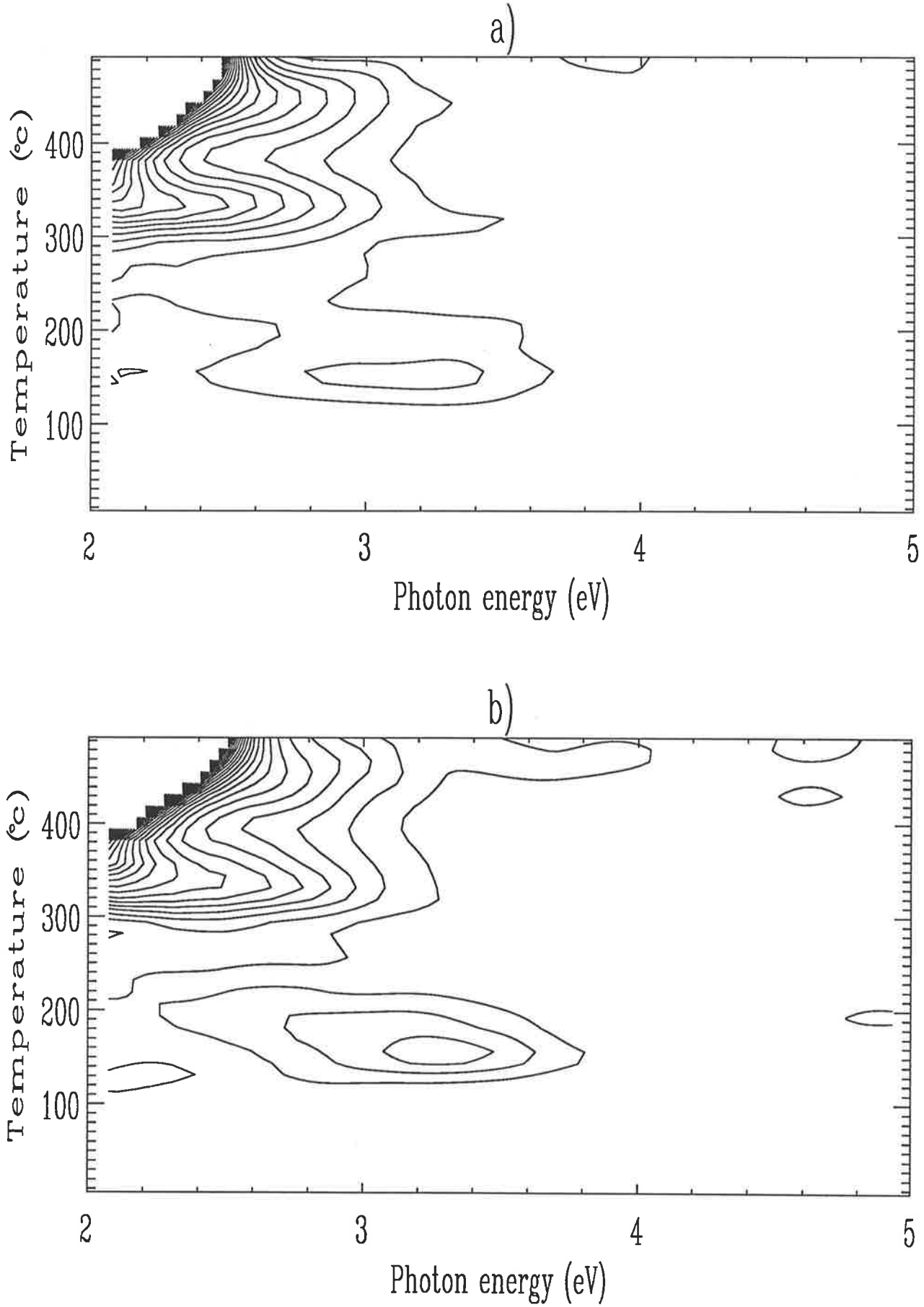

Figure 5.39: Contour diagrams of irradiated PJ quartz for a) 49 and b) 146 minutes of bleaching by 650 nm light.

Comparisons between figure 5.35 and figures 5.37, 5.38 and 5.39 show that the 150°C peak is also bleached to some extent although the effect is not nearly so dramatic as that observed near to 300°C.

Figure 5.40 shows spectra for samples of irradiated PJ and irradiated PJ that had been bleached by 8 minutes of 550 nm light. These spectra were obtained by summing the equivalent spectral elements between 250 and 400°C. The result of subtracting these spectra is also shown in figure 5.40 and clearly shows that only the high energy component was removed by the bleach. The peak of the emission is at 3.23 eV (384 nm) and has a full width at half maximum of about 0.5 eV. Fluctuations at the extremes of the spectral energy region have caused the difference spectrum to become negative there. These negative values are not significant though.

5.5 Discussion

The main conclusions that can be draw from the results of all the quartz samples studied are as follows:

the effect of the bleaching on all the quartz samples was very similar,

for the natural and irradiated samples the high photon energy emission component (above 3.0 eV) at about 300°C appeared to be highly sensitive to the bleaching light and was removed very quickly,

the lower energy component bleached only slowly (if at all for the illumination times used in this study),

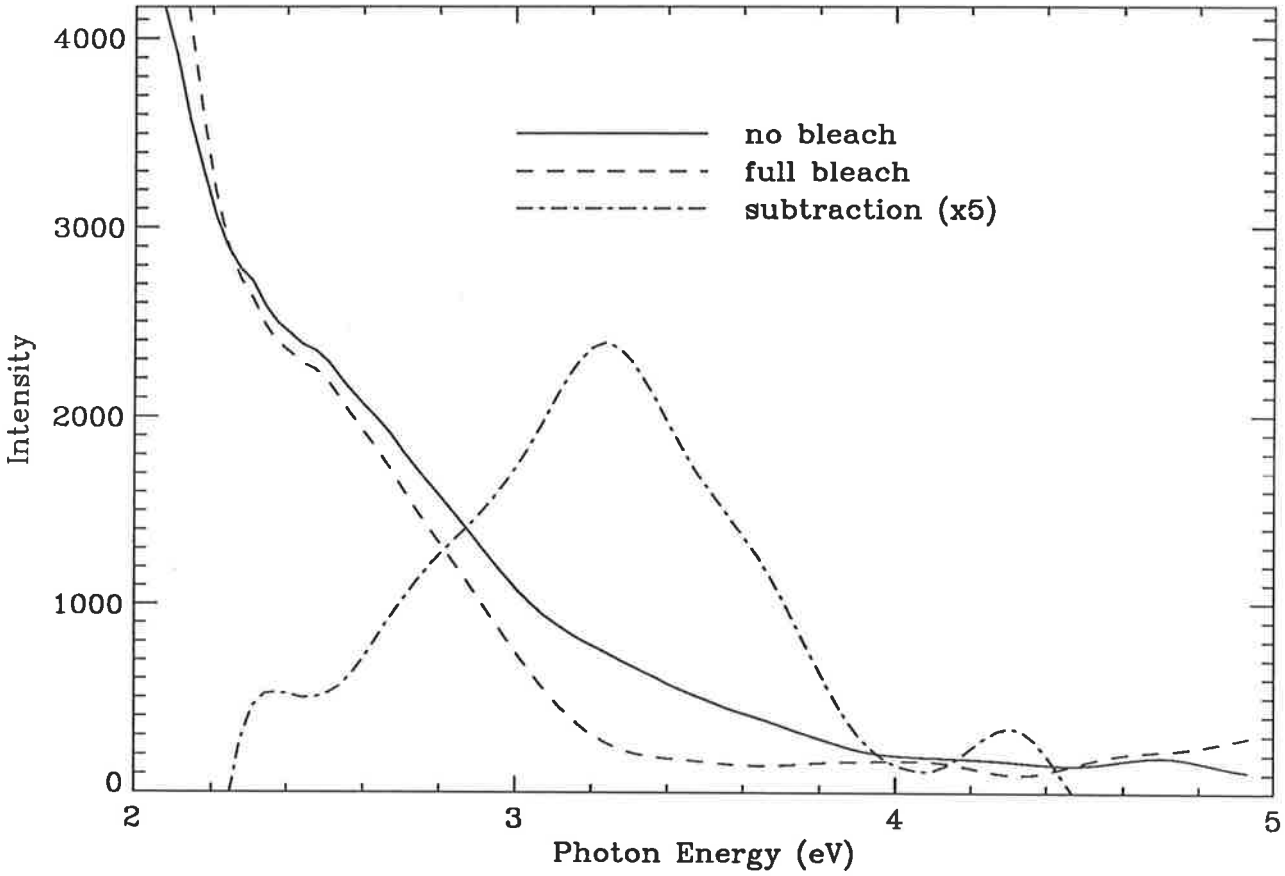

Figure 5.40: Spectra for irradiated PJ and bleached PJ quartz. The third spectrum is the difference between the first two. Negative values are not shown.

the 300°C component was bleached quickly down to a remnant which persisted throughout the sequence of bleaches – the remnant could, of course, be a component that has regenerated during the wait between the bleach and the glow of the sample,

for the natural samples (LW and WK) there was very little growth of the lower temperature peaks after the bleach,

for the irradiated samples there was some indication that a small component of the 150°C was also bleached, although not to the same extent as the 300°C peak,

the bleaching effect of all the three wavelengths did not appear to be significantly different apart from their relative bleaching efficiencies and the suggestion of a wavelength dependence for the bleaching of the 150°C peak in irradiated WK.

Certain of these conclusions have been noted by other workers. Huntley (unpublished data) has used a sequence of narrow band pass filters to measure the wavelength of the photoluminescence emitted during the bleaching of a sample of quartz from the South East of South Australia, near Naracourt. He found a narrow emission peak at about 370 nm (3.35 eV). Also Prescott (unpublished data) has used separate wavelength filters for two separate wavelength regions corresponding to the high and low photon energies discussed here, to show that only the 300°C TL emission from the high photon energy regions is affected. The bleaching, in this case, was performed using both white and yellow light, with a wavelength cutoff of 475 nm.

It is possible to advance some tentative models which may be consistent with the data. The main fact which would seem to mould any initial model would be the observation that the bleaching reduces only the one emission component leaving all the others largely unaffected. If there was only one species of quartz grain type, that is, all the grains were the same, then a model which had the bleached electrons ejected into the conduction band should also reduce the emission below 3.0 eV. One could not get around this by insisting that the recombination cross–section of the high energy component was much higher than for the lower energy emission. This is because at 300°C there is emission in both these energy regions and so the differing cross–sections should apply to the normal TL process as well, that is, there would not be any low energy TL emission at 300°C.

There is some independent evidence (Hashimoto *et al* 1986) that different quartz grains emit their TL at separate wavelengths. This was observed by photographing a disc of quartz grains with colour film. Each grain was dominated by either a red or blue emission. In this case it may be that only one species of grain is subject to bleaching and these grains would have predominantly one type of emission centre corresponding to the high energy region. If the bleaching now proceeds as before with electrons from the 300°C peak being ejected straight into the conduction band, then the same problem as before would arise. That is the low energy component should also be bleached. The tentative explanation of this may well be that the route of the bleached electrons is not direct into the conduction band but is via a second trap or even directly to the emission centre. The results presented in chapter 6 show that the 110°C trap in quartz seems to play an important role in the bleaching mechanism.

The emission from this trap is at about 3.45 eV (360 nm) (see figures 4.31, 4.33, 4.35 and Akber *et al* 1988), close to the subtracted emission band shown in figure 5.40. Conceivably then, the sensitivity of the 300°C trap would be due to the fact that it is closely associated with the 110°C trap. The electrons now reach the conduction band from the 110°C traps and not directly from the 300°C traps. There may well be two populations of 300°C traps, one which is associated with 110°C traps and one which is not. This could explain why there is a remnant of the 300°C peak still evident after bleaching. As mentioned earlier this remnant could also be due to regeneration from shallow peaks and could be tested by further bleaching or by glowing the sample directly after the bleach.

The above discussion is strictly true for only the natural quartz samples. For the irradiated samples the situation is complicated by the generation of TL peaks below 250°C. For most of the samples it is clear that the 150°C peak is also sensitive to the bleaching light, although not to the same extent as the 300°C peak. The thermal depth of the 150°C trap would be significantly less than for the 300°C trap, but if the electrons were bleached straight into the conduction band then a much smaller remnant peak should be observed. Hence a similar mechanism to that for the 300°C peak may be in operation for this peak.

The results and conclusions of this chapter will be used in chapter 7 to develop realistic theoretical models which can be tested on a computer.

In the next chapter, the experimental investigation of the bleaching process is continued. The actual photoluminescent decay signal is measured while samples were held at different temperatures. This will provide data which also can be used to

compare with the computer generated decay curves described in chapter 7.

Chapter 6

Photoluminescence of Quartz

6.1 Introduction

In the previous chapter the results were presented of investigations of the TL spectra of several natural and bleached quartz samples. In this chapter an experiment and its results are described which were designed to measure the photo–luminescence (PL) of a quartz sample whilst it was being illuminated with intense optical light.

This method has been developed over the past few years as a new tool for dating sediments, loess and sand–dunes. The usual procedure is to shine the 514 nm light from an Argon ion laser onto a disc loaded with the sample and then to measure the PL emitted. The detector is protected from the scattered laser light by a stack of filters which transmit the PL from the sample only (Huntley *et al* 1985).

The intention of the present study was to modify the existing apparatus, described in chapter three, and , in conjunction with a 150 W Xenon lamp, to measure the PL *versus* bleaching time decay curves for two types of quartz as each was held at different temperatures ranging from room temperature up to 150°C in steps of 25°C. The aim was to attempt to understand which of the traps and centres were involved in the decay process during the bleach. The results presented in this chapter also provided

experimental data to compare with the solutions of the mathematical models of the decay process which are given in the next chapter.

6.2 Experimental Apparatus

Modifications made to the existing apparatus were slight and involved changes mainly to the laser input calibration assembly. This piece of apparatus had been designed to fit on top of the glow oven, to provide an artificial sample disc of randomly scattered laser light, in order to mimic a normal sample disc. The artificial disc consisting of a plastic diffuser and two sheets of tissue paper was then illuminated from below with a HeNe laser.

Figure 6.1 shows the new experimental setup. The light from a 150W Xenon lamp whose output was stable to within a few percent over many hours after an initial 15 minute warmup was focussed by a 60 cm focal length glass lens through, firstly a 550 nm Corion band–pass interference filter and then through two sheets of a Kodak gelatin filter (number "15"). The transmission curve of the band–pass filter is given in figure 5.3 and figure 6.2 shows the transmission curve of the gelatin filter. This combination attenuated the Xenon lamp emission below 500 nm to a negligible level. The resulting light was then guided onto the sample holder by two aluminium coated, front surface mirrors.

The aluminium sample holder itself was supported by a metal stand whose base was fixed onto the oven heating strip by thermal compound and this allowed the sample to be illuminated at different temperatures up to 150°C. The sample holder was detachable, so that samples could be loaded more conveniently. A slight modifi-

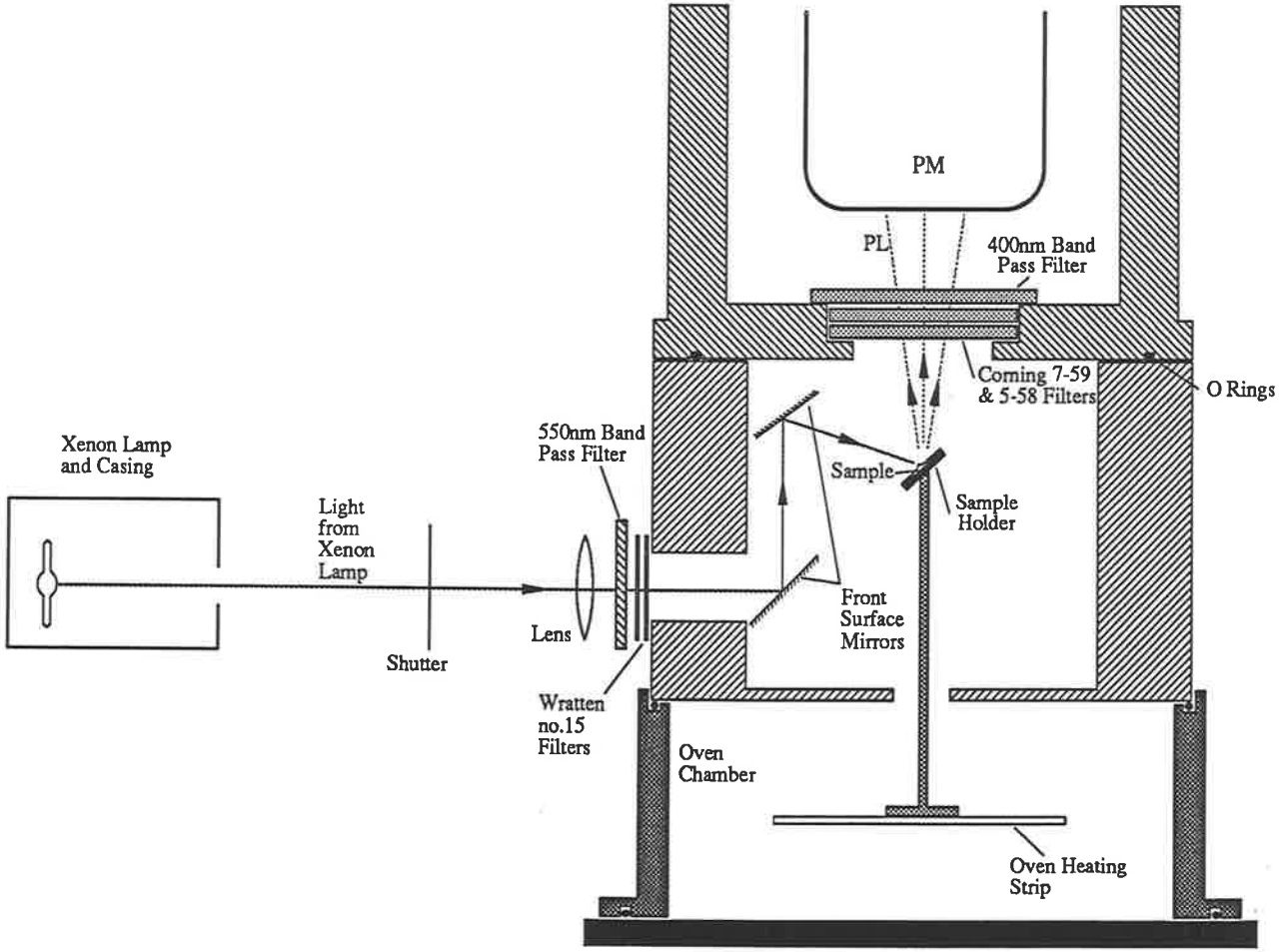

Figure 6.1: Schematic diagram showing the modified 3–D apparatus for measuring the PL emitted by the quartz samples.

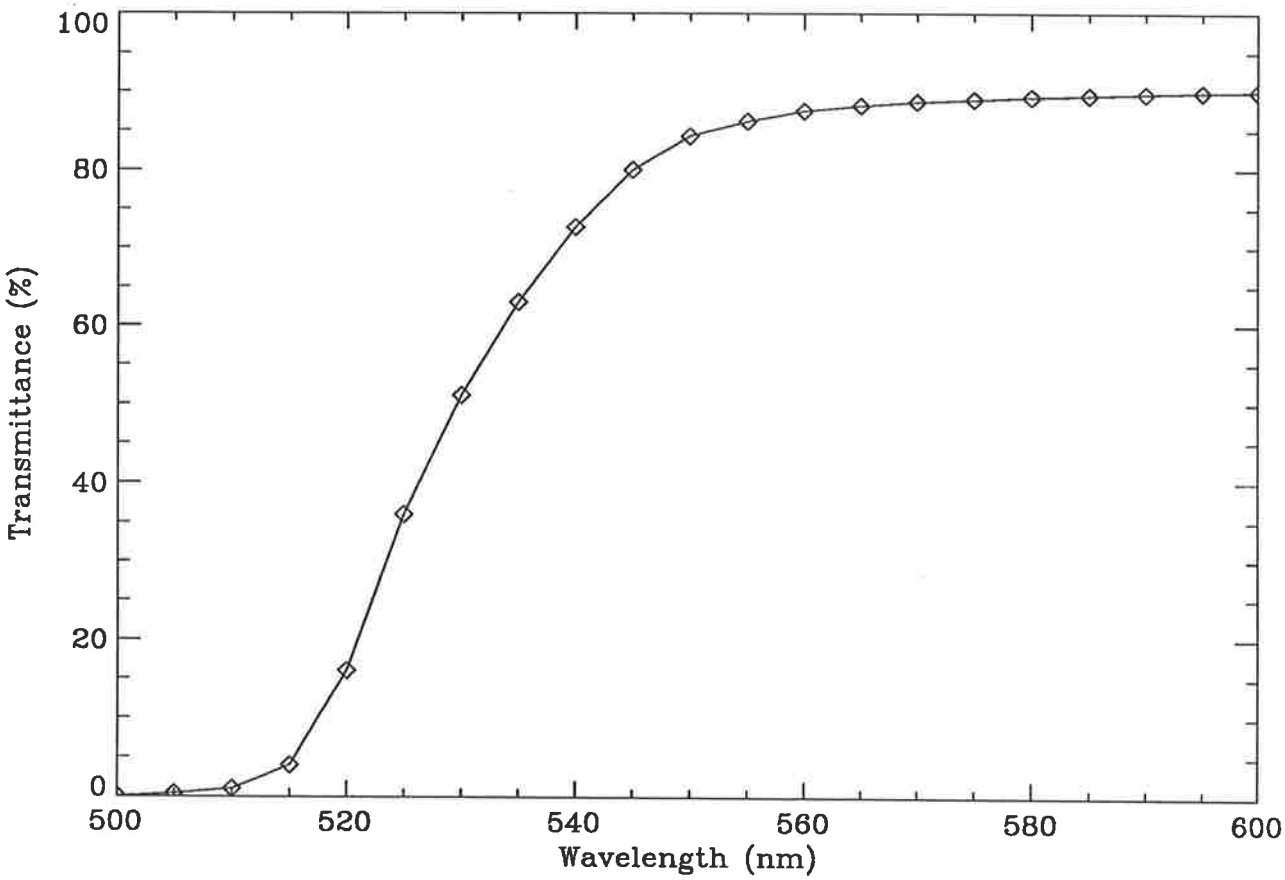

Figure 6.2: Graph of the transmission curve for the Kodak number "15" gelatin filter.

cation was made to the existing electronics in order to isolate the ramp signal, which normally controls the heating rate, from the heating strip. The temperature could then be controlled manually by the operator. A simple switch incorporated into the electronics ensured convenient change between normal automatic and manual operation.

The PL light emitted from the sample was detected by an EMI 9635QA PMT operated in photon counting mode and the PMT was protected from the scattered Xenon lamp light by a combination of a Corion 400 nm band–pass filter, a Corning 7–59 glass filter and a Corning 5–58 glass filter. A negligible fraction of the bleaching light was transmitted through this stack of filters. The resultant transmission curve of these three filters is shown in figure 6.3.

Two different quartz samples were used for the experiments: Lake Woods and Wokewine. The chemical preparation of these samples was identical to that described in chapter 5. East Bank and Puritjarra quartz were not used due to their low natural emission.

The decay curves were measured at room temperature 50°C, 75°C, 100°C, 125°C and 150°C for both LW and WK quartz. The total shine time was eight minutes for both samples.

The method of bleaching which is also called "shining" when measuring the PL, was to set the computer control program running and to then manually remove the light stop or shutter (see figure 6.1) about one second later. This computer program was identical to that used for normal operation. For these PL studies the method of normalisation was to shine the sample initially for about one second at room tem-

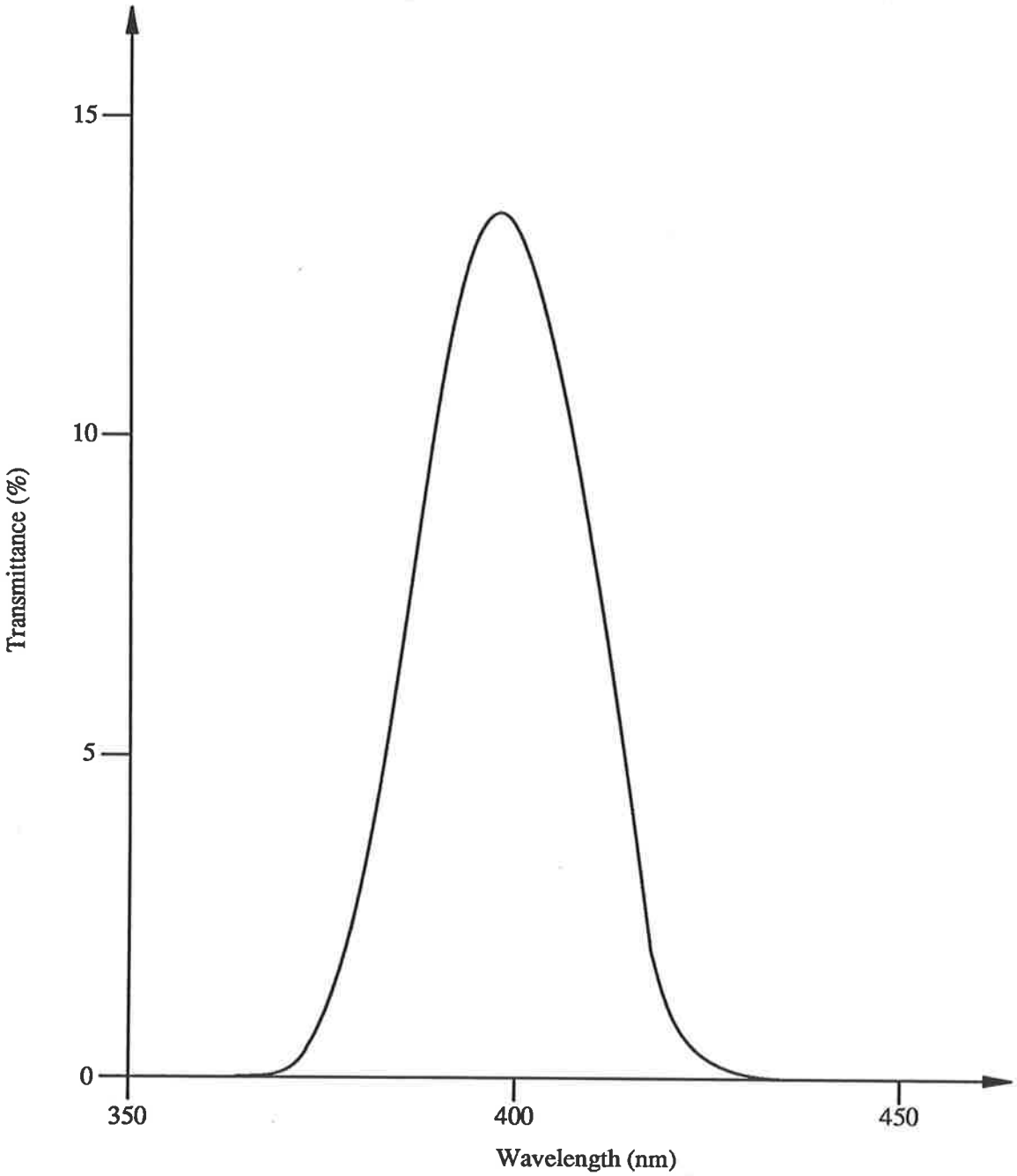

Figure 6.3: Graph of the overall transmission curve for the combination of filters between the sample and the PMT.

perature before any subsequent measurements were made. This procedure was also performed before the samples were heated to their respective elevated temperatures for continuous shining. This allowed the decay curves at different temperatures to be compared quantitatively.

It was anticipated that there would be a considerable thermal lag between the heater plate and the sample holder. Therefore the temperature dial on the apparatus was calibrated against the temperature of the sample holder measured with a separate chromel–alumel thermocouple.

6.3 Results

Figures 6.4a and 6.4b show the decay curves at room temperature for both LW and WK quartz. The graphs show the PL against the time, t, with both linear and logarithmic ordinate axes. There are several important features common to both curves which are immediately obvious. Firstly there is an initial very sharp rise in the PL signal when the shining begins – this rise is essentially instantaneous and any lag can be attributed to the time for the shutter to open. Secondly there is a rapid fall in the PL after the maximum followed by a "tail" of PL which decays slowly over the remaining shining time.

The light intensities of the 150 W Xenon lamp at the sample and the 550 nm light intensity of the Solar Simulator (used for the bleaching experiments described earlier) were both measured using an Oriel Radiometer. The Solar Simulator intensity was found to be (75±10)% of the intensity of the 150 W Xenon lamp. Hence the time scale of the decay curve compares quite well with the observed amount of 550 nm

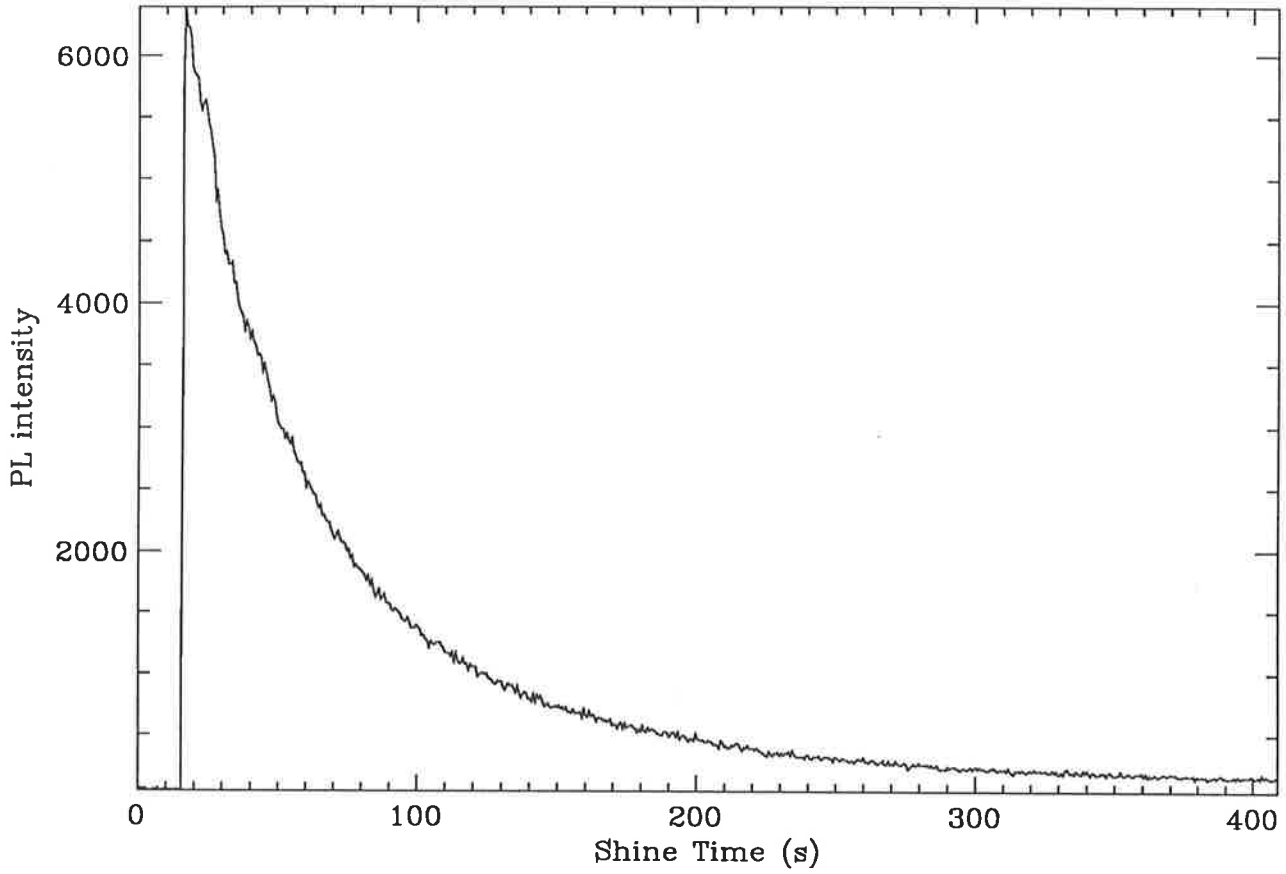

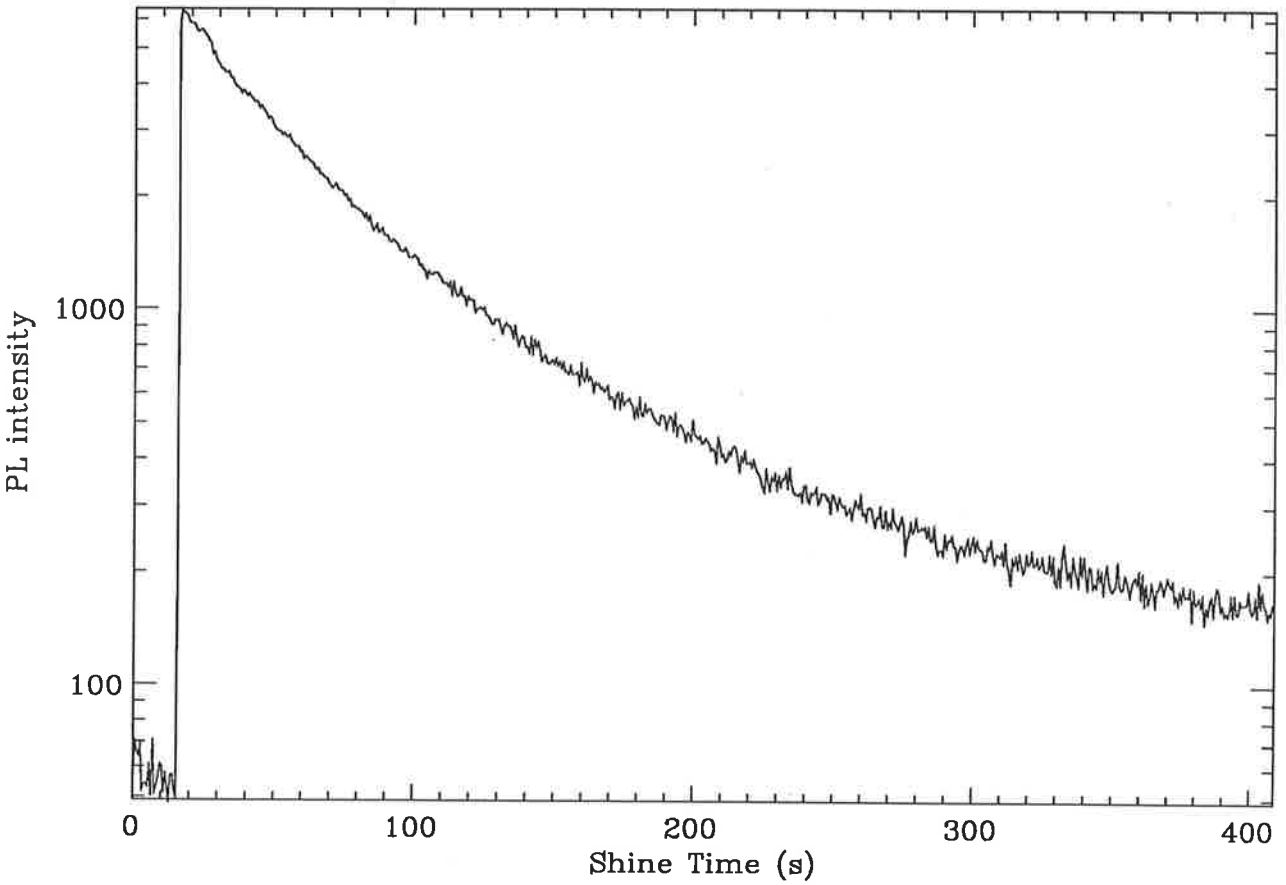

Figure 6.4a: PL decay curves at room temperature for LW. The top figure is with a linear ordinate axis and the bottom a logarithmic axis.

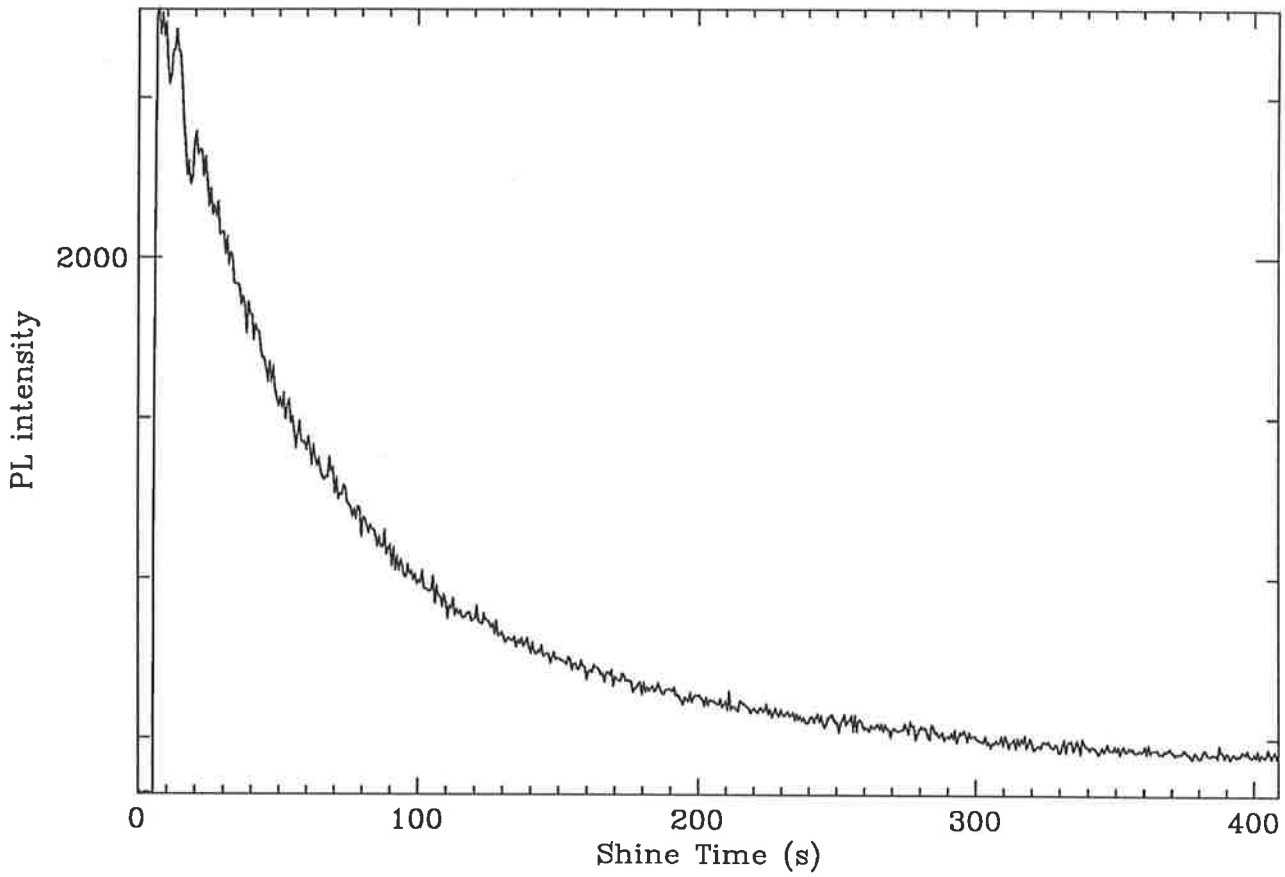

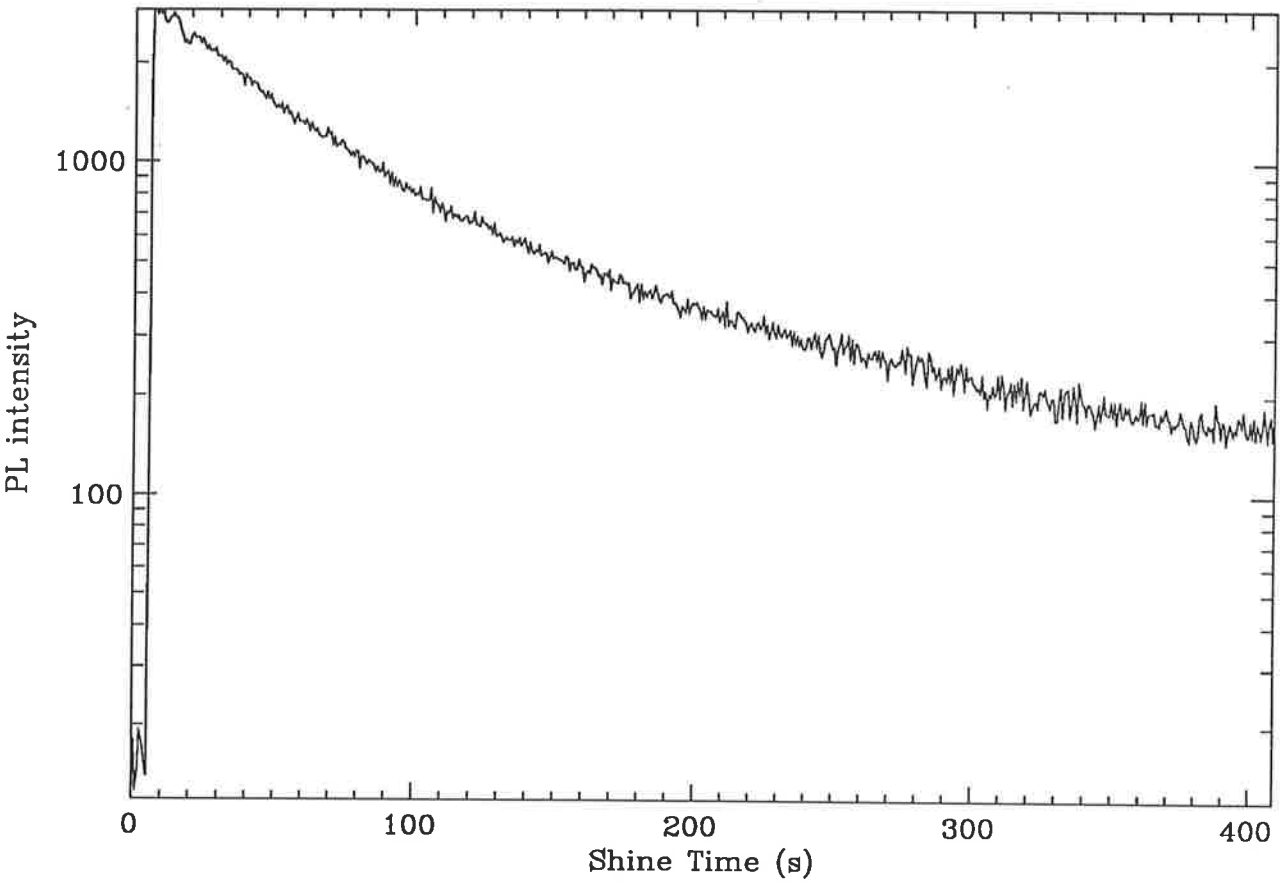

Figure 6.4b: PL decay curves at room temperature for WK. The top figure is with a linear ordinate axis and the bottom a logarithmic axis.

solar simulator light required to remove the 325°C TL glow peak (Spooner 1987).

Figures 6.5 and 6.6 show the normalised decay curves plotted separately for both LW and WK when the samples were held at elevated temperatures up to 150°C. This figure shows the decay curves plotted twice, with a linear ordinate axis and a logarithmic ordinate axis. Figure 6.7 shows these data plotted together which allows a better comparison between the curves. The form or shape of the 125°C and the 150°C decay curves are practically the same. This may indicate that the decay route of the bleached charge is the same at temperatures above about 120°C. Also noticeable is the fact that for all the curves the initial rise remains just as sharp as for the curves at room temperature.

Clearly, the holding temperature has a crucial effect on the decay curves of both LW and WK. Figure 6.8 shows a plot of the number of counts in the first 20s of the shine against the holding temperature for the two samples. As the temperature increases the initial photoluminescence efficiency rises until it reaches a plateau at approximately 110°C for both LW and WK. At 150°C a decrease is observed which may be attributed to thermal quenching of the emission centres.

There are differences between the diagrams in figure 6.7. For LW the decay at 50°C is much steeper initially than for the corresponding decay for WK and in general, for LW, the temperature appears to have acted as though the 110°C trap were shallower than for the WK samples.

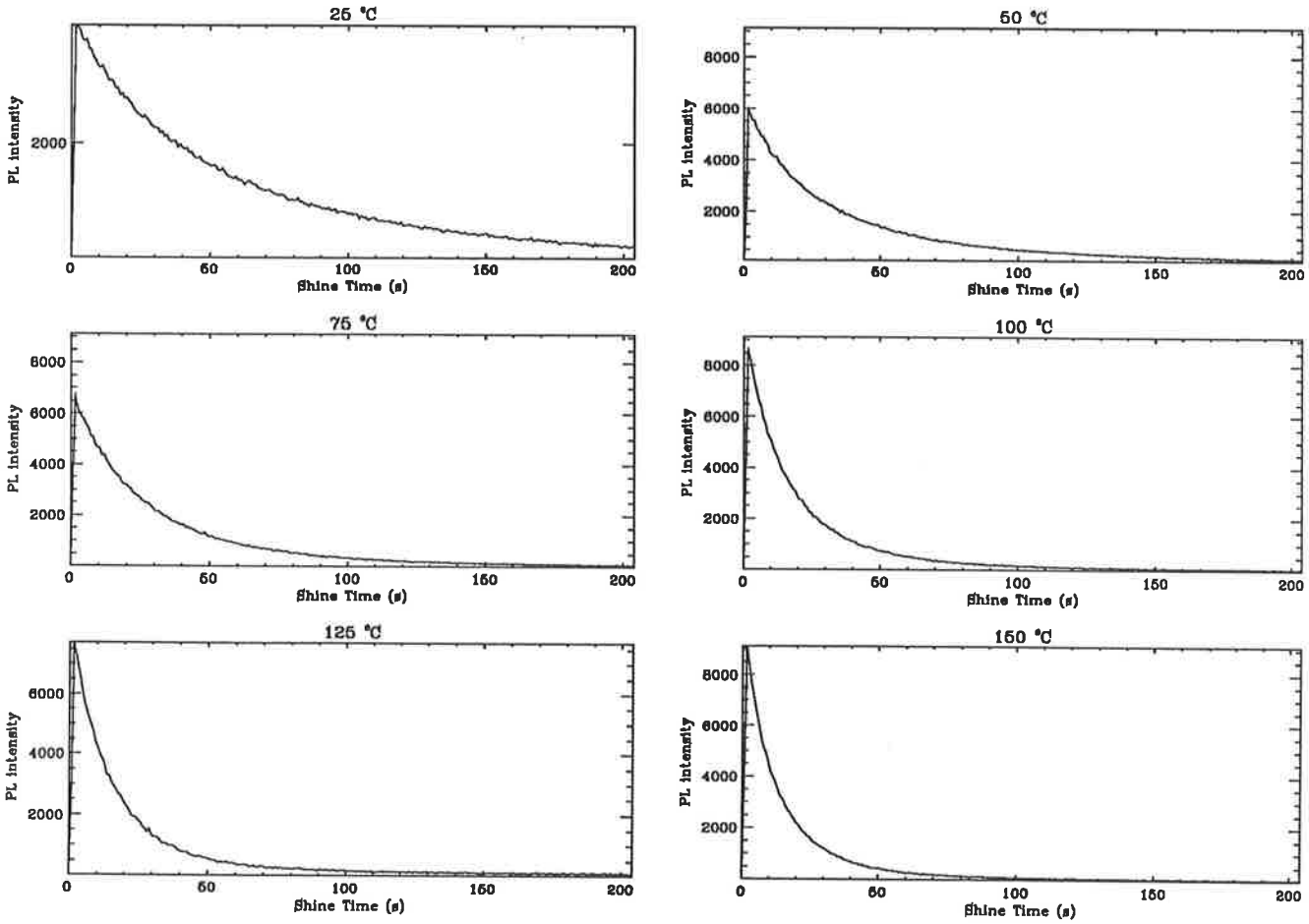

Figure 6.5a: LW decay curves for various temperatures shown above each plot.

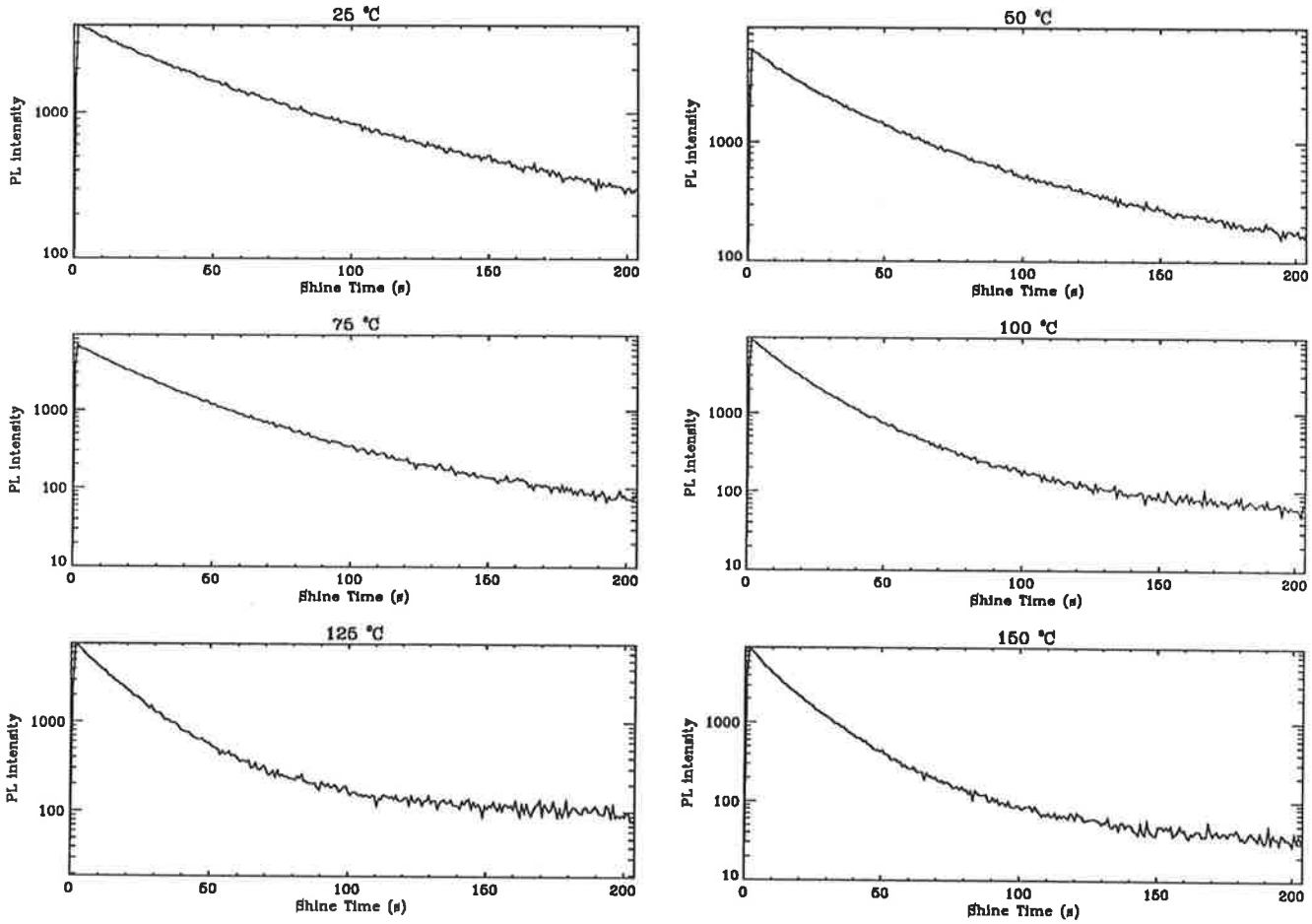

Figure 6.5b: LW decay curves plotted with a logarithmic ordinate axis for various temperatures shown above each plot.

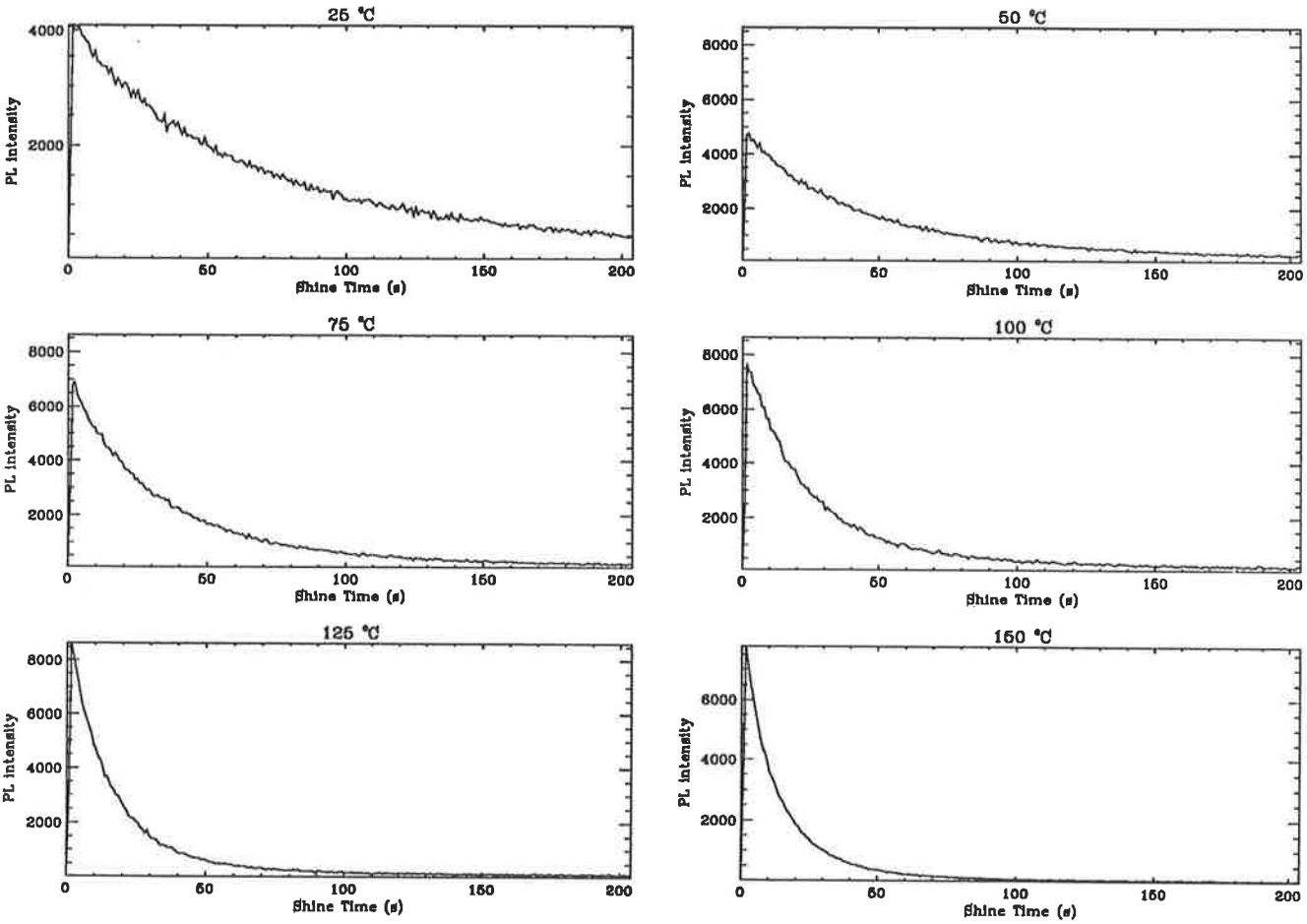

Figure 6.6a: WK decay curves for various temperatures shown above each plot.

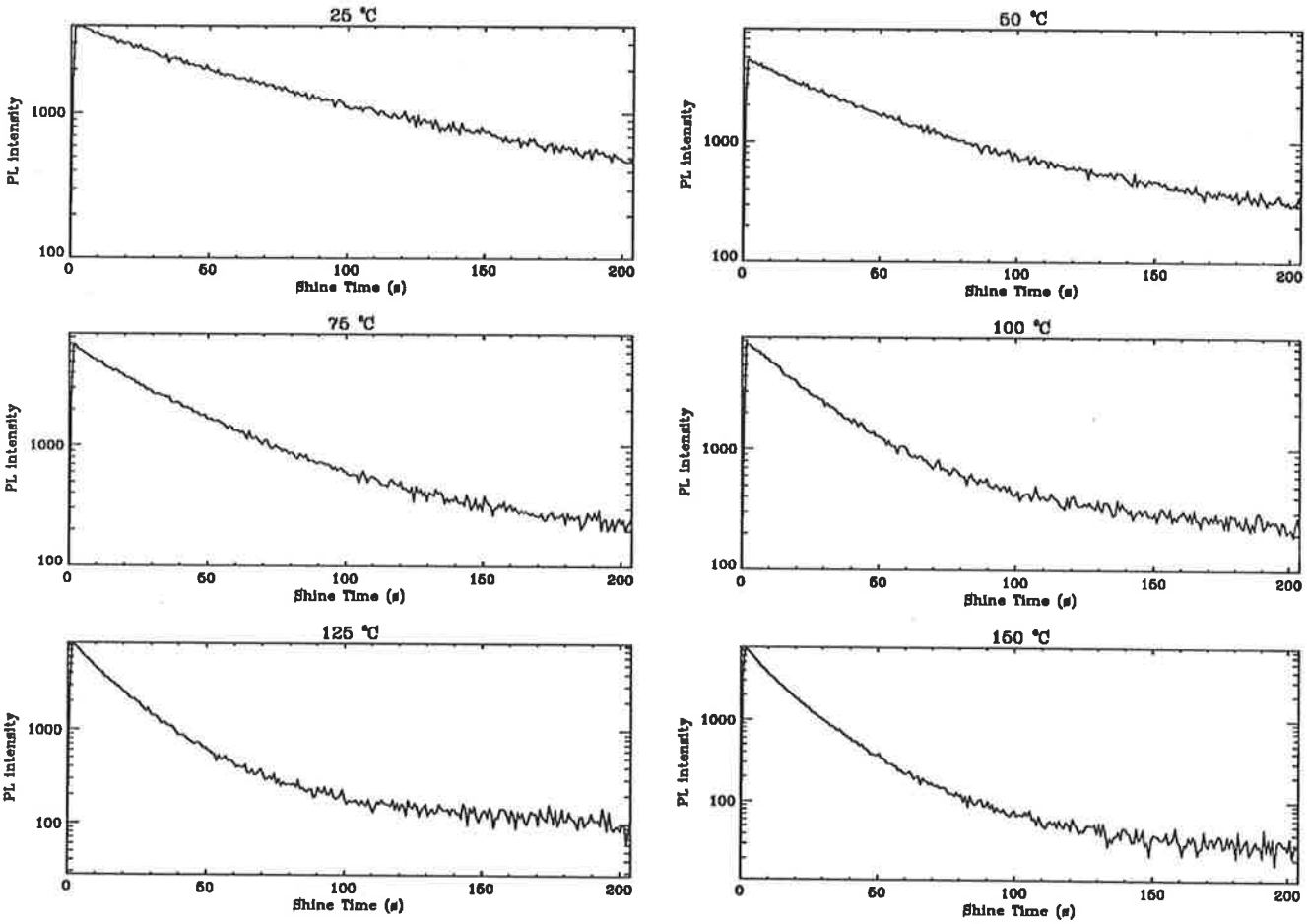

Figure 6.6b: WK decay curves plotted with a logarithmic ordinate axis for various temperatures shown above each plot.

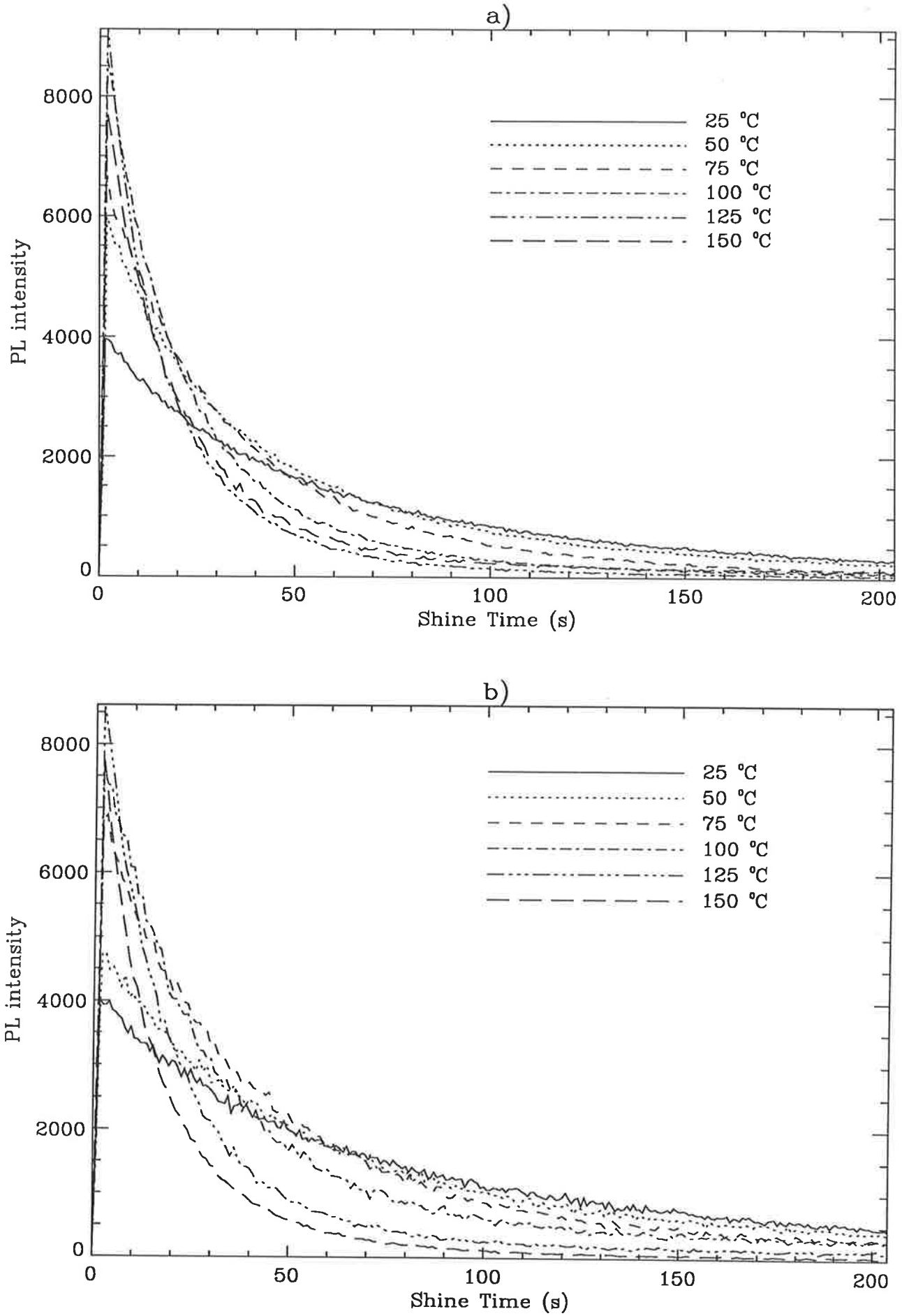

Figure 6.7: Decay curves for various temperatures plotted together for a) LW and b) WK.

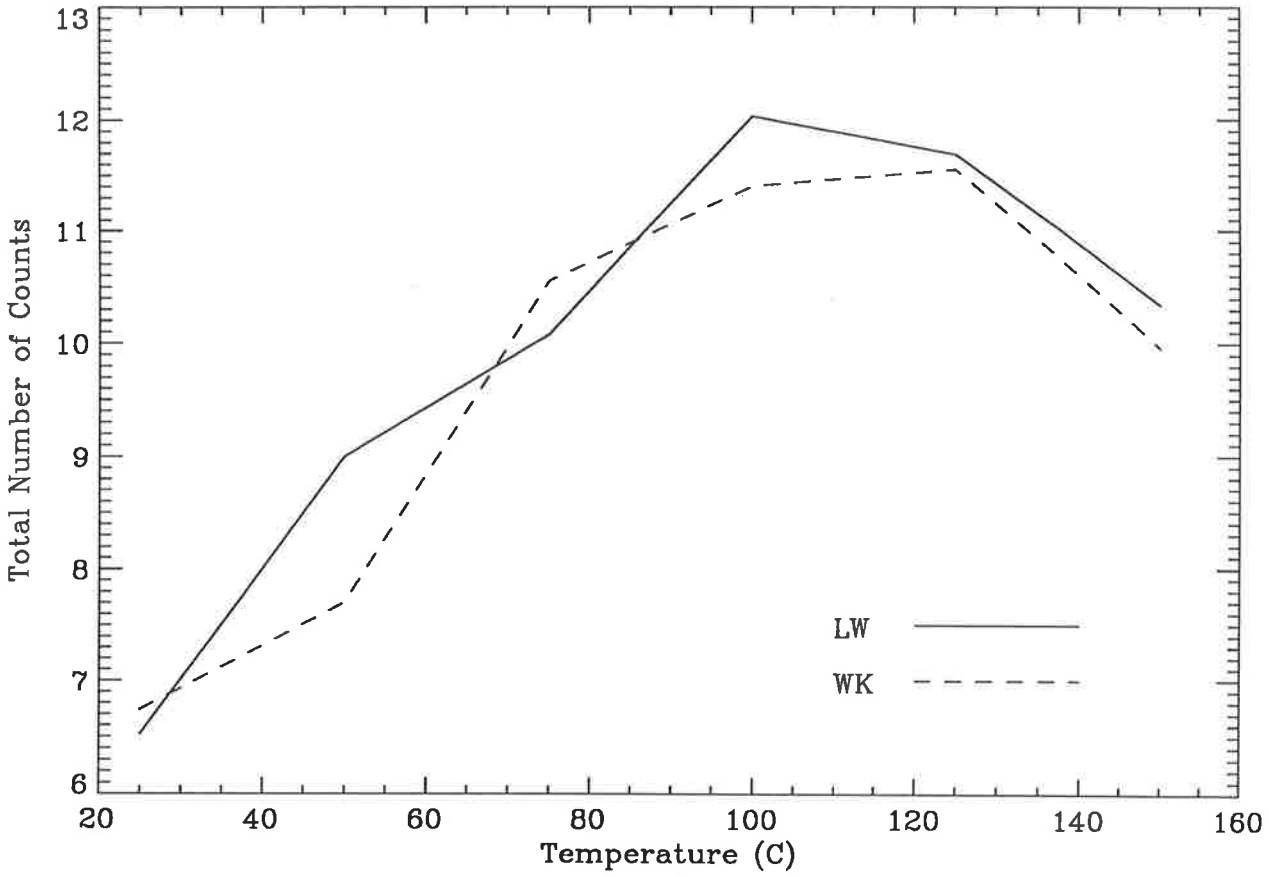

Figure 6.8: Graph of the total number of counts against the temperature for LW and WK.

6.4 Discussion

The results from this chapter have shown that it is possible to use relatively cheap optical components in order to measure the photoluminescence from natural quartz samples.

The logarithmic plots of the decay curves show that for both LW and WK the decay is not exponential since a straight line is not obtained. This means that the decay process cannot be viewed as simply the emptying of electrons from one trap followed by recombination. The evidence for "tails" or slowly decaying components is clearest on the logarithmic plots for temperatures of 100°C and above. The tail shows up as a distinct region above about 120s whose gradient is much less than for the early part of the bleach.

The time constants obtained by fitting straight lines to the following time regions: $0 < t(s) < 30$ and $130 < t(s) < 200$, for the 100°C decay curves in figures 6.5b and 6.6b are about 18s and 165s and 22s and 175s respectively. The decay constants from the logarithmic plots in figures 6.4a and 6.4b for the time region $300 < t(s)$ are about 350s, significantly greater than for the equivalent region at 100°C. If these tails are due to the slower bleaching of secondary traps which have retrapped ejected charge carriers then this may suggest that a likely trap would be near to 150°C. At 100°C thermal effects would become significant for such a trap and hence reduce the time constant. The results from chapter 5 would seem to contradict this model however, since the 2–D glow curves of natural and bleached LW and WK show very little TL at these temperatures.

The differences seen between the decay curves in figure 6.7 may indicate that the

thermal depth of the shallow competitor trap, which gives rise to the temperature effect, may be somewhat less for LW than for WK or that the concentration of these traps is different.

A number of decay models are studied in the next chapter where the results from this chapter are compared with the results of the theoretical models.

Chapter 7

Modelling of the Photoluminescence Process

In the previous two chapters experimental results were presented about the bleaching process in quartz. The results from chapter 5 will be used in this chapter to help in the development of reaistic theoretical models, in particularly the last one. Chapter 6 provides the direct experimental data with which to compare the results from the theoretical calculations described in this chapter.

7.1 Introduction

In the past 15 years the numerical solution of the differential equations describing the movement of charge carriers has been useful in understanding several TL–related processes, for example the non–linearity of TL growth curves applied to the cases of ionizing radiation (Maxia 1978, Maxia 1980, McKeever *et al* 1980, Chen *et al* 1981 and Chen *et al* 1988) and to optical bleaching (Levy 1982 and Smith in press).

It seemed possible that the techniques of numerical modelling could be applied to the case of the photoluminescence (PL) decay curves shown in the previous chapter. It was hoped that by comparing the results of several different models with the ex-

perimentally obtained decay curves for quartz, the relationships between the bands, traps and centres participating in the PL process would become clearer.

Levy (1982) has used kinetic modelling to examine the effect of optical bleaching on the TL, mainly of feldspars, for the simple cases of a single bleachable trap plus a centre and also the same system but with one or more competing traps. He showed that if retrapping was not negligible the bleaching curves (graphs of the TL versus bleaching time) were not exponential and that the bleaching cannot reduce the TL to zero in a limited time.

Smith (in press) has used an iterative procedure to model the movement of charge in quartz during its laser exposure (usually refered to as its "shine"). This model has incorporated a thermally shallow trap (the 110°C trap in quartz) similar to that in section 7.3.4 and acceptable agreement was obtained for part of the PL decay curve.

In the present study it is not the curves of TL against bleach time which were considered but the PL versus bleach time. Additionally, thermal effects were introduced into the models. This chapter attempts to model the experimental decay curves of Wokewine quartz presented in chapter 6 (figure 6.7).

There were several features of the experimental decay curves which which it was hoped could be reproduced by the mathematical models:

the initial rapid rise in the PL following the start of the illumination,

the rapid initial decay of the PL,

the long slowly decaying PL "tails" and

quantitative agreement between the decay curves due to the temperature dependence of the decay process.

7.2 Analysis

The general methodology adopted followed that of Chen *et al* (1981). The simultaneous differential equations described the relationship between the number of charge carriers, whether in traps or in the conduction band, at a particular time and a numerical iterative method allowed the evolution of the system to be studied for different initial conditions. The advantage of solving the equations numerically was that the solutions are more exact than analytical methods which often need simplifying. Also quite complex models can be studied for which analytical solutions would be either extremely complex or impossible to obtain.

The numerical algorithm (written in Pascal) chosen to solve the equations was a fourth order Runge–Kutta method which was implemented on a Sun Systems File-server mainframe computer.

In the paper by Levy (1982) graphs were given of the TL remaining after the bleach. The case of PL versus time was different because the TL is not proportional to the PL. In fact the TL was proportional to the number of charge carriers trapped whereas the PL was proportional to the rate at which the bleached electrons recombined with the holes trapped at the centres.

7.2.1 Notation

Some consistent notational conventions were adopted to make the equations simpler to read, especially in conjunction with their accompanying diagram.

The time was always denoted by t, and a lower case n denoted the number of charge carriers at the instant t and the subscripts attached to n identified which

trap or band was being referred to. Hence n_C was the number of electrons in the conduction band and n_h the number of holes. An upper case A was the transition probability of the charge carrier – the 2 subscripts and their order referring to the two states taking part in the transition and the direction of the transition. Thus A_r was always the recombination transition probability and A_{1C} was the transition probability from trap 1 to the conduction band. An upper case N and its subscript signified the density of traps or centres and was thus a constant during the calculation. The bleaching effect was denoted by a lower case f (whose dimensions were the same as that for a transition probability multiplied by the appropriate n) with the meaning of the subscripts as before.

7.3 Results

7.3.1 One Trap Model

This model was the simplest one that could be studied. Figure 7.1 shows a simplified band diagram showing the electron and hole trap relative to the conduction and valence bands The bleaching light (with intensity given by f_{1C}) removed electrons from their traps into the conduction band where they could recombine with holes trapped at centres (resulting in PL) or where they could be retrapped at empty electron traps (whose number is given by $N_1 - n_1$).

Figure 7.2 shows the plots of the PL against the shine time (arbitrary units) determined by the following kinetic equations:

$$\frac{dn_1}{dt} = -f_{1C}n_1 + A_{C1}n_C(N_1 - n_1), \tag{7.1}$$

$$\frac{dn_C}{dt} = f_{1C}n_1 - A_{C1}n_C(N_1 - n_1) - n_C A_r n_h, \tag{7.2}$$

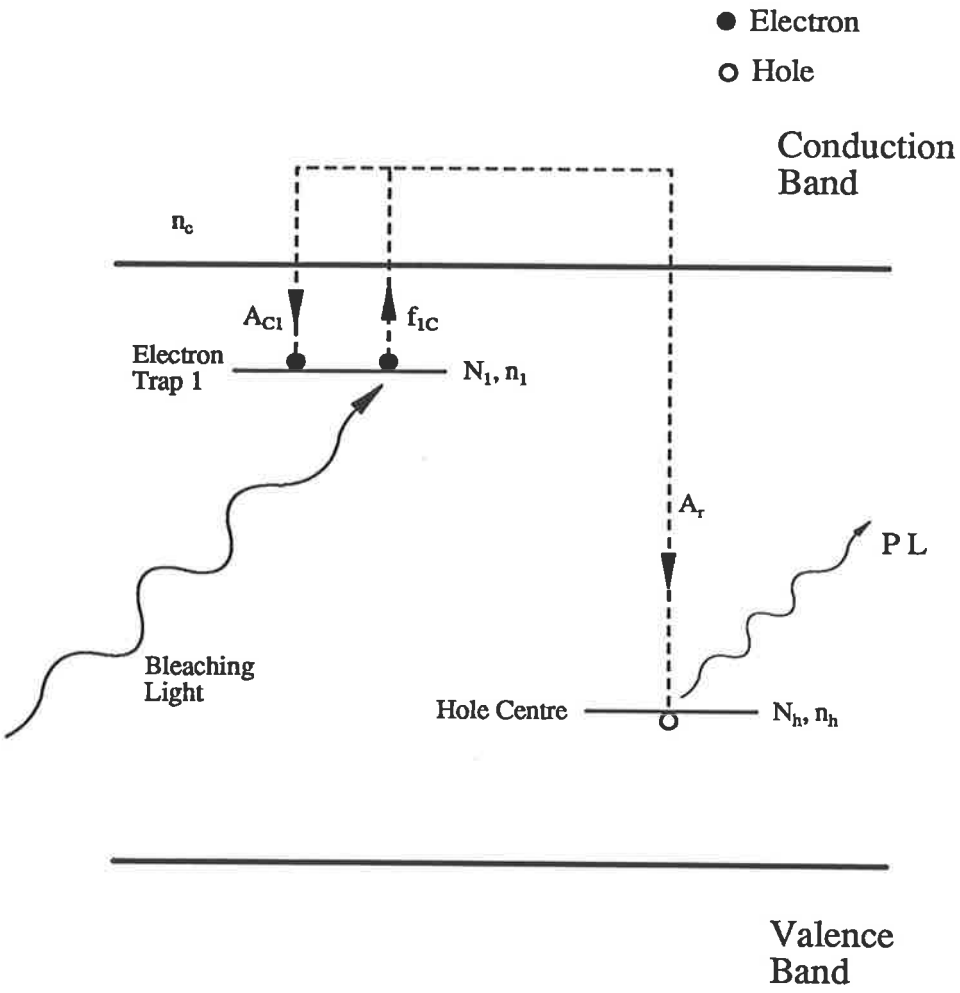

Figure 7.1: Schematic band diagram for the one trap model. The dotted lines indicate the general trajectory of the electrons and the arrows the direction of the transition.

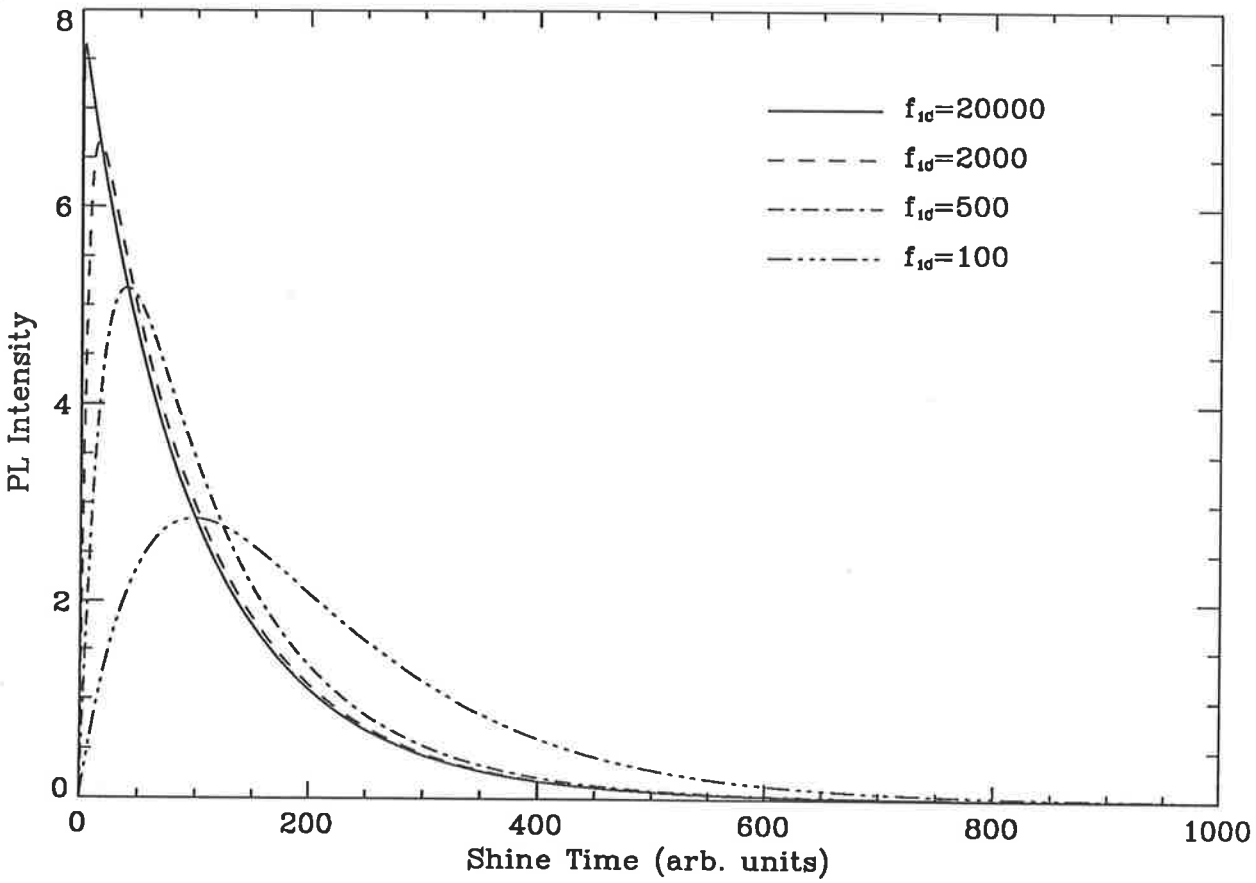

Figure 7.2: Results, for various values of f_{1C}, for the one trap model for $A_{C1} = 0$. The other parameters were: $N_1 = 1 \times 10^{12}$, $A_r = 1 \times 10^{-10}$.

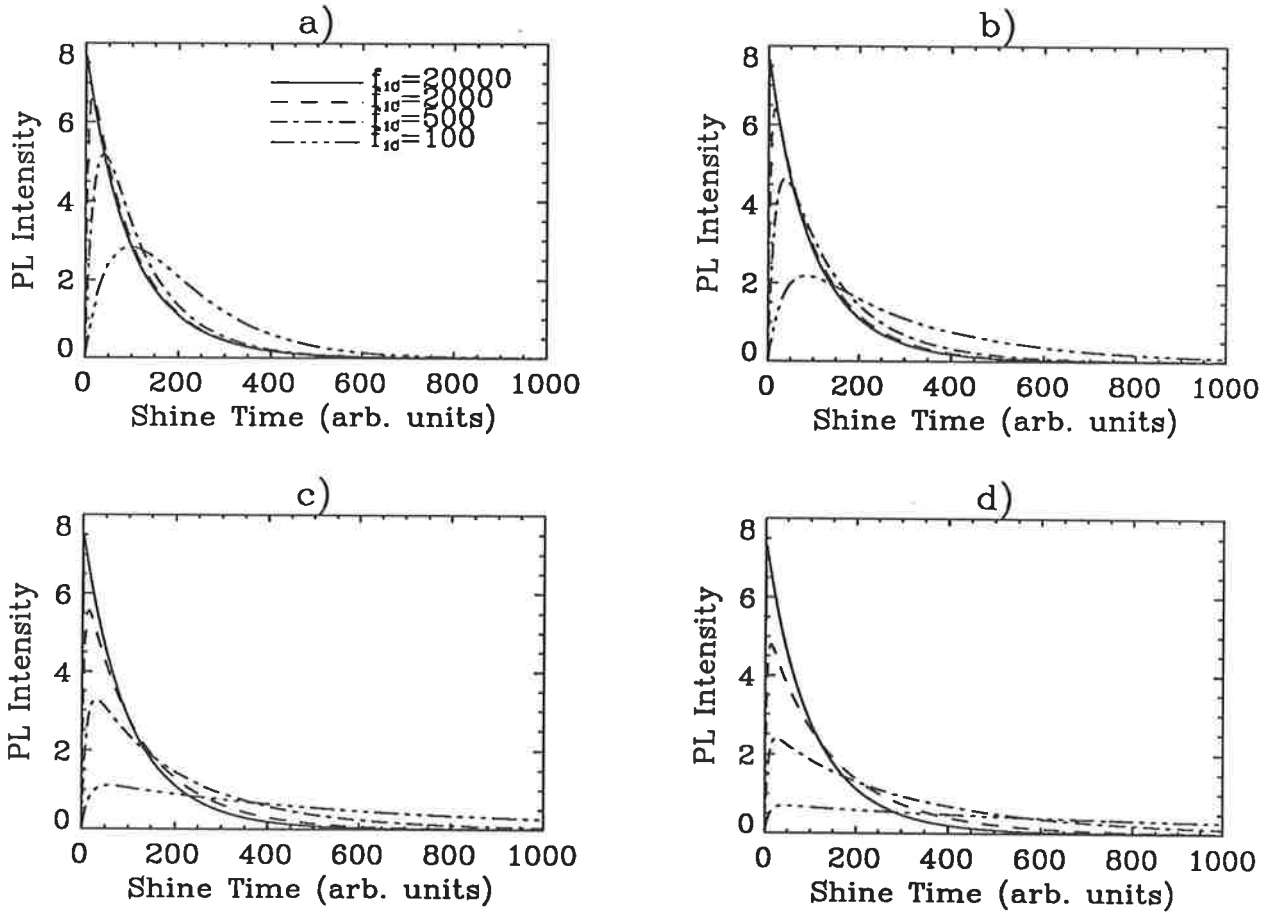

Figure 7.3: Results, for various values of f_{1C}, for the one trap model for: a) $A_{C1} = 1 \times 10^{-12}$, b) $A_{C1} = 1 \times 10^{-10}$, c) $A_{C1} = 5 \times 10^{-10}$ and d) $A_{C1} = 1 \times 10^{-9}$. The other parameters were: $N_1 = 1 \times 10^{12}$, $A_r = 1 \times 10^{-10}$.

$$\frac{dn_h}{dt} = -n_C A_r n_h. \tag{7.3}$$

In this figure A_{C1} was set to zero (that is, no retrapping) with several values of the bleaching intensity f_{1C}. Clearly for low values of f_{1C} the experimentally observed sharp initial rise in the PL was not observed since the number of electrons in the conduction band needed a finite time to build up. For higher values of f_{1C} the rate of promotion of electrons into the conduction band was much greater than the rate of decrease due to recombination with holes, so that all the electrons were pumped into the conduction band with little recombination. The electrons then recombined with the holes giving an exponential decay. Obviously, since the electron trap here is meant to represent the 325°C quartz trap, there was no temperature dependence (assuming the other parameters are not temperature dependent) and also there was no slowly decaying tail.

In figure 7.3 the value of A_{C1} (the retrapping probability of the electron trap) was varied from 10^{-12} to 10^{-9}. For plots a), b) and c) there appears to be little difference from figure 7.2. However when A_{C1} started to compete significantly with A_r (in curve d))there was a major change in the form of the decay curves. For all values of f_{1C} (except for $f_{1C} = 20000$) the initial rise was much sharper, with the peak value of the curve decreasing. This was most evident for the lower 2 values of f_{1C}. Also the decay from this peak value was much slower, indeed the decay curve for $f_{1C} = 100$ seems almost flat. The interpretation of this was that increasing the value of A_{C1} effectively reduces the value of A_r through greater competition, which means that the electrons have more time to be pumped into the conduction band without much recombination and the competition from the electron trap ensures that the number of electrons in

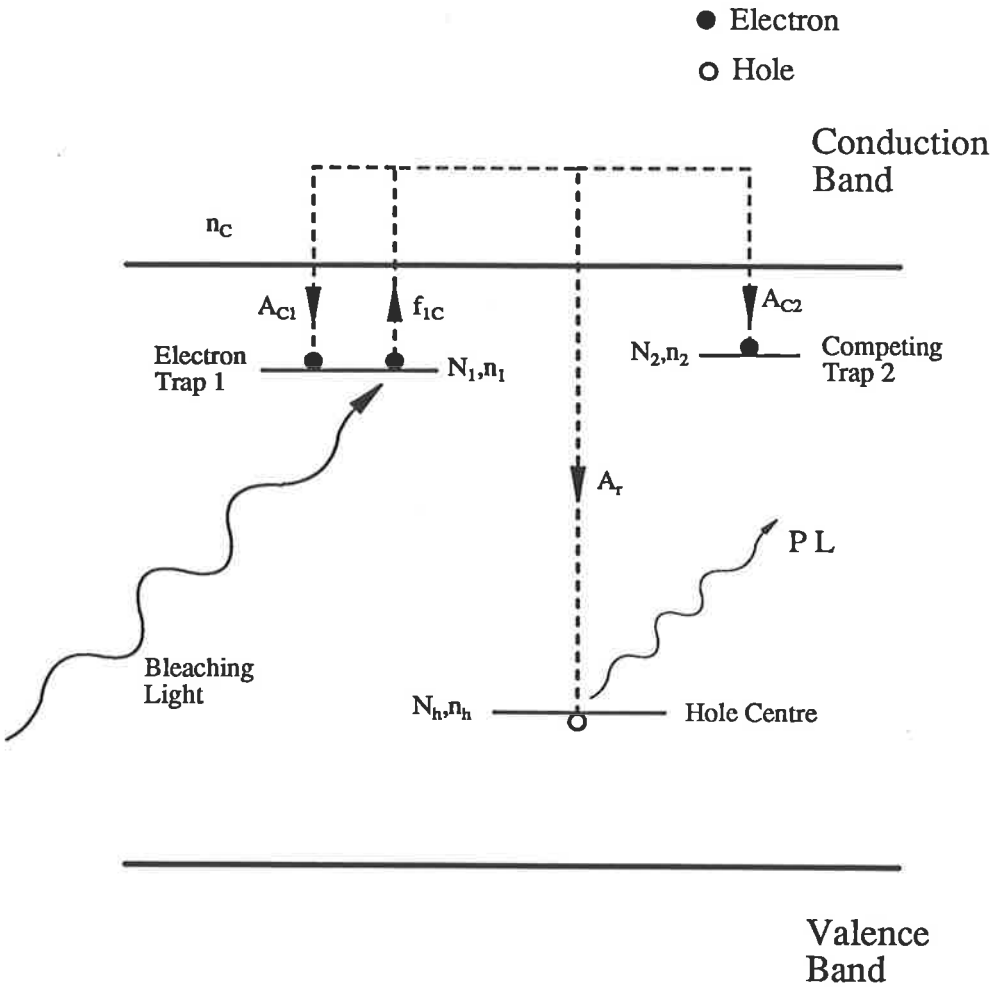

Figure 7.4: Schematic band diagram for the one trap with a competitor trap model. The dotted lines indicate the general trajectory of the electrons and the arrows the direction of the transition.

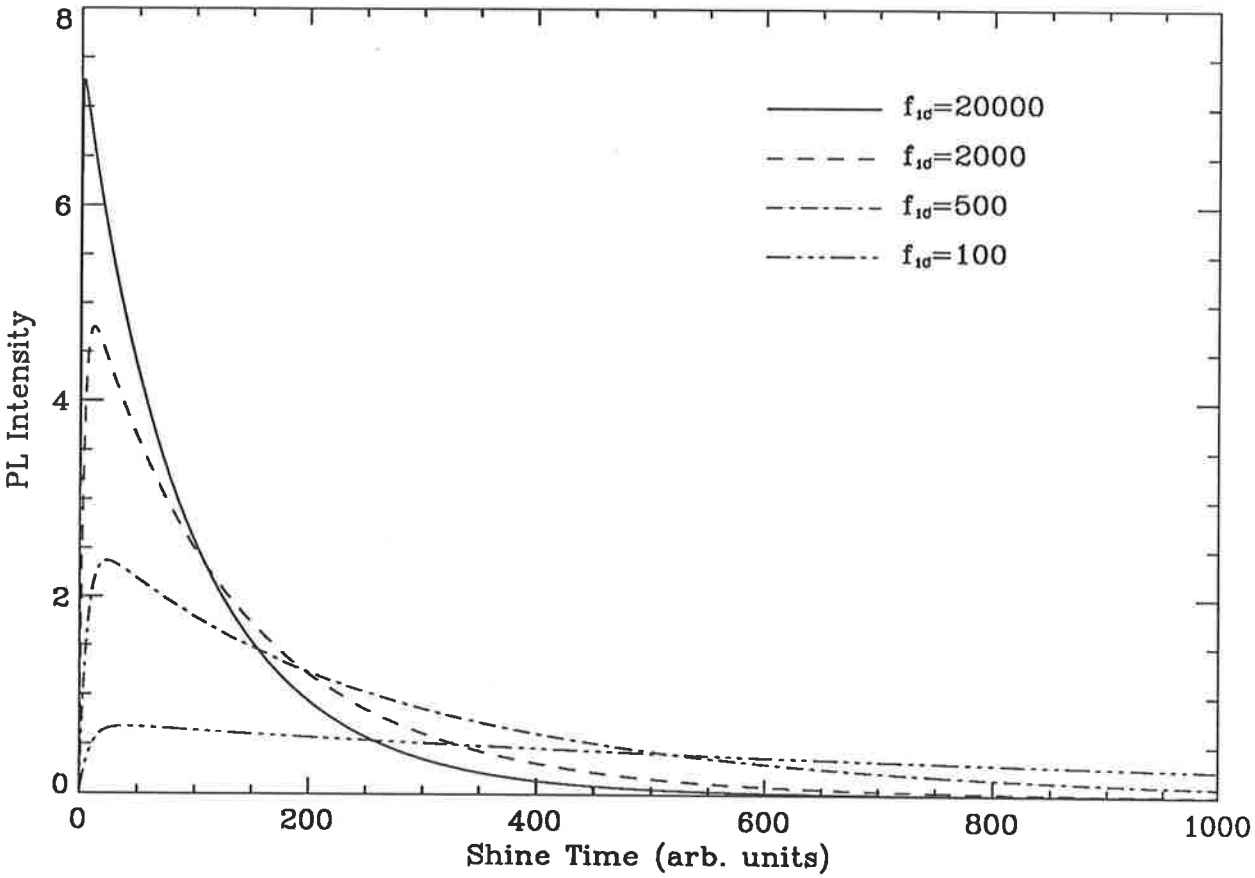

Figure 7.5: Results for $N_2 = 1 \times 10^{12}$ for the "single electron trap with a competitor" model. The values of f_{1C} are shown on the diagram. The other parameters were: $N_1 = 1 \times 10^{12}$,$A_{C1} = 1 \times 10^{-9}$, $A_{C2} = 1 \times 10^{-11}$ and $A_r = 1 \times 10^{-10}$.

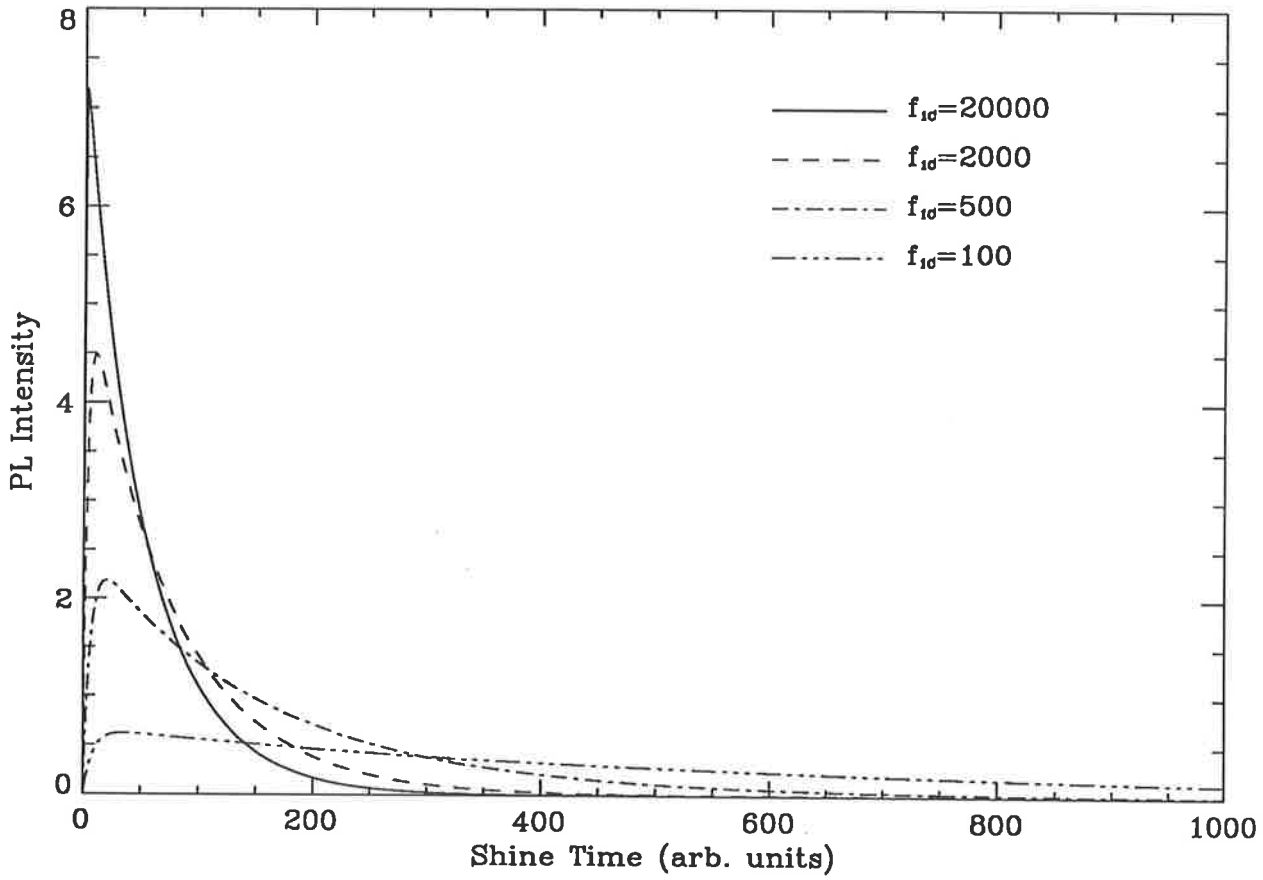

Figure 7.6: Results for $N_2 = 1 \times 10^{13}$ for the "single electron trap with a competitor" model. The values of f_{1C} are shown on the diagram. The other parameters were: $N_1 = 1 \times 10^{12}$, $A_{C1} = 1 \times 10^{-9}$, $A_{C2} = 1 \times 10^{-11}$ and $A_r = 1 \times 10^{-10}$.

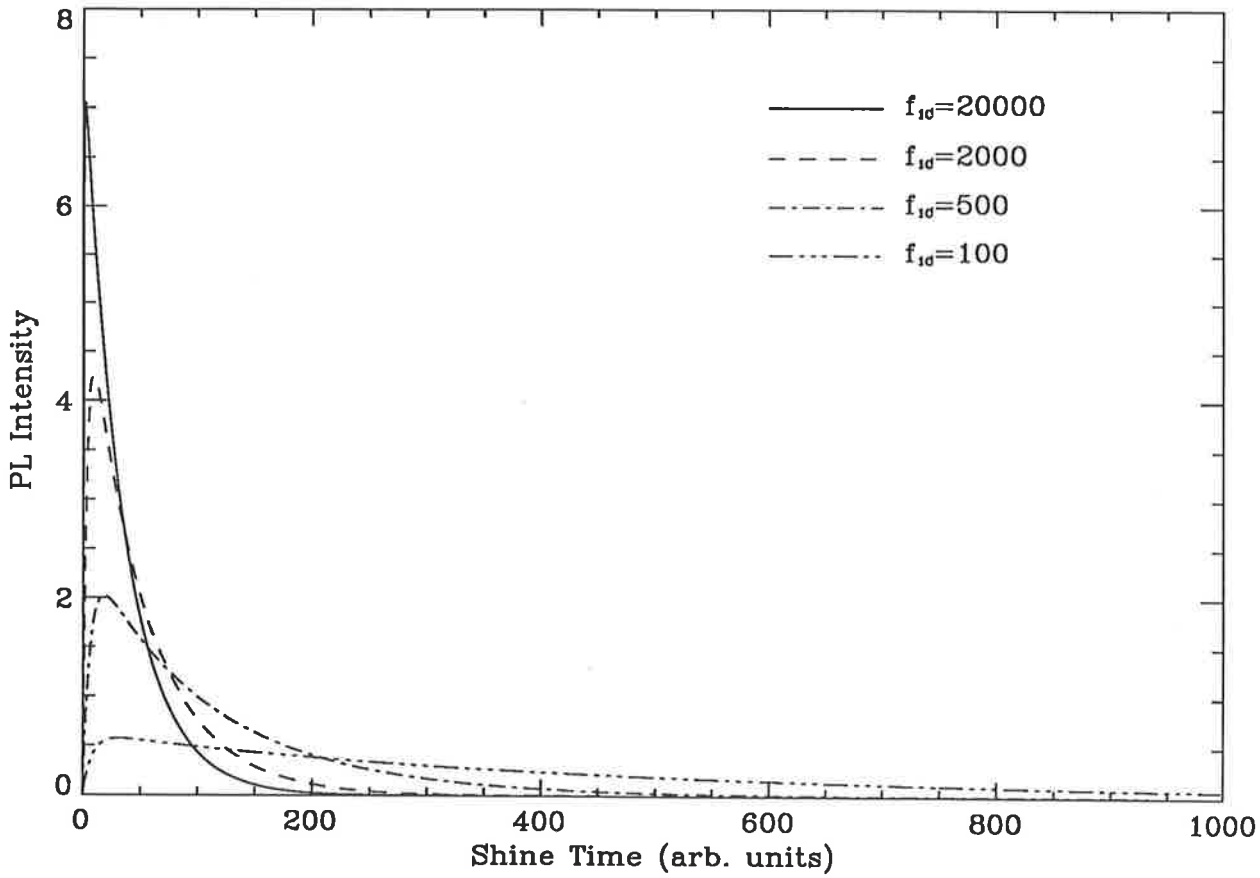

Figure 7.7: Results for $N_2 = 2 \times 10^{13}$ for the "single electron trap with a competitor" model. The values of f_{1C} are shown on the diagram. The other parameters were: $N_1 = 1 \times 10^{12}$, $A_{C1} = 1 \times 10^{-9}$, $A_{C2} = 1 \times 10^{-11}$ and $A_r = 1 \times 10^{-10}$.

the conduction band is less at any one time than for the case of $A_{C1} = 0$, hence the peak value is lower and the decay is slower. This slower decay has the appearance of a tail but this was really just a result of the slow decay.

7.3.2 Single Electron Trap with a Competitor

Figure 7.4 shows the band diagram of this model, which was identical to the previous model apart from the introduction of a deep competing electron trap (referred to as "trap 2"). The kinetic equations which describe this model were:

$$\frac{dn_1}{dt} = -f_{1C}n_1 + n_C A_{C1}(N_1 - n_1), \tag{7.4}$$

$$\frac{dn_C}{dt} = f_{1C}n_1 - n_C A_{C1}(N_1 - n_1) - n_C A_{C2}(N_2 - n_2) - n_C A_r n_h, \tag{7.5}$$

$$\frac{dn_2}{dt} = n_C A_{C2}(N_2 - n_2), \tag{7.6}$$

$$\frac{dn_h}{dt} = -n_C A_r n_h. \tag{7.7}$$

Figures 7.5, 7.6 and 7.7 show the effect of increasing the number of competing electron traps N_2 successively from 10^{12} to 10^{13} to 2×10^{13} (all other parameters are given in the figure captions). Increasing the value of N_2 had the effect of reducing the area under each graph which was equivalent to the total number of PL photons given off. Hence the horizontal scale was contracted (and to a certain extent the vertical scale as well) which was the same as a simple change of the time scale.

7.3.3 Bleaching Competitor Trap

The decay curve in figure 7.5 for $f_{1C} = 20000$ shows the sharp initial rise and decay of the experimental curves but without a tail. Figure 7.8 shows the band diagram for the case where the competing trap also bleaches at a rate f_{2C}. The equations for this

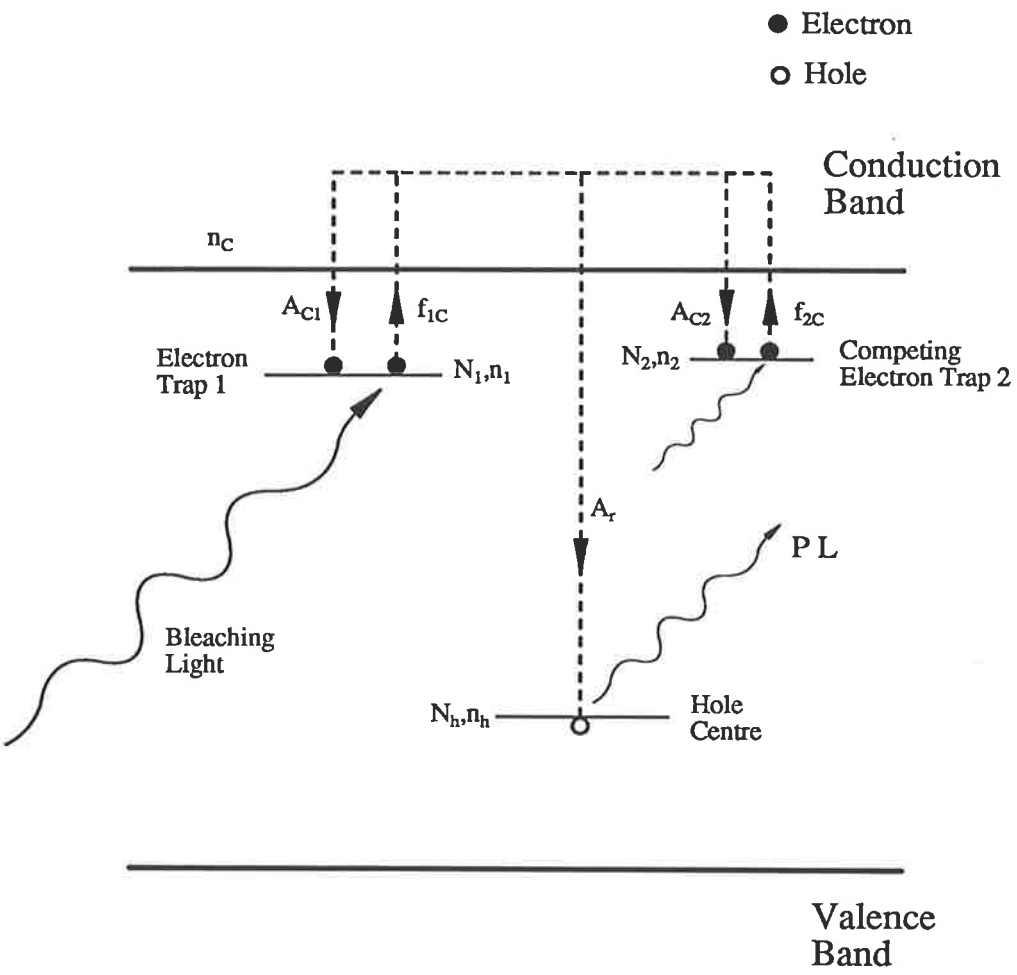

Figure 7.8: Schematic band diagram for the bleaching competitor trap model. The dotted lines indicate the general trajectory of the electrons and the arrows the direction of the transition.

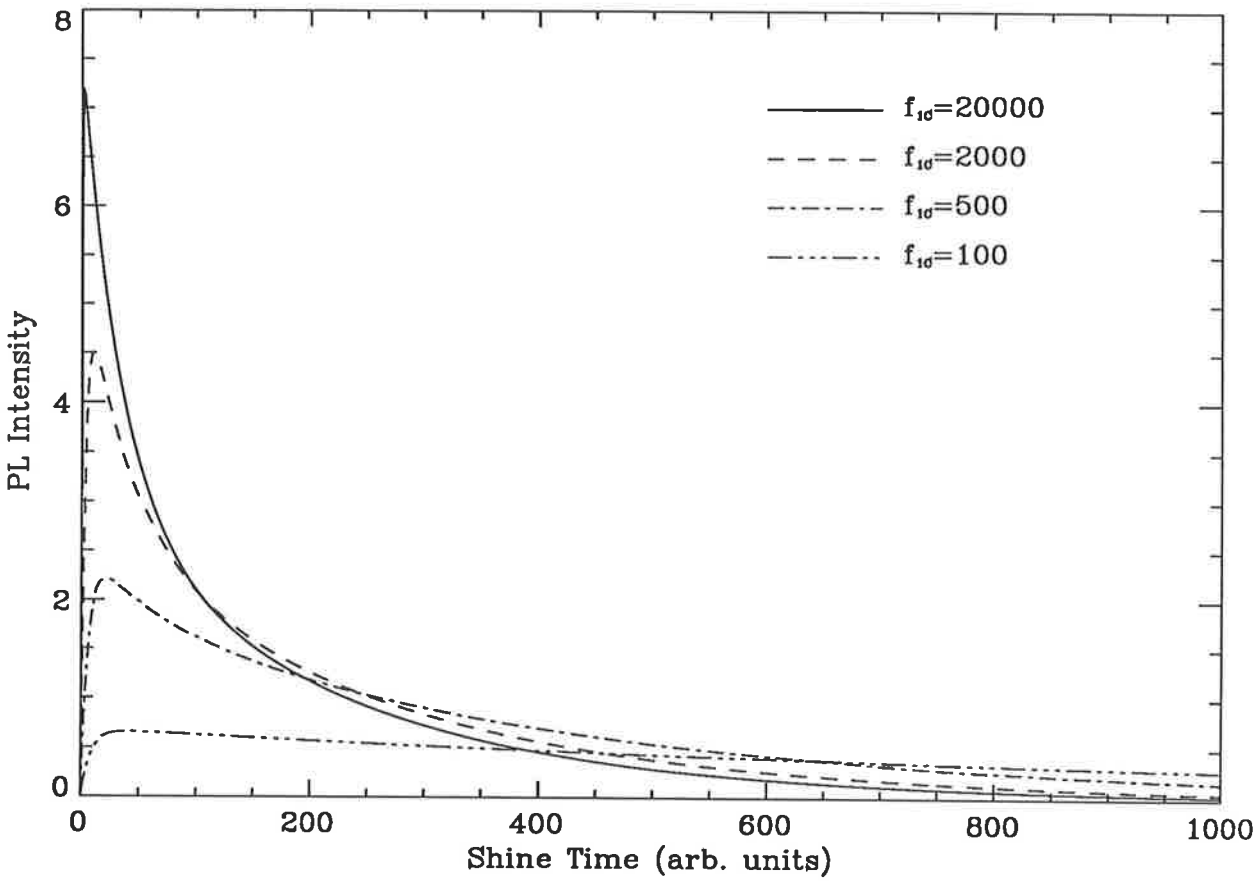

Figure 7.9: Results for $f_{2C} = 150$ for the "bleaching competitor trap" model. The values of f_{1C} are shown on the diagram. The other parameters were: $N_1 = 1 \times 10^{12}$, $N_2 = 1 \times 10^{13}$, $A_{C1} = 1 \times 10^{-9}$, $A_{C2} = 1 \times 10^{-11}$ and $A_r = 1 \times 10^{-10}$.

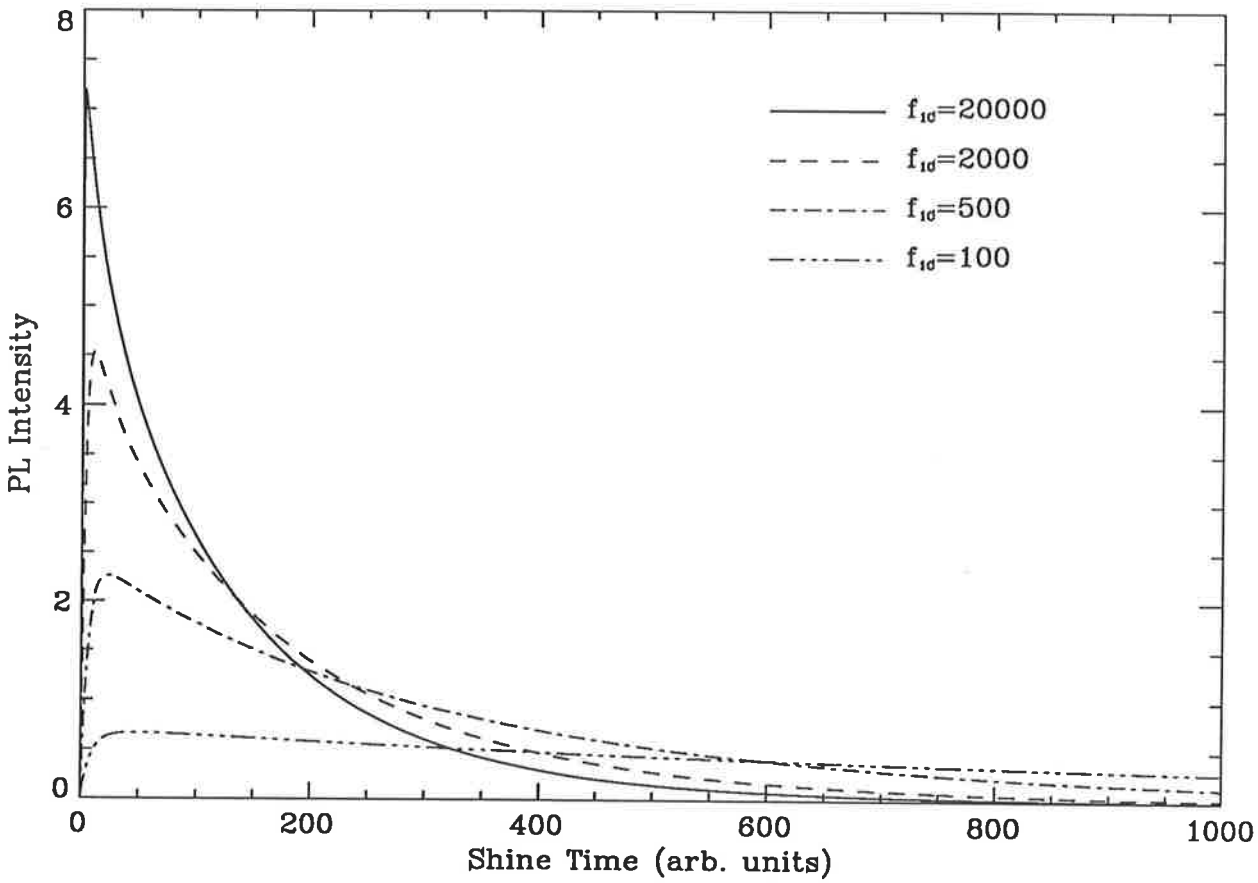

Figure 7.10: Results for $f_{2C} = 500$ for the "bleaching competitor trap" model. The values of f_{1C} are shown on the diagram. The other parameters were: $N_1 = 1 \times 10^{12}$, $N_2 = 1 \times 10^{13}$, $A_{C1} = 1 \times 10^{-9}$, $A_{C2} = 1 \times 10^{-11}$ and $A_r = 1 \times 10^{-10}$.

model were as follows:

$$\frac{dn_1}{dt} = -f_{1C}n_1 + n_C A_{C1}(N_1 - n_1), \tag{7.8}$$

$$\frac{dn_C}{dt} = f_{1C}n_1 + f_{2C}n_2 - n_C A_{C1}(N_1 - n_1) - n_C A_{C2}(N_2 - n_2) - n_C A_r n_h, \tag{7.9}$$

$$\frac{dn_2}{dt} = -f_{2C}n_2 + n_C A_{C2}(N_2 - n_2), \tag{7.10}$$

$$\frac{dn_h}{dt} = -n_C A_r n_h. \tag{7.11}$$

Figures 7.9 and 7.10 are essentially the same as figure 7.5 but with values of f_{2C} equal to 150 and 500 respectively. Clearly tails have been introduced into the decay curves (this is most noticeable for $f_{1c} = 20000$ and 2000). For $f_{2C} = 150$ the bleaching was relatively low and the tail extends much longer than for $f_{2C} = 500$. For $f_{2C} = 500$ and $f_{1C} = 20000$ the decay curve went to zero at about 900 shine time units and the initial decay was also not quite as sharp as for figure 7.9 since the contribution to the PL from the bleaching of the competing trap was greater at low shine times.

7.3.4 Thermally Shallow Competitor Trap

The results from the previous chapter indicated that a shallow trap near to 100°C may be playing a significant role in the decay process. For quartz the obvious candidate for this trap was the 110°C trap. Figure 7.11 shows the band diagram of the most obvious model that incorporated the 110°C trap (called "electron trap 2" in the figure). This was similar to the last model except for the addition of an extra term, T_{2C}, which acts exactly like the f_{2C} term but whose value depended on the temperature.

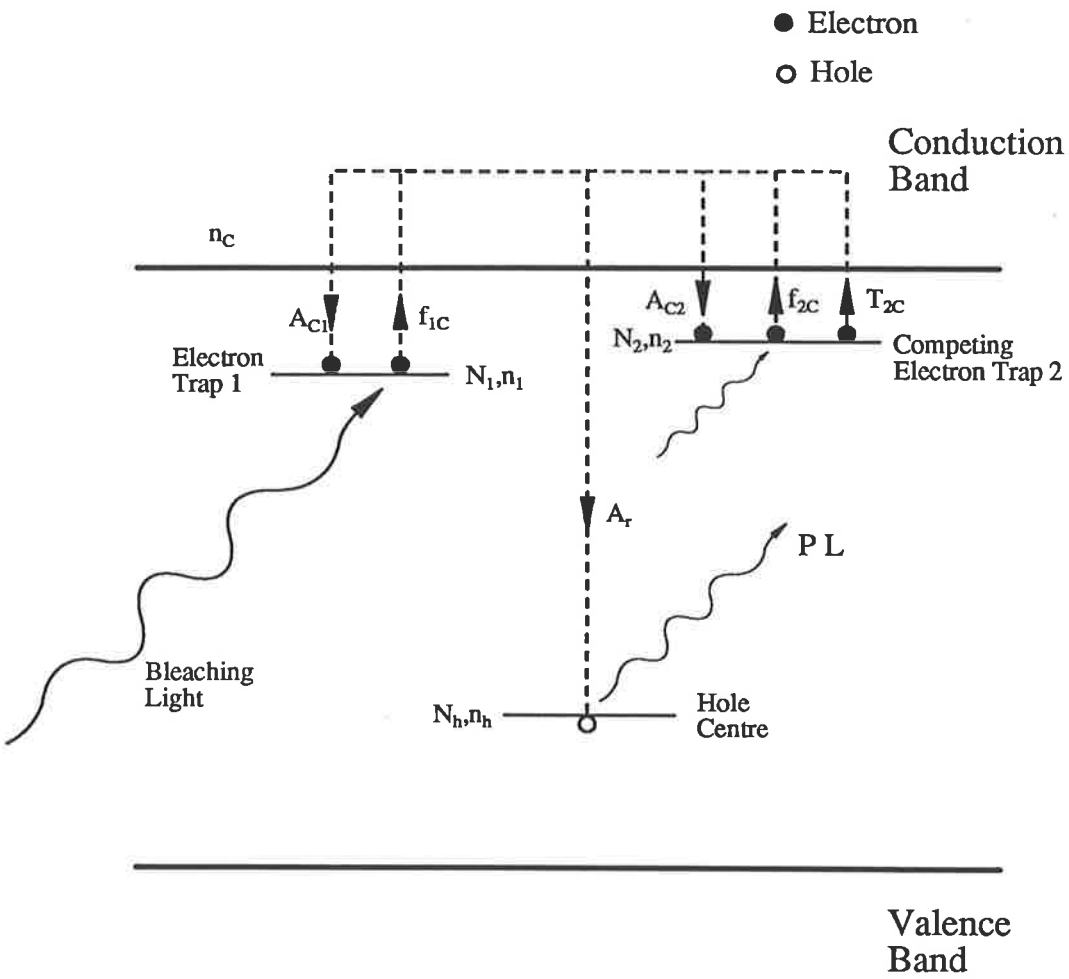

Figure 7.11: Schematic band diagram for the thermally shallow competitor trap model. The dotted lines indicate the general trajectory of the electrons and the arrows the direction of the transition.

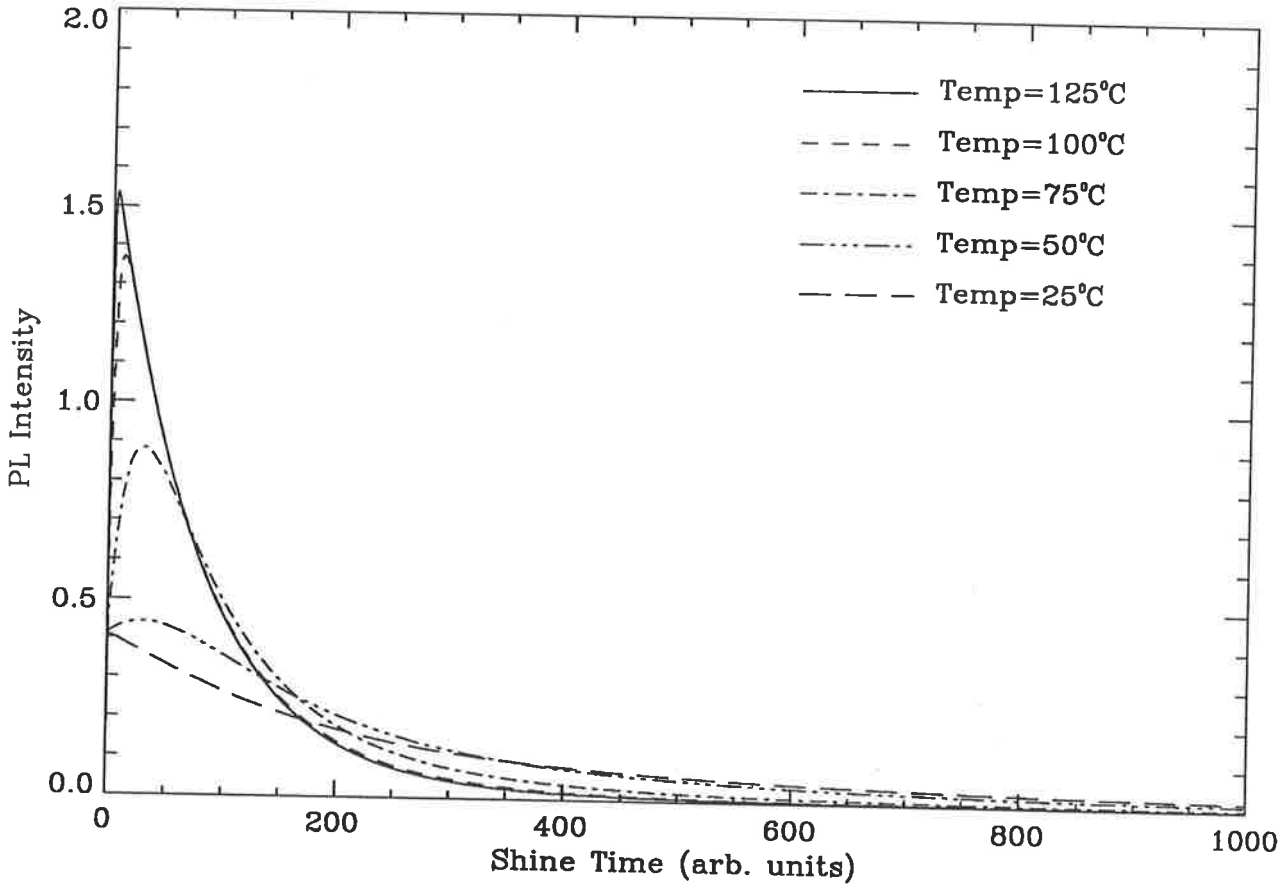

Figure 7.12: Results for $f_{1C} = 20$ and $f_{2C} = 20$ for the "thermally shallow competitor trap" model. The values of the temperatures which correspond to the parameters T_{2C} are shown on the diagram. The other parameters were: $N_1 = 1 \times 10^{13}$, $N_2 = 1 \times 10^{13}$, $A_{C1} = 1 \times 10^{-12}$, $A_{C2} = 1.5 \times 10^{-7}$ and $A_r = 1 \times 10^{-7}$.

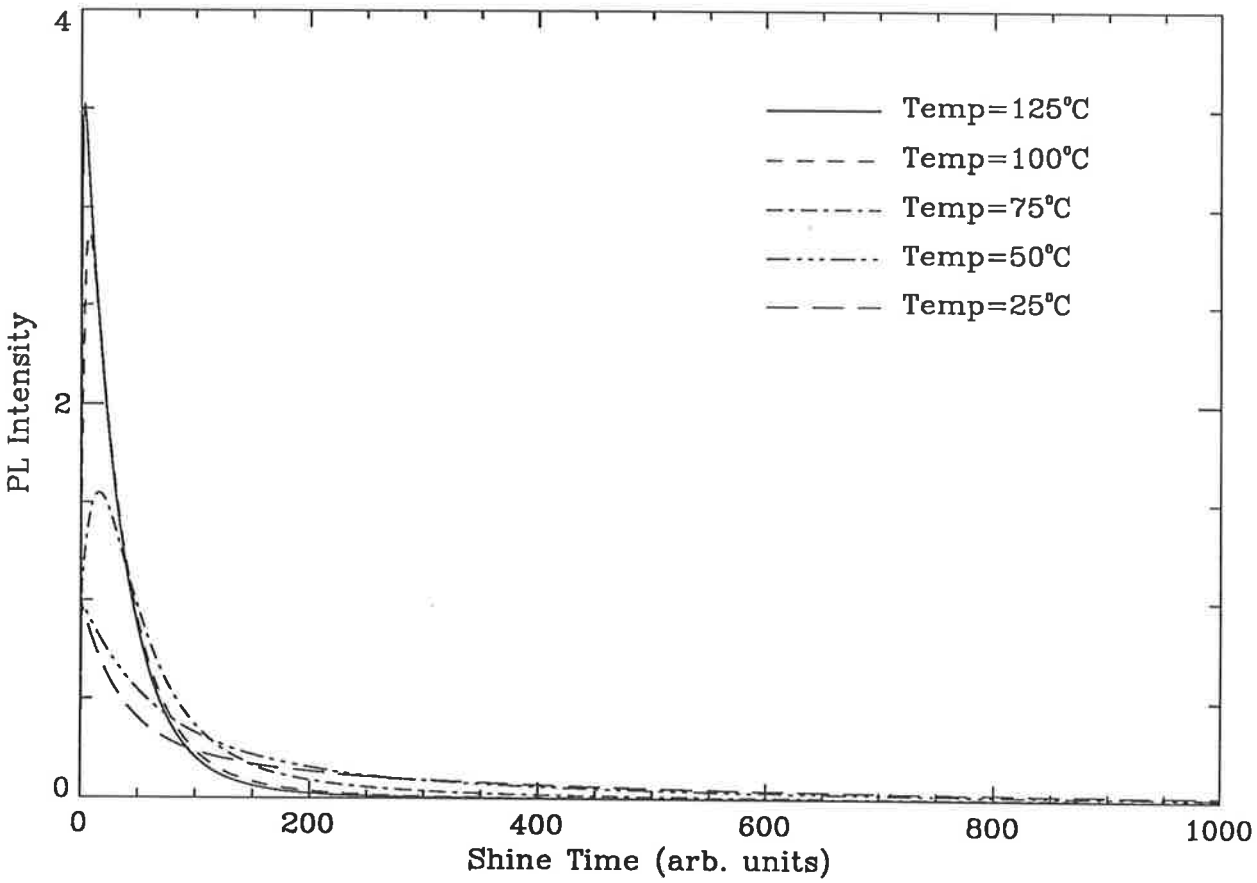

Figure 7.13: Results for $f_{1C} = 50$ and $f_{2C} = 20$ for the "thermally shallow competitor trap" model. The values of the temperatures which correspond to the parameters T_{2C} are shown on the diagram. The other parameters were: $N_1 = 1 \times 10^{13}$, $N_2 = 1 \times 10^{13}$, $A_{C1} = 1 \times 10^{-12}$, $A_{C2} = 1.5 \times 10^{-7}$ and $A_r = 1 \times 10^{-7}$.

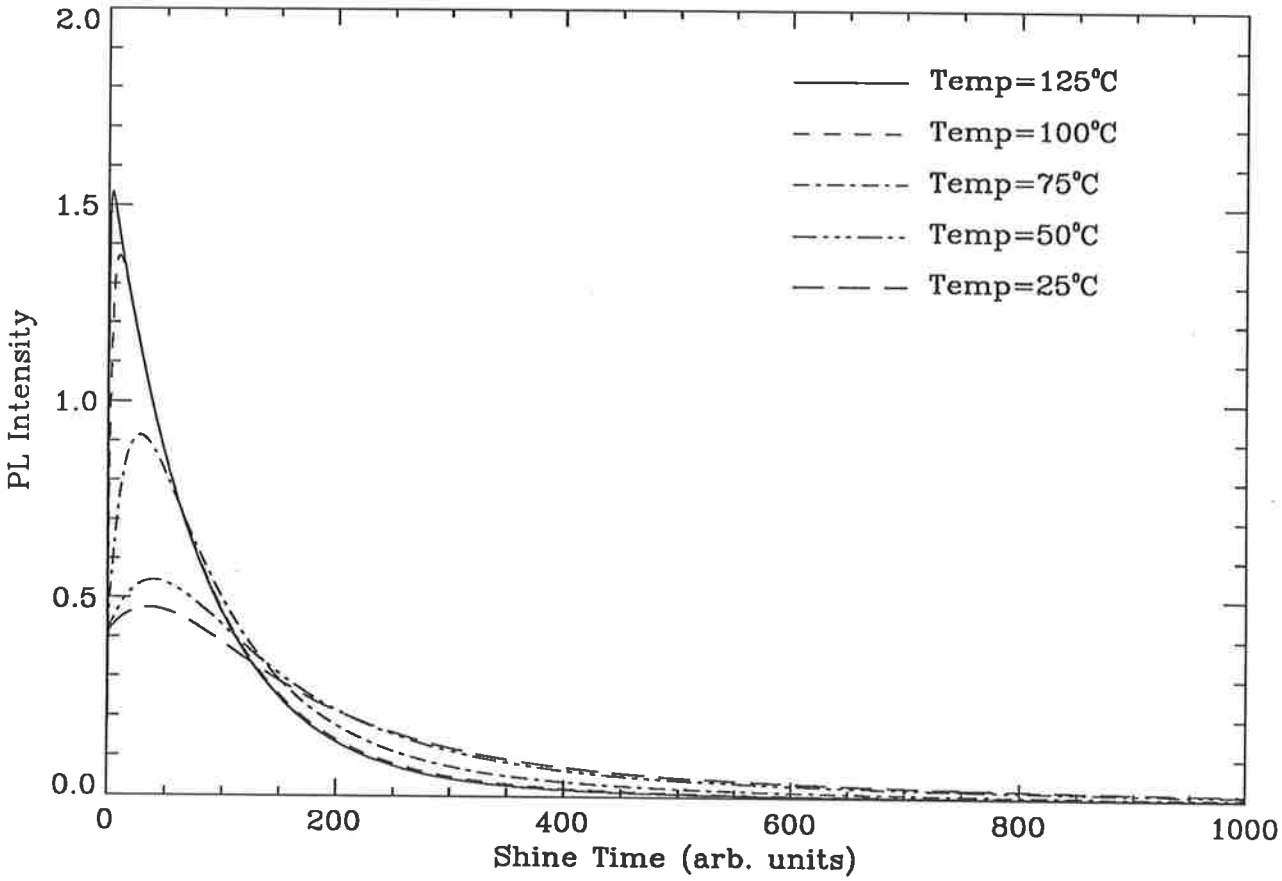

Figure 7.14: Results for $f_{1C} = 20$ and $f_{2C} = 50$ for the "thermally shallow competitor trap" model. The values of the temperatures which correspond to the parameters T_{2C} are shown on the diagram. The other parameters were: $N_1 = 1 \times 10^{13}$, $N_2 = 1 \times 10^{13}$, $A_{C1} = 1 \times 10^{-12}$, $A_{C2} = 1.5 \times 10^{-7}$ and $A_r = 1 \times 10^{-7}$.

The equations for this model were:

$$\frac{dn_1}{dt} = -f_{1C}n_1 + n_C A_{C1}(N_1 - n_1), \tag{7.12}$$

$$\frac{dn_C}{dt} = f_{1C}n_1 + f_{2C}n_2 + T_{2C}n_2 - n_C A_{C1}(N_1 - n_1)$$

$$-n_C A_{C2}(N_2 - n_2) - n_C A_r n_h, \tag{7.13}$$

$$\frac{dn_2}{dt} = -f_{2C}n_2 - T_{2C}n_2 + n_C A_{C2}(N_2 - n_2), \tag{7.14}$$

$$\frac{dn_h}{dt} = -n_C A_r n_h. \tag{7.15}$$

In this and the following models decay curves at 25°C, 50°C, 75°C, 100°C and 125°C were calculated. The actual temperature terms were calculated from

$$P = se^{-E/kT_\theta}, \tag{7.16}$$

where P (which was proportional to T_{2C}) was the probability per unit time for the thermal release of an electron from the trap, T_θ was the absolute temperature and the other terms are the same as in chapter 1, with the value of E equal to 0.99 (Aitken 1985). An important point to note here is that the absolute magnitude of the T_{2C} values is unimportant since this just changes the relative scale of the plots. What is important, though, is the relative magnitudes of the thermal terms and for this model, as for the following ones, these, naturally, remain the same. The five scaled values for the thermal term work out to be (for increasing temperatures) 0.15, 3.95, 45.0, 385 and 2450.

Figures 7.12, 7.13 and 7.14 show the decay curves for each of the temperature values with f_{1C} and f_{2C} varied. There is a clear temperature dependence related to the capture of electrons from the conduction band by trap 2 (the 110°C trap). At the lower temperatures the lifetime of a captured electron in trap 2 is quite long relative

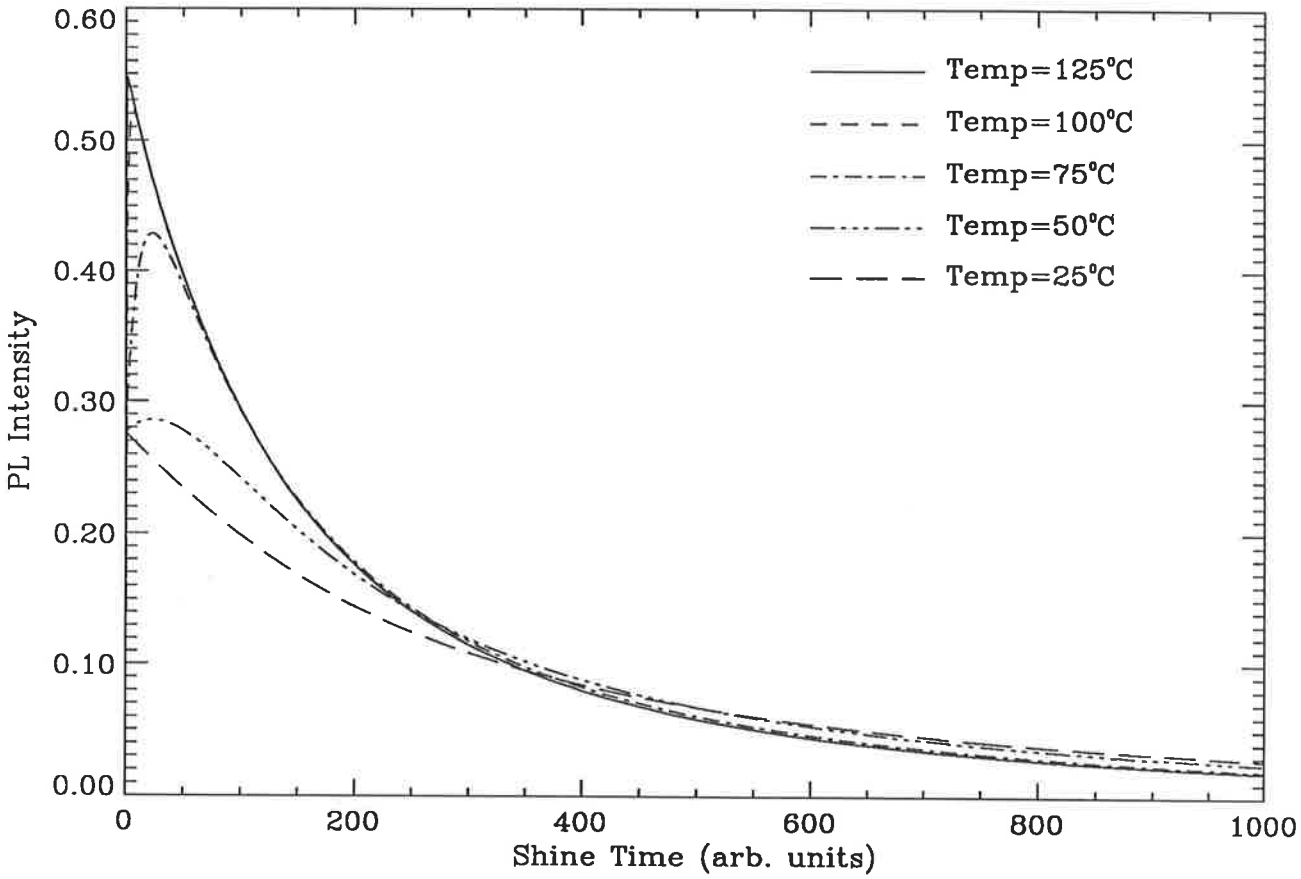

Figure 7.15: Results for $f_{1C} = 20$, $f_{2C} = 20$ and $A_{C1} = 1 \times 10^{-9}$ for the "thermally shallow competitor trap" model. The values of the temperatures which correspond to the parameters T_{2C} are shown on the diagram. The other parameters were: $N_1 = 1 \times 10^{13}$, $N_2 = 1 \times 10^{13}$,$A_{C2} = 1.5 \times 10^{-7}$ and $A_r = 1 \times 10^{-7}$.

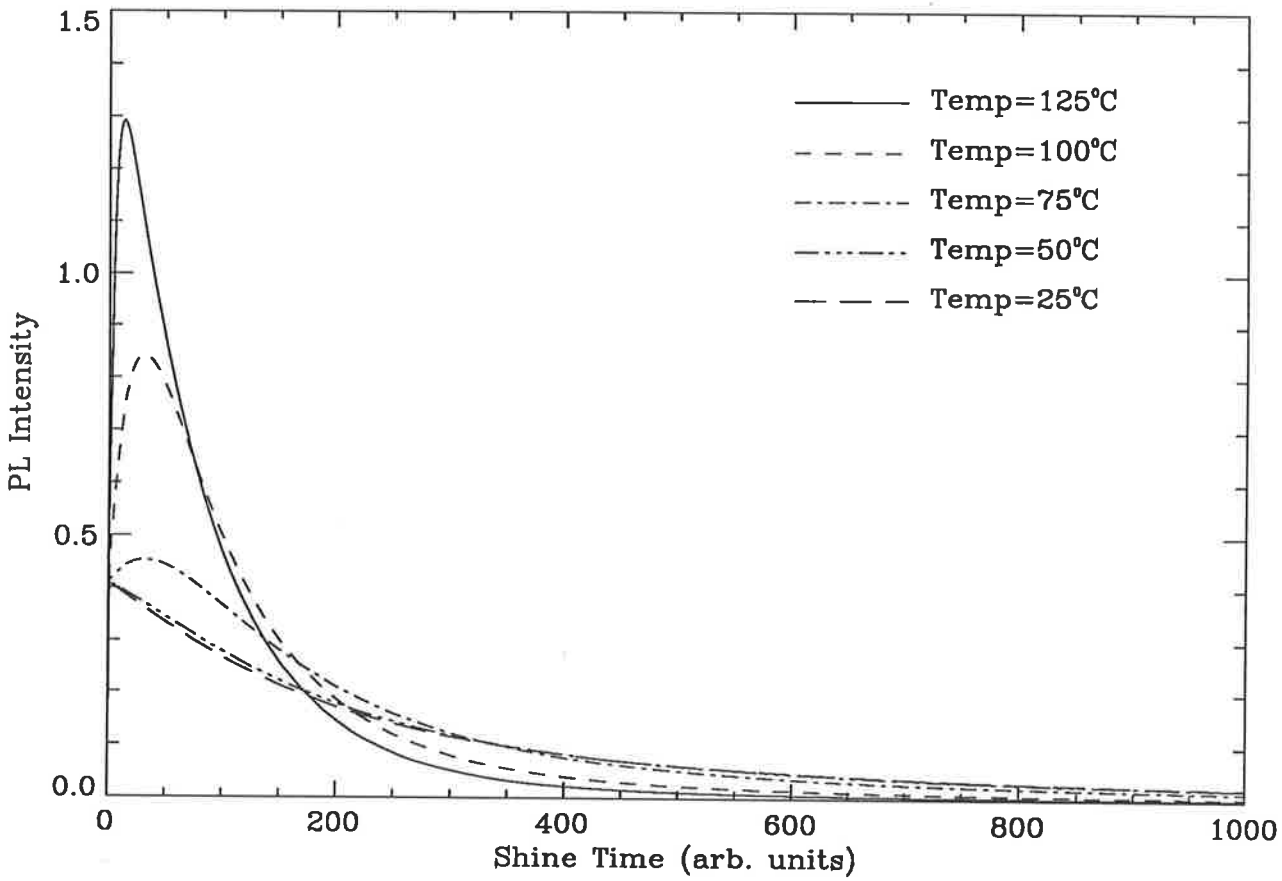

Figure 7.16: Results for $f_{1C} = 20$, $f_{2C} = 20$ and $A_{C1} = 1 \times 10^{-11}$ for the "thermally shallow competitor trap" model. The values of the temperatures which correspond to the parameters T_{2C} are shown on the diagram. The other parameters were: $N_1 = 1 \times 10^{13}$, $N_2 = 1 \times 10^{13}$,$A_{C2} = 1.5 \times 10^{-7}$ and $A_r = 1 \times 10^{-7}$.

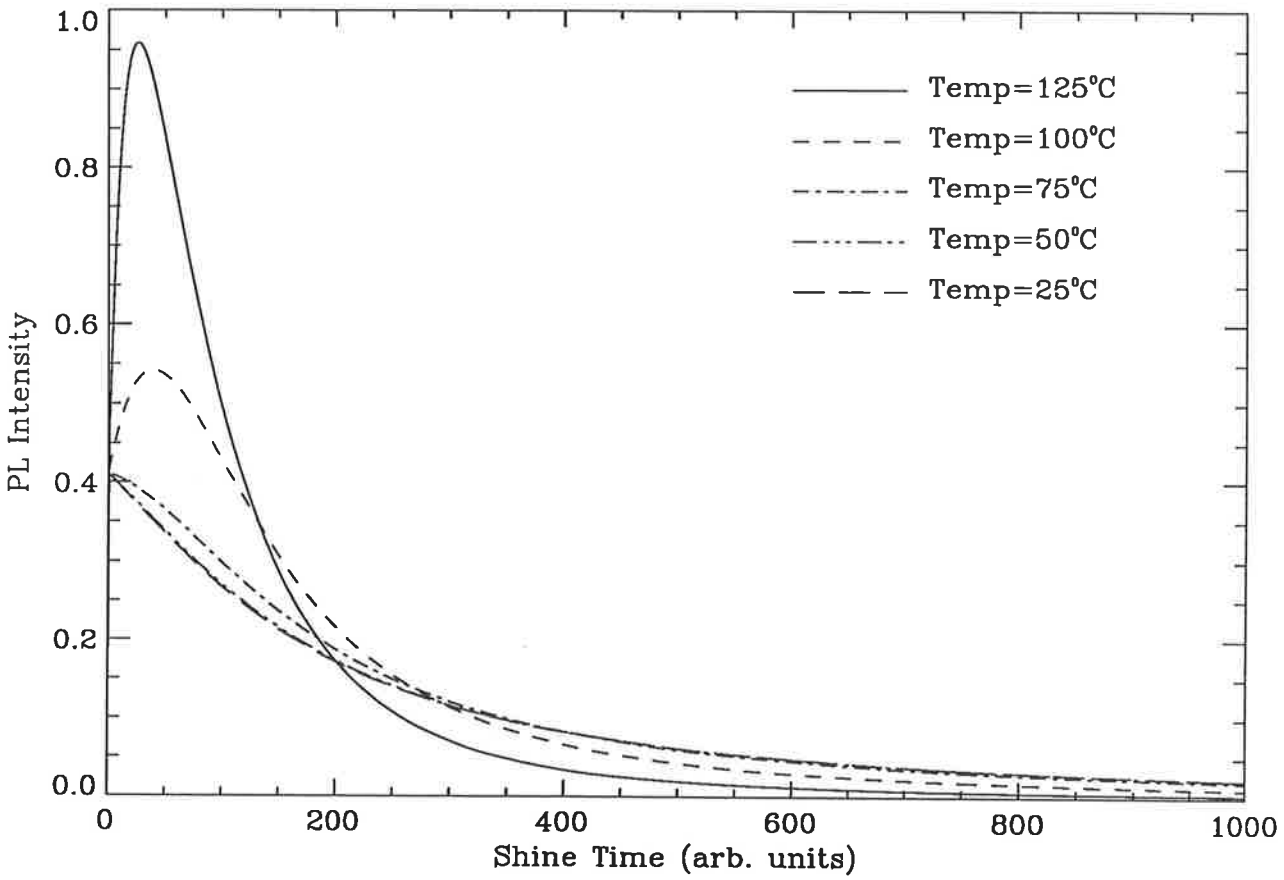

Figure 7.17: Results for $f_{1C} = 20$, $f_{2C} = 20$ and $A_{C1} = 1 \times 10^{-11}$ for the "thermally shallow competitor trap" model. The values of the temperatures which correspond to the parameters T_{2C} are shown on the diagram. The parameters in this figure were the same as for figure 7.16 but with the temperature scaling altered (see text). The other parameters were: $N_1 = 1 \times 10^{13}$, $N_2 = 1 \times 10^{13}$,$A_{C2} = 1.5 \times 10^{-7}$ and $A_r = 1 \times 10^{-7}$.

to its lifetime in the conduction band before recombination. At higher temperatures this thermal lifetime is so short that the trap has no effect on the decay curves at all and they resemble figure 7.5 (for $f_{1C} = 20000$). In figure 7.13 the value of f_{1C} has been increased from 20 to 50, which has essentially reduced the time scale (and hence the PL intensity scale).

In figure 7.12 at temperatures of 50°C, 75°C and to some extent 100°C, the initial sharp rise when the shine started has been lost due to the competition between electron capture and thermal ejection from trap 2. This effect is reduced somewhat in figure 7.13 for the 50°C curve but then this decay was slower than for the 25°C curve. Indeed, all the solutions for this model demonstrate such behaviour depending on the thermal term. Figure 7.14 shows the effect of increasing f_{2C} to 50 with f_{1C} held at 20. For the lowest two temperatures this parameter now dominates the thermal terms and the two curves become more similar. In figure 7.15 the value of A_{C1} was increased since in the earlier models this had the effect of producing sharp initial rises. Here however it has reduced the effect of A_{C2} and so all the curves have begun to resemble each other. This model also fails to account for the behaviour of the 125°C decay which was almost identical to the 100°C curve. The decay curves in figures 7.16 and 7.17 show the result of reducing the absolute magnitude of the temperature parameters, T_{2C}, but still keeping their relative values the same. This was successful in making the 125°C curve decay faster than the 100°C one but now the 25°C and 50°C curves are very close together and almost identical in figure 7.17.

So it appeared that this simple model which incorporated the 110°C trap fails to successfully account for the experimentally determined decay curves both quantita-

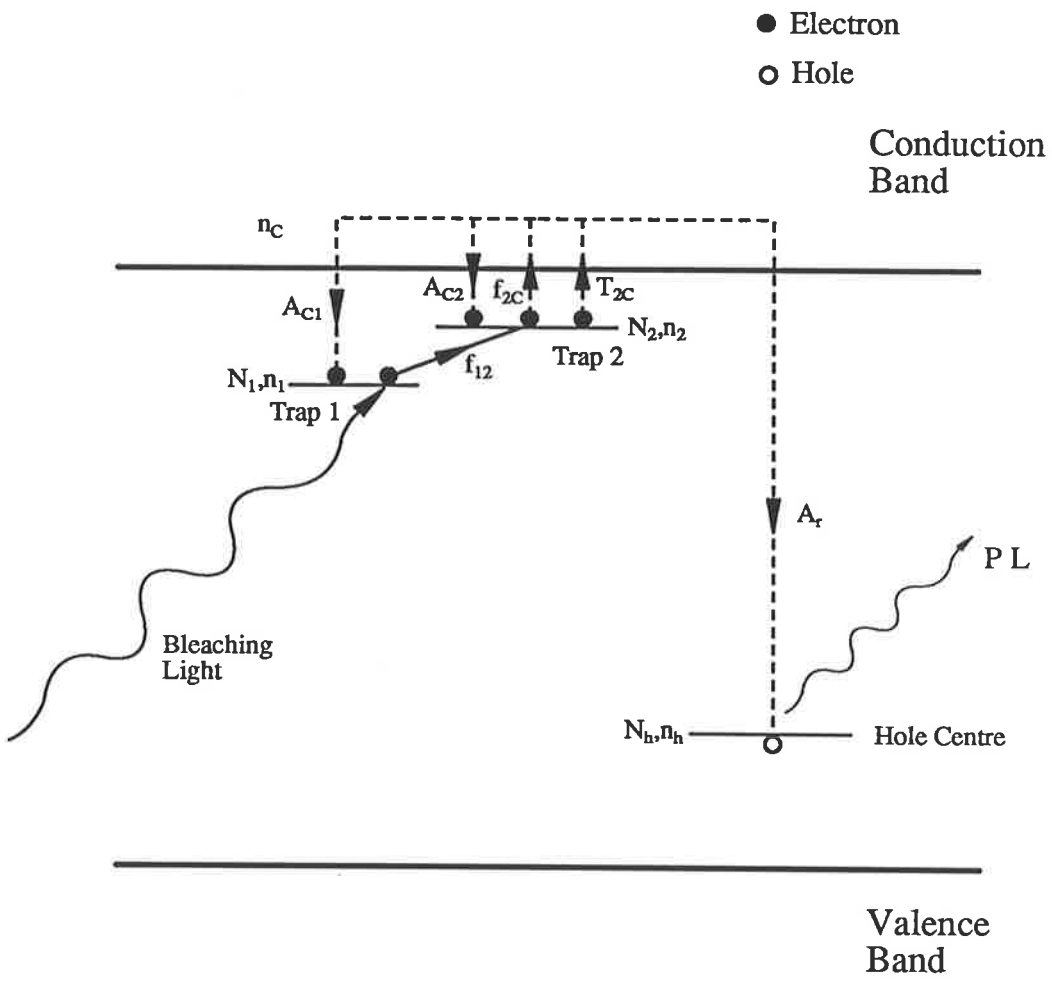

Figure 7.18: Schematic band diagram for the direct transfer model. The dotted lines indicate the general trajectory of the electrons and the arrows the direction of the transition.

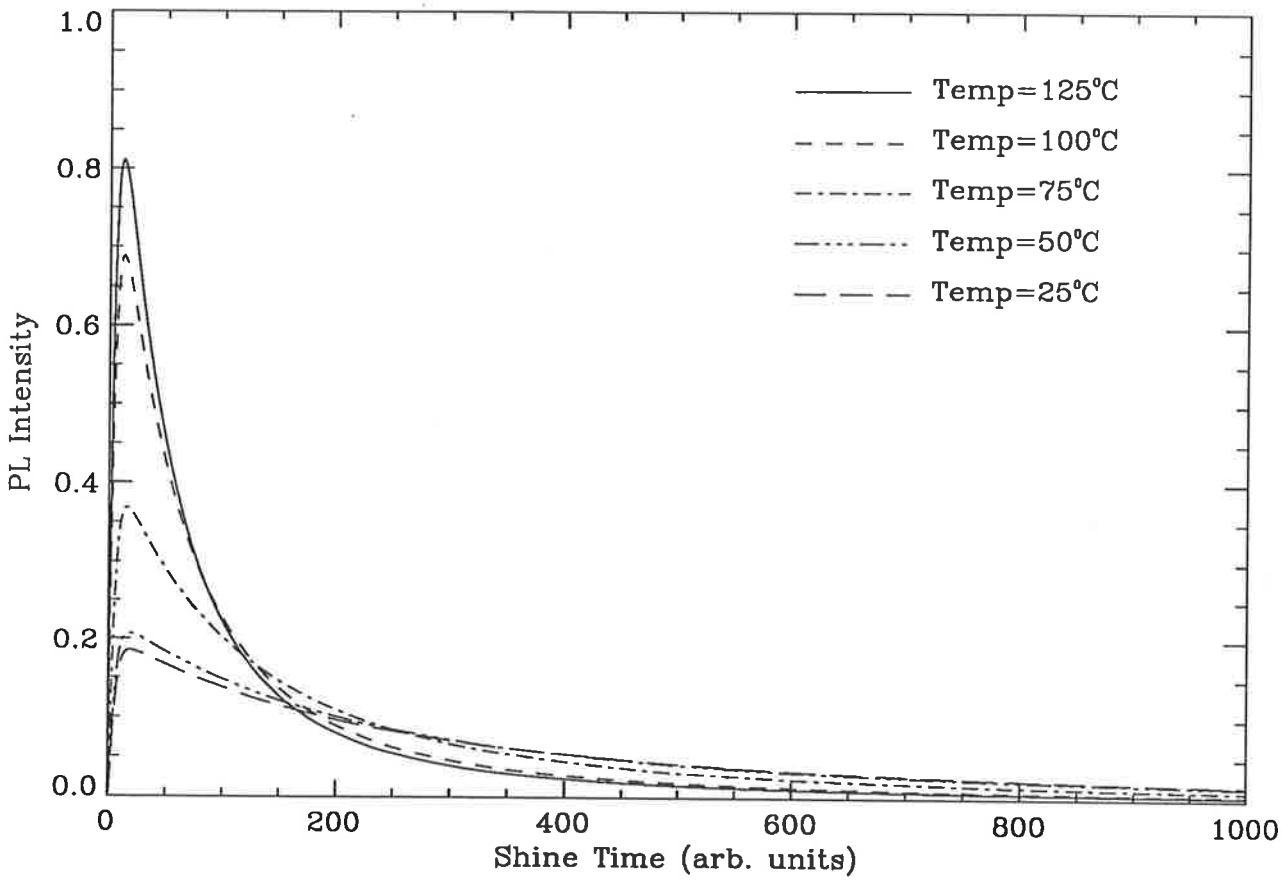

Figure 7.19: Results for $f_{12} = 30$, $f_{2C} = 100$ and $A_{C1} = 1 \times 10^{-11}$ for the "direct transfer" model. The values of the temperature parameters T_{2C} are shown on the diagram. The other parameters were: $N_1 = 1 \times 10^{13}$, $N_2 = 1 \times 10^{13}$,$A_{C2} = 1 \times 10^{-11}$ and $A_r = 5 \times 10^{-9}$.

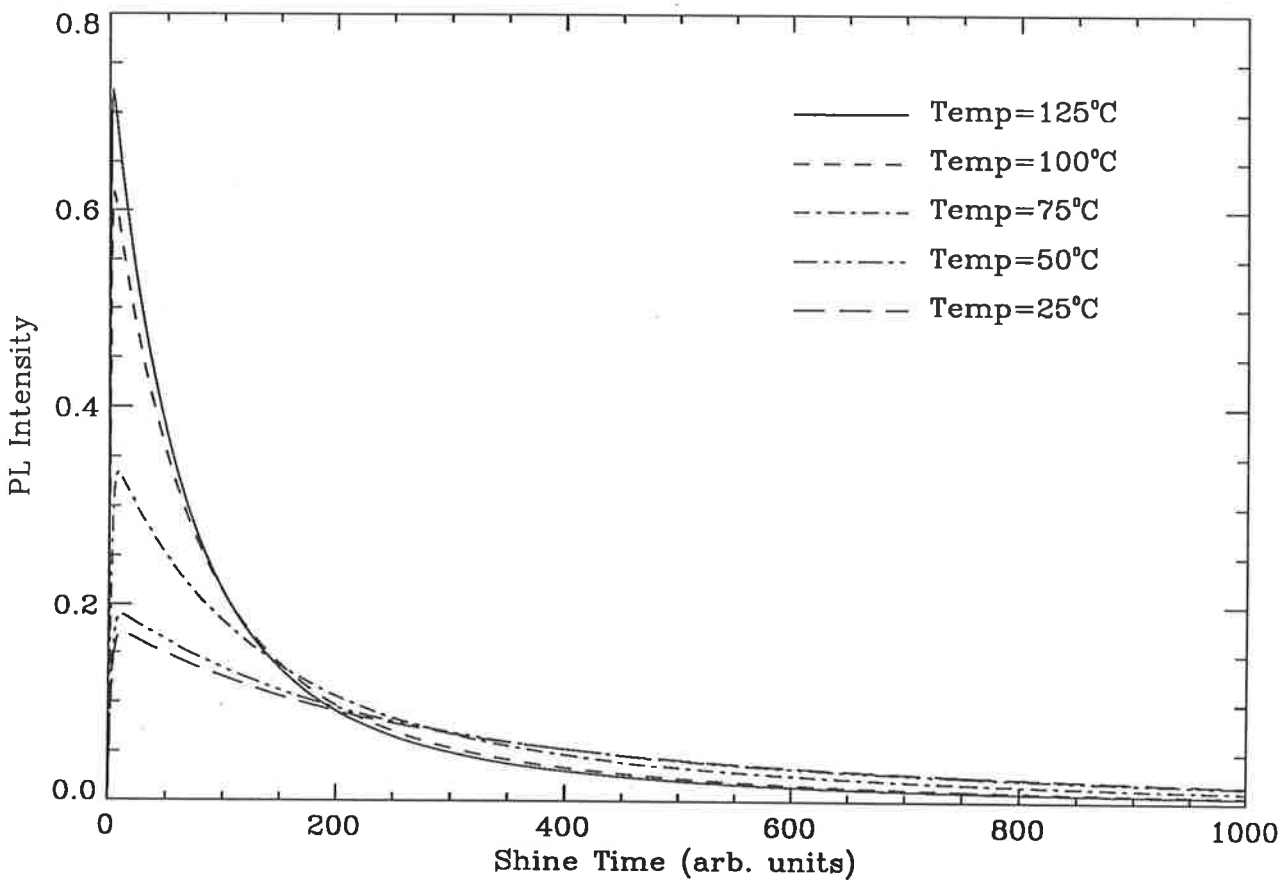

Figure 7.20: Results for $f_{12} = 30$, $f_{2C} = 100$ and $A_{C1} = 1 \times 10^{-10}$ for the "direct transfer" model. The values of the temperature parameters T_{2C} are shown on the diagram. The other parameters were: $N_1 = 1 \times 10^{13}$, $N_2 = 1 \times 10^{13}$,$A_{C2} = 1 \times 10^{-11}$ and $A_r = 5 \times 10^{-9}$.

tively and qualitatively.

7.3.5 Direct Transfer Model

Figure 7.18 shows the band diagram for this model. The main effect of the bleaching was to pump electrons straight into trap 2 independent of the conduction band. For the purpose of the model, the exact details of how the electrons were promoted from trap 1 to trap 2 were not important but presumably the defect centres responsible for both traps would need to be located relatively close to one another. The equations for this model are:

$$\frac{dn_1}{dt} = -(f_{12} + f_{1C})n_1 + n_C A_{C1}(N_1 - n_1), \tag{7.17}$$

$$\frac{dn_C}{dt} = f_{1C}n_1 + f_{2C}n_2 + T_{2C}n_2 - n_C A_{C1}(N_1 - n_1) - n_C A_{C2}(N_2 - n_2) - n_C A_r n_h, \tag{7.18}$$

$$\frac{dn_2}{dt} = f_{12}n_1 - f_{2C}n_2 - T_{2C}n_2 + n_C A_{C2}(N_2 - n_2), \tag{7.19}$$

$$\frac{dn_h}{dt} = -n_C A_r n_h. \tag{7.20}$$

The advantage of this model over the previous one was that the trapping parameter A_{C2} could be made quite small without reducing the role of trap 2 in the decay process, whereas previously this parameter was vital in order for trap 2 to capture enough electrons for the trap to play a significant role in the process. This type of mechanism has been independently proposed by Smith (1990).

In figure 7.19 the decay curves are shown as for the previous model, however now the initial rise of the decay curves are all identical qualitatively whereas for the

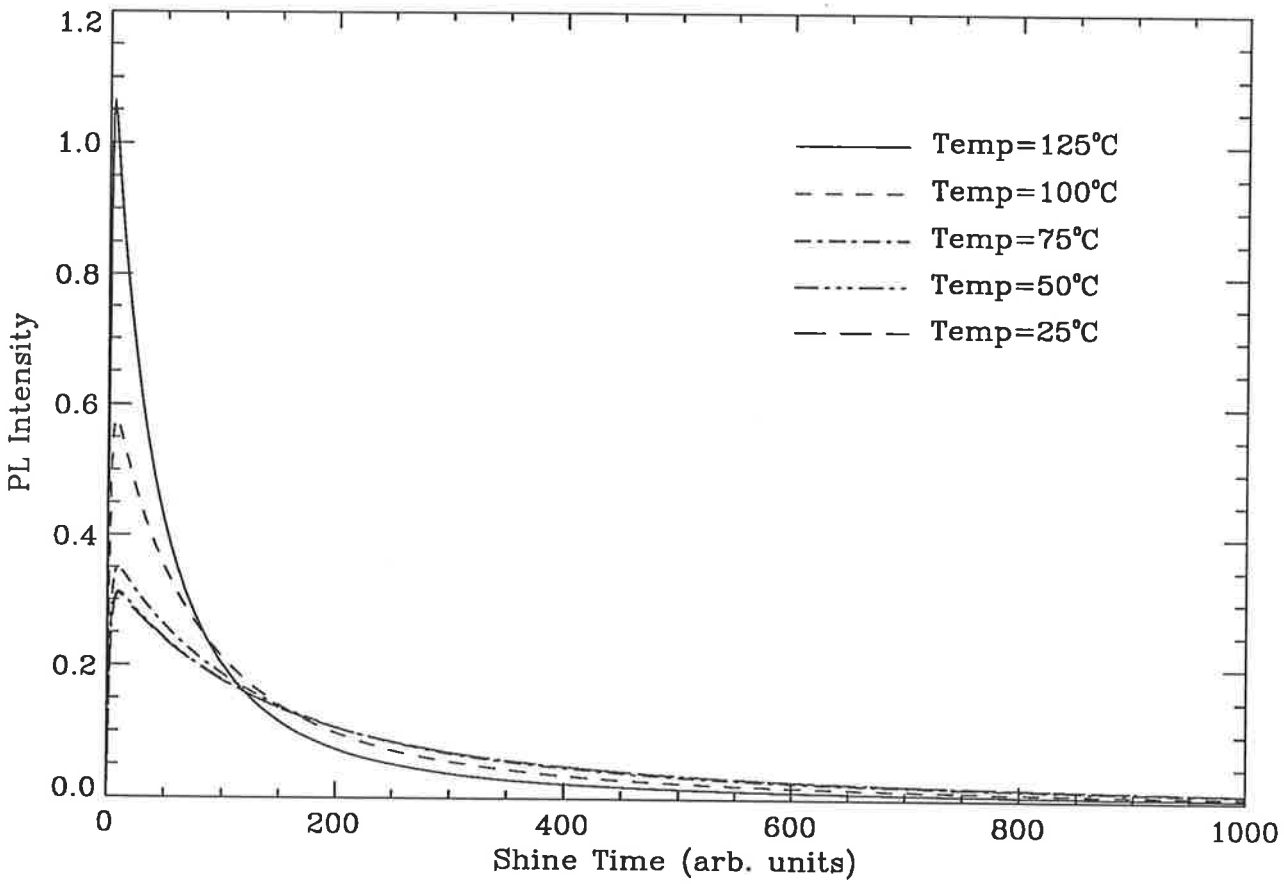

Figure 7.21: Results for $f_{12} = 60$, $f_{2C} = 100$ and $A_{C1} = 1 \times 10^{-10}$ for the "direct transfer" model. The values of the temperatures which correspond to the parameters T_{2C} are shown on the diagram and the temperature scaling has been reduced by a factor of 10 compared to figure 7.19. The other parameters were: $N_1 = 1 \times 10^{13}$, $N_2 = 1 \times 10^{13}$,$A_{C2} = 1 \times 10^{-11}$ and $A_r = 5 \times 10^{-9}$.

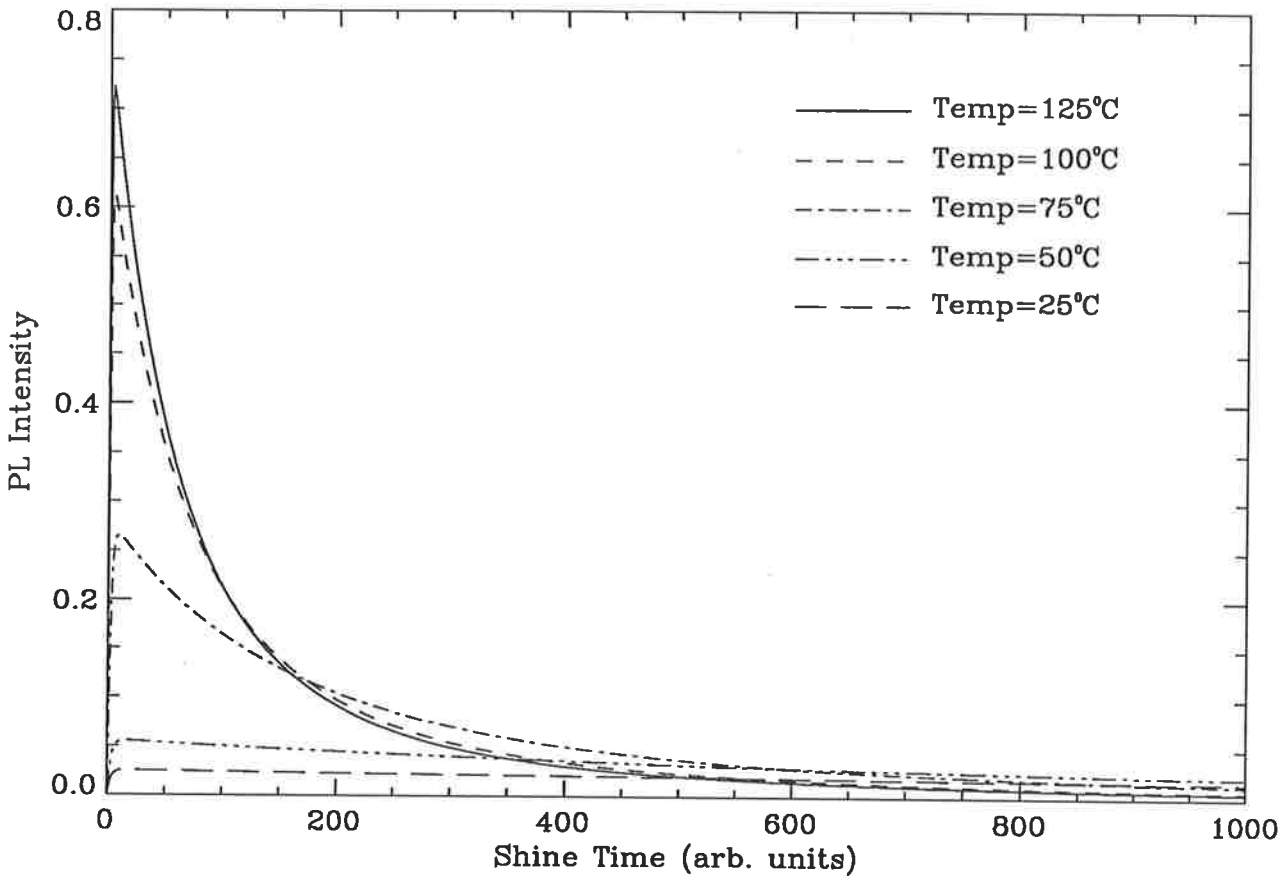

Figure 7.22: Results for $f_{12} = 30$, $f_{2C} = 10$ and $A_{C1} = 1 \times 10^{-10}$ for the "direct transfer" model. The values of the temperatures which correspond to the parameters T_{2C} are shown on the diagram. The other parameters were: $N_1 = 1 \times 10^{13}$, $N_2 = 1 \times 10^{13}$,$A_{C2} = 1 \times 10^{-11}$ and $A_r = 5 \times 10^{-9}$.

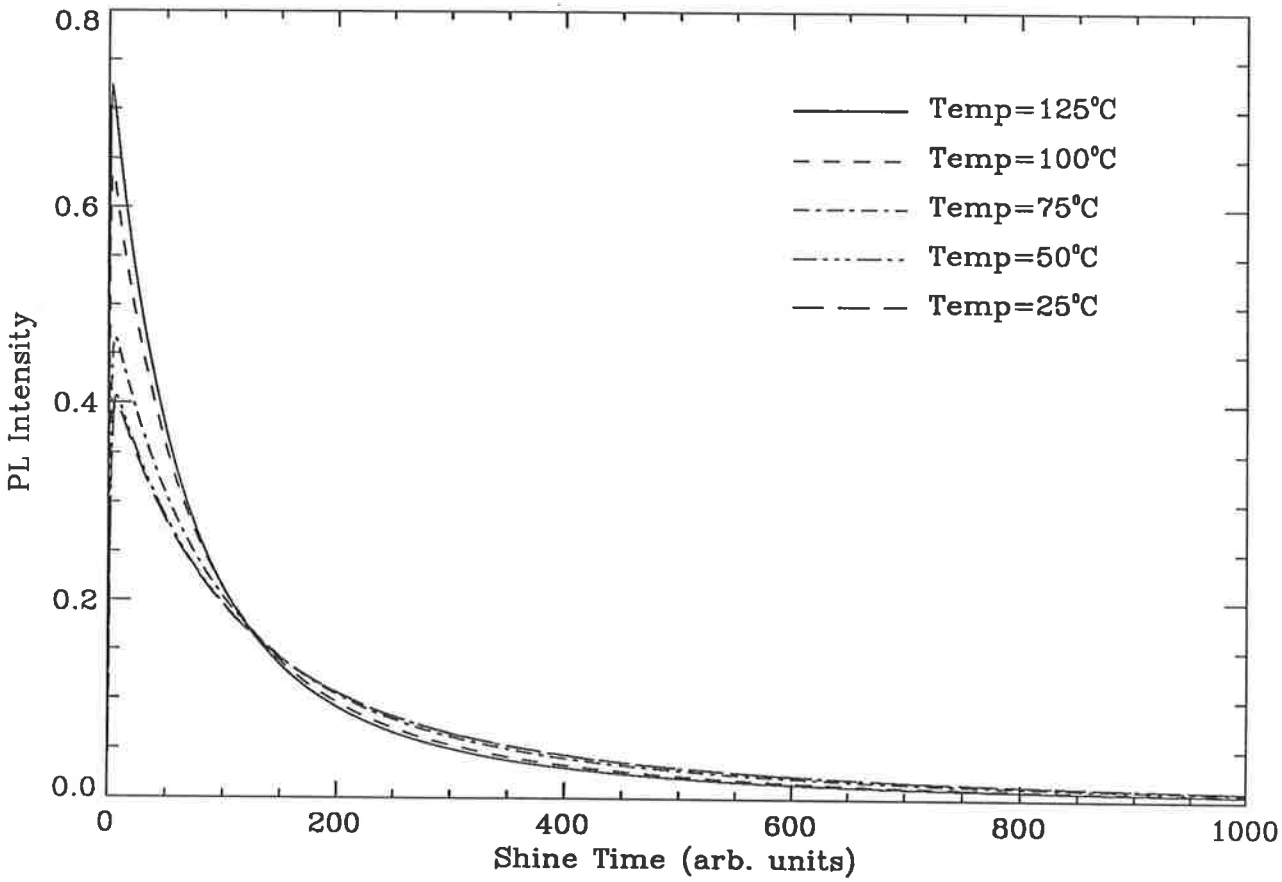

Figure 7.23: Results for $f_{12} = 30$, $f_{2C} = 400$ and $A_{C1} = 1 \times 10^{-10}$ for the "direct transfer" model. The values of the temperatures which correspond to the parameters T_{2C} are shown on the diagram. The other parameters were: $N_1 = 1 \times 10^{13}$, $N_2 = 1 \times 10^{13}$,$A_{C2} = 1 \times 10^{-11}$ and $A_r = 5 \times 10^{-9}$.

previous model there was a mixture of sharp and slower, "curved" rises. There is still a slight curve evident in the initial rise for this set of parameters but figure 7.20 shows essentially identical decays but with very sharp initial rises. This was achieved by increasing the value of A_{C1} which was shown earlier to have this effect and by increasing the value of A_r to compensate for the slower time scale of the decays.

The decay curves now begin to resemble much more closely the experimental ones although, as for the previous model, the 125°C curve decays too slowly and there is a problem quantitatively with the values of the maxima of the various decays. The relative experimental maxima were much closer to one another and any thermal quenching would not seem to be able to account for the difference seen between theory and experiment.

In figure 7.21 the absolute temperature values were decreased (in a similar way to as before) which had the same effect as before, namely to make the lower temperature decays almost identical and the higher temperature decays, at least qualitatively, resemble experiment.

In figure 7.22 the value of f_{2C} was reduced with the predictable effect of changing the lower temperature decays (whose thermal decay parameters were of the same order) but not the higher temperature ones. By increasing f_{2C}, as in figure 7.23, the decays begin to resemble each other as f_{2C} begins to dominate over the thermal terms.

7.3.6 Direct Recombination Model

This model was essentially a derivative of the last model and was an attempt to obtain better quantitative agreement between the model and experiment. This was done by introducing a direct transition of the electron from the shallow trap (trap 2) to the hole trap without the conduction band having any role. This mechanism was examined in chapter 5. A similar type of mechanism has been previously proposed as a model for anomalous fading (Chen and Kirsch 1981, Templer 1986). Figure 7.24 shows the band diagram of the model whose kinetic equations were:

$$\frac{dn_1}{dt} = -f_{12}n_1 + n_C A_{C1}(N_1 - n_1), \tag{7.21}$$

$$\frac{dn_C}{dt} = f_{2C}n_2 + f_{3C}n_3 + T_{2C}n_2 - n_C A_{C1}(N_1 - n_1) - n_C A_{C2}(N_2 - n_2) - n_C A_{C3}(N_3 - n_3) - n_C A_r n_h, \tag{7.22}$$

$$\frac{dn_2}{dt} = f_{12}n_1 - f_{2C}n_2 - T_{2C}n_2 - A_{23}n_2 + n_C A_{C2}(N_2 - n_2), \tag{7.23}$$

$$\frac{dn_3}{dt} = -f_{3C}n_3 + n_C A_{C3}(N_3 - n_3), \tag{7.24}$$

$$\frac{dn_h}{dt} = -n_C A_r n_h - A_{23}n_2. \tag{7.25}$$

The basic idea behind this model was as follows: at low temperatures (say below about 75°C) the dominant recombination process would be via A_{23}, that is the direct route to the hole centre, but at higher temperatures the thermal term begins to dominate and the main recombination process is now via the conduction band and A_r. The difference introduced by this model was that at higher temperatures, A_r had competition from the deep trap 3 which means that a significant fraction of the electrons could not recombine with holes. This would reduce the higher temperature

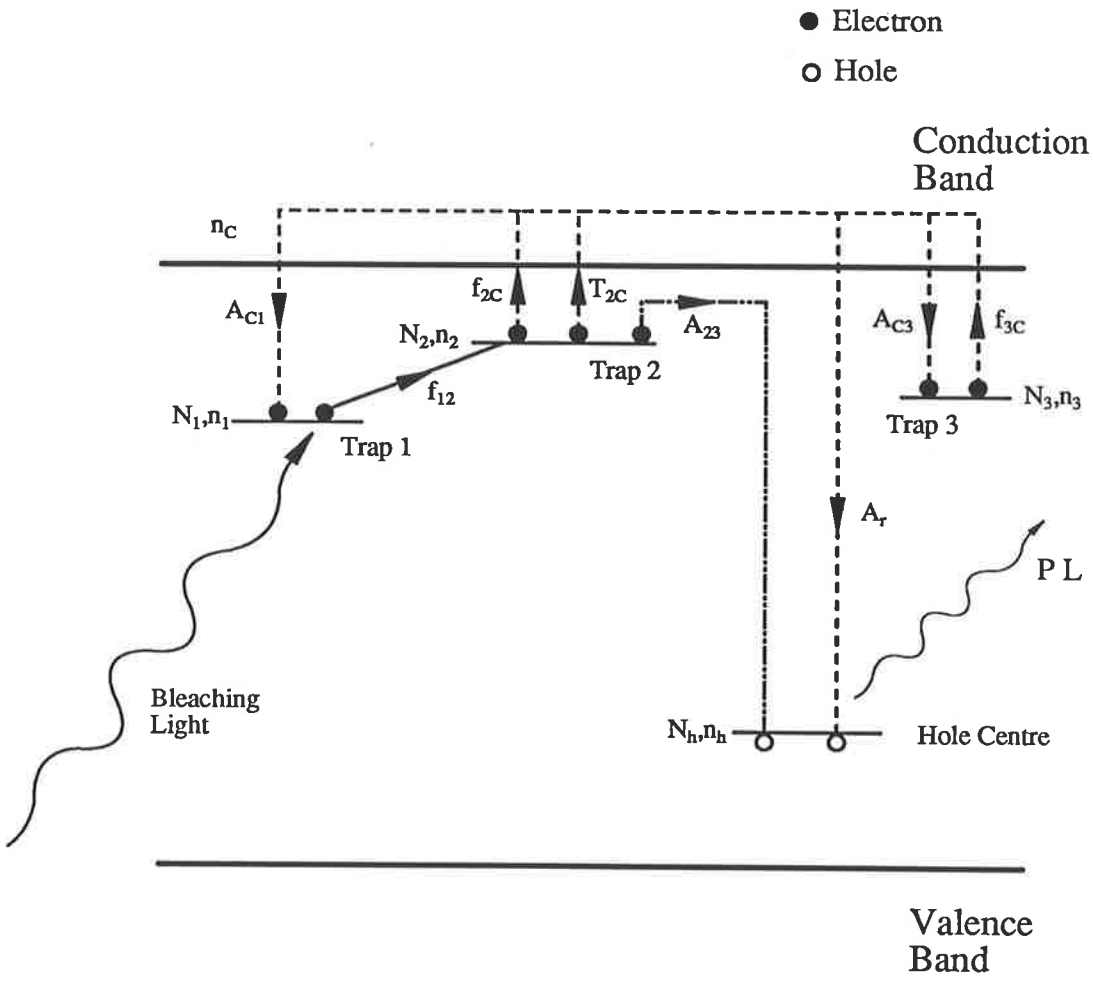

Figure 7.24: Schematic band diagram for the direct recombination model. The dotted lines indicate the general trajectory of the electrons and the arrows the direction of the transition.

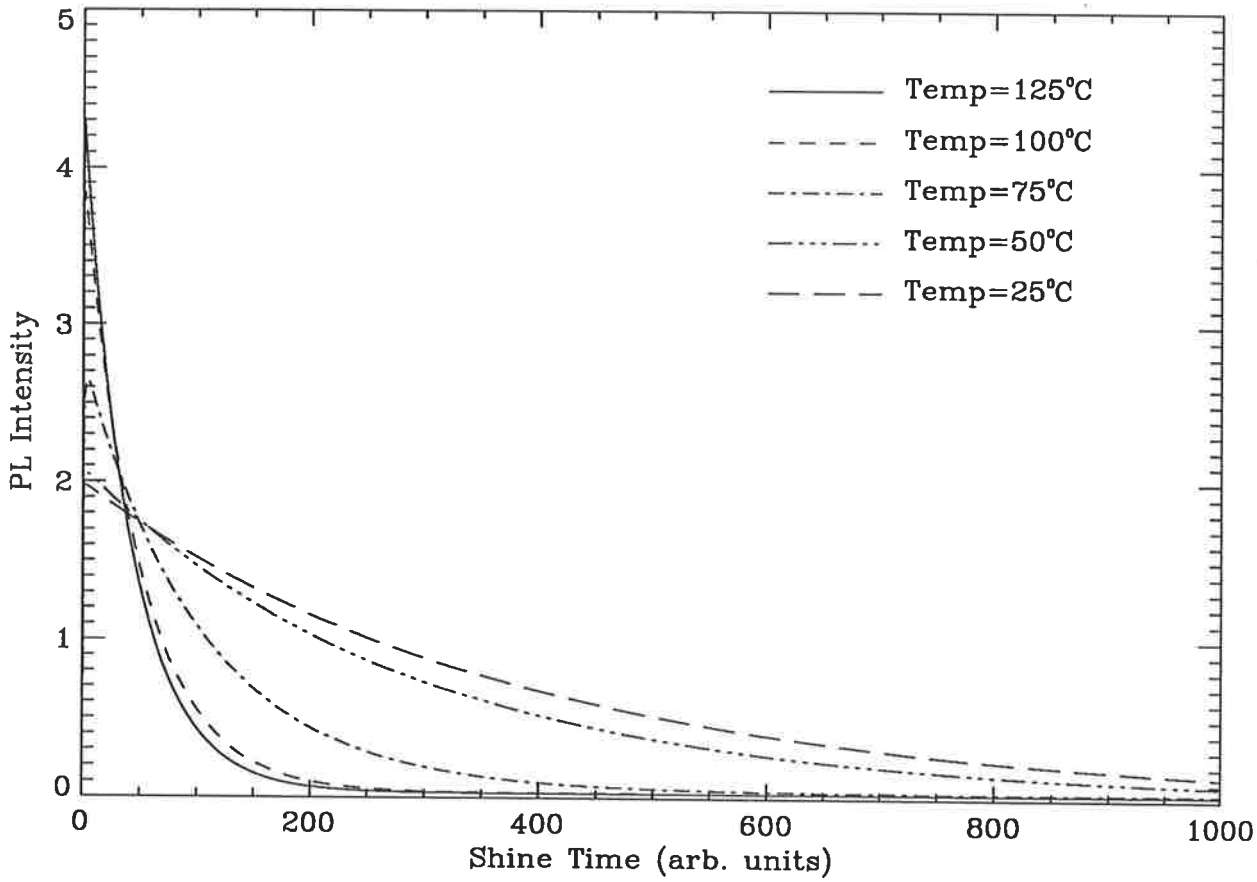

Figure 7.25: Results for $f_{12} = 1 \times 10^5$, $f_{2C} = 100$ and $A_{C1} = 5 \times 10^{-10}$ for the "direct recombination" model. The values of the temperatures which correspond to the parameters T_{2C} are shown on the diagram. The other parameters were: $f_{3C} = 2, f_{24} = 50$, $N_1 = 1 \times 10^{13}$, $N_2 = 1 \times 10^{13}$, $N_3 = 1 \times 10^{13}$, $A_{C2} = 1 \times 10^{-11}$, $A_{C3} = 5 \times 10^{-11}$, $A_{23} = 25$ and $A_r = 5 \times 10^{-9}$.

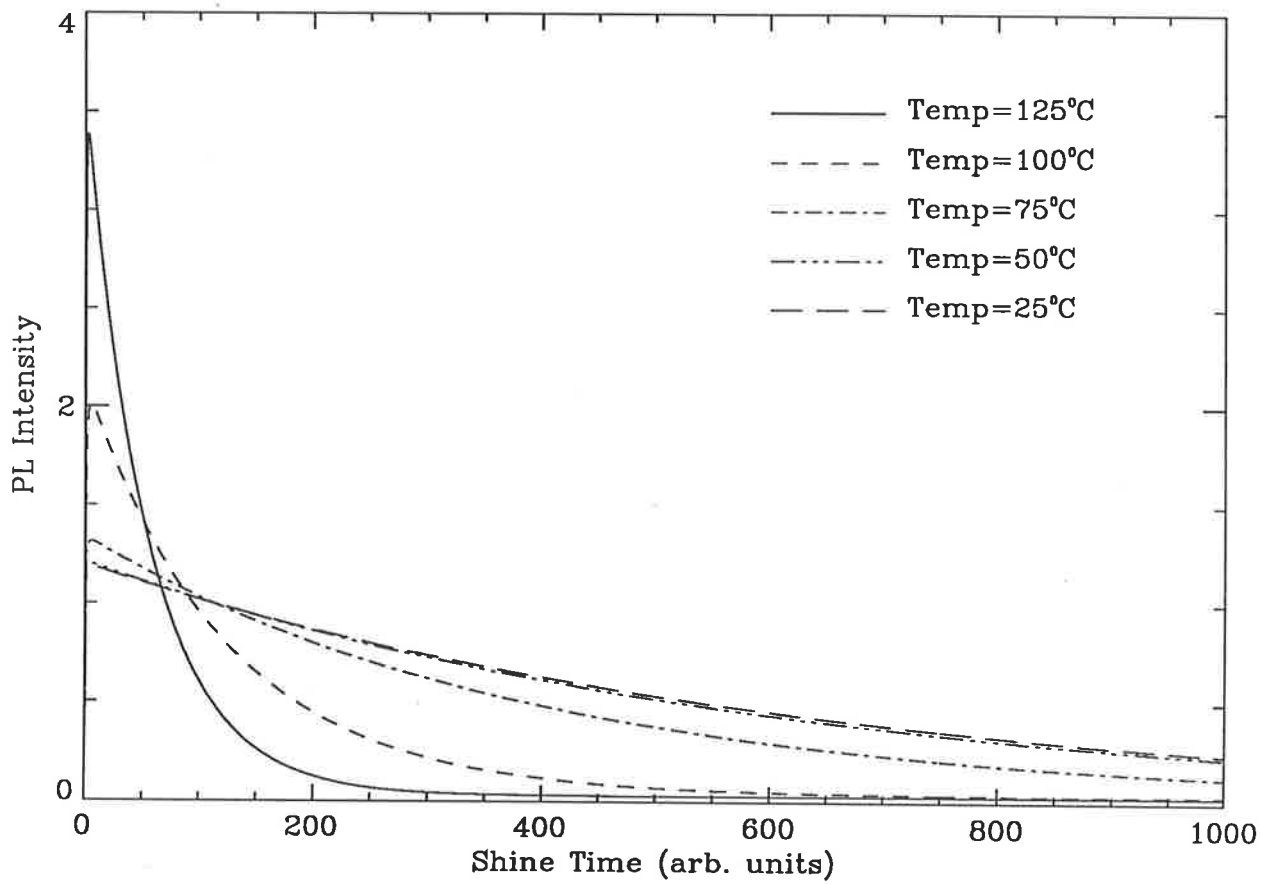

Figure 7.26: Results for $f_{12} = 1 \times 10^5$, $f_{2C} = 30$ and $A_{C1} = 5 \times 10^{-10}$ for the "direct recombination" model. The values of the temperatures which correspond to the parameters T_{2C} are shown on the diagram and were scaled relative to figure 7.25 (see text). The other parameters were: $f_{3C} = 2$,$f_{24} = 50$, $N_1 = 1 \times 10^{13}$, $N_2 = 1 \times 10^{13}$, $N_3 = 1 \times 10^{13}$, $A_{C2} = 1 \times 10^{-11}$, $A_{C3} = 5 \times 10^{-11}$, $A_{23} = 15$ and $A_r = 5 \times 10^{-9}$.

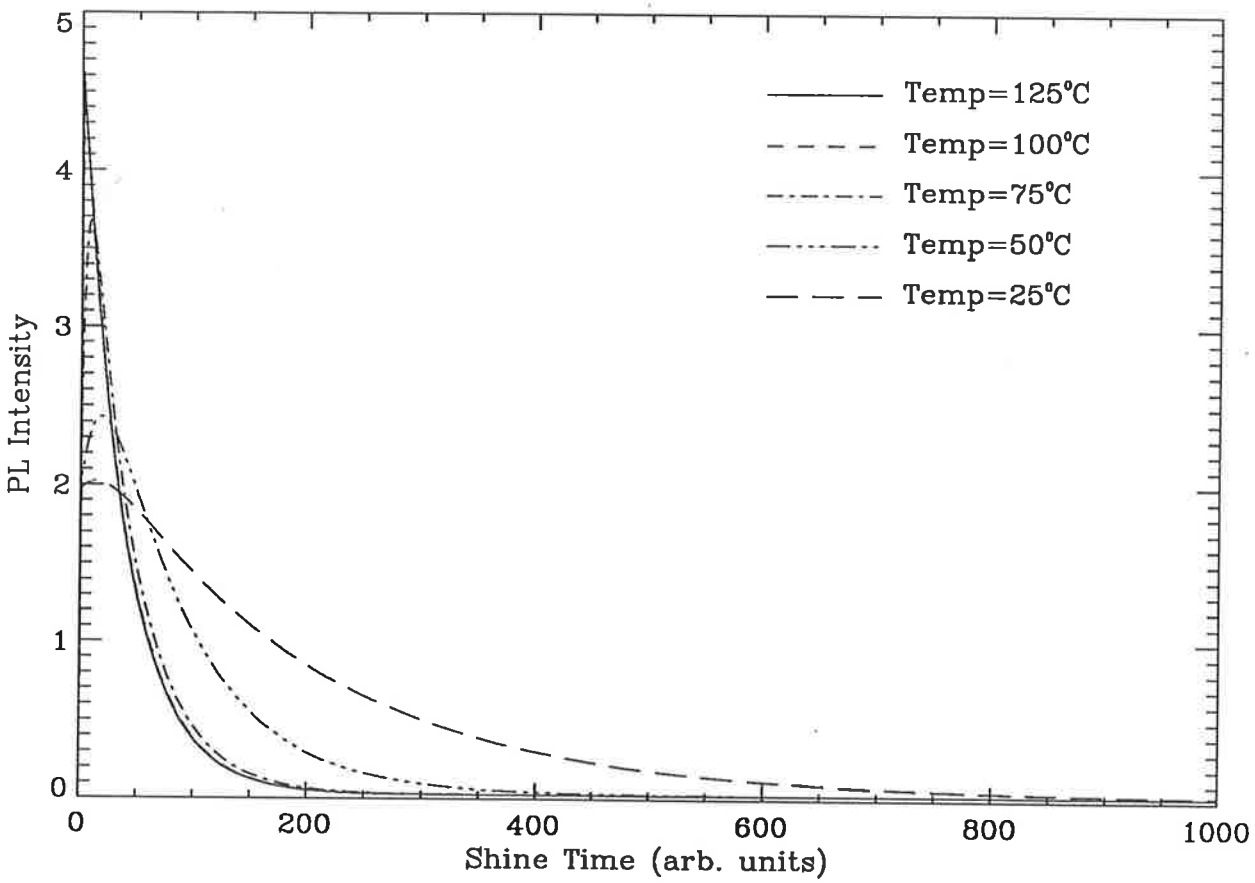

Figure 7.27: Results for $f_{12} = 1 \times 10^5$, $f_{2C} = 100$ and $A_{C1} = 5 \times 10^{-12}$ for the "direct recombination" model. The values of the temperatures which correspond to the parameters T_{2C} are shown on the diagram. The other parameters were: $f_{3C} = 2, f_{24} = 50$, $N_1 = 1 \times 10^{13}$, $N_2 = 1 \times 10^{13}$, $N_3 = 1 \times 10^{13}$, $A_{C2} = 1 \times 10^{-11}$, $A_{C3} = 5 \times 10^{-11}$, $A_{23} = 25$ and $A_r = 5 \times 10^{-9}$.

decay maxima relative to the lower temperature ones without the need for thermal quenching.

Figure 7.25 shows what is probably the best fit to the experimental decays obtained from this model. Qualitatively the decays are similar to those of figure 7.20 and quantitatively there is a considerable improvement although, as before, the 125°C decay was still not steep enough relative to the 100°C decay curve. To obtain this necessary relative decay rate, in figure 7.26 the temperature scale was reduced but with the loss of any discrimination between the lower temperature peaks and also a loss in any qualitative agreement with experiment.

In figure 7.27 the value of A_{C1} was reduced by a factor of 100 with the expected result of the loss of the initial sharp rise and fall.

7.4 Discussion

The last two models studied were reasonably successful in qualitatively matching the experimental decay curves except for the 125°C curve. The difference between the various decay curves depends on the parameters calculated from equation 7.16. These, in turn, depend on the value of the thermal depth, E, of the shallow trap. A smaller value of E would have the effect of reducing the relative range of these parameters so that the difference between the 100° and 125° decays curves would be larger.

Figure 7.28 shows the decay curves for the last model studied with the thermal parameters calculated from $E = 0.80eV$ (Aitken 1985). There is now improved high and low temperature decay discrimination which could indicate that for quartz

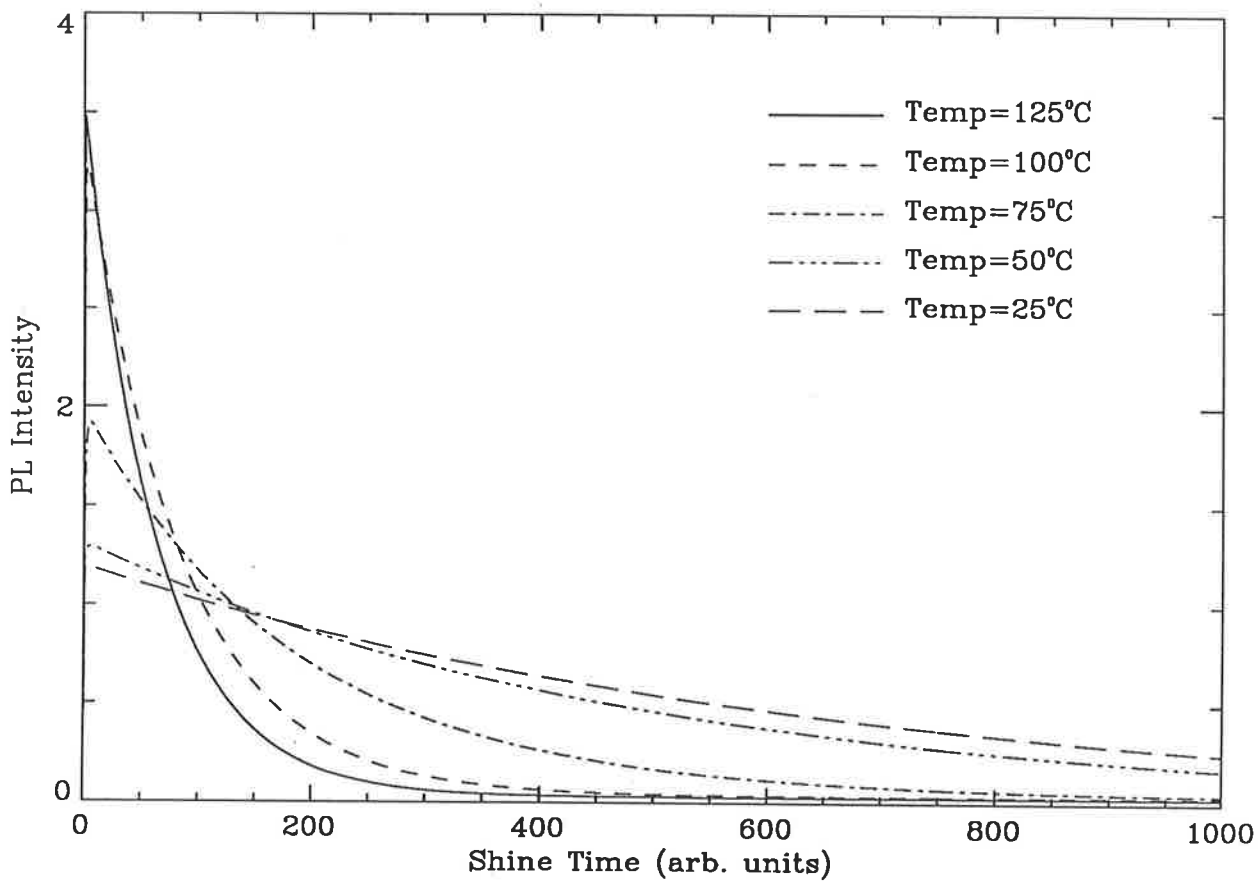

Figure 7.28: Results for $f_{12} = 1 \times 10^5$, $f_{2C} = 100$ and $A_{C1} = 5 \times 10^{-10}$ for the "direct recombination" model. The values of the temperatures which correspond to the parameters T_{2C} are shown on the diagram. In this figure the values of the temperature parameters were calculated using a trap depth parameter E of 0.80eV. The other parameters were: $f_{3C} = 2, f_{24} = 50$, $N_1 = 1 \times 10^{13}$, $N_2 = 1 \times 10^{13}$, $N_3 = 1 \times 10^{13}$, $A_{C2} = 1 \times 10^{-11}$, $A_{C3} = 5 \times 10^{-11}$, $A_{23} = 25$ and $A_r = 5 \times 10^{-9}$.

bleaching, the thermal depth of the 110°C trap is effectively lower than is usually quoted.

In conclusion then, it has been demonstrated that the models studied in this chapter have the ability to reproduce, with varying degrees of success, many of the features observed experimentally, with the last model the most successful of all. It therefore, would seem that the decay process was not a simple one. A direct relationship between the 325°C trap ("trap 1") and the 110°C trap ("trap 2"), together with a direct transition to the recombination centre seemed to be sufficient to explain the experimental data. The results from the models may indicate that, for some of the decays at certain temperatures, the conduction band is relatively unimportant.

These findings are partially comparable to those of Smith (1990). Smith used essentially the "thermally shallow competitor trap" model at room temperature to obtain good agreement with experimental decay curves for a sample of quartz. No calculated results were presented for decays at other temperatures.

In one way, at least, this last model makes a definite prediction concerning the emission spectrum of quartz bleached at different temperatures. Assuming that the decay process was exactly as described by this model, the emission spectra for low temperature (at 25°C) bleached quartz should show a reduction in primarily one wavelength band relative to any others. For quartz bleached at higher temperatures, though, all spectral emission centres should be reduced since the main decay route is via the conduction band and hence all emission centres are accessible to the electrons in the conduction band for recombination. Figure 7.29 shows experimental glow curves similar to those in chapter 5 for WK quartz (compare with figure 5.9.2). The

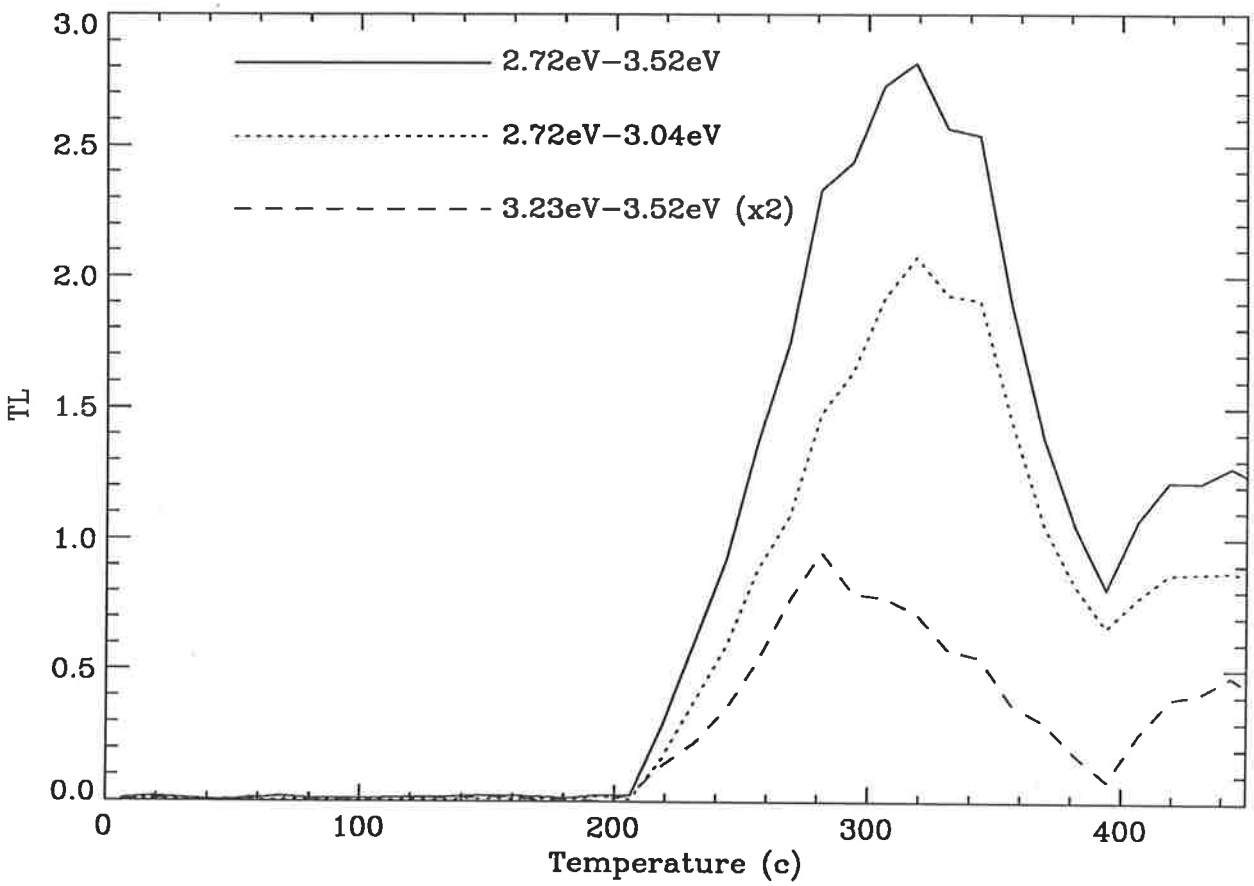

Figure 7.29: Glow curves of natural WK quartz which was bleached for 8.0 minutes with 550 nm light. The holding temperature of the sample during the bleach was 110°C.

only difference is that for this sample the temperature of the quartz was 110°C during the 8 minute bleach by 550 nm light. There appears to be no significant difference caused by bleaching the sample at this temperature. The lower energy curve has not been affected in the way the last model predicted. This result is only preliminary and a more detailed series of bleaching experiments conducted at many more holding temperature would be required to categorically rule out this model.

Chapter 8

Final Chapter: Where Next?

The last chapter of this thesis has been reserved for a brief summary of the results presented and to suggest possible future directions.

The early chapters dealt mainly with developments aimed at extending the spectral response of the Fourier transform spectrometer. This was achieved mainly by replacing the optical components with ultra–violet transmitting ones and by replacing the existing photomultiplier with one with an extended red response. In addition the software for analysing the raw data was also modified to reduce the level of noise carried over from the interferograms to the spectra during Fourier transformation.

Ideally the MS–DOS computer currently used to analyse the data would also control the equipment recording the data. This would avoid the need for transferring the data from one computer to another and would allow the spectra to be calculated immediately if desired. A more modern MS–DOS computer would also allow greater flexibility in the analysis procedure and reduce the amount of time required for transforming large batches of files.

The photomultiplier used in each experiment depended on the temperature of the TL peaks to be measured. For materials with peaks above about 300°C a photo-

multiplier with little red response had to be used because of the incandescent glow from the sample and its disc. If a filter could be found which attenuated this glow below about 550 nm then it may be possible to use the extended red response PMT for all the experiments. The equipment has the potential to be further automated particularly with regard to an automatic flow valve for the argon oven gas and also an automatic electronic shutter for the PMT.

Chapter four dealt with a brief review of many TL materials namely: phosphors, calcites, sulphur activated minerals and a small selection of unusual feldspars. The work on the dosimeters and feldspar samples continued research previously carried out in this department. These studies showed the effectiveness of the modified spectrometer and allowed quite dim materials to be studied. Some interesting results were found particularly for the calcite samples where a previously unreported dysprosium impurity was discovered. The feldspar samples examined proved the effectiveness of the spectrometer modifications by the recording of emission in the ultra–violet and in the red. These feldspar samples were unusual in that they contained a large fraction of quartz which was shown up by its characteristic 110°C emission. Akber (1986) has suggested that with the extended spectral response of the equipment the effect of anomalous fading could be investigated. There is also great scope for work aimed at understanding the bleaching of feldspars and experiments similar to those described in chapter five for quartz might be helpful to this end, that is to see if any of the emission centres of the feldspar samples show particular sensitivity to bleaching. If this proved to be the case then PL dating techniques, similar to those used to date sand dunes, may be applicable. The extension of the spectral range of the spectrometer

means that many more emission centres can be examined to see if this proposition is, in fact, feasible.

The work on the changes with bleaching in the TL emission spectra of several quartz samples, showed an interesting effect. Only one emission band, above about 3.0 eV, was affected. The research carried out sought to examine the effect of many different bleaching treatments on both natural and irradiated samples. This work has indicated the possible directions of future research both at furthering our understanding of the bleaching mechanisms and at developing experimental techniques for sediment dating. One problem encountered was the intrinsic sample variability of the quartz samples and so a specific study on one sample, bleached at one wavelength, using many discs would reduce statistical uncertainty by averaging and would allow a more definitive study of which emission centres were being bleached. It is difficult to be too definite about how a particular series of experiments would further our knowledge of this unusual process because very little research has been done and hence there is great scope for many research directions. In this study only a limited number of bleach times were used and information about changes in the emission spectra after much longer bleach times would be useful. This would be particularly useful for ultra–violet bleaches to see how all the emission centres respond. Also similar research on quartz samples from different parts of the world could enable a standardization of dating techniques. As mentioned earlier, if a red attenuating filter could be found, most of this research could be repeated and the fluctuations in the red end of the spectra caused by the poor response of the PMT used could be lessened. Also the effect of bleaching on centres emitting above about 600 nm could

be studied. This study concentrated on the bleaching of peaks above about 150°C. In later chapters the 110°C peak was shown to be important in the decay process. A study aimed at examining the bleaching of this peak might help to narrow down possible models for this process. These results were used in chapter 7 to aid in the development of realistic models to describe the decay mechanism of a quartz sample. The findings in this chapter have been used already to demonstrate a possible new dating technique (Prescott personal communication). This technique is largely independent of the amount of resetting that might have occurred and hence removes one of the problems of earlier techniques (see chapter 1). The method involves the use of selective filters to specifically measure the 380 nm emission and to remove only this component during laboratory illumination. In this way the regeneration of the 325°C peak after bleaching can be measured. This technique has also been independently suggested by Franklin and Hornyak (personal communication).

The final part of this thesis described research carried out on the phenomenon of photoluminescence of quartz and followed on from the work done earlier in chapter 5. Experimentally the study showed that a Xenon lamp is suitable for measuring this emission and avoids the need for expensive laser systems. The decay curves of two quartz samples were measured at different holding temperatures and showed the importance of the 110°C peak in the decay process at room temperature. This was evident from the way the decay curves were modified by the holding temperature and that above about 100°C little change in the shape of the decay curves was observed. These decay curves were not simple exponentials, but exhibited slowly decaying tails. The decay curves of one of the samples were used in chapter 7 to compare with

theoretical models of the decay process generated on a computer. Once more it would be useful to perform similar measurements on a variety of samples of differing provenance. Also previous work indicated how peaks near 150°C may also bleach and so decay measurements on irradiated samples would be useful. Measurements could be performed with different combinations of output filters to see how the photoluminescence varied (if at all) when samples are bleached at the different temperatures. The decay curves of one of the samples were used in chapter 7 to compare with theoretical models of the decay process generated on a computer.

Finally in chapter 7, a quantitative model is suggested to account for the decay curves presented in the preceding chapter. Several models were examined with the result that it appeared that the 110°C peak was closely linked with the light sensitive 325°C peak. The last model studied made some predictions concerning the possibility that a direct transition between the 325°C peak and the 110°C peak may exist. These predictions were only briefly tested here and more extensive experimental tests need to be made in order to validate these models or to suggest new ones. Only one sample of quartz was used as a comparison and it would be useful to see how similar the decay process might be between samples of different origin.

Sed haec pruis fuere

Catullus – Carmina.

References

Aitken M.J., (1985),"Thermoluminescence Dating", Academic Press, London.

Akber R.A., (1986), *Ph.D. Thesis*, University of Adelaide, Adelaide, South Australia.

Akber R.A. Robertson G.B. and Prescott J.R., (1988), *Nucl. Tracks Radiat. Meas.*, **14**, 21–25.

Aryamany–Mugisha H and Williams R.P., (1985), *Appl. Spect.*, **39**, 693–697.

Bailiff I.K., Morris D.A. and Aitken M.J., (1977), *J. Phys E*, **10**, 1156–1160.

Bakas G.V., (1984), *Rad. Prot. Dosim.*, **9**, 301–305.

Bakhtin A.I., (1976), *Sov. Phys. Crystallogr.*, **21**, 596–598.

Becker K., (1973), *"Solid State Dosimetry"*, CRC, Cleveland.

Becker K., (1974), *Health Physics* , **27**, 321–334.

Bell R.J., (1972), *"Introductory Fourier Transform Spectroscopy"*, Academic Press, New York.

Berger G.W., (1988), *Geol. Soc. of America Special Paper 227*, 13–50.

Binder W. and Cameron J.R., (1969), *Health Physics*, **17**, 613–618.

Binder W., Disterhoft S. and Cameron J.R., (1968), *Proc. of Second Int. Conf. on Lumin. Dosim.*, (Gatlinberg, U.S.A.) US Atomic Energy Com. Conf 680 920 43–53.

de Boer J.H. and van Geel W., (1935), *Physica*, **2**, 286–298.

Bothner M.H. and Johnson N.M., (1969), *J. Geophys. Research*, **74**, 5331–5338.

Brunner G.O., (1964), *Helv. Phys. Acta*, **37**, 51–54.

Calvert R.L. and Danby R.L., (1984), *Phys. Status Solidi a*, **83**, 597–604.

Chamberlain J., (1979), *"The Principles of Interferometric Spectroscopy"*, J. Wiley and Sons, Chichester.

Chen R. and Kirsh Y., (1981), *"Analysis of Thermally Stimulated Processes"*, International series on the Science of the Solid State 15, Oxford, Pergamon Press.

Chen R., McKeever S.W.S. and Durrani S.A., (1981), *Phys Rev. B*, **24**, 4931–4944.

Chen R., Yang X.H. and McKeever S.W.S., (1988), *J. Phys D:Appl. Phys.*, **21**, 1452–1457.

Connes J., (1960), *Thesis*, University of Paris, France, unsighted.

Connes P., (1984), *Infrared Phys.*, **24**, 69–93.

Cooke D.W., Roberts H.E. and Alexander C., (1977), *J. Appl. Phys.*, **49**, 3451–3457.

Danby R.J., Boas J.F., Calvert R.L. and Pilbrow J.R., (1982), *J. Phys. C: Solid State Phys.*, **15**, 2483–2493.

Daniels F. and Saunders D.F., (1951), *"The Thermoluminescence of Crystals"*, Final Rep. USAEC, AECU 1983.

David M. and Sunta M., (1981), *Indian J. Pure Appl. Phys*, **19**, 1041–1047.

Debenham N.C., (1983), *Nature*, **304**, 151–156.

Debenham N.C. and Aitken M.J., (1984), *Archaeometry*, **26**, 155–170.

Dieke G.H. and Crosswhite H.M., (1963), *Appl. Opt.*, **2**, 675–686.

Down J.S., Flower R., Strain J.A. and Townsend P.D., (1985), *Nucl. Tracks*, **10**, 581–589.

Duke C.B. and Holonyak Jr.N., (1973), *Physics Today (Dec.)*, **26**, 23–31.

Durrani S.A., Groom P.J., Khazal K.A.R. and McKeever S.W.S., (1977), *J. Phys. D:Appl. Phys.*, **10**, 1351–1361.

Dutta B.C. and Ghosh A.K., (1956), *Indian J. Phys.*, **30**, 570–581.

Ellis S.C. and Rossiter M.J., (1969), *Int. J. Appl. Rad. Isotop.*, **20**, 201–203.

Evans R.C., (1966), *"An Introduction to Crystal Chemistry"*, Cambridge Universty Press, Cambridge.

Fairchild R.G., Mattern P.L., Lengweiler K. and Levy P.W., (1978), *J. Appl. Phys.*, **49**, 4512–4522.

Fellgett P.B., (1951), *Thesis*, University of Cambridge.

Fox P.J., Akber R.A. and Prescott J.R., (1988), *J. Phys. D: Appl. Phys.*, **21**, 189–193.

Gebbie H.A., (1984), *Infrared Phys.*, **24**, 105–109.

Griffiths J.H.E., Owen J. and Ward I.M., (1954), *"Defects in Crystalline Solids, report of Bristol conference"*, London, Physical Society.

Halliburton L.E., Koumvakalis N., Markes M.E. and Martin J.J., (1981), *J. Appl. Phys.*, **52**, 3565–3574.

Halperin A. and Kristianpoller N., (1958), *J. Opt. Soc. Am.*, **48**, 996–1000.

Harris A.M. and Jackson (1970), *J. Phys. E: Sci. Instrum.*, **3**, 374–376.

Hashimoto T., Koyanagi A., Hayashi Y and Sotobayashi T., (1986), *Geochem J.*, **20**, 111–118.

Herring D.F. and Compton D.M.J., (1971), *in Proc. Third Int. Conf. Computers in Radiotherapy*, Glasgow, 51.

Hornyak W.F. and Franklin A.D., (1988), *J. of Luminescence*, **42**, 89–96.

Horowitz Y.S., (1984), *in "Thermoluminescence and Thermoluminescence Dosimetry"*, vol 1, Y.S.Horowitz ed., (C.R.C., Boca Raton), 1–17.

Horowitz Y.S., (1984), *in "Thermoluminescence and Thermoluminescence Dosimetry"*, vol 1, Y.S.Horowitz ed., (C.R.C., Boca Raton), 89–172.

Huntley D.J., (1985), *Phys. Chem. Minerals*, **12**, 122–127.

Huntley D.J., Godfrey-Smith D.I., Thewalt M.L.W., (1985), *Nature*, **313**, 105–107.

Huntley D.J., Godfrey-Smith D.I., Thewalt M.L.W. and Berger G.W., (1988a), *J. Luminescence*, **39**, 123–136.

Huntley D.J., Godfrey-Smith D.I., Thewalt M.L.W., Prescott J.R. and Hutton J.T., (1988b), *Nucl. Tracks Radiat. Meas.*, **14**, 27–33.

Huntley D.J. and Johnson H.P., (1976), *Can. J. Earth Sci.*, **13**, 593–596.

Imaeda K., Kitajima T., Kuga K., Miono S., Misaki A., Nakamura M., Ninagawa K., Okamoto Y., Saavedra O., Saito T., Takahashi N., Takano Y., Tomyama T., Wada T., Yamamoto I. and Yamashita Y., (1985), *Nucl. Inst. Meth.*, **A241**, 567–571.

Jacquinot P., (1954), *J. Opt. Soc. Am.*, **44**, 761–765.

Jacquinot P., (1984), *Infrared Phys.*, **24**, .

Jacquinot P. and Dufour C., (1948), *J. Rech. du Centre Nat. Rech. Sci. Lab. Bellevue (Paris)*, **6**, 91.

Jensen H.E., (1982), *Ph.D. Thesis*, University of Adelaide, Adelaide, South Australia.

Jensen H.E. and Prescott J.R., (1982), *PACT*, **6**, 542–549.

Kittel C., (1976), *"Introduction to Solid State Physics"*, J. Wiley and Sons, New York.

Klasens H.A., (1946), *Nature*, **158**, 306–307.

Koumvakalis N., (1980), *J. Appl. Phys.*, **51**, 5528–5532.

Kristianpoller N., (1983), *PACT*, **9**, 153–162.

Krystek M., (1980), *Phys. Status Solidi a*, **57**, 171–178.

Levy P.W., (1979), *PACT*, **3**, 466–480.

Levy P.W., (1982), *PACT*, **6**, 224–242.

Levy P.W., Mattern P.L. and Lengweiler K., (1971), *Modern Geology*, **2**, 295–297.

Loewenstein E.V., (1966), *Appl Optics*, **5**, 845–854.

MacKey J.H., (1963), *J. Chem. Phys.*, **39**, 74–??.

McKeever S.W.S., Ahmed K., Chandler P.J., Stain J.A., Rendell H.M. and Townsend P.D., (1983), *PACT*, **9**, 187–204.

McKeever S.W.S., (1984), *J. Appl.Phys.*, **56**, 2883–2889.

McKeever S.W.S., (1984), *"Thermoluminescence of Solids"*, Cambridge University Press, Cambridge.

McKeever S.W.S., (1984), *Radiat. Prot. Dosim.*, **8**, 81–98.

McKeever S.W.S., Chen C.Y. and Halliburton L.E., (1985), *Nucl. Tracks*, **10**, 489–495.

McKeever S.W.S., Chen R., Groom P.J. and Durrani S.A., (1980), *Nucl. Inst. Methods*, **175**, 43–44.

McKeever S.W.S. and Sears D.W., (1979), *Meteoritics*, **14**, 29–41.

McMorris D.W., (1971), *J. Geophys. Res.*, **76**, 7875–7887.

Malik D.M., Kohnke E.E. and Sibley W.A., (1981), *J. Appl. Phys.*, **52**, 3600–3605.

Marfunin A.S., (1979), *"Spectroscopy, Luminescence and Radiation Centers in Minerals"*, Springer, Berlin.

Mariano A.M., Ito J. and Ring P.J., (1973), *Geol. Soc. Amer. Abstr. Progr*, **5**, 726.

Matthews R.J. and Stoebe T.G., (1982), *J. Phys C:Solid State Phys.*, **15**, 6271–6280.

Mattern P.L., Lengweiler K. and Levy P.W., (1971), *Mod. Geol.*, **2**, 293–294.

Maxia V., (1978), *Phys. Rev. B*, **17**, 3262–3268.

Maxia V., (1980), *Phys. Rev. B*, **21**, 749–759.

Medlin W.L., (1963), *J. Chemical Phys.*, **38**, 1132–1143.

Mehta S.K. and Sengupta S., (1979), *Nucl. Inst. Meth.*, **164**, 349–354.

Mertz L., (1965), *"Transformations in Optics"* , Wiley, New York.

Merz J.L. and Pershan P.S., (1967), *Phys. Rev.*, **162**, 217–247.

Michelson A.A., (1887), *Phil. Mag.*, **24**, 463.

Mitchell E.W. and Paige E.G.S., (1956), *Phil. Mag.*, **1**, 1085–1115.

Morse H.W., (1905), *Astrophys. J.*, **21**, 410–417.

Mott N.F. and Gurney R.W., (1940), *"Electronic Processes in Ionic Crystals"*, Oxford University Press, Oxford.

Nambi K.S.V., Bapat V.N. and Ganguly A.K., (1974), *J. Phys. C:Solid State Phys.*, **7**, 4403–4415.

Nelson C.M. and Weeks R.A., (1960), *J. Amer. Ceramic Soc.*, **43**, 396–399.

O'Brien M.C.M., (1955), *Proc. Royal Soc.*, **A231**, 404–414.

Okamoto Y., Kawaguchi S. Kino S., Miono S., Kitajima T., Misaki A. and Saito T, (1986), *Nucl. Instrum. Methods Phys. Res. A*, **243**, 219–224.

Prescott J.R., Akber R.A. and Gartia R.K., (1990), *in "Spectroscopic Characterization of Minerals and Their Surfaces"*,L.M. Coyne, S.W.S. McKeever and D.F. Blake eds., (Am. Chem. Soc.), ACS Symposium Series No.415, 180–189.

Prescott J.R., Fox P.J., Akber R.A. and Jensen H.E., (1989), *Applied Optics*, **27**, 3496–3502.

Press O., Flannery B.P., Teukolsky A. and Vetterling W.T., (1986), *"Numerical Recipes"*, Cambridge University Press, New York.

Roberts W.L., Rapp Jr.G.R. and Weber J., (1974), *"Encyclopedia of Minerals"*, van Nortrand Reinhold Company, New York.

Robertson G.B. and Prescott J.R., (1988), *Nucl. Tracks Radiat. Meas.*, **14**, 299–305.

Rubens H. and Wood R.W., (1911), *Phil. Mag.*, **21**, 249–261.

Schlesinger M., (1964), *Phys. Letters*, **10**, 49–50.

Schön M., (1951), *Naturwiss*, **38**, 235.

Schonkeren J.M., (1970), *"Photomultipliers"*, Philips Publication Dept., Eindhoven.

Serebrennikov A.I., Valter A.A., Mashkovtrev R.I. and Scherbakova M., (1982), *Phys. Chem. Miner.*, **8**, 153–157.

Singhvi A.K., Sharma Y.P. and Agrawal D.P., (1982), *Nature*, **295**, 313–315.

Smith B.W., (1990), in press.

Smith B.W. and Prescott J.R., (1987), *Australian J. Earth Sci.*, **34**, 335–342.

Smith B.W., Smart P.L., Andrews J.N. and Symons M.C.R., (1985), *in "ESR Dating and Dosimetry"*, Ikeya M. and Miki T. ed.s, (Ionics, Tokyo), 49–59.

Smith B.W., Smart P.L., Fox P.J., Prescott J.R. and Symons M.C.R., (1989), *Appl. Rad. Isotop.*, **40**, 1095–1103.

Spooner N.A., (1987), *M.Sc. Thesis*, University of Adelaide, Adelaide, South Australia.

Staplebroek M, Griscom D.L., Friebele E.J. and Sigel G.H., (1976), *J. non-Crys. Solids*, **32**, 313–326.

Stoebe T.G. and Morgan M.D., (1984), *in "Thermoluminescence and Thermoluminescence Dosimetry"*, vol 1, Y.S.Horowitz ed., (C.R.C., Boca Raton), 19–47.

Stubley E.A. and Horlich G., (1985), *Appl. Spec.*, **39**, 800–804.

Sunta C.M., (1984), *Radiat. Prot. Dosim.*, **8**, 25–44.

Tarashchan A.N., (1978), *"Luminescence of Minerals"*, Naukova Dumka, Kiev.

Templer R.H., (1986), *Radiat. Prot. Dosim.*, **17**, 493–497.

Thorne A.P., Harris C.J., Wynne-Jones I., Learner R.C.M. and Cox G., (1987), *J. Phys E:Sci. Intrum.*, **20**, 54–60.

Tittel H.O., Thiel E., Trakowski W., Schneider M and Heinrich W., (1984), *Infrared Phys.*, **24**, 323–328.

Townsend P.D. and Kelly J.C., (1973), *" Colour Centres and Imperfections in Insulators and Semiconductors"*, Sussex University Press, London.

Townsend P.D., Ahmed K., Chandler P.J., McKeever S.W.S. and Whitlow H.J., (1983), *Radiat. Effects*, **72**, 245–257.

Vanessa G.A. and Sakai H., (1967), *Prog. Opt.*, **6**, 261–330.

Weil J.A., (1975), *Radiat. Effects*, **26**, 261–265.

Weil J.A., (1984), *Phys. Chem. Miner.*, **10**, 149–165.

Wintle A.G. and Huntley D.J., (1979), *PACT*, **3**, 374–380.

Wintle A.G. and Huntley D.J., (1980), *Canadian J. Earth Sci.*, **17**, 348–360.

Wintle A.G. and Huntley D.J., (1982), *Quat. Sci. Rev.*, **1**, 31–53.

Wyckoff R.G., (1960), *"Crystal Structures Volume 1"*, Interscience Publishers, New York.

Yamashita T., Nada N., Onishi H. and Kitamura S., (1968), *Proc. Second Int. Conf. Luminescence Dosimetry*, (Gatlinberg, U.S.A.), U.S. Atomic Energy Commission Conf. 680 920, 4–17.

Yamashita N., Yamamoto I., Ninagawa K., Wada T., Yamashita Y. and Nakao Y., (1985), *Japan. J. Appl. Phys.*, **24**, 1174–1180.